

PhD-Thesis in Theoretical Physics

# Thermal Dilepton Rates from Quenched Lattice QCD

A study of thermal spectral functions in the continuum  
limit of quenched lattice QCD, at vanishing and finite  
momentum



## Dissertation

zur Erlangung des Doktorgrades  
an der Fakultät für Physik  
der Universität Bielefeld

vorgelegt von  
Anthony Francis

Bielefeld  
September 2011



# Thermal Dilepton Rates from Quenched Lattice QCD

## A study of thermal spectral functions in the continuum limit of quenched lattice QCD, at vanishing and finite momentum

---

ABSTRACT: We study light valence quark Euclidean correlation functions in finite temperature lattice QCD. The calculations have been performed in quenched lattice QCD at  $T \simeq 1.45T_c$  for four values of the lattice cut-off on lattices up to size  $128^3 \times 48$ . This allows to perform a continuum extrapolation of the correlation function in the Euclidean time interval  $0.2 \leq \tau T \leq 0.5$  to better than 1% accuracy. Additionally we study the temperature dependence of our results on  $128^3 \times 40$ , 32 and 16 lattices corresponding to the temperatures  $T \simeq 1.2$ , 1.45 and  $3.0T_c$ , as well as the momentum dependence in the vector case at  $T \simeq 1.45T_c$  on a lattice sized  $128^3 \times 48$ . Subsequently we compute the first two non-vanishing thermal moments of the vector and pseudo scalar meson spectral functions on all lattices. Using the constraints gained by our data analysis, we then proceed to extract information on the spectral representation of the vector correlator and discuss resulting consequences for the electrical conductivity and the thermal dilepton rate in the plasma phase. Finally we discuss the spectral function of the pseudo scalar and examine renormalization errors using the degeneracy conditions of the symmetry restored plasma phase of QCD.

---

*Dissertation zur Erlangung des Doktorgrades.*

*Vorgelegt der:* Universität Bielefeld,  
Fakultät für Physik,  
Theoretische Physik,  
Universitätsstraße 25,  
D-33615 Bielefeld.

*Datum der Abgabe:* 14. September, 2011

*Betreuung und Begutachtung durch:*  
Prof. Dr. Edwin Laermann  
Prof. Dr. Frithjof Karsch

*Author:* Anthony Sebastian Francis

*Geboren:* 26.08.1982

*E-mail Adresse:* afrancis@physik.uni-bielefeld.de

*Gedruckt auf alterungsbeständigem Papier nach DIN-ISO 9706*



# Contents

<b>Preface</b>	<b>xiii</b>
<b>1 Introduction and Motivation</b>	<b>1</b>
1.1 Quantum Chromodynamics and Yang-Mills Theory . . . . .	2
1.2 Heavy-Ion Collisions . . . . .	5
1.2.1 Production of Photons and Dileptons in Heavy-Ion Collisions . . . . .	9
1.2.2 Status of Experimental Dilepton Production Data . . . . .	11
<b>2 Foundations of Lattice Quantum Field Theory</b>	<b>13</b>
2.1 Lattice Quantum Field Theory . . . . .	14
2.2 Lattice Quantum Chromodynamics . . . . .	16
2.2.1 SU(3) Pure Yang-Mills Theory . . . . .	17
2.2.2 Quantum Chromodynamics . . . . .	18
2.2.3 Quenched QCD . . . . .	20
2.3 Fermion Discretization in Lattice QCD . . . . .	21
2.3.1 Wilson-Clover Fermions . . . . .	23
2.4 Connecting to Physics . . . . .	27
2.4.1 Renormalization . . . . .	29
2.4.2 Continuum Limit . . . . .	35
2.5 Parameters and Systematics . . . . .	37
<b>3 The Phenomenology of Spectral Functions</b>	<b>41</b>
3.1 Spectral Functions in Non-Interacting Theory . . . . .	45
3.1.1 Free Continuum Spectral Functions . . . . .	45
3.1.2 Properties of the Free Continuum Spectral Function . . . . .	51
3.1.3 Free Discretized Spectral Functions . . . . .	56
3.2 Expectations for Interacting Theory . . . . .	61
3.2.1 Linear Response and Transport Coefficients . . . . .	63
3.2.2 Heavy Quark Diffusion from the Langevin Equation . . . . .	65
3.2.3 Light Quarks in a Boltzmann Gas . . . . .	68
3.3 Hard Thermal Loops and Alternative Approaches . . . . .	71
3.3.1 Dileptons from Hard Thermal Loops . . . . .	71
3.3.2 Spectral Functions from <i>AdS/CFT</i> Correspondence . . . . .	73
<b>4 Lattice Methodology</b>	<b>75</b>
4.1 Lattice Correlation Functions and the Kernel . . . . .	76
4.2 Thermal Moments of the Correlation Function . . . . .	78

Contents

4.3	An Ill Posed Problem and its Bayesian Solution . . . . .	81
4.3.1	Maximum Entropy Method . . . . .	82
4.3.2	Remarks on the Bayesian solution . . . . .	84
4.4	An Alternative Route . . . . .	86
<b>5</b>	<b>The Vector Spectral Function at Vanishing Momentum</b>	<b>89</b>
5.1	The Vector SPF and Dilepton Rate in the Continuum at $T \simeq 1.45T_c$ . . . . .	90
5.1.1	The Spectral Function of the Time-Time Vector Correlator . . . . .	91
5.1.2	Spatial and Full Vector Correlation Functions . . . . .	93
5.1.3	Continuum Extrapolation of the Vector Correlation Function . . . . .	96
5.1.4	Computation of Thermal Moments . . . . .	97
5.1.5	Analyzing the Vector Correlator and computing the SPF . . . . .	100
5.1.6	The Thermal Dilepton Rate and Electrical Conductivity . . . . .	109
5.2	Temperature Dependence of the Vector SPF on the Lattice . . . . .	111
5.2.1	Temperature Evolution of the Thermal Moments . . . . .	114
5.2.2	Consequences for the Spectral Functions . . . . .	116
<b>6</b>	<b>The Vector Spectral Function at Finite Momentum</b>	<b>119</b>
6.1	Analyzing the Vector Correlation Function at Finite Momentum . . . . .	121
6.1.1	Thermal Moments of the Finite Momentum Correlators . . . . .	123
6.1.2	Toy Models of the Correlation Function . . . . .	125
6.2	The Time-Time Vector Channel and its Thermal Moments . . . . .	130
6.2.1	On a Non-Zero Intercept in the Longitudinal Channel . . . . .	133
6.3	Consequences for the Spectral Functions at Finite Momentum . . . . .	135
<b>7</b>	<b>Notes on the Pseudo Scalar and Other Spectral Functions</b>	<b>137</b>
7.1	The Pseudo Scalar Correlator and its Thermal Moments . . . . .	137
7.1.1	The Correlator Ratio at $T \simeq 1.45T_c$ . . . . .	138
7.1.2	The Continuum Extrapolation . . . . .	140
7.1.3	Thermal Moments of the Pseudo Scalar Correlator . . . . .	140
7.1.4	MEM analysis of the Pseudo Scalar Channel . . . . .	141
7.2	Midpoints of the Current Correlators at Finite Temperature . . . . .	143
	<b>Summary and Concluding Remarks</b>	<b>147</b>
	<b>Bibliography</b>	<b>151</b>
	<b>Acknowledgements</b>	<b>157</b>
	<b>Eigenständigkeitserklärung</b>	<b>159</b>

# List of Tables

2.1	<i>Table of renormalization constants from non-perturbative (NP) and tadpole-improved perturbative (TI) calculations in the case of vanishing mass at scale <math>\mu = 1/a</math>.</i>	35
2.2	<i>Overview of basic calculation parameters.</i>	37
2.3	<i>The AWI, RGI quark masses and their values in <math>\overline{MS}/T</math>.</i>	38
2.4	<i>Table of quark masses in the <math>\overline{MS}</math>-scheme in units of temperature at <math>T \simeq 1.45T_c</math> and in [MeV].</i>	39
2.5	<i>Number of configurations analyzed on lattices sized <math>N_\sigma^3 \times N_\tau</math>.</i>	39
3.1	<i>The trace operation yields the channel specific constants <math>a_H^{(1)}</math>, <math>a_H^{(2)}</math> and in case of non-vanishing mass <math>a_H^{(3)}</math>.</i>	47
5.1	<i>Quark number susceptibility (<math>\chi_q/T^2</math>) calculated on lattices of size <math>128^3 \times N_\tau</math>.</i>	92
5.2	<i>Several values of the vector correlation functions expressed in units of the corresponding free field values and normalized with the quark number susceptibility.</i>	95
5.3	<i>The ratio of the second thermal moment and its corresponding free value for our lattices <math>128^3 \times N_\tau</math>.</i>	100
5.4	<i>Parameters for the fits shown in Fig. 5.12.</i>	107
5.5	<i>Table of results for the quark number susceptibility over temperature <math>T/T_c</math>.</i>	113
5.6	<i>The fit parameters of the simple Breit-Wigner+continuum Ansatz for <math>T \simeq 1.45T_c</math>, <math>1.2T_c</math> and <math>T \simeq 3.0T_c</math>.</i>	117
6.1	<i>Table of available momenta in <math> p /T</math> at <math>T \simeq 1.45T_c</math> on lattices sized <math>128^3 \times 48</math>, <math>32</math>, <math>24</math> and <math>16</math>.</i>	119
6.2	<i>The ratio <math>R_H^{(2,0)}/R_H^{(2,0),free}</math> for the full, spatial, transverse and longitudinal vector channels.</i>	125
6.3	<i>The parameters of the toy models used to generate the data in Fig. 6.4.</i>	126



# List of Figures

1.1	<i>The eightfold way and the properties of quarks.</i>	2
1.2	<i>The production of hadrons by that of muons from <math>e^+e^-</math>-annihilation.</i>	4
1.3	<i>Sketch of the standard interpretation of a relativistic heavy-ion collision [18].</i>	6
1.4	<i>Experimental spectral density and the vacuum polarization in Euclidean theory.</i>	8
1.5	<i>Evolution of a HIC event and dilepton production [26].</i>	9
1.6	<i>a.) Emission of an on-shell photon. b.) Emission of a virtual photon decaying into dileptons.</i>	9
1.7	<i>Sketch of the dilepton spectrum, taken from [28].</i>	11
1.8	<i>Experimental results for dilepton rate from p-p and Au-Au collisions.</i>	12
2.1	<i>Lattice discretization of finite temperature field theory in (1+1)-Dimensions, due to the periodic boundary conditions space-time is a torus.</i>	14
2.2	<i>Infinitesimal parallelogram of continuum theory (left) and the elementary plaquette on the lattice (right).</i>	17
2.3	<i>Vacuum polarization effects are excluded in quenched QCD.</i>	21
2.4	<i>Doublers appear at the corners of the Brillouin zone.</i>	22
2.5	<i>The improvement term in the plaquettes is seen to resemble a four leaf clover, hence clover term.</i>	26
2.6	<i>The lattice spacing <math>a(\beta)</math>[fm].</i>	29
2.7	<i>The critical hopping parameter <math>\kappa_c</math> over bare lattice coupling <math>\beta = 6/g^2</math>.</i>	31
2.8	<i>The temporal and spatial AWI quark masses as measured from the lattices sized <math>128^3 \times 32</math> and <math>128^3 \times 48</math> at <math>1.5T_c</math>.</i>	32
2.9	<i>The autocorrelation of the plaquette and the vector channel for several temporal separations.</i>	40
3.1	<i>The limits <math>\omega \nearrow p</math> and <math>\omega \searrow p</math> of the <math>V_{00}</math> channel are shown over momentum <math> p /T</math> in the massless limit.</i>	53
3.2	<i>The free <math>V_{00}</math> channel spectral function at fixed momentum <math> p /T = 2.5</math> and taking the limit <math>m/T \rightarrow 0</math>.</i>	54
3.3	<i>The free <math>V_{\mu\mu}</math>, <math>V_{ii}</math>, <math>V_T</math> and <math>V_L</math> vector current-current spectral functions at <math> p /T = 2.5</math> in the massless limit.</i>	56
3.4	<i>The free lattice full vector spectral function at <math> p /T = 2.3562</math> and vanishing mass with varying spatial <math>N_\sigma</math>.</i>	59
3.5	<i>The free lattice vector spectral function <math>\rho(\omega)/\omega^2</math> with varying <math>N_\tau</math>.</i>	60
3.6	<i>Sketch of the spectral functions in the free (<math>T \rightarrow \infty</math>) and confined (<math>T \sim 0</math>) case in units of <math>1/\omega^2</math>.</i>	62

List of Figures

3.7	<i>The time-time and longitudinal spectral functions divided by frequency from the Langevin approach for diffusive heavy quarks. . . . .</i>	67
3.8	<i>The transversal and longitudinal spectral functions for massless quarks from the Boltzmann equation. . . . .</i>	70
3.9	<i>The hard thermal loop spectral function. . . . .</i>	72
3.10	<i>The spectral function from AdS/CFT. . . . .</i>	74
4.1	<i><math>G(\tau, \vec{x})</math> is made up of connected and disconnected diagrams. . . . .</i>	75
4.2	<i>The kernel <math>K(\tau T, \omega/T)</math> at <math>\tau T = 0.1</math> and <math>\tau T = 0.5</math>, as well as the ratio of the free lattice to free continuum correlation functions. . . . .</i>	77
4.3	<i>Thermal moments and the free correlation function. . . . .</i>	79
4.4	<i>Mockdata test of MEM to highlight its problems. . . . .</i>	85
5.1	<i>The full vector correlation function <math>G_V(\tau T)</math> at <math>T \simeq 1.45T_c</math> and varying cut-off scale. . . . .</i>	91
5.2	<i>The time-time component of the vector correlation function, <math>-G_{00}(\tau T)/T^3</math>. . . . .</i>	92
5.3	<i>The vector correlation function, <math>G_V(\tau T)</math>, calculated on lattices of size <math>N_\sigma^3 \times N_\tau</math> at <math>T \simeq 1.45T_c</math>. . . . .</i>	93
5.4	<i>The spatial and full vector correlation functions normalized by their free continuum and free lattice counterparts at <math>T \simeq 1.45T_c</math>. . . . .</i>	94
5.5	<i>The extrapolation of the full vector correlation function at several <math>\tau T</math>. . . . .</i>	97
5.6	<i>Continuum extrapolation of the vector correlation function. . . . .</i>	98
5.7	<i>The mid-point subtracted vector correlation function normalized to the corresponding difference for the free vector correlation function. . . . .</i>	99
5.8	<i>The reduced version of Eq. 5.13 for a number of widths over Euclidean time shows the monotonic rise of our Ansatz. . . . .</i>	101
5.9	<i>Fit and continuum extrapolation of the vector correlation function. . . . .</i>	102
5.10	<i>The vector spectral function obtained from the fit compared to its free continuum counterpart. . . . .</i>	103
5.11	<i>The truncation factor for the Ansatz at <math>\omega_0 = 3</math> and several values of <math>\Delta\omega</math>. . . . .</i>	105
5.12	<i>Spectral functions obtained from fits to the vector correlation function using the Ansatz given in Eq. 5.19. . . . .</i>	106
5.13	<i>The ratio of second and zeroth thermal moment of the correlation function <math>G_{ii}(\tau T)</math> obtained from fits with different values for the continuum cut-off parameter <math>\omega_0/T</math> and fixed <math>\Delta_\omega</math>. . . . .</i>	106
5.14	<i>Spectral functions obtained from a maximum entropy analysis. . . . .</i>	108
5.15	<i>Thermal dilepton rate in 2-flavor QCD (left). . . . .</i>	109
5.16	<i>The full and spatial vector correlation functions normalized by their free continuum counterparts at varying temperature. . . . .</i>	112
5.17	<i>The quark number susceptibility over temperature <math>T/T_c</math>. . . . .</i>	113
5.18	<i>The ratio <math>\Delta_{ii}(\tau T)</math> for <math>T \simeq 1.2, 1.45</math> and <math>3.0T_c</math>. . . . .</i>	114
5.19	<i>The ratio <math>R_{ii}^{(2,0)}/R_{ii}^{(2,0),free}</math> over <math>T/T_c</math> above and below <math>T_c</math>. . . . .</i>	115

6.1	<i>The vector correlator at varying momentum and the ratio of the finite momentum case and its corresponding vanishing momentum result. . . . .</i>	120
6.2	<i>The vector correlation functions at finite momentum normalized by its free continuum counterparts over Euclidean time. . . . .</i>	122
6.3	<i>The normalized midpoint subtracted correlator <math>\Delta_H(\tau T)</math> at finite momentum.</i>	124
6.4	<i>Comparison of the transverse (left) and longitudinal (right) data to results obtained by toy models at <math>p_z = 1, 2, 3</math>. . . . .</i>	127
6.5	<i>Comparison of the thermal moments encoded in <math>\Delta_H(\tau T, \vec{p})</math> in the transverse and longitudinal channels where <math>\vec{k} = (0, 0, p_z)</math> for <math>p_z = 2, 3</math> and the corresponding results from the toy models. . . . .</i>	129
6.6	<i>The time-time correlation function normalized by its free continuum counterparts at finite momentum. . . . .</i>	130
6.7	<i>The ratio <math>\Delta_0(\tau T, \vec{p})</math> defined in Eq. 6.11 for the momenta <math> p /T = 2.3562, 4.7124</math> and 7.0686. . . . .</i>	132
6.8	<i>The longitudinal correlator and the second derivative of the time-time correlation function for the momenta <math> p /T = 2.3562, 4.7124</math> and 7.0686 . . .</i>	133
6.9	<i>Longitudinal vector spectral function for various momenta in the hot case for <math>ma = 0.01</math> from [114]. . . . .</i>	134
7.1	<i>The pseudo scalar correlation function. . . . .</i>	138
7.2	<i>The pseudo scalar correlation functions normalized by the free continuum and free lattice correlation functions, calculated on lattices sized <math>N_\sigma^3 \times N_\tau</math> at <math>T \simeq 1.45T_c</math>. . . . .</i>	139
7.3	<i>The ratio of the pseudo scalar correlator without normalization by <math>G_{PS}(\tau T = 0.5)</math> and its free counterparts <math>R_{PS}(\tau T)</math> including its continuum extrapolation. . . . .</i>	140
7.4	<i>The pseudo scalar quantity <math>\Delta_{PS}(\tau T)</math> normalized by <math>G_{PS}^{(0)}</math>. . . . .</i>	141
7.5	<i>Results of a MEM analysis on the pseudo scalar correlator. . . . .</i>	142
7.6	<i>The ratio of midpoints of the vector to axial vector and pseudo scalar to scalar channels. . . . .</i>	144



# Preface

This thesis is a compilation of results obtained from a research period starting 01.01.2009 at Bielefeld University in the Graduiertenkolleg “Quantum Fields and Strongly Interacting Matter” in collaboration with and under supervision of Prof. Dr. Edwin Laermann, Prof. Dr. Frithjof Karsch and Dr. Olaf Kaczmarek. The on-going main objective of this research project is the reliable computation of spectral functions from Euclidean lattice correlation functions as obtained from numerical calculations.

We were able to develop an approach to the resulting set of problems that improves upon more standard methods. Subsequently we computed the phenomenologically interesting spectral functions of QCD particle currents and continue to do so in ever more relevant cases with unprecedented reliability.

Part of the content of this thesis is based on the following research articles [1], [2]:

- **Continuum extrapolation of finite temperature meson correlation functions in quenched lattice QCD**

*Anthony Francis, Frithjof Karsch (Bielefeld U. & Brookhaven)*  
PoS LATTICE2010 (2010) 191; arXiv:1101.5571 [hep-lat]

- **Thermal dilepton rate and electrical conductivity: An analysis of vector current correlation functions in quenched lattice QCD**

*H.-T. Ding (Bielefeld U. & Brookhaven), A. Francis, O. Kaczmarek (Bielefeld U.), F. Karsch (Bielefeld U. & Brookhaven), E. Laermann, W. Söldner (Bielefeld U.)*  
Phys.Rev. D83 (2011) 034504; arXiv:1012.4963 [hep-lat]

Both publications focus on determining the spectral functions of QCD particle currents from corresponding Euclidean correlation functions. To this extent the correlators have been established to unprecedented precision in the quenched approximation enabling an extrapolation to the continuum. The continuum results were then carefully analyzed, employing also the notion of thermal moments of the correlation function. Consequences for the spectral functions were drawn and the dilepton rate at  $T \simeq 1.45T_c$  could be established.

Quite naturally the format of scientific publication limits the scope and detail of a discussion. Therefore in this thesis we present the arguments and the discussion of [1] and [2] in a broader and more detailed context. The published results are naturally embedded in the following and can be seen to contribute a part of what has been researched in the course of this PhD-phase.

## *Preface*

This thesis is organized in two parts comprising chapters 1 through 4 and 5 through 8. Roughly speaking the first contains the theoretical groundwork while the second gives the analysis and results.

To this extent chapter 1 sets the scene and introduces QCD and heavy-ion collisions. At the same time the dilepton rate and its connection to the vector spectral function as the main physics objective in this work is identified.

Chapter 2 goes on to give an introduction to finite temperature lattice QCD, with special emphasis on the quenched approximation, Wilson-Clover fermions and the connection of the resulting lattice theory to physics.

In chapter 3 the concept of spectral functions is presented. Continuing with a detailed phenomenology of the spectral functions in the non-interacting case and highlighting expectations in the interacting case derived in the Langevin and Boltzmann models as well as Hard Thermal Loop perturbation theory and gauge-gravity duality.

The fourth chapter focuses on presenting the machinery, together with its drawbacks, that is employed to compute the spectral function from a Euclidean correlation function. Additionally the notion of thermal moments of the correlation function as especially sensitive observables is introduced. The now standard maximum entropy method is critically analyzed and finally a scheme is developed that improves over this approach.

Having concluded the first part the second begins in chapter 5 with the analysis of the vector correlation function at vanishing momentum. Special emphasis is put on the results at  $T \simeq 1.45T_c$ , as here the data permits a continuum extrapolation. Subsequently the computation of the vector spectral function and the dilepton rate in the continuum of quenched lattice QCD is presented.

Additionally first results are shown on the temperature dependence of the vector correlation function and the consequences for the spectral function are discussed.

In Chapter 6 the study is extended to finite momentum in the case of the vector correlation function at  $T \simeq 1.45T_c$ . The consequences of different contributions in the spectral function are discussed using a number of toy models. Finally a special emphasis is put on the connection between the longitudinal and time-like spectral functions. As a consequence a non-zero intercept linear in frequency of the former is excluded.

After the detailed analysis of the vector correlator and its spectral functions chapter 7 turns to the other particle channels, specifically the pseudo scalar. Afterwards the mid-points of the correlators of different particle channels are used to quantify possible errors due to renormalization constants, especially in the case of the pseudo scalar channel.

Finally chapter 8 summarizes the results of the presented analysis and gives an outlook on the interesting questions that still remain to be answered.

# Introduction and Motivation

What holds the nucleus of the atom together? - This is the question one needs to ask to find the strong nuclear force. Given the positive electric charge of a proton and a nucleus being made up of protons and charge neutral neutrons, one is led to this question quite naturally, as the coulombic repulsion of the positively charged protons should push the nucleus apart. This is decidedly not the case as the material world is indeed made up of atoms. Consequently one needs a force that is strong enough to negate the electromagnetic interaction and pulls the nucleons together, while at the same time only has an effective range of the size of the nucleus. This is the strong interaction or strong nuclear force.

There exist quite a number of strongly interacting particles, two of them, the proton and neutron, we already mentioned. These two are examples of the class of baryons, from the Greek “baryos” heavy, as at the time of their discovery they were considered very heavy particles. The other class of strongly interacting particles are the mesons, from Greek “mesos” meaning intermediate, examples of these particles are the pions. Together they make up the family of hadrons and the study of strong interactions is very much the study of hadrons [3].

By the late 1950’s a great number of seemingly unrelated hadrons had been found and the study of strong interactions seemed to drift more into the realm of zoology. As in zoology all particles were cataloged by certain properties they possessed, most importantly these were electric charge, isospin and strangeness. In 1960 the ‘eightfold way’ of Gell-Mann [4] finally brought order to the chaos. The eightfold way implies that mesons and baryons can be ordered and placed in a representation of  $SU(3)$ . Two of these representations are an octet and a decuplet, not only could Gell-Mann sort all known strongly interacting particles into these representations but he could also predict the still unobserved  $\Omega^-$  along with its strangeness, charge and approximate mass. The resulting scheme is shown in Fig. 1.1. In 1964 the  $\Omega^-$  particle was found [5] and 1969 Gell-Mann was awarded the Nobel prize for his achievement [6].

Bolstered by this success Gell-Mann went on to postulate that also the fundamental group of  $SU(3)$  should be realized in nature, the corresponding particles would lay in a triplet and he named these particles quarks [7]. However as all representations of a group may be built up of the fundamental representation this postulation goes further than to suggest three new particles, it also entails that all other particles should be composed of different combinations of the three quarks.

At the time these quarks were the up, down and strange quarks, today we know there

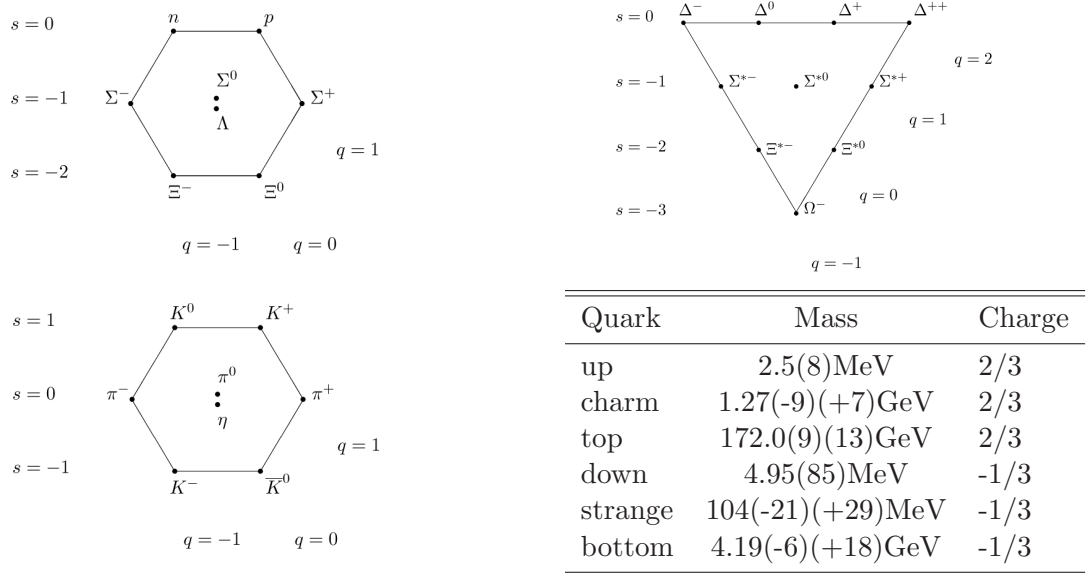


Figure 1.1: *The eightfold way may be seen as the “periodic table” of QCD, the hadrons may be arranged into the octet and decuplet representations of the SU(3) non-abelian group according to their electric charge  $q$  and strangeness  $s$  (top: baryons, bottom left: mesons). Bottom right: properties of the six quarks [3].*

are in fact six quarks consisting of the afore mentioned three and the charm, bottom and top quarks. Their properties are quickly listed in Fig. 1.1.

## 1.1 Quantum Chromodynamics and Yang-Mills Theory

At the point of its conception in the 1950’s Yang-Mills theory [8] was very much a theory in search of a world it could describe, nowhere in nature did the exact local symmetry it required seem to be realized. The theory of strong interaction at that time was instead governed by the approximate symmetries of isospin and later the eightfold way. Three fundamental ingredients were needed to put Yang-Mills theory into the limelight and to make SU(3) Yang-Mills theory or quantum chromodynamics (QCD) the dominant description of the strong nuclear force [9].

One obstacle was the persistent belief that Yang-Mills theories are non-renormalizable. This belief was shattered with ’t Hooft and Veltman rigorously proving the opposite in 1972 [10]. The consequence was that suddenly these theories in fact could yield sensible results on observables that could in turn be compared to experiment.

The other ingredient is asymptotic freedom [11]. With the strong interaction it became quickly clear that the coupling constant of the theory is in fact large  $\alpha_s \sim \mathcal{O}(1)$ . This is in stark contrast to quantum electrodynamics (QED), where the coupling has the famous value  $\alpha = 1/137$ . However what if the coupling constant is not a constant after all? The phenomenon that the strength of the coupling constant of a quantum field theory may in

## 1.1 Quantum Chromodynamics and Yang-Mills Theory

fact vary with the energy scale the theory is probed at is called asymptotic freedom, and it could be shown to be a property of QCD in 1973 Wilczek and Gross, and independently Politzer, [11]. As such asymptotic freedom for QED meant that it had been tested only at energy scales at which its change was so absolutely insignificantly small that it made the coupling seem constant. For QCD it meant that at sufficiently high energies or short distances the theory in fact could be handled by the advanced diagrammatic approach proposed by Feynman for QED [12, 13]. As a consequence the successful search for an asymptotically free quantum field theory could yield a theory of strong interactions. Yang-Mills Theory is asymptotically free and recently it could be shown that it is in fact the only asymptotically free theory in our space-time [14].

The running of the coupling can be seen as one of the reasons for confinement. On the one hand the quarks behave effectively as free particles at short distances, as the coupling is small. As the distance to the next quark increases however also does the coupling strength and the quarks feel the strong force get stronger and stronger. In effect, in the regime where the coupling grows large  $\sim 1\text{fm}$ , it takes an absolutely large effectively infinite amount of energy to separate two quarks from one another. This is how the strong force is able to negate the electromagnetic repulsion and to subsequently keep the nucleus from flying apart.

Even with these insights however we have not arrived at QCD, one part is still missing. At the end of the 1960's deep inelastic scattering experiments had given hints that nucleons might be made up of partons and many were ready to believe in quarks but the quarks could not satisfy the exact gauge symmetry needed for Yang-Mills theory to work. The up, down and strange quarks might satisfy the approximate  $SU(3)$  symmetry of the eightfold way, but they are certainly different particles, with e.g. different masses. With hindsight we identify that a key observable is the ratio of the production of hadrons from  $e^+e^-$ -collisions compared with that of muons:

$$R(E) \equiv \frac{\sigma(e^+e^- \rightarrow \text{hadrons})}{\sigma(e^+e^- \rightarrow \mu^+\mu^-)} \approx N_c \cdot \sum_i Q_i^2 \theta(E - m_i) \quad , \quad (1.1)$$

where the  $Q_i$  are the charges of the different quark species and  $E = 2E_{beam} = \sqrt{s}$ . Without knowing what the extra  $N_c$  is or that it existed, physicists at the time were puzzled as their calculation of this ratio was off by a constant equal to three [3]. From the experiments it suddenly seemed as if there were three times as many quarks as was believed. At the time the term color was introduced in order to handle this triplication, consequently quarks now came not only in different flavors as in up, down, strange... but also in three colors red, yellow and blue.

In view of Yang-Mills theory physicists soon realized the implications of this observation. As mentioned above the quark flavors were certainly different, however the different colored triplets of a given flavor were exactly identical modulo the color. Here the exact gauge symmetry required by Yang-Mills revealed itself and with the number of colors  $N_c = 3$  it implied it to be  $SU(3)_c$ .

Today the ratio in Eq. 1.1 has been measured very precisely [3] and  $N_c = 3$  is firmly established. To illustrate note the experimental world data results shown in Fig. 1.2

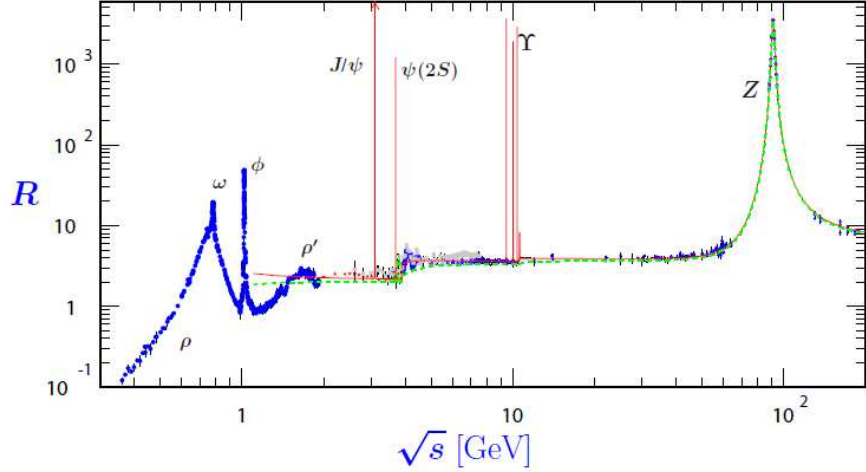


Figure 1.2: The ratio  $R(E)$  of the production of hadrons to muons from  $e^+e^-$ -annihilation. Figure provided by [3]

match up nicely with the approximation to  $R(E)$  given the different quark content:

$$\begin{aligned}
 R_{u,d,s} &\approx N_c \left[ \left(\frac{2}{3}\right)^2 + \left(-\frac{1}{3}\right)^2 + \left(-\frac{1}{3}\right)^2 \right] = \frac{2}{3} N_c, & R_{u,d,s,c} &\approx N_c \left[ \frac{2}{3} + \left(\frac{2}{3}\right)^2 \right] = \frac{10}{9} N_c \\
 R_{u,d,s,c,b} &\approx N_c \left[ \frac{10}{9} + \left(-\frac{1}{3}\right)^2 \right] = \frac{11}{9} N_c & , & R_{u,d,s,c,b,t} &\approx N_c \left[ \frac{11}{9} + \left(\frac{2}{3}\right)^2 \right] = \frac{5}{3} N_c
 \end{aligned}
 \tag{1.2}$$

## The Lagrangian of QCD

Finally we have arrived at the possibility to define a theory of the strong interaction via Yang-Mills theory [8] and to compute its observables via the diagrammatic approach, as long as the energy scale is sufficiently high for the strong coupling to be small. As Yang-Mills theory is a gauge theory there naturally also are gauge bosons in the theory. In QCD these are called gluons and it is these particles that constitute the great difference of properties between QED or the electroweak theories and QCD.

Above it became clear that in QCD the color charge is associated with the non-Abelian gauge group  $SU(3)$ . Recapitulating the particle content of QCD there subsequently are quarks and anti-quarks of three color charges and additionally the gluons, which transform under the adjoint representation of  $SU(3)$ , consequently they carry eight charges ( $3 \times 3$  combinations of color and anti-color). This implies gluons may interact directly via their own color charge and this is a prime reason for confinement. As the direct gluon interaction contracts the lines of force between two color charges into a flux-tube or color-string, the three-dimensional Poisson-equation that leads to the Coulomb potential in non-relativistic QED,  $V \sim 1/r$ , now becomes effectively one-dimensional with the confining form  $V \sim r$  [15].

The governing Lagrangian density of quantum chromodynamics derived in this way is given by:

$$\mathcal{L} = \mathcal{L}_{fermion} + \mathcal{L}_{gluon} \quad (1.3)$$

where the fermionic part is

$$\mathcal{L}_{fermion} = \sum_f \bar{\Psi}_f^\alpha \left( i\delta_{\alpha\beta}\gamma^\mu \partial_\mu - gT_{\alpha\beta}^a \gamma^\mu A_\mu^a \right) \Psi_f^\beta \quad , \quad (1.4)$$

here  $A_\mu^a$  denotes the gluon vector field of color  $a$  ( $a = 1, 2, \dots, 8$ ) and  $\Psi_f^\alpha$  the quark spinor field of color  $\alpha$  ( $\alpha = 1, 2, 3$ ) with flavor  $f$ ,  $T_{\alpha\beta}^a$  is a matrix, fixed by the gauge group, that connects the fundamental and anti-fundamental quark spinors to the adjoint gluon representation. The gluon or pure Yang-Mills part on the other hand may be written as

$$\mathcal{L}_{gluon} = -\frac{1}{4} F_{\mu\nu}^a F_a^{\mu\nu} \quad (1.5)$$

with the field strength tensor:

$$F^{\mu\nu} = \partial_\mu A_\nu^a - \partial_\nu A_\mu^a + g[A_\mu, A_\nu] = \partial_\mu A_\nu^a - \partial_\nu A_\mu^a + gf_{bc}^a A_\mu^b A_\nu^c \quad . \quad (1.6)$$

The structure constants  $f_{bc}^a$  are fixed by the gauge group and its generators  $\lambda_a$ :

$$[\lambda_a, \lambda_b] = if_{bc}^a \lambda_c \quad . \quad (1.7)$$

It is this term proportional to the coupling  $g$  that encodes the non-Abelian nature of the theory and its greatest difference to QED. This term gives rise to a self-interaction term of the gluons and corresponds to an additional pure glue vertex in the language of Feynman diagrams.

The observables of QCD are the (conserved) currents of the action. In particular we will be interested in meson operators that define the currents:

$$J_\nu \equiv \bar{q}(\tau, \vec{x}) \gamma_\nu q(\tau, \vec{x}) \quad , \quad (1.8)$$

choosing the appropriate gamma matrix we obtain the particle channels according to their transformation behavior under space-time, in our case these are the vector particle channels (V) for  $\gamma_\nu = \gamma_\mu$  where  $\mu = 0, \dots, 3$ , the pseudo scalar (PS) for  $\gamma_\nu = \gamma_5$ , the scalar (S) for  $\gamma_\nu = 1$  and the axial vector (A) for  $\gamma_\nu = \gamma_\mu \gamma_5$ .

## 1.2 Heavy-Ion Collisions

Quantum chromodynamics and ultimately confinement leads to the conclusion that single free quarks or gluons cannot be studied or observed in the physical vacuum. Subsequently in our physical world all observable particles are colorless or color neutral.

However, in a regime with large enough particle densities that one can safely define a

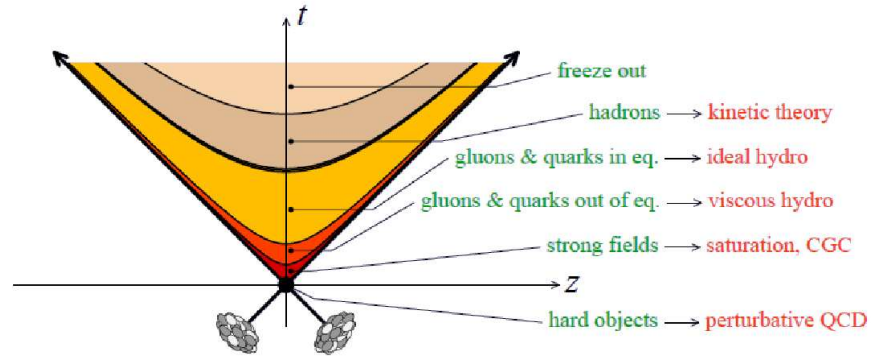


Figure 1.3: *Sketch of the standard interpretation of a relativistic heavy-ion collision [18].*

temperature  $T$  and chemical potentials  $\mu$ , the strong tie that binds quarks and gluons may weaken and ultimately release them into a deconfined state, see e.g. [15].

These high particle densities may be created in heavy-ion collisions (HIC) and they have been the experimental approach to studying the properties of QCD and extreme states of matter since the 1970's.

In a HIC-event nuclei are accelerated to ultra-relativistic speeds, i.e. near light-speed, and then smashed into one another.

However, even if inside a heavy-ion collision two nucleons hit head-on, they do not simply stop each other. As a nucleon is of the size of  $\sim 1\text{fm}$  it takes a certain time  $\tau_0$  before the entire nucleon realizes it hit something [15, 16]. At the high collision energies typically available at e.g. RHIC this time is much larger than the extent of the nucleus  $\tau_0 \gg 1\text{fm}$ . Hence instead of stopping, the two colliding nucleons pass through each other leaving behind a 'vapour trail' of deposited energy droplets [15].

In this fashion large amounts of energy are concentrated in a small reaction volume and high particle densities are indeed reached, for example a proton-proton collision at beam energies of  $\sqrt{s} = 20\text{GeV}$  leads to an energy density of  $\epsilon_{pp} \sim 0.36\text{GeV}/\text{fm}^3$ , which is roughly twice that of standard nuclear matter.

In the next step each droplet expands, thereby cools and eventually materializes by forming a number of hadrons of different species.

Naturally the situation is much more complicated if nuclei composed of many nucleons are collided, as is the case in gold-gold collisions e.g. at RHIC, however here one may expect energy densities in region of  $\sim 2.5\text{GeV}/\text{fm}^3$ , which is a factor 14 larger than standard nuclear matter.

In such a collision  $\sim \mathcal{O}(10^3)$  particles are produced and recorded by the detector. The task is then to reconstruct the evolution of the extremely high temperature initial energy droplets through the thermal and freeze-out processes to the low temperature purely hadronic state from the properties of this huge amount of produced particles.

The inner workings of such a HIC-event are naturally very complicated and the current theoretical picture is quickly outlined in the following (see sketch in Fig. 1.3).

At the initial collision time the color fields are liberated from the wave functions of the incoming nuclei and then pass through a phase of strongly interacting fields that create quantum number of quarks and gluons. This is a prediction of perturbative QCD, as pQCD implies that in the 'very hot' phase of a heavy-ion collision the color charge is transported by weakly interacting quasiparticles with quark and gluon quantum numbers. The corresponding state of matter in this phase is called a "glasma" [19] and most of the energy is deposited in highly coherent field degrees of freedom, as opposed to quarks and gluons.

In the next step the latter begin to interact and start to thermalize, as the initial energy droplet further expands and cools. This process ultimately forms the so called "quark gluon plasma" (QGP), see e.g. [15]. The quark gluon plasma is a phase where most energy is deposited in the quarks and gluons however the color charges cannot yet be associated with a single hadron, as such it is part of the deconfined regime of QCD.

With the system further cooling however the "mixed phase" is reached, theoretically it is unclear what the degrees of freedom are in this region.

A simple picture however is to think of it as a "transition region" between the deconfined and confined regimes of QCD. In this case heavy hadrons begin to drop out of the QGP as their production threshold is reached and a phase described both by the QGP and hadrons emerges. Note here it could be shown using lattice QCD that charmonium particles exist already at temperatures  $T \simeq (225 - 255)\text{MeV}$  [22] in support of the notion of heavy hadrons coexisting with the QGP phase.

As the system further cools it reaches a critical temperature  $T_c$  and the QGP changes into a confined hot hadron gas now containing also the light hadrons and especially pions. Studying the phase diagram in QCD in this region recent calculations using lattice QCD found the transition to be a rapid crossover and the critical temperature to be  $T_c \simeq (150 - 170)\text{MeV}$  [21] at vanishing baryon density.

At temperatures below  $T_c$  the hadron gas first remains in an interacting state until the system reaches the freeze-out temperature  $T_f \simeq 120\text{MeV}$ , see e.g. [15, 20], where they stop interacting, the hadrons freeze-out and are eventually recorded by the detector.

Another powerful tool to understanding HIC-events is the study of spectral functions, see e.g. the recent review [23]. As an example consider the QCD electromagnetic current with vector transformation behavior at vanishing temperature  $T = 0$ :

$$j_\mu^{em}(x) = \sum_f Q_f \bar{q}^f(\tau, \vec{x}) \gamma_\mu q^f(\tau, \vec{x}) = \frac{2}{3} \bar{u} \gamma_\mu u - \frac{1}{3} \bar{d} \gamma_\mu d - \frac{1}{3} \bar{s} \gamma_\mu s \dots \quad (1.9)$$

Note the correlation function of this current quantifies the polarization of the vacuum by virtual particles induced by the passage of a photon [24]:

$$\int d^4x \langle j_\mu(x) j_\nu(0) \rangle e^{iq \cdot x} = (q_\mu q_\nu - q^2 g_{\mu\nu}) \Pi(q^2) \quad . \quad (1.10)$$

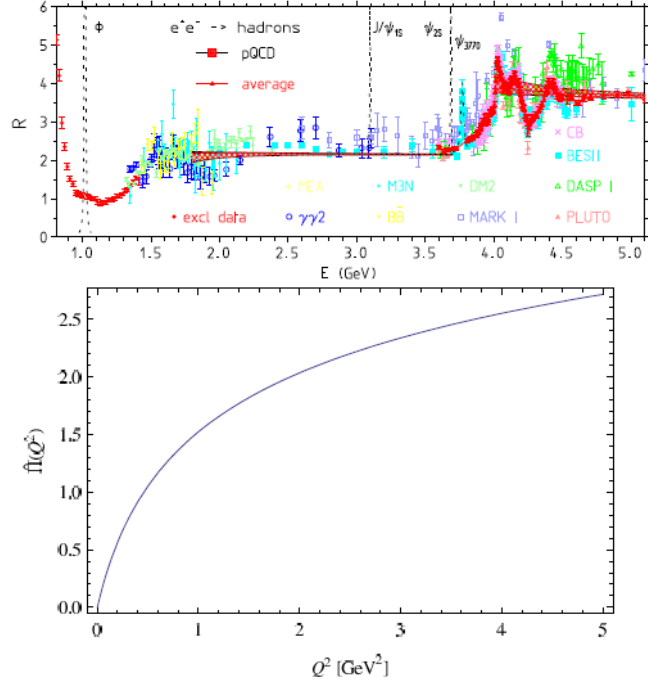


Figure 1.4: *The spectral density from the cross section of the production of hadrons in  $e^+e^-$ -annihilations from experiments (top) and the vacuum polarization as computed in theory (bottom). Extracting the spectral function from the latter is a difficult problem. Note the energy scales in the plots are not the same. Figure taken from [23]*

The spectral representation of the vacuum polarization in the Euclidean world of lattice calculations may be shown to read [25]:

$$\Pi(0) - \Pi(q^2) = q^2 \int_0^\infty ds \frac{\rho(E)}{E(E+q^2)} \quad , \quad (1.11)$$

while via the optical theorem the spectral density  $\rho(E)$  is directly accessible to experiments:

$$\rho(E) = \frac{E}{4\pi^2\alpha(E)} \sigma_{tot}(e^+e^- \rightarrow \text{hadrons}) := \frac{\alpha(E)}{3\pi^2} R_{had}(E) \simeq \frac{\alpha(E)}{3\pi^2} R(E) \quad . \quad (1.12)$$

As such the spectral density is simultaneously connected to theory as well as experiment. In Fig. 1.4 we show the spectral density  $\rho(s)$  (top) from experiments [3] and the vacuum polarization  $\Pi(0) - \Pi(q^2) := \Pi(Q^2)$  (bottom) from lattice QCD [25] where  $Q^2 = E^2 = s$ . Clearly the rich structure of the spectral density can be seen. Also the first problems in case of the theory connection are revealed, as the Euclidean calculation leads to an almost featureless result. Such issues pose major problems for theoretical calculations especially from Euclidean lattice methods and tackling them is at the core of this thesis.

## 1.2.1 Production of Photons and Dileptons in Heavy-Ion Collisions

From the above example of the QCD electromagnetic current let us turn to the main topic of this work. The QED coupling constant is small, as mentioned before  $\alpha_{em} = 1/137$ , and thus photons and dileptons (i.e. lepton pairs) produced in a HIC-event essentially pass through to the detector without further interactions. However photons and dileptons are produced at every stage of the space-time evolution of the HIC-event (see sketch). They are produced from the first stage, as the nuclei pass through another, through the quark gluon plasma phase until the hadrons freeze out, decouple and also move freely to the detector. Consequently the production rate of photons and dileptons carries the full information of the full evolution of the collision directly to the experimenter.

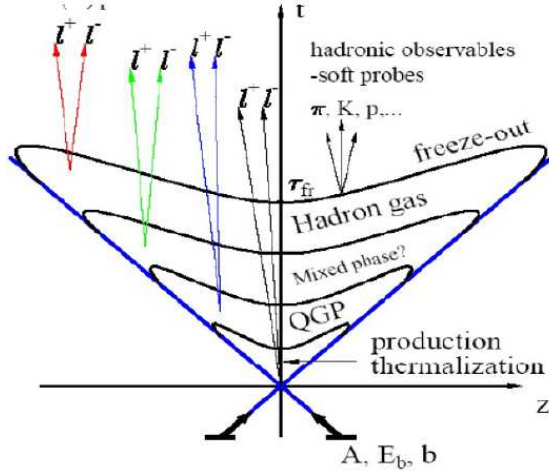


Figure 1.5: *Evolution of a HIC event and dilepton production [26].*

From the point of theory we are thus interested in the emission of on-shell photons from the transition of some initial to final state and the similar process of a virtual photon decaying into dileptons [27].

To get an idea of these transition amplitudes and consequently the physics one invokes the vector dominance model [27] and the according processes for photon and dilepton emission are sketched in a.) and b.). This model implies that all electromagnetic interactions of hadrons are described by the intermediate coupling of hadrons to vector mesons. As such the hadronic initial  $|i\rangle$ -state first forms a vector meson that decays and subsequently emits the photons and lepton pairs. The central observable is then the vector channel and consequently the vector spectral function  $\rho_V(\omega, T, \vec{p})$ .

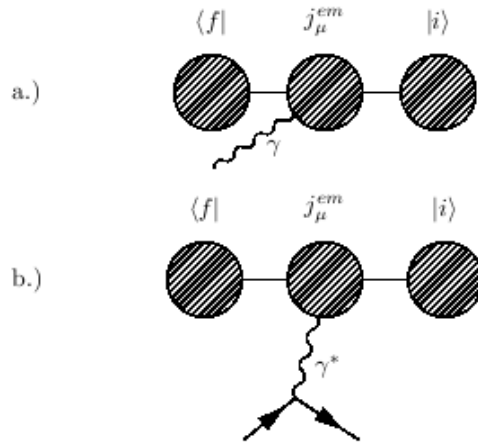


Figure 1.6: *a.) Emission of an on-shell photon. b.) Emission of a virtual photon decaying into dileptons.*

The production rate of real photons is defined as the number of photons per unit time

and volume [28, 29]:

$$R_\gamma = \frac{1}{\Omega} \int \frac{d^3p}{2\omega(2\pi)^3} \frac{1}{Z(T)} \sum_{f,i,\lambda} e^{-E_i/T} |M_{fi}^{(\lambda)}|^2 \quad , \quad (1.13)$$

where  $\Omega$  is the space-time volume where the interaction takes place, the factor  $1/Z(T)$  must be included as the production rate is given by a thermal expectation value. Note here  $M_{fi}^{(\lambda)}$  is the transition amplitude from the hadronic initial state  $|i\rangle$  to the final hadronic state  $\langle f|$  and a single real photon with momentum  $p^\mu = (\omega = |p|, \vec{p})$ , polarization  $\lambda$  and the polarization vector  $\epsilon_\mu^{(\lambda)}$

$$M_{fi}^{(\lambda)} = -ie \int d^4x e^{ipx} \epsilon_\mu^{(\lambda)}(p) \langle f | j_\mu^{em} | i \rangle \quad . \quad (1.14)$$

Similar expressions to Eq. 1.13 and Eq. 1.14 can be derived also in the case of dilepton production [28, 29], this time however the process is that of the hadronic initial state  $|i\rangle$  to the final hadronic state  $\langle f|$  plus a pair of leptons:

$$R_{l+l-} = \frac{1}{\Omega} \int \frac{d^3p_1}{2E_1(2\pi)^3} \int \frac{d^3p_2}{2E_2(2\pi)^3} \frac{1}{Z(T)} \sum_{f,i} e^{-E_i/T} |M_{fi}|^2 \quad , \quad (1.15)$$

with the amplitude:

$$M_{fi}(p_1, p_2) = -i \frac{e^2}{p^2} [\bar{u}(p_1) \gamma_\mu v(p_2)] \int d^4x e^{ipx} \langle f | j_\mu^{em} | i \rangle \quad . \quad (1.16)$$

here  $e\bar{u}(p_1)\gamma_\mu v(p_2)$  is the electromagnetic current of the outgoing lepton pair.

Using direct relations between the amplitudes and the spectral functions, which we will derive in a later chapter, the photon and dilepton rates may be written as [32, 33]:

$$\omega \frac{dR_\gamma}{d^3p} = C_{em} \frac{\alpha_{em}}{4\pi^2} \frac{\rho_T(\omega = |\vec{p}|, T)}{\exp[\omega/T] - 1} \quad (1.17)$$

and, introducing the total four momentum of the lepton pair  $\vec{p} = p_1 + p_2$ , [32–35]

$$\frac{dR_{l+l-}}{d\omega d^3p} = C_{em} \frac{\alpha_{em}^2}{6\pi^3} \frac{2\rho_T(\omega, \vec{p}, T) + \rho_L(\omega, \vec{p}, T)}{(\omega^2 - \vec{p}^2)(\exp[\omega/T] - 1)} \quad , \quad (1.18)$$

where  $C_{em} = \sum_f Q_f^2$  and  $\rho_{T,L}$  denotes the spectral function polarized in transversal and longitudinal direction compared to the momentum  $\vec{p}$ . In the limit of vanishing momentum one may neglect the polarization and write

$$2\rho_T(\omega, \vec{p}, T) + \rho_L(\omega, \vec{p}, T) \xrightarrow{\vec{p} \rightarrow 0} \rho_{ii}(\omega) \quad , \quad (1.19)$$

subsequently the above relations reduce to [28–35]:

$$\omega \frac{dR_\gamma}{d^3p} \xrightarrow{\vec{p} \rightarrow 0} \frac{3\alpha_{em}}{2\pi^2} \sigma(T) T \quad (1.20)$$

and

$$\frac{dR_{l+l-}}{d\omega d^3p} \xrightarrow{\vec{p} \rightarrow 0} C_{em} \frac{\alpha_{em}^2}{6\pi^3} \frac{\rho_{ii}(\omega, T)}{\omega^2 (\exp[\omega/T] - 1)} \quad (1.21)$$

with the electrical conductivity:

$$\sigma(T) = \frac{C_{em}}{6} \lim_{\omega \rightarrow 0} \frac{\rho_{ii}(\omega)}{\omega} \quad (1.22)$$

The important consequence of these relations is that the more detailed the knowledge of the vector spectral function is, the better is our understanding of the experimental data. This is our prime motivation in this thesis given that the experimental data is in fact quite puzzling as we will illuminate in the next section. Note however that we will restrict ourself to dilepton production in the following.

### 1.2.2 Status of Experimental Dilepton Production Data

Computing the production rate of dileptons in heavy-ion collisions via the spectral function is not the only possibility to handle the subject. One may also use approaches based on perturbative computation and approximation. Indeed these more standard methods have been able to describe most of the processes that contribute to the dilepton rate [27–31].

As such the production of lepton pairs from the early initial hard collisions between the partons of the colliding nuclei constitutes the best known part of the dilepton spectrum as asymptotic freedom guarantees the validity of perturbative methods, these processes are part of the so called Drell-Yan mechanism [36] (far right in the sketch).

The invariant-mass spectrum of dileptons contains also the peaks corresponding to two-body decays of various mesons, as e.g.  $\rho^0 \rightarrow e^+e^-$ , these peaks appear above the background three-body Dalitz decays [37] (far left in the sketch). Note the positions and widths of these peaks reveal information on the hadron properties at the later stages of the HIC-event. The main goal of this thesis however is to quantify the contribution of the QGP in the low to intermediate mass region [27].

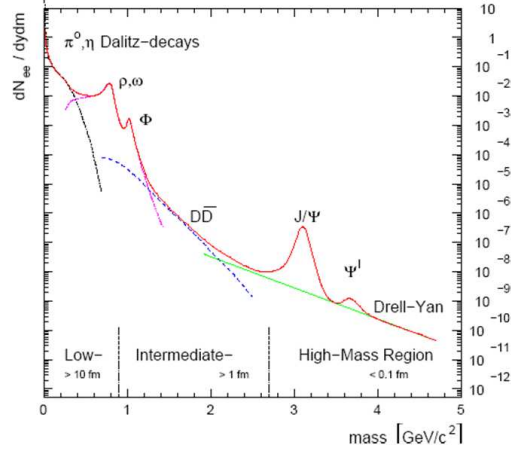


Figure 1.7: *Sketch of the dilepton spectrum, taken from [28].*

In practice one tries to understand the production rate of dileptons from HIC experiments by comparing it to a so called hadron cocktail. As such the hadron cocktail

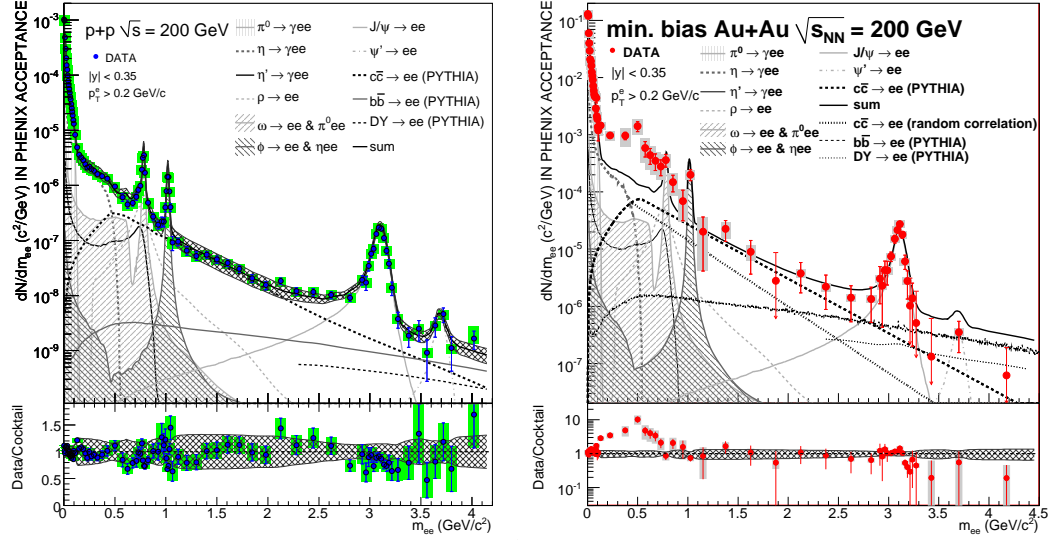


Figure 1.8: *Left: The experimental results of the dilepton spectrum from proton-proton collisions as measured by PHENIX@RHIC. At the top of the figure the dilepton rate over energy and the components of the hadron cocktail are shown, while at the bottom the ratio of the data to hadron cocktail is given. Right: The same as left except with gold-gold collisions. The hadron cocktail is unable to reproduce the measured data in the low-to-intermediate mass regime. Figures provided by [38].*

combines everything that is known of the processes that might contribute to the dilepton rate. Whereby the information encoded in the hadron cocktail may be perturbative, non-perturbative and even experimental. On the left of Fig. 1.8 the current dilepton rate data of proton-proton collisions over invariant-mass retrieved by the PHENIX experiment located at RHIC is shown [38]. In the bottom of the figure the data is once more given as a ratio with the hadron cocktail. Clearly the provided model coincides with the actual data very well. This situation however changes drastically in the case of gold-gold collisions [38]. The corresponding data on the right of Fig. 1.8 show clear deviation in the low-to-intermediate-mass region. As noted above this is exactly the region where one expects the largest contribution from QGP effects.

Lattice QCD is an ideal tool to study the nature of the quark gluon plasma, and using it we will explore the non-perturbatively dominated intermediate-mass region of the dilepton rate in the deconfined phase of QCD. With the work presented in this thesis we hope to give hints as to clarify the situation encountered in the gold-gold collisions explained above. Even though lattice QCD is the only fully non-perturbative method available, it is not suited to calculate the spectral function directly and tackling the problems that this fact entails constitutes the bulk of the work, which will be presented in the following.

# Foundations of Lattice Quantum Field Theory

The following work revolves around asking what happens to a system of elementary particles described by a quantum field theory, in our case quantum chromodynamics, if it is heated [29–31].

Clearly, given the Lagrangian density, as e.g. in Eq. 1.3, this requires computing the grand canonical partition function  $\mathcal{Z}(T, V, \dots)$  generically written as:

$$\mathcal{Z} = \text{Tr}[e^{-\beta H}] = \sum_n \langle n | e^{-\beta H} | n \rangle \quad , \quad (2.1)$$

where the Hamiltonian is derived from the Lagrangian density via Legendre transform and  $\beta = 1/T$  is connected to the temperature of the system.

The Hamiltonian form of the partition function of Eq. 2.1 may be replaced by an equivalent form in terms of a Euclidean path integral. Recall the standard derivation of the path integral yields:

$$\sum_{\phi_i} \langle \phi_t | e^{-iHt} | \phi_0 \rangle = \int d\phi \exp\left[i \int_0^t dt \int d^3x \mathcal{L}(\phi)\right] \quad . \quad (2.2)$$

To see that it is now possible to obtain an equivalent form for the partition function given above, introduce imaginary time  $\tau = it$  and identify it with the inverse temperature direction. The above path integral then becomes

$$\sum_{\phi_i} \langle \phi_\beta | e^{\beta H} | \phi_0 \rangle = \int d\phi \exp\left[- \int_0^\beta d\tau \int d^3x \mathcal{L}_E(\phi)\right] \quad . \quad (2.3)$$

To respect the trace operation in Eq. 2.1 requires the boundary conditions of the path integral to be fixed appropriately [29–31, 39]. For bosons and fermions these can be shown to be:

$$\begin{aligned} \phi(\tau = 1/T) &= \phi(0) && \text{for bosonic fields} \\ \psi(\tau = 1/T) &= -\psi(0) && \text{for fermionic fields} \quad . \end{aligned} \quad (2.4)$$

In principle the temporal direction in the Euclidean path integral at finite temperature is compactified by the periodic boundary conditions and kept finite due to the integration

from 0 to  $\beta$ . In effect finite temperature field theory lives on a torus whose radius in time direction defines the inverse temperature via  $\beta = 1/T$ . Subsequently the vacuum theory is retrieved in the limit of infinite radius in the temporal direction  $\lim_{\beta \rightarrow \infty}$ .

In total the partition function formulated as a Euclidean path integral reads:

$$\mathcal{Z} = \sum_n \langle n | e^{-\beta H(\phi)} | n \rangle = \int_{\text{periodic}} d\phi \exp\left[-\int_0^\beta d\tau \int d^3x \mathcal{L}_E(\phi)\right]. \quad (2.5)$$

Note from here onwards, if not stated otherwise, all expressions are assumed in Euclidean space-time.

## 2.1 Lattice Quantum Field Theory

One possibility to rigorously define quantum field theory is to discretize it [40–47]. This is achieved by introducing a hypercubic, Euclidean lattice as space-time background.

Space now becomes a finite volume\* and the theory is effectively “put into a box” while the finite number of points in each direction induces a crystalline structure. The fourth Euclidean direction is then associated with the imaginary time direction introduced above. Demanding also periodic boundary conditions the system temperature can be controlled by the number of points in the  $x_4 = \tau$  direction.

$$V = (aN_\sigma)^3, \quad \beta = T^{-1} = aN_\tau. \quad (2.6)$$

In addition to introducing a lattice the corresponding lattice spacing  $a$  is defined as the distance between neighboring sites. It is in essence the only dimensionful unit of the theory with  $[a] = \text{length} = 1/\text{energy}$ , as such it sets the scale of the lattice theory and is consequently an important property for connecting to physics.

After replacing the continuous space-time of continuum theory with a hypercubic Euclidean lattice<sup>†</sup>, the spinor fields  $\Psi$  and  $\bar{\Psi}$  are defined on each of the  $N_\sigma^3 N_\tau$  lattice sites  $n_i$ . While the gauge fields  $A_\mu$  are defined on the links connecting two neighboring sites in order to maintain gauge invariance. This is achieved by a change of variables,

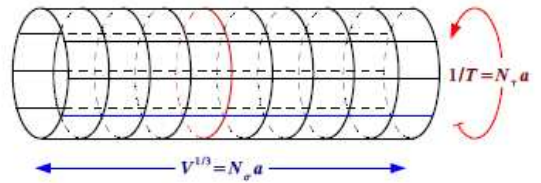


Figure 2.1: *Lattice discretization of finite temperature field theory in (1 + 1)-Dimensions, due to the periodic boundary conditions space-time is a torus.*

\*In a numerical setup, as will be done here. This is not mandatory using analytical methods.

†In the following all continuum entities will be distinguished by a hat, e.g.  $\hat{\Psi}$

replacing the individual gauge fields  $A_\mu$  by a link matrix  $U_{ij}$  between two neighboring lattice sites  $n_i$  and  $n_j$ :

$$\begin{aligned} \hat{U}(x_i, x_j) &= \exp[-ig \int_{x_i}^{x_j} dx'^\mu \hat{A}_\mu(x')] \\ \xrightarrow{l.o.} U(n_i, n_j) &= \exp[-ig(n_i - n_j)^\mu A_\mu(\frac{n_i - n_j}{2})] \quad . \end{aligned} \quad (2.7)$$

On the lattice the partial derivative of a fermion field  $\Psi(n)$  may be written as:

$$\partial\Psi(n) = (\Psi(n+a) - \Psi(n-a))/2a + \mathcal{O}(a^2) \quad , \quad (2.8)$$

whereby the discretization scheme is not unique and different discretizations may be found and utilized [40–47]. Using these two relations it is straight forward to find the discretized covariant derivative:

$$\begin{aligned} D\hat{\Psi}(x) &= (\partial_\mu + igA_\mu(x))\Psi(x) \\ \Rightarrow D\Psi(n) &= (U(n, n+a_\mu)\Psi(n+a_\mu) - U(n, n-a_\mu)\Psi(n-a_\mu))/2a + \mathcal{O}(a^2) \quad (2.9) \\ &= (\bullet \longrightarrow \bullet (n, n+a_\mu)\Psi(n+a_\mu) - \bullet \longleftarrow \bullet (n, n-a_\mu)\Psi(n-a_\mu))/2a + \mathcal{O}(a^2) \end{aligned}$$

On a Euclidean lattice there is no principal distinction between space and time directions, as long as we impose the same boundary conditions. This means that lattice theories are effectively done at a finite temperature, which in turn is small if  $N_\sigma < N_\tau$ . To study high temperature systems however this implies the spatial extent must be larger than that of the temporal direction  $N_\sigma > N_\tau$ .

Additionally it should be emphasized that what the quantum fields on the lattice “feel” as a temperature is in fact an effect of the boundary conditions and the finite size of the temporal direction. Naturally these finite size effects are also present in the spatial directions, however here they are unwanted. This entails the spatial direction must be large enough for these effects to be negligible in the calculation.

Together the necessity that  $N_\sigma = \text{large}$  and  $N_\sigma > N_\tau$  for high temperature systems, while at the same time requiring  $N_\tau = \text{large}$  in order to be able to reduce the lattice spacing  $a$ , makes calculations in this regime computationally highly demanding.

Given the similarities of the vacuum and finite temperature path integrals it is appropriate to emphasize the fundamental difference of the two that becomes evident in the Fourier expansion of bosonic ( $A_\mu(\tau, \vec{x})$ ) and fermionic ( $\Psi(\tau, \vec{x})$ ) fields on a finite volume  $V = L^3$ :

$$A_\mu(\tau, \vec{x}) = C_b \cdot \sum_n \sum_{\vec{p}} \exp[i(\omega_n \tau + \vec{p}\vec{x})] A_{\mu,n}(p), \quad \omega_n = 2n\pi T, \quad (2.10)$$

$$\Psi(\tau, \vec{x}) = C_f \cdot \sum_n \sum_{\vec{p}} \exp[i(\omega_n \tau + \vec{p}\vec{x})] \psi_n(p), \quad \omega_n = (2n+1)\pi T, \quad (2.11)$$

here  $C_b$  and  $C_f$  are factors that ensure the Fourier modes or Matsubara frequencies are dimensionless. The momenta are also discretized and their allowed values are

$p_i = (2\pi k_i)/L$ . Notice that although the momenta become continuous in the so called thermodynamic limit:

$$\frac{1}{V} \sum_n \xrightarrow{V \rightarrow \infty} \int \frac{d^3 p}{(2\pi)^3} \quad , \quad (2.12)$$

the Matsubara frequencies remain discrete, as they are connected to the time direction. This leads to modified Feynman rules in the finite temperature theory and the four momentum integrals in vacuum theory must be replaced by a three momentum integral and a Matsubara sum:

$$\int \frac{d^4 p}{(2\pi)^4} \longrightarrow T \sum_n \int \frac{d^3 p}{(2\pi)^3} \quad . \quad (2.13)$$

At the same time the regularizing capabilities of lattice theory become clear as the discretized momenta are limited to values between  $p_{min} = (2\pi)/aN$  and  $p_{max} = (2\pi)/a$ , as such a cut-off scale proportional to the lattice spacing is introduced, all momentum integrations are rendered finite and the theory is thus regularized.

Concluding this section and before moving to lattice QCD note that formally a continuum quantum field theory may be translated into a lattice quantum field theory using the following dictionary:

$$\begin{aligned} \int_0^\beta d\tau \int d^3 x &\longleftrightarrow a^4 \sum_n \\ \int \frac{d^4 p}{(2\pi)^4} &\longleftrightarrow T \sum_n \int \frac{d^3 p}{(2\pi)^3} \\ \partial \hat{\Psi}(x) &\longleftrightarrow \partial \Psi(n) = (\Psi(n+a) - \Psi(n-a))/2a + \mathcal{O}(a^2), \\ \hat{U}(x_i, x_j) &\longleftrightarrow U(n_i, n_j) = \exp[-ig(n_i - n_j)^\mu A_\mu(\frac{n_i - n_j}{2})] \\ D \hat{\Psi}(x) &\longleftrightarrow D \Psi(n) = (U(n, n+a)\Psi(n+a) - U(n, n-a)\Psi(n-a))/2a + \mathcal{O}(a^2) \\ \hat{\Psi}(x) &\longleftrightarrow \Psi(n) = a^{3/2} \hat{\Psi}(an) \\ \hat{A}_\mu(x) &\longleftrightarrow A_\mu(n) = a \hat{A}_\mu(an) \\ \hat{p}_i &\longleftrightarrow p_i = 2\pi k_i / (aN_\sigma) \\ x_\mu &\longleftrightarrow n_\mu = x_\mu / a \\ \hat{m} &\longleftrightarrow m = \hat{m}a \end{aligned} \quad (2.14)$$

## 2.2 Lattice Quantum Chromodynamics

After having defined the tools needed to construct a lattice finite temperature quantum field theory let us now turn to discretizing the strong interaction and its underlying dynamics.

### 2.2.1 SU(3) Pure Yang-Mills Theory

As was shown in Chp. 1.1 the gauge field dynamics of  $T = 0$ , vacuum QCD are described by SU(3) Yang-Mills theory:

$$\hat{S}_G = \frac{1}{2} \int d^4x \text{Tr}[\hat{F}_{\mu\nu}\hat{F}^{\mu\nu}] = \frac{1}{4} \int d^4x \hat{F}_{\mu\nu}^c \hat{F}_c^{\mu\nu} \quad , \quad (2.15)$$

where the field strength tensor is defined as the commutator of two covariant derivatives:

$$\hat{F}_{\mu\nu}(x) = \frac{i}{g} [\hat{D}_\mu, \hat{D}_\nu] = \partial_\mu \hat{A}_\nu(x) - \partial_\nu \hat{A}_\mu(x) + ig[\hat{A}_\mu(x), \hat{A}_\nu(x)] \quad . \quad (2.16)$$

This object can be found to correspond to the curvature tensor of general relativity [43] and its geometrical meaning can be seen from a closed path of a “continuum link” (Eq. 2.7) or parallel transporter around an infinitesimal parallelogram spanned by  $dx$  and  $dy$ :

$$\hat{U}(\mathcal{C}_{xx}) = \mathbb{1} - \hat{F}_{\mu\nu}(x) dx^\mu dy^\nu \quad . \quad (2.17)$$

In analogy to this relation define the shortest length loop or plaquette on the lattice:

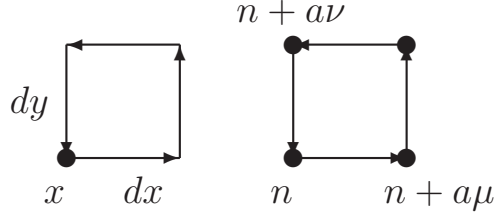


Figure 2.2: *Infinitesimal parallelogram of continuum theory (left) and the elementary plaquette on the lattice (right).*

$$U_{\mu\nu}(n) = U_\mu(n) U_\nu(n + \mu) U_\mu^\dagger(n + \nu) U_\nu^\dagger(n) \quad , \quad (2.18)$$

where we have introduced the shorthand  $U_\mu(n) = U(n, n + a_\mu)$ . Taking the trace over all colors  $N_c = 3$  this object is gauge invariant, as

$$\begin{aligned} U_\mu(n) &\longrightarrow \Lambda(n) U_\mu(n) \Lambda^{-1}(n + a_\mu), \quad \text{where: } \Lambda \in SU(3) \\ P_{\mu\nu} = \text{Tr}[U_{\mu\nu}(n)] &\longrightarrow P_{\mu\nu} \end{aligned} \quad (2.19)$$

Exploiting the Baker-Hausdorff-formula to combine the links and expanding around the center of the plaquette, one finds:

$$\begin{aligned} U_{\mu\nu}(n) &= \exp [ ig a^2 [ \partial_\mu A_\nu - \partial_\nu A_\mu + ig [A_\mu, A_\nu] ] + \mathcal{O}(ga^3) ] \\ &= \mathbb{1} + ig a^2 F_{\mu\nu} - \frac{g^2 a^4}{2} F_{\mu\nu} F_{\mu\nu} + \mathcal{O}(ga^3) + \mathcal{O}(g^2 a^5) \end{aligned} \quad (2.20)$$

Taking the trace over all colors the Wilson gauge action is obtained:

$$S_G = \beta \sum_{n, \mu < \nu} \left( \frac{1}{N_c} \text{Re} \text{Tr}[\mathbb{1} - U_{\mu\nu}(n)] \right) \quad , \quad \text{where } \beta = 2N_c/g^2. \quad (2.21)$$

It is then straight forward to obtain the continuum SU(3) Yang-Mills action:

$$\begin{aligned}
 S_G &= \frac{a^4}{4} \left[ \sum_{n,\mu<\nu} \text{Tr}[F_{\mu\nu}(n)F_{\mu\nu}(n)] + \mathcal{O}(a^2) + \mathcal{O}(g^2 a^2) \right] \\
 &\xrightarrow{a \rightarrow 0} \frac{1}{4} \int d^4x \text{Tr}[\hat{F}_{\mu\nu}^c \hat{F}_c^{\mu\nu}] \quad . \quad (2.22)
 \end{aligned}$$

With the Wilson gauge action Eq. 2.21 the pure glue QCD partition function becomes:

$$\mathcal{Z}(V, T) = \int \prod_{n,\mu} dU_\mu \exp[-S_G(U)] = \int [dU_\mu] \exp[-S_G(U)] \quad . \quad (2.23)$$

This expression can be easily modified to obtain finite temperature quantum field theory as outlined in Chp. 2. From a mathematical standpoint the integrals in Eq. 2.23 are now well defined and furthermore amiable to numerical calculation. However the number of integration variables is very large, for instance on a lattice of size  $N_\sigma^3 N_\tau = 16^4$  there are  $\sim \mathcal{O}(10^5)$  points each possessing another factor four degrees of freedom due to the link directions  $\prod_{n,\mu} dU_\mu(n = N_\sigma^3 N_\tau, \mu = 4)$ . Consequently the only possibility to solve for this large number of degrees of freedom is to use Monte Carlo integration schemes [41–47].

Trivially one would then randomly generate field configurations and integrate over them for a very large number of statistics, but note that only a very few configurations are actually statistically significant as  $\exp[-S_G(U)] \ll 1$  for most possible field configurations. Consequently one requires importance sampling of the field configuration generation process given the weight  $W_e[U] = \exp[-S_G(U)]$ . Without going into details here in practice configurations are generated out of one another as a sequence of updating processes and it can be shown that the mentioned importance sampling is part of the detailed balance condition of a Markov chain.

The Wilson gauge action Eq. 2.21 is ideally suited for such an updating process as it only contains next neighbor interactions, is thus local and is additionally of a bosonic nature, which entails standard integrals.

The SU(3) Yang-Mills or pure glue QCD partition function already incorporates a large amount of non-trivial physics. As such a theory in the limit of infinitely heavy quarks can be shown to be describable by pure Yang-Mills with Wilson loops as observables. Additionally the theory possesses a rich phase structure, which can be explored using exact order parameters like the Polyakov loop. As a consequence of the self coupling of gluons the theory contains a gluonic spectrum, with glueballs as possibly observable quantities. The existence of a mass gap in this spectrum plays a major part in why the world is as we literally see it.

### 2.2.2 Quantum Chromodynamics

To arrive at full QCD and thus the full theory of strong interactions the quark sector must be added to the gluon action. For two flavors of light quarks  $q$  the vacuum fermionic

action of QCD is given by:

$$\begin{aligned}\hat{S}_F &= \int d^4x \sum_{q=u,d} \hat{\Psi}_q^\alpha(x) [(\partial_\mu + ig\hat{A}_\mu)\gamma_{\alpha\beta}^\mu + \hat{m}_q\delta_{\alpha\beta}] \hat{\Psi}_q^\beta(x) \\ &= \int d^4x \sum_{q=u,d} \hat{\Psi}_q^\alpha(x) [\hat{D}_\mu\gamma_{\alpha\beta}^\mu + \hat{m}_q\delta^{\alpha\beta}] \hat{\Psi}_q^\beta(x) \quad ,\end{aligned}\quad (2.24)$$

where  $\alpha, \beta$  denote the Dirac spinor indexes. This expression is easily translated to lattice field theory [40–47] using the dictionary of Eq.2.14 and defining the fermion matrix  $M = (\not{D} + m)$  the lattice quark Lagrangian becomes:

$$\begin{aligned}\mathcal{L}_F &= \sum_{q=u,d} \bar{\Psi}_q(n) \left[ \gamma_\mu \frac{U_\mu(n)\Psi_q(n+\mu) - U_{-\mu}(n)\Psi_q(n-\mu)}{2a} + \hat{m}_q\Psi_q(n) \right] \\ &= \sum_{q=u,d} \bar{\Psi}_q(n) M[U] \Psi_q(n)\end{aligned}\quad (2.25)$$

Due to the bilinear nature of Eq.2.24 and Eq.2.25 it is possible to integrate out the fermion fields completely. To see this consider a general integration over Grassman valued fields:

$$\int d\bar{\eta}_1 d\eta_1 \dots d\bar{\eta}_N d\eta_N \exp\left[-\sum_{ij} \bar{\eta}_i M_{ij} \eta_j\right] = \det[M] \quad .$$

This is exactly the form of the lattice fermion action and the integration over the fields  $d\Psi$  and  $d\bar{\Psi}$  may be carried out directly. Thus the full QCD partition function may be written as:

$$\begin{aligned}\mathcal{Z}_{QCD}(U, \Psi, \bar{\Psi}) &= \int dU d\Psi d\bar{\Psi} \exp[-(S_F(U, \Psi, \bar{\Psi}) + S_G(U))] \\ \Rightarrow \mathcal{Z}_{QCD}(U) &= \int dU \det[M[U]] \exp[-S_G(U)] \quad .\end{aligned}\quad (2.26)$$

Numerically speaking the price one has to pay is the calculation of the intrinsically non-local determinant of the fermion matrix. Fortunately having to handle the latter is circumvented by realizing that bosonically:

$$\begin{aligned}\int dz_1 dz_1^* \dots dz_N dz_N^* \exp\left[-\sum_{ij} z_i^* M_{ij} z_j\right] &= 1/\det[M] \\ \Rightarrow \det[M[U]] &= (1/\det[M^{-1}[U]]) \quad ,\end{aligned}\quad (2.27)$$

so by using this “pseudofermion-trick” [41–45] all variables become bosonic and thus suited for numerical calculation.

However for the Monte Carlo methods described above to work the Boltzmann weight in the partition function must be positive and real:

$$\det[M[U]] \exp[-S_G(U)] \xrightarrow{!} \text{positiv definite} \quad (2.28)$$

At vanishing chemical potential  $\mu = 0$  this property can be fulfilled exploiting  $\gamma_5$ -hermicity of the Dirac operator:

$$\begin{aligned}
 (\mathcal{D} + m)^\dagger &= \gamma_5(\mathcal{D} + m)\gamma_5 \\
 \det[M]^\dagger &= \det[\gamma_5 M \gamma_5] = \det[M] \\
 \det[M]^2 &= \det[M] \det[M]^\dagger = \det[MM^\dagger] \\
 MM^\dagger &= \text{hermitian} \longrightarrow \text{positiv definite.}
 \end{aligned}
 \tag{2.29}$$

This entails that the Boltzmann weight is positive definite and Monte Carlo methods may be successfully applied, if the number of quark flavors is doubled, i.e. a single flavor theory cannot be calculated directly.

### 2.2.3 Quenched QCD

As mentioned the determinant is a non-local object, furthermore the fermion matrix is a matrix with  $N \times N$  entries where  $N = N_\sigma^3 \times N_\tau$  for every spinor and flavor index. For a numerical implementation this is an enormous number of d.o.f.'s and requires an equally enormous amount of computing capacity. This is the reason calculations are often done in what is known as the quenched approximation [41–47].

The flavor of the quenched approximation can be appreciated when parametrically rewriting the fermion matrix  $M[U]$  into [43, 44]:

$$M[U] = \mathbb{1} - \kappa D[U] \quad \text{with: } \kappa \sim 1/a\hat{m}, \tag{2.30}$$

where  $\kappa$  is the so called hopping parameter. Note the details of Eq. 2.30 depend on the chosen lattice discretization and will be shown below, still the fermion matrix can be recast in this form for all discretization schemes.

The immediate advantage of this form can be seen by sending  $\kappa \rightarrow 0$ :

$$\lim_{\kappa \rightarrow 0} M[U] = \mathbb{1} \quad \Rightarrow \quad \det[M[U]] = 1 \quad , \tag{2.31}$$

in this limit the numerical updating procedure can thus be restricted to updating the pure gauge action only.

From a numerical standpoint this is an absolutely enormous simplification, as the fermion determinant may be neglected in the updating process.

Physically speaking as  $\kappa \sim 1/am$  the situation is equivalent to  $am \rightarrow \infty$  and as a consequence only infinitely heavy static quarks live in the Dirac sea.

Another angle on this situation is realizing that in perturbation theory the fermion determinant is given by the sum of Feynman diagrams consisting of virtual fermion loops and an arbitrary number of external gluons. It is thus intimately connected to vacuum polarization effects.

The quenched approximation then entails these loops are explicitly removed from the theory. In principle this is an uncontrollable systematic error in lattice calculations employing this approximation.

Nevertheless the effect of neglecting these vacuum polarization effects is small and less than  $< 5 - 10\%$  in many interesting observables, one of these being the light hadron spectrum [48].

The statement that the virtual quark loops have only a little effect on certain observables can also be argued phenomenologically by e.g. the OZI rule, which states that a QCD process whose Feynman diagram can be split into two parts by cutting only internal gluon lines is suppressed.

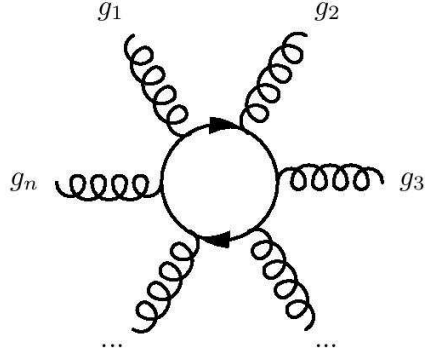


Figure 2.3: Vacuum polarization effects are excluded in quenched QCD.

## 2.3 Fermion Discretization in Lattice QCD

After these more general statements on lattice quantum field theories and different flavors of QCD we now turn to the details of discretizing the fermion action [40–47].

Recall the naively discretized fermion action Eq. 2.25 obtained via the lattice dictionary Eq. 2.14:

$$\begin{aligned} \mathcal{S}_F &= a^4 \sum_n \sum_{q=u,d} \bar{\Psi}_q(n) M[U] \Psi_q(n) \\ &= a^4 \sum_{n,q} \bar{\Psi}_q(n) \left[ \sum_{\mu} \gamma_{\mu} \frac{U_{\mu}(n) \Psi(n + \mu) - U_{-\mu}(n) \Psi(n - \mu)}{2a} + \hat{m}_q \Psi_q(n) \right]. \end{aligned} \quad (2.32)$$

The free fermion propagator is then given by the inverse Fourier transform of the fermion matrix where  $U_{\mu}(n) = \mathbf{1}$ :

$$\begin{aligned} \tilde{S}_F &= a^4 \sum_n \sum_{p,p'} \left( \frac{1}{a^4 N^4} \right)^2 \bar{\Psi}_q(p) e^{-i(p-p')n} \left[ \sum_{\mu} \gamma_{\mu} \frac{e^{ip_{\mu}a} - e^{-ip'_{\mu}a}}{2a} + \hat{m} \right] \Psi_q(p') \\ &= \frac{1}{a^4 N^4} \sum_p \bar{\Psi}_q(p) \underbrace{\left[ \sum_{\mu} \gamma_{\mu} \frac{i \sin(ap_{\mu})}{a} + \hat{m} \right]}_{G(p)} \Psi_q(p), \end{aligned} \quad (2.33)$$

using the following general relation for the inverse of linear combinations of  $\gamma$ -matrices:

$$\left( a\mathbb{1} + i \sum_{\mu} \gamma_{\mu} b_{\mu} \right)^{-1} = \frac{a\mathbb{1} - i \sum_{\mu} \gamma_{\mu} b_{\mu}}{a^2 + \sum_{\mu} b_{\mu}^2} , \quad (2.34)$$

the free fermion lattice propagator becomes:

$$G^{-1}(p) = \frac{\hat{m}\mathbb{1} - i \sum_{\mu} \gamma_{\mu} \bar{p}_{\mu}}{\hat{m}^2 + \sum_{\mu} \bar{p}_{\mu}^2}, \quad \text{where: } \bar{p}_{\mu} = \frac{\sin(ap_{\mu})}{a} . \quad (2.35)$$

The poles of the propagator correspond to the fermion species described by the Dirac operator, naturally in the continuum this would be a single species. However it is easy to find that the pole structure of Eq. 2.35 is much more complex as the  $\sin(p_{\mu}a)$ -function has additional zeros at  $p_{\mu} = \pi/a$ . Thus instead of a single Dirac fermion we find 16 doublers actually given by:

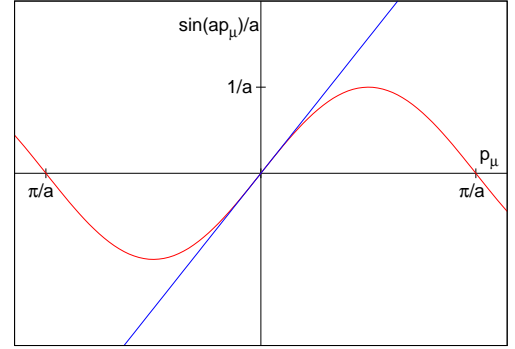


Figure 2.4: *Doublers appear at the corners of the Brillouin zone.*

$$\frac{\sinh(Ea)}{a} = \pm \sqrt{m^2 + \sum_{k=1}^3 \bar{p}_k^2} \quad (2.36)$$

The existence of these fermion doubler species follows from very general assumptions on the fermion matrix [43, 49], as such let  $G(p)$  be the inverse fermion propagator of a theory, then assume:

- Invariance under the cubic group:

$$G(p) = \gamma_{\mu} G^{\dagger}(p_{\nu}(1 - 2\delta_{\mu\nu})) \gamma_{\mu} \quad , \quad \text{where: } \mu = 1, 2, 3, 4 \quad (2.37)$$

- Chiral invariance ( $m = 0$ ):

$$G(p) = -\gamma_5 G(p) \gamma_5 \quad \rightsquigarrow \quad \{\gamma_5, G(p)\} = 0 \quad (2.38)$$

- Locality:

$$\frac{d}{dp} G(p) = \text{continuous} \quad . \quad (2.39)$$

Taken together it follows that:

$$G(p) = -G(-p) \quad . \quad (2.40)$$

## 2.3 Fermion Discretization in Lattice QCD

As the lattice theory is defined with periodic or anti periodic boundary conditions,  $G(p)$  must be a periodic function with period  $p_\mu \rightarrow p_\mu + 2\pi$ . Then Eq. 2.40 implies  $G(p)$  must vanish for every  $p_\mu = 0, \pm\pi$ . Hence doublers enter the theory [43, 49].

For the naive discretization described above this manifests itself as the so called spectrum doubling symmetry [43, 49] of the action:

$$\Psi'_x = e^{-ix\pi_h} M_h \Psi_x \quad \text{and} \quad \bar{\Psi}'_x = e^{ix\pi_h} M_h \bar{\Psi}_x \quad , \quad (2.41)$$

where  $\pi_h = \{\pi, \text{if: } p_h = \pi, h = 1, 2, 3, 4 \parallel 0, \text{ else}\}$  and  $M_h = \prod_{\mu \in h} i\gamma_5 \gamma_\mu$ , i.e. it is only defined on the corners of the Brillouin zone. In momentum space its effect is the exchange of the latter:

$$\Psi'_p = M_h \Psi_{p+\pi_h} \quad \text{and} \quad \bar{\Psi}'_p = \bar{\Psi}_{p+\pi_h} M_h^\dagger \quad . \quad (2.42)$$

Note projecting onto the left and right handed chirality states via  $P_{L,R}$  respectively one may write:

$$G(p) \sim i \sum_{\mu} \gamma_{\mu} (P_L + P_R), \quad (2.43)$$

subsequently exploiting the spectrum doubling symmetry and the above equation it can be shown that the spectrum doubling transformation changes the chirality of a fermion for  $h = \text{odd}$  and preserves it for  $h = \text{even}$ , due to the relation:

$$M_h^\dagger i\gamma_{\mu} (-1)^{\delta_{\mu,h}} P_L M_h = i\gamma_{\mu} P_R \quad . \quad (2.44)$$

Furthermore topological arguments provide the possibility to assign the index +1 to the chirality preserving and  $-1$  to chirality transforming case. For the hypertorus defined by the Euclidean lattice the Poincaré-Hopf theorem implies the sum of all indices must be equal to zero [49].

Thus under the general assumptions stated above a lattice theory always contains as many left- as right-handed fermions in the propagator and a total of  $n_d = 15$  additional fermion species located at the corners of the Brillouin zone.

In principle the famous Nielsen-Ninomya No-Go theorem [49] states that this result holds unless one gives up part of the above assumptions.

### 2.3.1 Wilson-Clover Fermions

The philosophy of the Wilson fermion formulation is to break the spectrum doubling symmetry explicitly with an additional chiral symmetry breaking term in the action [40]. It is clear that such a term must respect the symmetries of the action with the exception of the spectrum doubling symmetry and vanish in the continuum limit  $a \rightarrow 0$  in order to reproduce the continuum action.

The simplest choice for a term respecting gauge invariance is proportional to a second order derivative in the fermion fields:

$$S_{\partial^2} = a^4 \sum_n r \cdot \bar{\Psi}(n) \sum_\mu \frac{\Psi(n + \mu) + \Psi(n - \mu) - 2\Psi(n)}{2a} . \quad (2.45)$$

To show this term indeed vanishes in the continuum limit perform a Taylor expansion:

$$\begin{aligned} S_{\partial^2} &= a^4 \sum_n \frac{r}{2a} \bar{\Psi}(n) \sum_\mu \left[ \Psi(n) + a\partial_\mu \Psi(n) + \frac{a^2}{2} \partial_\mu^2 \Psi(n) + \dots \right. \\ &\quad \left. + \Psi(n) - a\partial_\mu \Psi(n) + \frac{a^2}{2} \partial_\mu^2 \Psi(n) + \dots - 2\Psi(n) \right] \\ &= a^4 \sum_n \left[ \frac{r}{2} a \sum_\mu \bar{\Psi}(n) \partial_\mu^2 \Psi(n) + \mathcal{O}(a^3) \right] \xrightarrow{a \rightarrow 0} 0 . \end{aligned} \quad (2.46)$$

Subsequently a term of this form indeed satisfies the demands of gauge invariance and vanishing continuum limit.

The crucial question is now whether or not this term lifts the spectrum doubling symmetry. To see this consider its inverse Fourier transform as in Eq. 2.33:

$$\begin{aligned} \tilde{S}_{\partial^2} &= a^4 \sum_n \sum_{q,q'} \left( \frac{1}{a^4 N^4} \right)^2 \bar{\Psi}(p) e^{-i(p-p')n} \left[ \sum_\mu r \cdot \frac{e^{ip_\mu a} + e^{-ip'_\mu a} - 2}{2a} \right] \Psi(p) \\ &= \frac{1}{a^4 N^4} \sum_p \bar{\Psi}(p) \underbrace{\left[ \sum_\mu r \cdot \frac{2 \cos(ap_\mu) - 2}{2a} \right]}_{G(p)} \Psi(p) . \end{aligned} \quad (2.47)$$

As before the key is to look at the pole structure of Eq. 2.47, here one finds:

$$\begin{aligned} p_\mu a = 0 &\Rightarrow G(p_\mu a) = 0 , \\ p_\mu a = \pi &\Rightarrow G(p_\mu a) \sim -\frac{2r}{a} . \end{aligned} \quad (2.48)$$

This means subtracting  $S_{\partial^2}$  from the naive fermion action  $S_F$  indeed removes the doublers from the theory as they are given a mass proportional to the inverse lattice spacing  $E \sim 1/a$ , i.e. the fermion at  $p_\mu a = 0$  remains unmodified while the masses of the doublers located at  $p_\mu a = \pi$  are pushed up towards the lattice cut-off and thus effectively removed from the theory.

Note the additional free parameter  $r$  controls the strength of the doubling removing mass shift, as such to avoid “near doubling” in the propagator a sensible choice is to set  $r = 1$  and we will do so in this thesis.

### 2.3 Fermion Discretization in Lattice QCD

The fermion discretization based on the above results is the Wilson fermion action:

$$\begin{aligned}
S_W &= S_F - S_{\partial^2} \\
&= a^4 \sum_n \left[ \sum_\mu \bar{\Psi}(n) \gamma_\mu \partial_\mu \Psi(n) + m \bar{\Psi}(n) \Psi(n) - \frac{r}{2} a \sum_\mu \bar{\Psi}(n) \partial_\mu^2 \Psi(n) \right] \\
&= a^4 \sum_n \bar{\Psi}(n) \left[ m \Psi(n) - \frac{1}{2a} \sum_\mu \left[ (r - \gamma_\mu) \Psi(n + \mu) + (r + \gamma_\mu) \Psi(n - \mu) - 2r \Psi(n) \right] \right] \\
&= a^4 \sum_n \bar{\Psi}(n) \left[ \left( m + \frac{4r}{a} \right) \Psi(n) - \frac{1}{2a} \sum_\mu \left[ (r - \gamma_\mu) \Psi(n + \mu) + (r + \gamma_\mu) \Psi(n - \mu) \right] \right]
\end{aligned} \tag{2.49}$$

Transforming the fermion fields according to  $\Psi' = \sqrt{m + 4r/a} \Psi$  the action Eq. 2.49 may be rewritten as:

$$\begin{aligned}
S_W &= a^4 \sum_n \left[ \bar{\Psi}'(n) \Psi'(n) - \frac{1}{2ma + 8r} \sum_\mu \bar{\Psi}'(n) \left[ (r - \gamma_\mu) \Psi'(n + \mu) + (r + \gamma_\mu) \Psi'(n - \mu) \right] \right] \\
&= a^4 \sum_n \left[ \bar{\Psi}'(n) \Psi'(n) - \kappa \sum_\mu \bar{\Psi}'(n) \left[ (r - \gamma_\mu) \Psi'(n + \mu) + (r + \gamma_\mu) \Psi'(n - \mu) \right] \right],
\end{aligned} \tag{2.50}$$

with the hopping parameter  $\kappa = 1/(2ma + 8r)$ .

In the continuum limit this action reduces to:

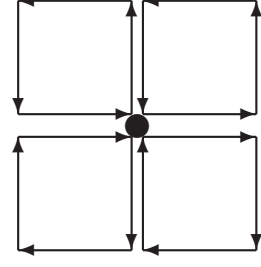
$$\begin{aligned}
S_W &= a^4 \sum_n \left[ \sum_\mu \bar{\Psi}(n) \gamma_\mu \partial_\mu \Psi(n) + m \bar{\Psi}(n) \Psi(n) - \frac{r}{2} a \sum_\mu \bar{\Psi}(n) \partial_\mu^2 \Psi(n) \right] \\
&\xrightarrow{a \rightarrow 0} S_F^{cont} + \mathcal{O}(a) \quad ,
\end{aligned} \tag{2.51}$$

as such it incorporates lattice discretization errors linear in the lattice spacing. However following the Symanzik improvement scheme [50] other terms may be added to the action and tuned to reduce the discretization errors order by order. Given the dimension of the fermion fields to be  $d_\Psi = 3/2$ , dimensional analysis shows the Wilson term of  $S_{\partial^2}$  is of dimension  $d = 5$ . In a next step it can be proven that there is only one more allowed term of  $d = 5$  that is not a mass term  $\sim m^2 \bar{\Psi} \Psi$ . This term is in fact proportional to the imaginary part of the gauge plaquettes and corresponds to an anomalous magnetic moment [51]:

$$S_{SW} = a^5 \sum_n \frac{c_{SW}}{2} \bar{\Psi}(n) \sum_{\mu\nu} \sigma_{\mu\nu} P_{\mu\nu}(n) \Psi(n) \quad , \tag{2.52}$$

with

$$\begin{aligned}\sigma_{\mu\nu} &= \frac{i}{2}[\gamma_\mu, \gamma_\nu] \quad , \\ P_{\mu\nu}(n) &= \frac{i}{8} \sum_{j=1}^4 \left[ U_{\mu\nu}^j(n) - U_{\mu\nu}^{j\dagger}(n) \right] \\ &\sim ga^2 F_{\mu\nu} + \mathcal{O}(a^3) \quad , \quad (2.53)\end{aligned}$$



thus the so called clover term vanishes in the continuum limit  $a \rightarrow 0$  and in the limit of vanishing coupling  $g \rightarrow 0$ .

Figure 2.5: *The improvement term in the plaquettes is seen to resemble a four leaf clover, hence clover term.*

Adding this and the Wilson term to the naive fermion discretization one obtains the Wilson-Clover or Sheikholeslami-Wohlert action [51]:

$$\begin{aligned}S_C &= S_F - S_{\partial^2} - S_{SW} \\ &= a^4 \sum_n \left[ \bar{\Psi}(n)\Psi(n) \right. \\ &\quad \left. - \kappa \sum_\mu \bar{\Psi}(n) \left[ (r - \gamma_\mu)\Psi(n + \mu) + (r + \gamma_\mu)\Psi(n - \mu) \right] \right] \\ &\quad - a^5 \frac{c_{SW}}{2} \sum_{\mu\nu} \bar{\Psi}(n) \sum_{\mu\nu} \sigma_{\mu\nu} P_{\mu\nu}(n) \Psi(n)\end{aligned}\quad (2.54)$$

Tuning the clover coefficient  $c_{SW}$  one can then complete the Symanzik improvement scheme to remove all discretization errors linear in the lattice spacing  $\mathcal{O}(a)$ :

$$\begin{aligned}S_C &= S_F - S_{\partial^2} - S_{SW} \\ &\xrightarrow{a \rightarrow 0} S_F^{cont} + \mathcal{O}(a^2) \quad .\end{aligned}\quad (2.55)$$

Choosing the appropriate value for the clover coefficient  $c_{SW}$  can be guided perturbatively and non-perturbatively by imposing the PCAC relation be correct to  $\mathcal{O}(a^2)$ . Without going into details the value of the clover coefficient for tree-level improvement is  $c_{SW} = 1 = r$ . The fully non-perturbative result in quenched QCD can be parametrized as [52]:

$$c_{SW} = \frac{1 - 0.656g^2 - 0.152g^4 - 0.054g^6}{1 - 0.922g^2} \quad \text{for: } 0 \leq g \leq 1 \quad (2.56)$$

In this work the clover coefficients are tuned according to the above expression Eq. 2.56.

Not to spoil the  $\mathcal{O}(a^2)$  improvement also the pseudo scalar (PS), scalar (S), axial vector (A) and vector (V) currents must be improved, one finds:

$$\begin{aligned} PS^I &= PS \quad , \quad S^I = S \\ V_\mu^I &= V_\mu + ac_V \partial_\nu T_{\mu\nu} \\ A_\mu^I &= A_\mu + ac_A \partial_\mu PS \quad , \end{aligned} \quad (2.57)$$

with the tensor current  $T_{\mu\nu} = \hat{\Psi} \sigma_{\mu\nu} \Psi$ . Note the axialvector current is now explicitly coupled to the pseudoscalar and while the coefficient  $c_V$  becomes negligible for  $\beta > 6.4$ , the non-perturbatively determined coefficient  $c_A$  reads [52, 53]:

$$c_A = -0.00756 g^2 \frac{1 - 0.748g^2}{1 - 0.977g^2} \quad . \quad (2.58)$$

As a consequence we will restrict ourselves to using only the improved axialvector currents in the following.

## 2.4 Connecting to Physics

Even though all the integrals are well defined and calculations can be done in lattice gauge theory, it is not real-world physics. The theory essentially lives in a box with crystalline structure admitting only a finite number of discretized momenta. Consequently it must be connected to physics and the procedure to do so requires taking the thermodynamic limit ( $V \rightarrow \infty$ ), the continuum limit ( $a \rightarrow 0$ ) and renormalization ( $\mathcal{O}_{bare} \rightarrow \mathcal{O}_{physics}$ ).

In the preceding chapters a complete definition of the lattice QCD partition function  $\mathcal{Z}(N_\tau, N_\sigma, g, \kappa)$  was given. Here  $\kappa$  is the hopping parameter of the fermionic action, in itself it acts like a fermion-gluon coupling and is subsequently itself dependent on  $g$ . Thus to connect with the physical continuum partition function  $\mathcal{Z}_{cont}(T^{-1}, V)$  we must find a relation between the lattice spacing  $a$  and the coupling  $g^2 = 2N_c/\beta = 6/\beta$ , as then the lattice partition function is fixed and the relations  $V = (N_\sigma a)^3$  and  $T^{-1} = N_\tau a$  give us  $\mathcal{Z}_{cont}(T^{-1}, V)$  from  $\mathcal{Z}(N_\tau, N_\sigma, g(a), \kappa(g))$ .

To motivate a relation between the coupling and the lattice spacing postulate that the results of our lattice theory should be independent of the specific lattice we used and in particular should not depend on lattice size or lattice spacing. Such a postulation can be assured to hold in renormalization group theory around  $g = 0$ , i.e. in the perturbative regime, through the Callan-Symanzik equation (see e.g. [13, 15]):

$$a \frac{dg(a)}{da} = \beta(g) \quad , \quad (2.59)$$

where  $\beta(g)$  is the so called beta-function.

It can be shown that the first two orders of the  $\beta$ -function are independent of the renormalization scheme and may be written as:

$$\begin{aligned}\beta(g) &= \beta_0 g^3 + \beta_1 g^5 + \mathcal{O}(g^7) \\ &= \frac{1}{(4\pi)^2} \left(11 - \frac{2}{3} N_f\right) g^3 + \frac{1}{(4\pi)^4} \left(102 - \frac{38}{3} N_f\right) g^5 + \mathcal{O}(g^7) \quad ,\end{aligned}\quad (2.60)$$

where  $N_f$  denotes the number of quark flavors. Inserting this result and solving the differential equation Eq. 2.59 one obtains:

$$a\Lambda = R(g^2) = (\beta_0 g^2)^{-\beta_1/2\beta_0^2} \exp\left[-\frac{1}{2\beta_0 g^2}\right] \quad ,\quad (2.61)$$

note  $\Lambda$  is an integration constant of dimension  $\Lambda = [\text{length}^{-1}]$ . Here this means that all physical quantities calculated in the lattice theory are given in units corresponding to this scale parameter  $\Lambda$ .

However, the continuum theory of QCD only contains one dimensionless coupling  $g$  and cannot set a dimensionful scale for the theory. The scale of QCD is introduced only during the renormalization process, where the coupling must be set according to the invoked scheme. Before renormalization this means only ratios of actually experimentally observable quantities can be predicted by the theory, e.g. hadron mass ratios or hard scattering processes by perturbation theory. In our case the consequence is that the lattice scale parameter  $\Lambda$  is arbitrary.

To nevertheless connect the lattice theory with experimentally observable quantities the scale must be either canceled in dimensionless ratios of observables or fixed by a measured quantity such as the proton mass or the deconfinement temperature  $T_c$ .

In this thesis we set the scale by use of the square root of the string tension  $\sqrt{\sigma}$ . The string tension can be calculated from the long distance behavior of infinitely heavy static quarks in the vacuum case of pure gauge theory and describes the potential that keeps the quarks confined:  $V_{\bar{q}q} = -\alpha/r + \sigma r$ .

The chosen value for the string tension here is  $\sqrt{\sigma} = 428\text{MeV}$  [54], to obtain the physical temperature in units of the deconfinement temperature we set:

$$\frac{T}{T_c} = \left(\frac{T}{\sqrt{\sigma}}\right) \cdot \left(\frac{\sqrt{\sigma}}{T_c}\right) \quad ,\quad (2.62)$$

which using  $T_c/\sqrt{\sigma} = 0.630(5)$  from [54] gives the deconfinement temperature  $T_c = 270\text{MeV}$ .

Strictly speaking the two-loop scaling function shown in Eq. 2.61 is only applicable in the perturbative regime  $g \sim 0$ , fortunately a non-perturbative calculation for the Wilson gauge action exists and the string tension can be parameterized in terms of  $R(g^2)$  with  $\beta \in [5.6 : 6.5]$  as [55, 56]:

$$\begin{aligned}a\sqrt{\sigma}(g) &= R(g^2) \frac{1 + c_2 r^2(g) + c_4 r^4(g) + c_6 r^6(g)}{\lambda/\sqrt{\sigma}} \quad , \\ r(g) &= \frac{R(g^2)}{R(g^2(\beta = 6.0))} \quad ,\end{aligned}\quad (2.63)$$

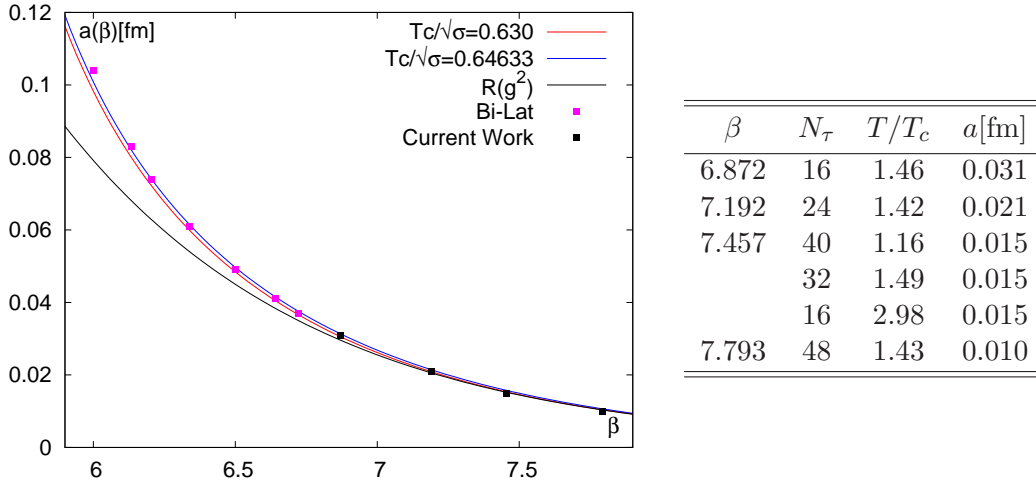


Figure 2.6: The lattice spacing  $a(\beta)[\text{fm}]$  computed from Eq. 2.63. The black points labeled “Current Work” represent the chosen values and are given in the table on the right, while the magenta give those chosen by the Bielefeld lattice group in the past.

the constants are given by  $c_2 = 0.2731$ ,  $c_4 = -0.01545$ ,  $c_6 = 0.01975$  and  $\lambda/\sqrt{\sigma} = 0.01364$ . In Fig. 2.6 we show the lattice spacing in physical units for  $T_c/\sqrt{\sigma} = 0.630(5)$  from [54],  $T_c/\sqrt{\sigma} = 0.6463$  from [57] and the perturbative first term. The values for  $\beta$  as well as the estimated  $T/T_c$  and lattice spacings  $a[\text{fm}]$  chosen for our  $N_\tau$  are shown on the right of Fig. 2.6. For the finest lattice spacings our calculations are seen to be close to the perturbative regime.

### 2.4.1 Renormalization

The renormalization of observables, i.e. the connection of  $\mathcal{O}_{bare} \rightarrow \mathcal{O}_{physics}$  is particularly difficult in the Wilson fermion formulation.

In general for QCD with only light quarks one would employ mass-independent renormalization schemes, the procedure generically can be written as:

$$g_R^2 = g^2 Z_g(g^2, a\mu) \quad , \quad m_R = m_q Z_m(g^2, a\mu) \quad , \quad (2.64)$$

with the bare quark mass  $m_q$ . As such the renormalization factors  $Z(g^2, a\mu)$  depend only on the normalization mass scale  $\mu$  and the bare coupling  $g$ , on its own this is multiplicative renormalization. However Wilson fermions break chiral symmetry and this leaves the mass unprotected from additive renormalization  $m_q \rightarrow m_q = m_o - m_c$ . To see this recall the hopping parameter of the Wilson action in the free case:

$$\kappa = \frac{1}{2ma + 8r} \quad \Rightarrow \quad ma = \frac{1}{2\kappa} - 4r \equiv \frac{1}{2\kappa} - \frac{1}{2\kappa_c} \quad , \quad (2.65)$$

in the free case  $\kappa_c = 1/8$  and as  $U_\mu(n) = \mathbb{1}$  there is no explicit dependence on the coupling, this however changes in the interacting case where  $\kappa_{c,free} \rightarrow \kappa_c(g)$ . Note e.g. in the strong coupling limit  $\kappa_c = 1/4$ . The renormalization of  $\kappa_c$  implies both multiplicative as well as additive renormalization.

To see the origin is indeed the Wilson term proportional to  $r$  recall that to satisfy chiral symmetry implies  $\{\gamma_5, G\} = 0$ , however in the Wilson case  $\{\gamma_5, (r \cdot \mathbb{1} \pm \gamma_\mu)G_W\} \neq 0$ , as the unit matrix does not anti-commute with  $\gamma_5$ .

In the improved theory of Wilson-Clover fermions the simple renormalization prescription above must be recast into [46]:

$$\begin{aligned} g_R^2 &= g^2(1 + b_g am_q) Z_g(g^2(1 + b_g am_q), a\mu) \\ m_R &= m_b(1 + b_m am_q) Z_m(g^2(1 + b_g am_q), a\mu) \quad , \end{aligned} \quad (2.66)$$

where the additional coefficients  $b_g$  and  $b_m$  must be calculated ideally non-perturbatively.

### Quark Masses and Wilson-Clover Fermions

Another consequence of the Wilson fermion formulation is that in a sense the quark mass itself becomes an observable. Instead of being unambiguously fixed before a calculation it must be checked a posteriori. This is apparent as the parameters needed to tune the calculation are  $\mathcal{Z}(N_\tau, N_\sigma, g(a), \kappa(g))$  where  $\kappa(g)$  is the hopping parameter in the fully interacting theory. To nevertheless estimate the quark mass at the chiral point  $m_b = m_R = 0$  the critical hopping parameter  $\kappa_c$  must be calculated.

One possibility to achieve this for any given lattice spacing is to assume the chiral relation  $M_\pi^2 \sim m_q$ , then compute the pion mass as a function of  $1/2\kappa$  and extrapolate to zero. The  $\kappa$ -value where the pion becomes massless is by definition  $\kappa_c$ .

For light quarks the bare quark mass  $m_q$  can be estimated for any given value of  $\kappa$  from Eq. 2.65 once  $\kappa_c$  is known. With the bare quark mass in hand one can then define the renormalized quark mass along the lines of Eq. 2.66. Here we invoke a definition of the quark mass that does not depend on the renormalization scheme and the renormalization scale. Such a definition leads to the renormalization group invariant (RGI) quark mass and the  $\mathcal{O}(a^2)$  relation to the lattice bare quark mass is:

$$m_{\text{RGI}} = Z_m Z[1 + b_m am_q] m_q \quad . \quad (2.67)$$

In this case the renormalization coefficients have been calculated non-perturbatively [58, 59] and may be parameterized in terms of the bare coupling  $g$  as:

$$\begin{aligned} Z_m(g^2) &= 1.752 + 0.321(6/g^2 - 6) - 0.220(6/g^2 - 6)^2 \\ Z(g^2) &= (1 + 0.090514g^2) \frac{1 - 0.9678g^2 + 0.04284g^4 - 0.04373g^6}{1 - 0.9678g^2} \\ b_m(g^2) &= -(0.5 + 0.09423g^2) \frac{1 - 0.6905g^2 + 0.0685g^4}{1 - 0.6905g^2} \quad . \end{aligned} \quad (2.68)$$

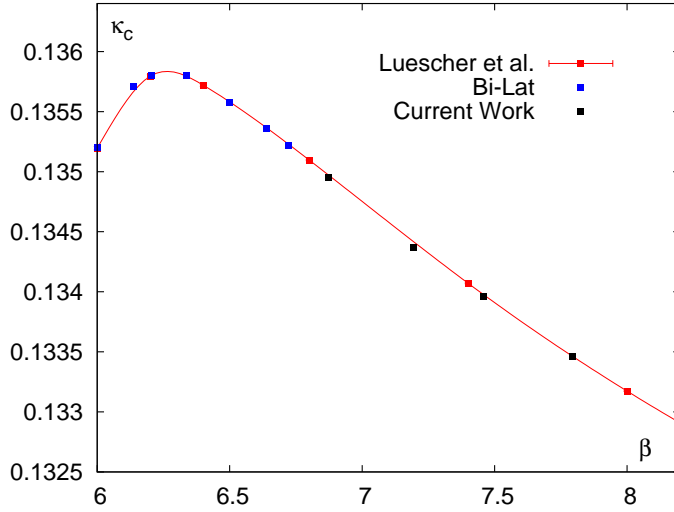


Figure 2.7: *The critical hopping parameter  $\kappa_c$  over bare lattice coupling  $\beta = 6/g^2$  as obtained in [52] (red). Values used in the past by the Bielefeld lattice group are given in blue, while the black points correspond to the values chosen in this work.*

Tuning  $\kappa_c$  via the pion mass is a procedure that naturally requires the pions to be massless Goldstone bosons. As a result it breaks down in the high temperature phase of QCD where chiral symmetry is restored and pions acquire a mass.

A temperature independent definition of the quark mass can be given by the axial Ward identity (AWI) [61]:

$$Z_A \partial_\mu A_\mu^I = (m_u + m_d) Z_{PS} PS = 2m_q Z_{PS} PS \quad , \quad (2.69)$$

here u and d denote the flavor indices, note the quark mass degeneracy  $m_u = m_d = m_q$  due to the pseudofermion-trick in lattice calculations. This expression can be re-expressed in terms of 2-point correlation functions and thus in terms of directly calculable quantities as:

$$\frac{Z_A \langle \partial_\mu A_\mu^I(\tau) PS(0) \rangle}{Z_{PS} \langle PS(\tau) PS(0) \rangle} = 2m_{\text{AWI}} \quad . \quad (2.70)$$

This definition of a temperature independent quark mass subsequently enables the indirect computation of the critical hopping parameter  $\kappa_c$ . To do so the hopping parameter is adjusted in simulation until the AWI quark mass vanishes. This gives  $\kappa_c$  by the same reasoning as mentioned above, such a procedure was followed in [52]. The results of this computation are shown in Fig. 2.7 and were used in this thesis to estimate  $\kappa_c$ , additionally the  $\kappa_c$ -values for our calculation and those chosen by the Bielefeld lattice group in the past are shown.

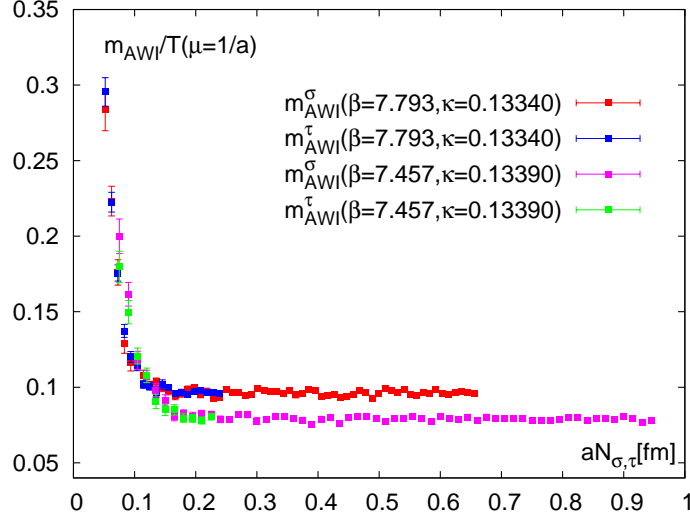


Figure 2.8: The temporal and spatial AWI quark masses as measured from the lattices sized  $128^3 \times 32$  and  $128^3 \times 48$  at  $1.5T_c$ .

The possibility to use the axial Ward identity in order to define the quark mass  $m_{\text{AWI}}$  independent of the temperature originates in the fact that it is an operator identity. Thus it should be independent of the spatial and temporal extent of the lattice, as it holds for all distances. As a direct consequence the spatial direction may be used to compute the AWI quark mass, this is an advantage as in finite temperature calculations the spatial extent of the lattice is much larger than the temporal. In Fig. 2.8 we show the temporal and spatial AWI quark masses obtained from our lattices. Clearly the operator identity holds as the temporal and spatial directions are indeed degenerate.

The renormalized AWI quark mass is given by:

$$m_R = Z'_m(1 + b'_m am_q)m_q = \frac{Z_A(1 + b_A am_q)}{Z_{PS}(1 + b_{PS} am_q)} m_{\text{AWI}} \quad , \quad (2.71)$$

expanding in powers of  $a$  the axial Ward identity mass becomes:

$$m_{\text{AWI}} = Z(1 + [b'_m + (b_A - b_{PS})]am_q)m_q \quad \text{with: } Z = Z'_m Z_{PS}/Z_A \quad , \quad (2.72)$$

where the improvement coefficients  $(b_A - b_{PS})$  have been calculated non-perturbatively [59]:

$$(b_A - b_P)(g^2) = -0.00093 g^2 \frac{1 + 23.3060g^2 - 27.3712g^4}{1 - 0.9833g^2} \quad . \quad (2.73)$$

Given the AWI quark mass, which can be directly calculated on the lattice, we can relate the relevant RGI mass via:

$$m_{\text{RGI}} = Z_m[1 + (b_A - b_{PS})am_q]m_{\text{AWI}} \quad . \quad (2.74)$$

In principle the renormalization procedure for the quark mass is complete at this point. However it is customary to quote the quark mass in the  $\overline{\text{MS}}$ -scheme at the scale  $\mu = 2\text{GeV}$  for light quarks. Consequently the RGI quark mass is recast in terms of the running quark mass  $m(\mu)$ :

$$m_{\text{RGI}} = \lim_{\mu \rightarrow \infty} m(\mu) (2\beta_0 g^2(\mu))^{-d_0/(2\beta_0)} \quad , \quad (2.75)$$

where  $d_0 = 8/(4\pi^2)$  and  $\beta_0$  is the first term of the  $\beta$ -function encountered before.

Given the RGI quark mass  $m_{\text{RGI}}$  at the starting scale  $\mu_0 = 1/a$  and the coupling at this scale in the  $\overline{\text{MS}}$ -scheme  $g_{\overline{\text{MS}}}^2(\mu_0)$ , the evolution of  $m_{\overline{\text{MS}}}(\mu)$  can be done via the perturbative renormalization group functions, which are known to four-loop accuracy [62] and are implemented in the ‘‘RunDec.m’’ package [63]. This entails computing the coupling in the  $\overline{\text{MS}}$ -scheme  $g_{\overline{\text{MS}}}^2(\mu_0)$  and we will be returning to this topic very shortly.

Concluding this section we outline the general flow of computing the quark mass of a finite temperature lattice calculation:

1. Generate a small number of configurations and calculate the AWI quark mass directly from the lattice using Eq. 2.70.
2. Use the results to compute the RGI quark mass via Eq. 2.74 and ...
3. ... do the evolution to  $m_{\overline{\text{MS}}}(\mu = 2\text{GeV})$  given the coupling  $g_{\overline{\text{MS}}}^2(\mu_0)$  via the ‘‘RunDec.m’’ package.

### Renormalized Coupling and Renormalization Group Constants

Having elucidated the special situation of renormalizing the quark mass in lattice QCD with Wilson fermions, we now turn to the renormalization of the coupling and the conserved currents [64–68].

As noted above the key interest is to quote quark masses and couplings in the  $\overline{\text{MS}}$ -scheme, one possibility to do this for the coupling is to compute it in the so called V-scheme. Whereby the V-scheme is defined by the potential:

$$V(\mu) = -C_F \frac{g_V^2(\mu)}{\mu^2} \quad , \quad (2.76)$$

where  $C_F = 4/3$  denotes the value of the quadratic Casimir operator. The V-scheme coupling  $g_V^2$  can be related to the plaquette expectation value on the lattice [64–66]:

$$u_0 \simeq \left\langle \frac{1}{N_c} \sum_n \text{Re Tr}[U_{\mu\nu}(n)] \right\rangle^{1/4} \quad (2.77)$$

via Taylor expansion, in the quenched case the resulting expression is:

$$-\ln(u_0^4) = \frac{C_F g_V^2(\mu^*)}{4} \left[ 1 - \frac{g_V^2(\mu^*)}{4\pi} \left( \frac{11N_c}{12\pi} \ln \left( \frac{6.7117}{\mu^*} \right)^2 \right) \right] + \mathcal{O}(g_V^6(\mu^*)) \quad , \quad (2.78)$$

with  $\mu^* = 3.4018/a$  being the most accurate matching scale [65,68]. Given the plaquette expectation value calculated on the lattice the rescaling of  $g_V^2(\mu^* = 1/a)$  can be carried out utilizing the two-loop renormalization group equation of Eq. 2.61, whereby the V- and  $\overline{\text{MS}}$ -scheme scales are related via:  $\Lambda_{\overline{\text{MS}}} = 0.6252\Lambda_V$ .

Finally also the observable currents must be renormalized for the renormalization program to be complete. Details on the currents will be given later, however generically the renormalization is of the form:

$$J_H^{ren} = \frac{2\kappa}{a^3} Z_H J_H \quad , \quad (2.79)$$

here  $J_H$  denotes the current, where  $H = PS, S, A, V$  as mentioned above. The renormalization group constant  $Z_H$  in quenched QCD with improved Wilson fermions has been computed in one-loop tadpole-improved perturbation theory and reads:

$$Z_H = u_0 \left( 1 - \frac{g^2}{16\pi^2} C_F (\gamma_{\mathcal{O}} \ln(a\mu) + C_F \Delta_H) \right) \quad , \quad (2.80)$$

where  $\gamma_{\mathcal{O}}$  denotes the anomalous dimension and  $\Delta_H$  is a channel specific constant, computed in [64]. Note here that tadpole-improvement is in fact used to cancel certain unphysical diagrams in the gauge sector of the lattice theory.

Plugging in the renormalized coupling  $g = g_{\overline{\text{MS}}}^2(\mu = 2\text{GeV})$  and inserting the channel specific constants  $\gamma_{\mathcal{O}}$  and  $\Delta_H$ , the perturbative renormalization group constants may be calculated.

Naturally more reliable results can be achieved using a non-perturbative computation of the renormalization constants. For the vector and axialvector currents close to the chiral limit in the range of  $6.0 \leq \beta \leq 24.0$  such a computation is available [53] and the resulting parameterization reads:

$$\begin{aligned} Z_V &= \frac{1 - 0.7663g_0^2 + 0.0488g_0^4}{1 - 0.6369g_0^2} \\ Z_A &= \frac{1 - 0.8496g_0^2 + 0.0610g_0^4}{1 - 0.7332g_0^2} \quad . \end{aligned} \quad (2.81)$$

In this work the non-perturbative results will be employed whenever possible and the resulting renormalization constants, couplings and necessary plaquette values are given in Tab. 2.4.1.

The procedure to compute the coupling  $g_{\overline{\text{MS}}}^2$ , which is needed for determining the quark mass, and the perturbative renormalization group constants may be outlined as follows:

$\beta$	$u_0$	$g_{\overline{\text{MS}}}^2(1/a)$	$P_{\text{TI}}$	$S_{\text{TI}}$	$A_{\text{TI}}$	$V_{\text{TI}}$	$A_{\text{NP}}$	$V_{\text{NP}}$
6.872	0.90263	1.70310	0.74	0.78	0.85	0.83	0.847	0.829
7.192	0.90890	1.54170	0.76	0.80	0.86	0.84	0.859	0.842
7.457	0.91345	1.43185	0.78	0.81	0.87	0.85	0.868	0.851
7.793	0.91854	1.31517	0.79	0.82	0.88	0.86	0.877	0.861

Table 2.1: Table of renormalization constants from non-perturbative (NP) and tadpole-improved perturbative (TI) calculations in the case of vanishing mass at scale  $\mu = 1/a$ .

1. Compute the plaquette expectation value  $u_0$  on a number of configurations on the lattice.
2. Use Eq. 2.78 to extract the coupling in the V-scheme  $g_V^2(\mu^* = 1/a)$ .
3. Rescale the coupling using the two-loop renormalization group equation and translate to  $\overline{\text{MS}}$  via  $\Lambda_{\overline{\text{MS}}} = 0.6252\Lambda_V$ .
4. Insert the renormalized coupling  $g_{\overline{\text{MS}}}^2$  and the channel specific constants into Eq. 2.80 to compute the renormalization group constants.

### 2.4.2 Continuum Limit

Renormalization, i.e. relating  $\mathcal{O}_{\text{bare}} \rightarrow \mathcal{O}_{\text{physics}}$  is only part of the procedure needed to connect lattice theories to physics.

To arrive at the continuum theory the lattice must be lifted and smoothly connected to the continuous space-time of physics. To this end two extrapolations must be carried out:

- Thermodynamic limit  $V \rightarrow \infty$  .
- Continuum limit  $a \rightarrow 0$  .

Naturally both limits are connected as shrinking the lattice spacing to zero implies shrinking the space-time volume of the theory to zero. Ideally one would thus first take the thermodynamic limit to eliminate all finite volume effects and then eliminate the lattice by taking the continuum limit. In practice this is not possible and in general one simultaneously decreases the lattice spacing while keeping the physical volume fixed. Taking the thermodynamic and continuum limit then would imply  $N_\sigma \rightarrow \infty$  and  $a \rightarrow 0$ . As a practitioner one is faced with a three-fold group of problems:

- Scaling of the computation in the continuum limit.
- Finite volume effects due to the size of the physical volume.

- Resolution effects due to the limited number of points available in a space-time direction.

Of these the first is probably the most severe. Scaling of the computation in the continuum limit in principle describes that decreasing the lattice spacing implies a decreasing physical volume, as mentioned above. On the lattice this implies the number of lattice points  $N = N_\sigma^3 \times N_\tau$  must be for example doubled in every direction for every factor half in the lattice spacing.

The second and third are actually intertwined and are often referred to as the same problem. To understand recall that the fields in the lattice theory “feel” the boundary conditions of the lattice, thus the smaller the lattice the bigger the effect originating from the boundaries. In the spatial direction these effects around the spatial torus can be shown to lead to exponential corrections to the observable particle masses  $\mathcal{O}(\exp[-\alpha L])$ . For small volumes numerical studies indicate that the volume dependence of hadron masses actually is proportional to  $\sim 1/L^n$  where  $n \approx 2 - 3$ . As a rule of thumb one generally postulates the volume dependence in a high temperature system to be small in physical volumes  $V \geq 1.5\text{fm}$ .

However a similar effect may arise if the number of lattice points in a spatial direction is too small. If this is the case the low resolution of the lattice leads to a systematic over-estimation of the observed particle masses, as the employed analysis methods cannot clearly distinguish the ground- and excited states.

Taking the ideal thermodynamic and continuum limit naturally cancels these effects. However when doing the calculation in practice both effects enter.

Generally the continuum limit is taken via controlled extrapolation of lattice calculations at different lattice spacings. It is important to realize here, that all quantities in a lattice calculation are including discretization errors, e.g.  $\mathcal{O}(a^2)$ . Given the order of these corrections the continuum extrapolation may be achieved quadratically ( $\mathcal{O}(a^2)$ ) or linearly  $\mathcal{O}(a)$ .

In this work we focus on the vector current-current correlation function calculated using Wilson-Clover fermions, as these fermions are improved we thus expect the continuum to be approached quadratically in the lattice spacing.

Following the above statements realize the connection to physics can be achieved doing either:

- a calculation of the observable in a fixed physical volume, sequentially increasing the number of points and decreasing the lattice spacing. After analyzing for resolution effects, by checking the dependence of the observed particle masses on the number of points, a controlled extrapolation to the continuum can be made given the discretization errors of the lattice theory.
- a calculation of the observable with fixed (large) number of lattice points in the spatial direction, sequentially increasing the number of points in the temporal

direction and decreasing the lattice spacing. To analyze for finite volume effects the particle masses are checked at one fixed lattice spacing while volume is varied. Subsequently a controlled extrapolation is possible exactly as above.

Taking the thermodynamic limit then implies repeating the procedure with ever larger physical volumes or larger number of spatial lattice points.

Numerically speaking the second option is more attractive as the spatial volume  $\sim N_\sigma^3$  remains fixed and must be varied only at one lattice spacing. Also one is enabled to go to small lattice spacings while keeping the spatial extent manageable. This is complementary to our aim and we will follow this procedure in the following.

## 2.5 Parameters and Systematics

Concluding this chapter we describe the numerical setup and parameters of the calculation presented in this thesis. As such all important background information of the lattice calculation presented in the following may be found here.

All our numerical results are obtained from an analysis of quenched QCD gauge field configurations generated with the standard SU(3) single plaquette Wilson gauge action [40], defined in Eq. 2.21. On these gauge field configurations current-current correlation functions as defined in Eq. 4.2 are calculated using a Wilson-Clover fermion action [51](Eq. 2.54) with non-perturbatively determined clover coefficients  $c_{SW}$  [52] following Eq. 2.56. The hopping parameter  $\kappa$  is chosen in a way that the quark masses are approximately constant and light over all our calculations [52, 53]. These basic parameters are summarized in Tab. 2.2.

$\beta$	$N_\sigma$	$N_\tau$	$T/T_c$	$a[\text{fm}]$	$a^{-1}[\text{GeV}]$	$L_\sigma[\text{fm}]$	$\kappa_c$	$c_{SW}$
6.872	128	16	1.46	0.031	6.432	3.93	0.13497	1.412488
	64	16	1.46	0.031	6.432	1.96	0.13497	1.412488
	48	16	1.46	0.031	6.432	1.47	0.13497	1.412488
	32	16	1.46	0.031	6.432	0.98	0.13497	1.412488
7.192	128	24	1.42	0.021	9.435	2.69	0.13437	1.367261
7.457	128	40	1.16	0.015	12.864	1.96	0.13398	1.338927
	128	32	1.49	0.015	12.864	1.96	0.13398	1.338927
	128	16	2.98	0.015	12.864	1.96	0.13398	1.338927
7.793	128	48	1.43	0.010	18.974	1.33	0.13346	1.310381

Table 2.2: *Overview of basic calculation parameters. The calculation of the parameters has been outlined in the text. For reference we also give the spatial size of the lattice  $L_\sigma$  in [fm] and the cut-off scale in [GeV].*

$\beta$	$\kappa$	$m_{\text{AWI}}/T(\mu = 1/a)$	$m_{\text{RGI}}/T(\mu = 1/a)$	$m_{\overline{\text{MS}}}/T(\mu = 2\text{GeV})$
6.872	0.13495	0.0182(4)	0.0340(8)	0.02429(5)
7.192	0.13440	0.0182(4)	0.0331(7)	0.02367(5)
7.192	0.13431	0.0816(2)	0.1487(2)	0.1062(2)
7.457	0.13390	0.0790(3)	0.1384(5)	0.0989(4)
7.793	0.13340	0.0964(2)	0.1562(3)	0.1117(2)

Table 2.3: *The quark masses in  $\overline{\text{MS}}$  as obtained from the AWI via the RGI quark masses. All values are given in units of temperature  $T$ , as we are in quenched QCD note  $T_c = 270\text{MeV}$ .*

The gauge couplings used for calculations at four different values of the cutoff are selected such that the temperature stays approximately constant at  $T \simeq 1.45T_c$  as the cutoff is varied. Additionally the temperature is varied for one value of the coupling by changing the number of points in  $N_\tau$  direction. To tune the couplings we follow the procedure outlined in Chp. 2.4, i.e. we use the Ansatz defined in [55], which is known to give the variation of the lattice cutoff as a function of the gauge coupling to better than 1% in the interval [5.6, 6.5] [56]. We add to this analysis new results for the critical coupling  $\beta_c(N_\tau)$  and the square root of the string tension  $\sqrt{\sigma}$  [57], then we extrapolate the fit results to the regime of couplings relevant for our analysis  $\beta \in [6.8, 7.8]$ . The relevant couplings, lattice spacings and lattice cut-off parameters are summarized in Tab. 2.2.

By tuning the hopping parameter  $\kappa$  we choose quark masses that are approximately constant for our four values of the cutoff. We estimate the quark mass using the axial Ward identity and calculate the AWI current quark mass [61] (Eq. 2.70). This is done using the improved axial vector current Eq. 2.57 with the non-perturbatively determined improvement coefficient  $c_A$  [52, 69] of Eq. 2.58. To compare the quark masses at a common scale we first convert the AWI quark mass to the renormalization group invariant (RGI) quark mass [58] defined in Eq. 2.74 with the non-perturbative coefficients of Eq. 2.73 [59, 60]. Then the RGI mass is rescaled in the  $\overline{\text{MS}}$ -scheme to the common scale  $\mu = 2\text{GeV}$  using the four loop perturbative running coupling and the “RunDec.m” package [63].

In both cases we calculate errors from a jackknife analysis on  $m_{\text{AWI}}$  and do not include systematic errors for the conversion to the  $\overline{\text{MS}}$ -scheme. The mass parameters are listed in Tab. 2.5 and Tab. 2.5.

Our central results are based on calculations performed with renormalized quark masses  $m_{\overline{\text{MS}}}/T \simeq 0.1$ . Through calculations performed with a factor four smaller quark mass, we check on lattices with temporal extent  $N_\tau = 24$  that results on the large distance behavior of the correlation functions agree within errors (see Fig. 5.3), these

$\beta$	$\kappa$	$m_{\overline{\text{MS}}}/T(\mu = 2\text{GeV})$	$m_{\overline{\text{MS}}}(\mu = 2\text{GeV})[\text{MeV}]$
6.872	0.13495	0.02429(5)	9.5
7.192	0.13440	0.02367(5)	9.3
7.192	0.13431	0.1062(2)	41.6
7.457	0.13390	0.0989(4)	38.7
7.793	0.13340	0.1117(2)	43.7

Table 2.4: Table of quark masses in the  $\overline{\text{MS}}$ -scheme in units of temperature at  $T \simeq 1.45T_c$  and in  $[\text{MeV}]$ .

$N_\tau$	$N_\sigma$	$\beta$	#conf
16	32	6.872	251
	48	6.872	229
	64	6.872	191
	128	6.872	191
24(I)	128	7.192	340
24(II)	128	7.192	156
16	128	7.457	208
	32	128	255
	40	128	189
	48	128	451

Table 2.5: Number of configurations analyzed on lattices sized  $N_\sigma^3 \times N_\tau$ . All configurations are separated by 500 iterations of a combined Heatbath-Overrelaxation Monte Carlo algorithm. Note at  $\beta = 7.192$  two quark masses are available, where the index (II) denotes the lighter case.

calculations are noted with the index (II) in the following. The smaller quark mass is also used for calculations on our coarsest lattice with temporal lattice size  $N_\tau = 16$ , where we analyze the sensitivity of our results to finite volume effects. We expect from the evaluation of Chp. 5 that quark mass effects play no role in all results presented here.

The gauge field configurations are generated using a standard over-relaxed heat bath algorithm [70]. Configurations are stored every 500 trajectories, whereby we list these numbers and the total statistics once more in Tab. 2.5. At several large temporal separations the correlation functions are checked to be statistically independent. Furthermore we measure the plaquette for every trajectory and obtain an estimate for the integrated autocorrelation time of order one.

For illustration the autocorrelation is shown in Fig. 2.9 both for the plaquette (left) and the full vector channel (right) at different temporal separations. Clearly the autocorre-

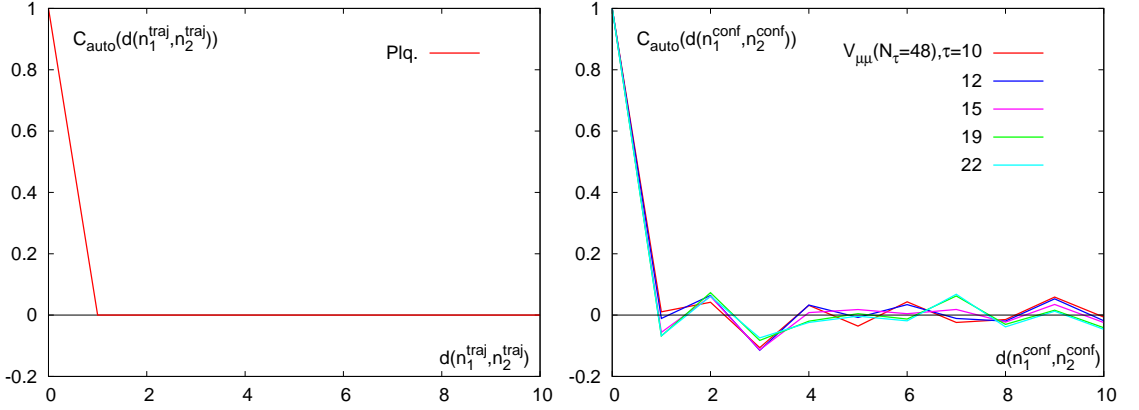


Figure 2.9: The autocorrelation of the plaquette (left) and the vector channel (right) for several temporal separations, shown are the results for the lattice sized  $128^3 \times 48$ .

lation drops immediately and the data is subsequently uncorrelated.

Note also that topologically non-trivial configurations die out quickly in calculations above the deconfinement temperature. This is mirrored by the observation that the scalar and pseudoscalar correlation functions reveal less than 3% exceptional configurations. The autocorrelation time of these configurations is seen to be of the order of  $\sim 3000$  trajectories.

For the computation of the quark propagators we use a plain conjugate gradient inverter [71]. The algorithm has a stable convergence behavior and we set the convergence criterion for the squared norm of the residue to  $10^{-23}$ . This value was selected by monitoring the nearly exponential decay of spatial correlation functions over many orders of magnitude due to the large spatial extent of the lattices and screening masses of the order of  $2\pi T$ .

As noted in Chp. 2.4.1 the observable current operators have to be renormalized multiplicatively. Wherever required we thus employ the renormalized current as defined in Eq. 2.79 with the non-perturbative renormalization group constants of Eq. 2.81 when possible [53], if not we use the two-loop tadpole improved perturbative results of Eq. 2.80. The corresponding constants are given in Tab. 2.4.1.

However note that many results presented in the following are given in terms of ratios of correlation functions where the renormalization constants drop out.

Before concluding this section on the parameters and systematics, note that, if not explicitly stated otherwise, all errors given in this thesis are obtained using suitable jackknife methods [72].

## The Phenomenology of Spectral Functions

Practically all observables of interest in the following can be rewritten in terms of two-point correlation functions of elementary or composite operators. The correlation functions on the other hand appear in different versions be it in imaginary time, real time, advanced or retarded. We will show in the following that all these versions depend on a single spectral function  $\rho(\omega)$ , which in turn naturally becomes the key quantity to compute. Note here we follow the derivations of [29–31].

The thermal ensemble is defined by the density matrix  $\hat{\rho} = \frac{1}{Z}e^{-\beta H}$ , where  $Z$  is the partition function and  $\text{Tr}[\hat{\rho}] = 1$ . Then the two-point correlation functions in real time may be defined as:

$$G^>(t) = \text{Tr}[\hat{\rho}\phi(t)\phi(0)] = \langle\phi(t)\phi(0)\rangle \quad (3.1)$$

$$G^<(t) = \text{Tr}[\hat{\rho}\phi(0)\phi(t)] = \langle\phi(0)\phi(t)\rangle = G^>(-t) \quad , \quad (3.2)$$

where  $\phi(t)$  is an operator in the Heisenberg picture. Inserting a complete set of eigenvectors  $G^>(t)$  may be re-expressed to read

$$G^>(t) = \frac{1}{Z} \sum_{n,m} e^{-\beta E_n} e^{i(E_n - E_m)t} |\langle n|\phi(0)|m\rangle|^2 \quad , \quad (3.3)$$

if the convergence of this expression is controlled by the exponentials on sees

$$G^>(t) \text{ is defined for } -\beta \leq \text{Im}(t) \leq 0 \quad (3.4)$$

$$G^<(t) \text{ is defined for } \beta \geq \text{Im}(t) \geq 0 \quad (3.5)$$

As  $\phi(t)$  is an operator in the Heisenberg picture one may write:

$$e^{-\beta H}\phi(t)e^{\beta H} = \phi(t + i\beta) \quad , \quad (3.6)$$

which in turn leads to the Kubo-Martin-Schwinger (KMS) relation [29–31]:

$$G^>(t) = G^<(t + i\beta) = G^>(-t - i\beta) \quad . \quad (3.7)$$

It can be shown that the KMS relation uniquely characterizes the density matrix and thus the thermal system. Defining the Euclidean correlator for  $\tau = it \in [0, \beta]$  as

$$G^E(\tau) = G^>(-i\tau) \quad (3.8)$$

one sees that the periodicity condition for the thermal system follows from the KMS relation.

At this point look also at the expectation value of a commutator:

$$G(t) = i\text{Tr}[\hat{\rho}[\phi(t), \phi(0)]] = i\langle[\phi(t), \phi(0)]\rangle = i(G^>(t) - G^<(t)) \quad , \quad (3.9)$$

which satisfies the relations

$$G(-t) = -G(t) \quad \text{and} \quad G^\dagger(t) = G(t^*)^* \quad . \quad (3.10)$$

Outside the light-cone this quantity vanishes and thus encodes the causality of the theory.

### Relating Correlators and the Spectral Function

To find the connection with the spectral function  $\rho(\omega)$  change into frequency space via Fourier transform:

$$G^>(\omega) = \int_{-\infty}^{\infty} dt e^{i\omega t} G^>(t) \quad (3.11)$$

$$G^<(\omega) = \int_{-\infty}^{\infty} dt e^{i\omega t} G^<(t) = \int_{-\infty}^{\infty} dt e^{i\omega t} G^>(t - i\beta) \quad (3.12)$$

$$\Rightarrow G^<(\omega) = G^>(-\omega) = e^{-\beta\omega} G^>(\omega) \quad (3.13)$$

In the following we will be especially interested in the retarded correlation function, which may now be defined as the integral transform over the positive half axis of the commutator  $G(t)$ :

$$G^R(\omega) = \int_0^{\infty} dt e^{i\omega t} G(t) \quad . \quad (3.14)$$

The spectral function  $\rho(\omega)$  is given by the full Fourier transform of the expectation value of the commutator:

$$\rho(\omega) := G^>(\omega) - G^<(\omega) \quad . \quad (3.15)$$

An explicit expression for  $\rho(\omega)$  may be found by using Eq. 3.3 and Eq. 3.13:

$$\rho(\omega) = \frac{1}{Z} \sum_{n,m} e^{-\beta E_n} \left[ \delta(\omega + E_n - E_m) - \delta(\omega + E_m - E_n) \right] |\langle n|\phi(0)|m\rangle|^2 \quad , \quad (3.16)$$

this form of the spectral function explicitly shows that it is an odd, real function of frequency  $\rho(\omega) = -\rho(-\omega)$  and that it obeys the positivity condition  $\text{sgn}(\omega)\rho(\omega) > 0$ .

Using Eqs.3.10-3.14 immediately find the connection between the retarded correlator and the spectral function:

$$\rho(\omega) = \frac{1}{2\pi i}(G^R(\omega) - G^{R\dagger}(\omega)) = \frac{1}{\pi}\text{Im}G^R(\omega) \quad , \quad (3.17)$$

while Eq. 3.13 gives the connection to the forward and backward correlation functions:

$$G^>(\omega) = \frac{e^{\beta\omega}}{e^{\beta\omega} - 1}\rho(\omega) \quad \text{and} \quad G^<(\omega) = \frac{1}{e^{\beta\omega} - 1}\rho(\omega) \quad . \quad (3.18)$$

With Eq. 3.8 the connection of all four desired correlators with the spectral function is obtained.

### Connecting Euclidean and Retarded Correlation Functions

Next we are interested in the relation between the retarded and the Euclidean correlation function. Ultimately the Euclidean correlator is the observable computed on the lattice while the retarded correlator is accessible to perturbative techniques and especially plays an important role in linear response theory.

To find the desired connection first write the retarded correlator of Eq. 3.14 in time:

$$G^R(t) = i\langle\theta(t)[\phi(t), \phi(0)]\rangle \quad , \quad (3.19)$$

then using the following representation of the  $\theta$ -function

$$\theta(t) = i \int_{-\infty}^{\infty} \frac{d\omega'}{2\pi} \frac{e^{-i\omega't}}{\omega' + i\delta} \quad (3.20)$$

one finds the Fourier transform of  $G^R(\omega)$  in terms of the spectral function:

$$G^R(\omega) = \int_{-\infty}^{\infty} \frac{d\omega'}{2\pi} \frac{\rho(\omega')}{\omega - \omega' + i\delta} \quad . \quad (3.21)$$

Now turn to the imaginary time correlator and using Eq. 3.8 with Eq. 3.11 write

$$G^E(i\omega_n) = \int_0^\beta d\tau e^{i\omega_n\tau} \int \frac{d\omega}{2\pi} e^{-\omega\tau} G^>(\omega) \quad , \quad (3.22)$$

introducing the spectral function via Eq. 3.18 one then obtains

$$G^E(i\omega_n) = \int_{-\infty}^{\infty} \frac{d\omega'}{2\pi} \frac{\rho(\omega')}{i\omega_n - \omega'} \quad . \quad (3.23)$$

Comparing the two expressions for the retarded and imaginary time correlator one finds they are indeed directly related via:

$$G^R(\omega) = G^E(i\omega_n \rightarrow \omega + i\delta) \quad . \quad (3.24)$$

Thus the retarded and Euclidean correlation functions are directly connected via analytic continuation, while they are both related to the spectral function as derived above.

### Mixed Representation of the Euclidean Correlator

The main objective of this thesis is to compute the spectral function of hadronic states. Correspondingly the interesting operators are the currents already defined in Eq. 1.8:

$$J_H \equiv \bar{q}(\tau, \vec{x}) \Gamma_H q(\tau, \vec{x}) , \quad (3.25)$$

note for clarity in the following we changed the notation slightly compared to Eq. 1.8 as  $\gamma_\nu \rightarrow \Gamma_H$  where  $\Gamma_H = \{\mathbf{1}, \gamma_5, \gamma_\mu, \gamma_\mu \gamma_5\}$ , the index  $H$  then corresponds to the particle channels  $H = \{S, PS, V, A\}$  respectively.

The Euclidean temporal current-current correlation functions we are interested in read:

$$G_H(\tau, \vec{p}) = \sum_{\vec{x}} G_H(\tau, \vec{x}) e^{i\vec{p} \cdot \vec{x}} , \quad (3.26)$$

where

$$G_H(\tau, \vec{x}) = \langle J_H(\tau, \vec{x}) J_H^\dagger(0, \vec{0}) \rangle . \quad (3.27)$$

This mixed representation correlation function ( $G_{\mu\nu}(\tau, \vec{p}) = G(\tau, \vec{p})$ ) can also be related to the spectral function via

$$\begin{aligned} G(\tau, \vec{p}) &= \int d^3 \vec{x} e^{i\vec{p} \cdot \vec{x}} G^>(-i\tau, \vec{x}) \\ &= \int d^3 \vec{x} \int \frac{d\omega}{2\pi} \int d^3 \vec{p}' e^{i(\vec{p}' - \vec{p}) \cdot \vec{x} - \omega\tau} G^>(\omega, \vec{p}') \\ &= \int \frac{d\omega}{2\pi} e^{-\omega\tau} G^>(\omega, \vec{p}) \\ &= \int_0^\infty \frac{d\omega}{2\pi} e^{-\omega\tau} G^>(\omega, \vec{p}) + \int_\infty^0 \frac{d\omega}{2\pi} e^{-\omega\tau} G^>(\omega, \vec{p}) \\ &= \int_0^\infty \frac{d\omega}{2\pi} e^{-\omega\tau} G^>(\omega, \vec{p}) + e^{\omega\tau} G^<(\omega, \vec{p}) , \end{aligned} \quad (3.28)$$

once more introducing the spectral function via Eq. 3.18 the above expression may be rewritten to read

$$\begin{aligned} G(\tau, \vec{p}) &= \int_0^\infty \frac{d\omega}{2\pi} \left( \frac{e^{\beta\omega - \omega\tau}}{e^{\beta\omega} - 1} + \frac{e^{\omega\tau}}{e^{\beta\omega} - 1} \right) \rho(\omega, \vec{p}) \\ &= \int_0^\infty \frac{d\omega}{2\pi} \frac{\cosh(\omega(\tau - \beta/2))}{\sinh(\omega \cdot \beta/2)} \rho(\omega, \vec{p}) \end{aligned} \quad (3.29)$$

$$= \int_0^\infty \frac{d\omega}{2\pi} K(\omega, \tau) \rho(\omega, \vec{p}) . \quad (3.30)$$

Mathematically speaking the quantity  $K(\omega, \tau)$  is an integration kernel, physically speaking however it is the free boson propagator in Euclidean time  $\tau$  with energy  $\omega$ . The spectral function  $\rho(\omega)$  subsequently is a factor that denotes the spectral distribution as a function of energy.

### 3.1 Spectral Functions in Non-Interacting Theory

After having introduced the spectral function  $\rho(\omega, \vec{p})$  and its basic relations to correlation functions, a good starting point for reaching at least a qualitative understanding of its properties can be gained by evaluating it in non-interacting theory. Due to asymptotic freedom this situation is equivalent to a system at infinitely high temperature  $T \rightarrow \infty$ . To this extent the free spectral functions will be explored in the continuum and lattice environments [74].

#### 3.1.1 Free Continuum Spectral Functions

The starting point of our calculation is the lowest order loop expansion Euclidean correlation function in momentum space:

$$G_H(i\omega_n, \vec{p}) = -T \sum_n \int_{\vec{k}} \text{Tr} \left[ S(K) \Gamma_H S(P + K) \gamma_0 \Gamma_H^\dagger \gamma_0 \right] , \quad (3.31)$$

as before  $i\omega_n$  with  $\omega_n = 2\pi nT$  are the Matsubara frequencies and we introduce the shorthand  $\int_{\vec{k}} = \int d^3k / (2\pi)^3$ . Similarly to Eq. 3.23 the fermion propagators are given by:

$$S(K) = - \int_{-\infty}^{\infty} \frac{d\omega}{2\pi} \frac{\rho_F(\omega, \vec{k})}{i\tilde{\omega}_n - \omega} , \quad (3.32)$$

with the fermionic Matsubara frequency  $\tilde{\omega}_n = (2n + 1)\pi T$  and the spectral function:

$$\rho_F(K) = (\not{K} + m)\rho(K) = (\not{K} + m)2\pi \text{sgn}(k_0)\delta(k_0^2 - \omega_k^2) , \quad (3.33)$$

where  $K = (k_0, \vec{k})$  and  $\omega_k = \sqrt{k^2 + m^2}$ .

Plugging the propagators into Eq. 3.31 one soon arrives at the spectral function:

$$\begin{aligned} \rho_H(\omega, \vec{p}) &= 2\text{Im}G_H(i\omega_n \rightarrow \omega + i\delta, \vec{p}) \\ &= N_c \int_{\vec{k}, k_0} \text{Tr} \left[ (\not{K} + m)\Gamma_H(\not{R} + m)\gamma_0\Gamma_H^\dagger\gamma_0\rho(K)\rho(R) \cdot [n_F(k_0) - n_F(r_0)] \right] , \end{aligned} \quad (3.34)$$

whereby we introduce the shorthand  $n_F(\omega) = (e^{\omega/T} + 1)^{-1}$  for the Fermi distribution along with  $R = P + K = (\omega + k_0, \vec{p} + \vec{k})$ .

The particle channel specific modifications of the spectral function are encoded in the traces of  $\text{Tr}[(\not{K} + m)\Gamma_H(\not{R} + m)\gamma_0\Gamma_H^\dagger\gamma_0]$ , so as to keep the computation as general as

possible first compare the possible different cases, e.g. in the vector channel:

$$\begin{aligned}
 (V) \quad \Gamma_H = \gamma_\mu : \quad & \text{Tr} \left[ (K + m) \Gamma_H (\mathcal{R} + m) \gamma_0 \Gamma_H^\dagger \gamma_0 \right] \\
 & \rightarrow \text{Tr} \left[ (K + m) \gamma_\mu (\mathcal{R} + m) \gamma_0 \gamma_\mu^\dagger \gamma_0 \right] \\
 & = \text{Tr} \left[ (K + m) \gamma_\mu (\mathcal{R} + m) \gamma_\mu \right] \\
 & = \text{Tr} \left[ \cancel{K} \gamma_\mu \cancel{\mathcal{R}} \gamma_\mu + m^2 \gamma_\mu \gamma_\mu \right] \\
 & = 4 (g_{\nu\mu} g_{\eta\mu} - g_{\nu\eta} g_{\mu\mu} + g_{\nu\mu} g_{\mu\eta}) K_\nu R_\eta + 4 g_{\mu\mu} m^2 \\
 & = 4 (K_\mu R_\mu - K \cdot R g_{\mu\mu} + K_\mu R_\mu) + 4 g_{\mu\mu} m^2 \\
 & = 4 (2 \cdot K_\mu R_\mu - g_{\mu\mu} K \cdot R) + 4 g_{\mu\mu} m^2 \tag{3.35}
 \end{aligned}$$

$$\begin{aligned}
 (V_{00}) \quad \Gamma_H = \gamma_0 : \quad & 4 (2 \cdot K_0 R_0 - K_0 R_0 + \vec{K} \cdot \vec{R}) + 4 m^2 \\
 & = 4 (K_0 R_0 + \vec{K} \cdot \vec{R} + m^2) \tag{3.36}
 \end{aligned}$$

$$\begin{aligned}
 (V_{ii}) \quad \Gamma_H = \gamma_i : \quad & 4 (2 \cdot K_0 R_0 + 3(K_0 R_0 - \vec{K} \cdot \vec{R})) + 4 \cdot 3 m^2 \\
 & = 4 (3 \cdot K_0 R_0 - \vec{K} \cdot \vec{R} - 3 m^2) \tag{3.37}
 \end{aligned}$$

$$\begin{aligned}
 (V_{\mu\mu}) \quad \Gamma_H = \gamma_\mu : \quad & V = -V_{00} + V_{ii} \\
 & = 4 (2 \cdot K_0 R_0 - 2 \vec{K} \cdot \vec{R} - 4 m^2) \quad . \tag{3.38}
 \end{aligned}$$

The coefficients of  $V_{00}$ ,  $V_{ii}$  and  $V_{\mu\mu}$  then give the channel specific constants  $a_H^{(1)}$ ,  $a_H^{(2)}$  and  $a_H^{(3)}$ . Repeating this computation for the other channels one can derive these constants for all particle channels, a summary of them is listed in Tab. 3.1.1.

Next the integration of  $k_0$  may be performed and the resulting expression can be shown to read [74]:

$$\begin{aligned}
 \rho_H(\omega, \vec{p}) = 2\pi N_c \int_{\vec{k}} & \left( a_H^{(1)} + a_H^{(2)} \frac{\vec{k} \cdot \vec{r}}{\omega_k \omega_r} + a_H^{(3)} \frac{m^2}{\omega_k \omega_r} \right) [n_F(\omega_k) - n_F(\omega_r)] \delta(\omega + \omega_k - \omega_r) \\
 & + \left( a_H^{(1)} - a_H^{(2)} \frac{\vec{k} \cdot \vec{r}}{\omega_k \omega_r} - a_H^{(3)} \frac{m^2}{\omega_k \omega_r} \right) [1 - n_F(\omega_k) - n_F(\omega_r)] \delta(\omega - \omega_k - \omega_r) \\
 & - (\omega \rightarrow -\omega) \quad . \tag{3.39}
 \end{aligned}$$

This equation may then be evaluated numerically or analytically to obtain the spectral function. As the key observables in this thesis are massless current-current correlators at finite and vanishing momentum the computation is shown in the massless limit in the following. Immediately note that in this case all contributions from terms proportional to  $a_H^{(3)}$  drop out.

Assuming the frequency to be positive  $\omega > 0$  three terms contribute to the spectral

### 3.1 Spectral Functions in Non-Interacting Theory

	$\Gamma_H$	$a_H^{(1)}$	$a_H^{(2)}$	$a_H^{(3)}$
$\rho_S$	$\mathbf{1}$	1	-1	1
$\rho_{PS}$	$\gamma_5$	1	-1	-1
$\rho_{00}$	$\gamma_0$	1	1	1
$\rho_{ii}$	$\gamma_i$	3	-1	-3
$\rho_V$	$\gamma_\mu$	2	-2	-4
$\rho_{A,00}$	$\gamma_0\gamma_5$	1	1	-1
$\rho_{A,ii}$	$\gamma_i\gamma_5$	3	-1	3
$\rho_A$	$\gamma_\mu\gamma_5$	2	-2	4

Table 3.1: The trace operation yields the channel specific constants  $a_H^{(1)}$ ,  $a_H^{(2)}$  and in case of non-vanishing mass  $a_H^{(3)}$ .

function:

$$\begin{aligned}
\rho_H(\omega, \vec{p}) &= \rho_H^{(1)}(\omega, \vec{p}) + \rho_H^{(2)}(\omega, \vec{p}) + \rho_H^{(3)}(\omega, \vec{p}) \\
\rho_H^{(1)}(\omega, \vec{p}) &= 2\pi N_c \int_{\vec{k}} \left( a_H^{(1)} - a_H^{(2)} \frac{\vec{k} \cdot \vec{r}}{\omega_k \omega_r} \right) [2n_F(\omega_k) - 1] \delta(\omega - \omega_k - \omega_r) \\
\rho_H^{(2)}(\omega, \vec{p}) &= 2\pi N_c \int_{\vec{k}} \left( a_H^{(1)} + a_H^{(2)} \frac{\vec{k} \cdot \vec{r}}{\omega_k \omega_r} \right) [n_F(\omega_k) - n_F(\omega_r)] \delta(\omega + \omega_k - \omega_r) \\
\rho_H^{(3)}(\omega, \vec{p}) &= -2\pi N_c \int_{\vec{k}} \left( a_H^{(1)} + a_H^{(2)} \frac{\vec{k} \cdot \vec{r}}{\omega_k \omega_r} \right) [-n_F(\omega_k) + n_F(\omega_r)] \delta(\omega - \omega_k + \omega_r) \quad . \quad (3.40)
\end{aligned}$$

The radial integration over the momentum can then be taken care of by using the  $\delta$ -functions. To this extent introduce the shorthand  $k = |\vec{k}|$  and  $p = |\vec{p}|$  to write:

$$\begin{aligned}
\delta(\omega - k - \sqrt{k^2 + p^2 - 2pkx}) &= \frac{1}{1 + \frac{px - k_0}{k_1}} \cdot \delta(k - k_0) \\
\delta(\omega - k + \sqrt{k^2 + p^2 - 2pkx}) &= \frac{1}{1 - \frac{px - k_0}{k_1}} \cdot \delta(k - k_0) \\
\delta(\omega + k - \sqrt{k^2 + p^2 - 2pkx}) &= \frac{1}{1 - \frac{px - k_0}{k_1}} \cdot \delta(k - k_0) \quad , \quad (3.41)
\end{aligned}$$

here  $k_0 = (\omega^2 - p^2)/(2(\omega - px))$  and  $k_1 = \sqrt{k^2 + p^2 - 2pkx}$ .

At this point also re-express

$$a_H^{(1)} \pm a_H^{(2)} \frac{\vec{k} \cdot \vec{r}}{\omega_k \omega_r} = a_H^{(1)} \pm a_H^{(2)} \frac{\vec{p} \cdot \vec{k} - k^2}{\omega_k \omega_r} = a_H^{(1)} \pm a_H^{(2)} \frac{px - k}{k_1} \quad (3.42)$$

Inserting Eq. 3.42 and Eqs.3.41 into Eqs.3.40 one can integrate numerically or analyti-

cally. As an example for the full vector channel, defined by  $\rho_V(\omega)$ , Eqs.3.40 become:

$$\begin{aligned}
 \rho_V^{(1)}(\omega, \vec{p}) &= 2\pi N_c \int_{\vec{k}} \left( 2 + 2 \frac{px - k}{k_1} \right) [2n_F(k) - 1] \left( 1 + \frac{px - k_0}{k_1} \right)^{-1} \cdot \delta(k - k_0) \\
 &= 4\pi N_c \int_{-1}^1 dx \int \frac{dk k^2}{(2\pi^2)} \frac{\tilde{f}(k)}{\tilde{f}(k_0)} \delta(k - k_0) [2n_F(k) - 1] \Theta(\omega - |p|) \\
 &= \frac{N_c}{\pi} \int_{-1}^1 dx k_0^2 [2n_F(k_0) - 1] \Theta(\omega - |p|)
 \end{aligned} \tag{3.43}$$

$$\begin{aligned}
 \rho_V^{(2)}(\omega, \vec{p}) &= 4\pi N_c \int_{\vec{k}} \left( 2 - 2 \frac{px - k}{k_1} \right) n_F(k) \left( 1 - \frac{px - k_0}{k_1} \right)^{-1} \cdot \delta(k - k_0) \\
 &= 8\pi N_c \int_{\omega/|p|}^1 dx \int \frac{dk k^2}{(2\pi^2)} \frac{\tilde{f}(k)}{\tilde{f}(k_0)} \delta(k - k_0) n_F(k) \Theta(|p| - \omega) \\
 &= \frac{2N_c}{\pi} \int_{\omega/|p|}^1 dx k_0^2 n_F(k_0) \Theta(|p| - \omega)
 \end{aligned} \tag{3.44}$$

$$\begin{aligned}
 \rho_V^{(3)}(\omega, \vec{p}) &= \rho_V^{(2)}(\omega, \vec{p}, x \rightarrow -x, k_0 \rightarrow -k_0) \\
 &= -\frac{2N_c}{\pi} \int_{-1}^{\omega/|p|} dx k_0^2 n_F(-k_0) \Theta(|p| - \omega) \quad .
 \end{aligned} \tag{3.45}$$

The final expression in this case then may be found to read [74, 75]:

$$\begin{aligned}
 \rho_V(\omega, \vec{p}) &= \Theta(\omega^2 - p^2) \frac{N_c T}{2\pi^2 |\vec{p}|} \left( (\omega^2 - p^2) \ln \left[ \frac{\cosh((\omega + \vec{p})/4T)}{\cosh((\omega - \vec{p})/4T)} \right] \right) \\
 &\quad + \Theta(p^2 - \omega^2) \frac{N_c T}{2\pi^2 |\vec{p}|} \left( (\omega^2 - p^2) \ln \left[ \frac{\cosh((\omega + \vec{p})/4T)}{\cosh((\omega - \vec{p})/4T)} - \frac{\omega}{2T} \right] \right) \quad , \tag{3.46}
 \end{aligned}$$

note in this last expression we included also factors of temperature  $T$  that have been omitted in the above derivation.

To obtain the spectral function at vanishing momentum  $\vec{p} = 0$  the calculation must be redone from Eq. 3.39, in case of the full vector spectral function one arrives at:

$$\rho_V(\omega, \vec{p} = 0) = \frac{2}{3\pi^2} \omega^2 \tanh \left( \frac{\omega}{4T} \right) \tag{3.47}$$

Even though we switched to computing the full vector spectral function as an example in the end, it is clear that the procedure may be generalized. In the following these more general results will be shown for the massive and massless cases both at finite and vanishing momentum. Whereby all calculations may be done following the scheme outlined above.

The procedure includes all necessary steps to compute the free spectral function in general. As such very similar schemes may be used when working out the free lattice spectral function and also the hard thermal loop result.

Consequently a general computation strategy may be outlined as:

### 3.1 Spectral Functions in Non-Interacting Theory

1. Write down the desired correlation function, e.g. in frequency space  $G(\tilde{\omega})$ , where  $\tilde{\omega}$  might be given in the imaginary time formalism or real time.
2. Insert the corresponding spectral representations of the propagators  $S(K)$ .
3. Identify the appropriate connection to the spectral function, e.g.  $\rho(\omega) = 2\text{Im}G_H(i\omega_n \rightarrow \omega + i\delta, \vec{p})$ .
4. Calculate the required traces of  $\gamma$ -functions and do the integral over  $k_0$ .
5. Use the appearing  $\delta$ -functions and kinematics to solve the remaining momentum integrals, either analytically or numerically.
6. Look at interesting limits, e.g.  $m \rightarrow 0$  or  $\vec{p} \rightarrow 0$ .

After these side remarks now turn once more to the free continuum spectral function computed in the fully general case at finite mass and finite momentum.

#### Massive Free Spectral Functions

In the general case at  $|\vec{p}| = p$  with admitting also a finite mass one needs to define:

$$p_{\pm} = \frac{1}{2} \left[ \omega \pm p\beta(\omega, \vec{p}) \right] \quad , \quad \beta(\omega, \vec{p}) = \sqrt{1 - \frac{4m^2}{s}} \quad \text{and} \quad s = \omega^2 - p^2 \quad . \quad (3.48)$$

Following the above outlined procedure with  $P = (\omega, \vec{p})$  the final analytic expression can be shown to read [74]

$$\begin{aligned} \rho_H(P) = & \Theta(s - 4m^2) \frac{N_c T^2}{2\pi^2} \left( \right. \\ & \frac{\beta(P)}{24T^2} \left[ (3\omega^2 - p^2 \beta^2(P)) a_H^{(1)} + (3p^2 - (3\omega^2 - 2p^2) \beta^2(P)) a_H^{(2)} - 12m^2 a_H^{(3)} \right] \\ & + \frac{1}{4pT} \left[ (\omega^2 - p^2 \beta^2(P)) a_H^{(1)} + (p^2 - \omega^2 \beta^2(P)) a_H^{(2)} - 4m^2 a_H^{(3)} \right] \ln \frac{1 + e^{-p_+/T}}{1 + e^{-p_-/T}} \\ & + (a_H^{(1)} + a_H^{(2)}) \left( \beta(P) \left[ \text{Li}_2(-e^{-p_+/T}) + \text{Li}_2(-e^{-p_-/T}) \right] \right. \\ & \quad \left. + \frac{2T}{p} \left[ \text{Li}_3(-e^{-p_+/T}) - \text{Li}_3(-e^{-p_-/T}) \right] \right) \left. \right) \\ & + \Theta(-s) \frac{N_c T^2}{2\pi^2} \left( \right. \\ & \frac{1}{4pT} \left[ (\omega^2 - p^2 \beta^2(P)) a_H^{(1)} + (p^2 - \omega^2 \beta^2(P)) a_H^{(2)} - 4m^2 a_H^{(3)} \right] \ln \frac{1 + e^{-p_+/T}}{1 + e^{p_-/T}} \\ & + (a_H^{(1)} + a_H^{(2)}) \left( \beta(P) \left[ \text{Li}_2(-e^{-p_+/T}) - \text{Li}_2(-e^{p_-/T}) \right] \right. \\ & \quad \left. + \frac{2T}{p} \left[ \text{Li}_3(-e^{-p_+/T}) - \text{Li}_3(-e^{p_-/T}) \right] \right) \left. \right) \quad , \quad (3.49) \end{aligned}$$

where  $\text{Li}_s(z) = \sum_{k=1}^{\infty} z^k/k^s$  is the polylogarithm function.

Taking the limit of vanishing momentum and recalculating from Eq. 3.39 the above expression simplifies significantly and reduces to:

$$\begin{aligned} \rho_H(\omega, 0) &= \frac{N_c}{16\pi^2} \Theta(\omega^2 - 4m^2) \omega^2 \tanh\left(\frac{\omega}{4T}\right) \sqrt{1 - \left(\frac{2m^2}{\omega}\right)} \\ &\quad \times \left[ (a_H^{(1)} - a_H^{(2)}) + \left(\frac{2m}{\omega}\right)^2 (a_H^{(1)} - a_H^{(3)}) \right] \\ &\quad + N_c \left[ (a_H^{(1)} + a_H^{(3)}) I_1 + (a_H^{(2)} - a_H^{(3)}) I_2 \right] \omega \delta(\omega) \quad , \end{aligned} \quad (3.50)$$

with

$$I_1 = -2 \int_k \frac{\partial n_F(\omega_k)}{\partial \omega_k} \quad \text{and} \quad I_2 = -2 \int_k \frac{k^2}{\omega_k} \frac{\partial n_F(\omega_k)}{\partial \omega_k} \quad (3.51)$$

### Massless Free Spectral Functions

Taking the analytic expression for the massive spectral function as starting point and using the relation:

$$1 + \exp[2x] = 2 \cosh[x] \exp[x] \quad (3.52)$$

one fairly quickly arrives at the massless counterpart of Eq. 3.49\*:

$$\begin{aligned} \rho_H(\omega, p) &= \Theta(\omega^2 - p^2) \frac{N_c T^2}{2\pi^2} \left( \right. \\ &\quad \frac{1}{4|\vec{p}|T} (\omega^2 - p^2) (a_H^{(1)} - a_H^{(2)}) \ln \left[ \frac{\cosh((\omega + p)/4T)}{\cosh((\omega - p)/4T)} \right] + \frac{1}{12T^2} (a_H^{(1)} + a_H^{(2)}) p^2 \\ &\quad + (a_H^{(1)} + a_H^{(2)}) \left( \text{Li}_2(-e^{-(\omega+p)/2T}) + \text{Li}_2(-e^{-(\omega-p)/2T}) \right) \\ &\quad \left. + \frac{2T}{p} \left[ \text{Li}_3(-e^{-(\omega+p)/2T}) - \text{Li}_3(-e^{-(\omega-p)/2T}) \right] \right) \\ &+ \Theta(p^2 - \omega^2) \frac{N_c T^2}{2\pi^2} \left( \right. \\ &\quad \frac{1}{4|\vec{p}|T} (\omega^2 - p^2) (a_H^{(1)} - a_H^{(2)}) \left( \ln \left[ \frac{\cosh((\omega + p)/4T)}{\cosh((\omega - p)/4T)} \right] - \frac{\omega}{2T} \right) \\ &\quad + (a_H^{(1)} + a_H^{(2)}) \left( \text{Li}_2(-e^{-(\omega+p)/2T}) - \text{Li}_2(-e^{(\omega-p)/2T}) \right) \\ &\quad \left. + \frac{2T}{p} \left[ \text{Li}_3(-e^{-(\omega+p)/2T}) - \text{Li}_3(-e^{(\omega-p)/2T}) \right] \right) \quad . \end{aligned} \quad (3.53)$$

---

\*Note: The expressions of Eqs.3.49-3.53 have been checked numerically starting from Eq. 3.39, the analytic expression of Eq. 3.49 was not explicitly computed.

### 3.1 Spectral Functions in Non-Interacting Theory

When going to vanishing momentum in the massless case  $I_1$  and  $I_2$  degenerate and become

$$I_1 = I_2 = \frac{T^2}{6} \quad , \quad (3.54)$$

while at the same time all dependence on  $a_H^{(3)}$  drops out in Eq. 3.39, as mentioned before. Consequently the vanishing momentum, massless spectral functions reduce to:

$$\rho_H(\omega, 0) = \frac{N_c}{16\pi^2} (a_H^{(1)} - a_H^{(2)}) \omega^2 \tanh\left(\frac{\omega}{4T}\right) + \frac{N_c T^2}{6} (a_H^{(1)} + a_H^{(2)}) \omega \delta(\omega) \quad . \quad (3.55)$$

Compared with the full expression in the massive case with non-vanishing momentum the above expression is a sizable simplification. As a consequence most of the work in this thesis focuses on computing the spectral function in exactly this limit. Nevertheless it is instructive to examine how this limit is achieved and what general properties the free spectral function possesses.

#### 3.1.2 Properties of the Free Continuum Spectral Function

From the above expressions the general limiting behavior of the free spectral functions regardless of mass, momentum and particle channel may be directly read off.

In the limit of large frequencies  $\omega$  for example one finds

$$\rho_H(\omega \rightarrow \infty, \vec{p}) = \Theta(s - 4m^2) \frac{N_c}{4\pi^2} \left( (a_H^{(1)} - a_H^{(2)}) \frac{\omega^2}{4} + (a_H^{(1)} + a_H^{(2)}) \left[ \frac{p^2}{3} + (a_H^{(1)} - a_H^{(3)}) 8m^2 \right] \right) . \quad (3.56)$$

Once more concentrating on the vector spectral function as an example, two of the possible three cases are immediately realized:

$$\rho_V(\omega \rightarrow \infty, \vec{p}) = \rho_{ii}(\omega \rightarrow \infty, \vec{p}) = \Theta(s - 4m^2) \frac{N_c}{4\pi^2} \omega^2 \quad (3.57)$$

$$\rho_{00}(\omega \rightarrow \infty, \vec{p}) = \Theta(s - 4m^2) \frac{N_c}{6\pi^2} p^2 \quad , \quad (3.58)$$

the last case is only realized for the time-time component of the axial vector current

$$\rho_{A,00}(\omega \rightarrow \infty, \vec{p}) = \Theta(s - 4m^2) \frac{N_c}{6\pi^2} (p^2 + 6m^2) \quad , \quad (3.59)$$

this case will not be further examined in the following, however it is interesting to note that the deviation from this behavior in the interacting case can be shown to be an effect due to the axial anomaly [74].

Let us now have a more detailed look at the three possible vector spectral functions in the channels  $V_{\mu\mu}$ ,  $V_{ii}$  and  $V_{00}$ .

To this extent let us begin with the time-time component described by  $\rho_{00}(\omega, \vec{p})$ . From Eq. 3.55 it is clear that at vanishing momentum the spectral function describing this channel is given by a delta function located at  $\omega = 0$ , while at the same time Eq. 3.56 shows that the contribution from  $\omega \neq 0$  smoothly vanishes as the momentum goes to zero. At this point note that in literature all spectral functions come with an extra factor of  $2\pi$  compared to our convention, from this point onwards we will explicitly include this factor:

$$\Rightarrow \rho_{00}(\omega) = 2\pi T^2 \omega \delta\omega \quad . \quad (3.60)$$

When the momentum is finite on the other hand the spectral function in the massless limit reads

$$\begin{aligned} \rho_{00}(\omega, p) = & 2\pi\Theta(\omega^2 - p^2) \frac{N_c T^2}{\pi^2} \left( \frac{p^2}{12T^2} + \text{Li}_2(-e^{-(\omega+p)/2T}) + \text{Li}_2(-e^{-(\omega-p)/2T}) \right. \\ & \left. + \frac{2T}{p} \left[ \text{Li}_3(-e^{-(\omega+p)/2T}) - \text{Li}_3(-e^{-(\omega-p)/2T}) \right] \right) \\ & + 2\pi\Theta(p^2 - \omega^2) \frac{N_c T^2}{\pi^2} \left( \text{Li}_2(-e^{-(\omega+p)/2T}) - \text{Li}_2(-e^{-(\omega-p)/2T}) \right. \\ & \left. + \frac{2T}{p} \left[ \text{Li}_3(-e^{-(\omega+p)/2T}) - \text{Li}_3(-e^{-(\omega-p)/2T}) \right] \right) \quad . \quad (3.61) \end{aligned}$$

It is interesting to investigate in what fashion the  $\delta$ -function in the limiting case of vanishing momentum is achieved, to do so in Fig. 3.1 the limits of  $\omega \searrow p$  and  $\omega \nearrow p$  are shown with decreasing momentum  $p$ . Both the above and below limits are necessary as the analytic expression in the massless limit clearly shows a discontinuity at  $\omega = p$ . Plotting the spectral function  $\rho_{00}(\omega \rightarrow p)$  directly establishes the expected behavior, as such the contribution above the lightcone vanishes with  $\sim p^2$ . The polylogarithms below the lightcone on the other hand go to a finite value as the momentum vanishes. This may be understood as the spectral function below the lightcone in the limit of vanishing momentum contributes a  $\delta$ -peak of finite height.

In the next step also the limit of vanishing mass should be examined and this is achieved by fixing the momentum to  $|p|/T = 2.5$  and then sending the mass from  $m/T = 2.5$  to zero. The result is shown in Fig. 3.2, in contrast to the massless case a finite mass induces a gap between the regimes below the lightcone ( $\omega < p$ ) and above, as can be seen already from the analytic expressions. Additionally however in the limit of vanishing mass the already noted discontinuity at  $\omega = p$  is encountered, which at finite mass does not exist.

The mass gap in principle enables the decoupling of the low frequency and the intermediate to high frequency range and it becomes possible to research the physics below the lightcone separately to that above. This is especially interesting as these two regimes are responsible for two different types of physics phenomena. As will be shown in a later

### 3.1 Spectral Functions in Non-Interacting Theory

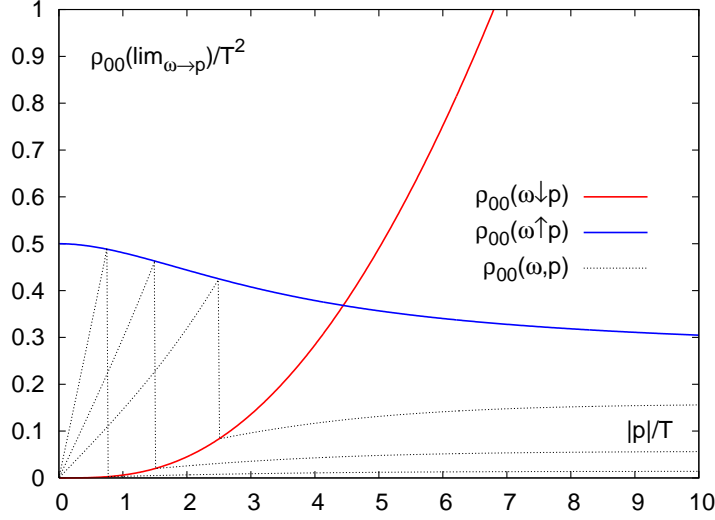


Figure 3.1: The limits  $\omega \searrow p$  (red) and  $\omega \nearrow p$  (blue) of the  $V_{00}$  channel are shown over momentum  $|p|/T$  in the massless limit. The dashed lines show the spectral functions at  $|p|/T = 0.75, 1.5,$  and  $2.5$  where the x-axes now shows frequency  $\omega/T$  in order to clarify where the limits fit in.

section the frequency region around and below the lightcone will give rise to transport phenomena, while that above is interesting from the point of view of hadron spectroscopy. In view of the results of Fig. 3.2 at vanishing mass these two regimes are intermixed and such a decoupling is not possible. Note here that the same holds for the  $V_{\mu\mu}$  and  $V_{ii}$  channels, as such the mass dependence will not be explicitly shown in the following as no new insight may be gained.

In the massless, vanishing momentum limit on the other hand the  $V_{\mu\mu}$  and  $V_{ii}$  channels may be analyzed jointly, as their expressions are very similar. In fact they only differ by a  $\delta$ -function:

$$\begin{aligned}\rho_{ii}(\omega, 0) &= \frac{3}{2\pi} \omega^2 \tanh\left(\frac{\omega}{4T}\right) + 2\pi T^2 \omega \delta(\omega) \\ \rho_V(\omega, 0) &= \frac{3}{2\pi} \omega^2 \tanh\left(\frac{\omega}{4T}\right) .\end{aligned}\quad (3.62)$$

Note here that the absence of the  $\delta$ -function in the full vector spectral function can be understood from the fact that it is the combination of the time-time and spatial components

$$\rho_V(\omega, 0) \equiv \rho_{ii}(\omega, 0) - \rho_{00}(\omega, 0) \quad , \quad (3.63)$$

hence the  $\delta$ -functions cancel. In the interacting theory this is no longer the case, here the time-time component can be linked to a conserved quantity, while the contribution

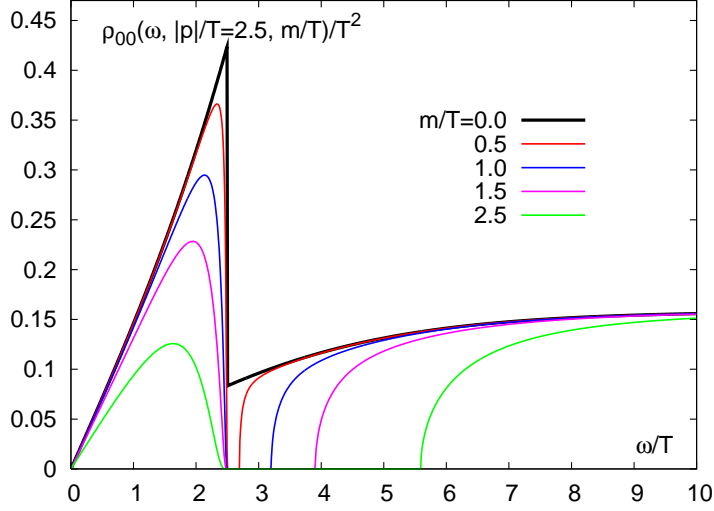


Figure 3.2: *The free  $V_{00}$  channel spectral function at fixed momentum  $|p|/T = 2.5$  and taking the limit  $m/T \rightarrow 0$ . Clearly at finite mass a gap appears that separates the below ( $\omega < p$ ) and above ( $\omega > p$ ) lightcone contributions. At vanishing mass however a discontinuity arises and this separation is no longer possible.*

from the spatial component is subject to thermal effects. More details on this will be given in the following.

An immediate advantage of the simple expressions encountered in the massless limit at vanishing momentum is that the integration to obtain the correlation function may be done analytically, one thus obtains the free Euclidean continuum correlation function depending on Euclidean time  $\tau T$  [73–75].

$$\frac{G_V(\tau T)}{T^3} = \pi 2N_c(1 - 2\tau T) \frac{1 + \cos^2(2\pi\tau T)}{\sin^3(2\pi\tau T)} + 4N_c \frac{\cos(2\pi\tau T)}{\sin(2\pi\tau T)} \quad (3.64)$$

$$\frac{G_{ii}(\tau T)}{T^3} = \frac{G_V(\tau T)}{T^3} + 1 \quad , \quad (3.65)$$

in the following it will be advantageous to heavily exploit these relations and to use the Euclidean time times temperature  $\tau T$  as variable. As we will be taking the continuum limit via different lattice sizes at the same temperature, using these variables ensures comparability.

At finite momentum the situation is more complicated. In the case of the  $V_{\mu\mu}$  channel the spectral function was already derived above and is given by Eq. 3.46

$$\begin{aligned} \rho_V(\omega, \vec{p}) = & \Theta(\omega^2 - p^2) \frac{N_c T}{2\pi^2 |\vec{p}|} \left( (\omega^2 - p^2) \ln \left[ \frac{\cosh((\omega + \vec{p})/4T)}{\cosh((\omega - \vec{p})/4T)} \right] \right) \\ & + \Theta(p^2 - \omega^2) \frac{N_c T}{2\pi^2 |\vec{p}|} \left( (\omega^2 - p^2) \ln \left[ \frac{\cosh((\omega + \vec{p})/4T)}{\cosh((\omega - \vec{p})/4T)} - \frac{\omega}{2T} \right] \right) \quad , \quad (3.66) \end{aligned}$$

### 3.1 Spectral Functions in Non-Interacting Theory

as such there is no discontinuity dependent on  $p^2$  and also the polylogarithmic part drops out. Subsequently at first sight this channel would be simplest to research. Unfortunately this is exactly the spectral function that is subject to the most diverse interaction effects, as it is the combination of all possible components. As a consequence we first focus on the spatial component  $V_{ii}$ , once this in combination with the  $V_{00}$  contribution is understood we return to the  $V_{\mu\mu}$ .

At finite momentum immediately note that the spatial component may be decomposed into one part that is polarized transversally and one that is polarized longitudinally with respect to the direction of the momentum

$$\rho_{ii}(\omega, \vec{p}) = 2\rho_T(\omega, \vec{p}) + \rho_L(\omega, \vec{p}) \quad . \quad (3.67)$$

Consequently there are two different spectral functions that are combined into the full expression of  $\rho_{ii}(\omega, \vec{p})$ , which is given by Eq. 3.53 inserting the appropriate constants  $a_H^{(i)}$  as before. Clearly this expression contains all possible contributions, i.e. from the cosh-term, the polylogarithmic term and the term proportional to the momentum squared. Compared to the expression in the  $\rho_V(\omega, \vec{p})$  case this is much more complicated to handle.

However in the next step it is possible to disentangle the transversal and longitudinal parts by exploiting a direct relation between the time-time and the longitudinal spectral functions.

To see this consider the generic tensor structure of the correlation function [74]. In this setting the conservation of charge is given by the expression [23]:

$$p_\mu G_R^{\mu\nu}(p) = 0 \quad . \quad (3.68)$$

For the time-time ( $\nu = 0$ ) and spatial ( $\nu = j$ ) components one may then write

$$p_0 G_R^{00} + p_i G_R^{i0} = 0 \quad (3.69)$$

$$p_0 G_R^{0j} + p_i G_R^{ij} = 0 \quad , \quad (3.70)$$

as  $G_R^{\mu\nu} - G_R^{\nu\mu} = 0$  one may combine both expressions to yield

$$p_0 \cdot (p_0 G_R^{00} + p_i G_R^{i0}) - p_j \cdot (p_0 G_R^{0j} + p_i G_R^{ij}) = 0 \quad \Rightarrow \quad p_0^2 \cdot G_R^{00} = p_i p_j \cdot G_R^{ij} \quad , \quad (3.71)$$

subsequently choosing  $\vec{p} = (0, 0, p)$  gives  $p_0^2 \cdot G_R^{00} = p_z^2 \cdot G_R^{zz}$ . Via Eq. 3.17 this expression may be rewritten to read

$$\rho_L(\omega, \vec{p}) = \frac{\omega^2}{p^2} \rho_{00}(\omega, \vec{p}) \quad (3.72)$$

Using Eq. 3.72 it is possible to compute the longitudinally polarized from the time-time spectral function. In the next step exploiting Eq. 3.67 enables the computation of the transversal spectral function. For  $|p|/T = 2.5$  the results for the full, spatial, transversal and longitudinal spectral functions are shown in Fig. 3.3. Here it is advantageous to

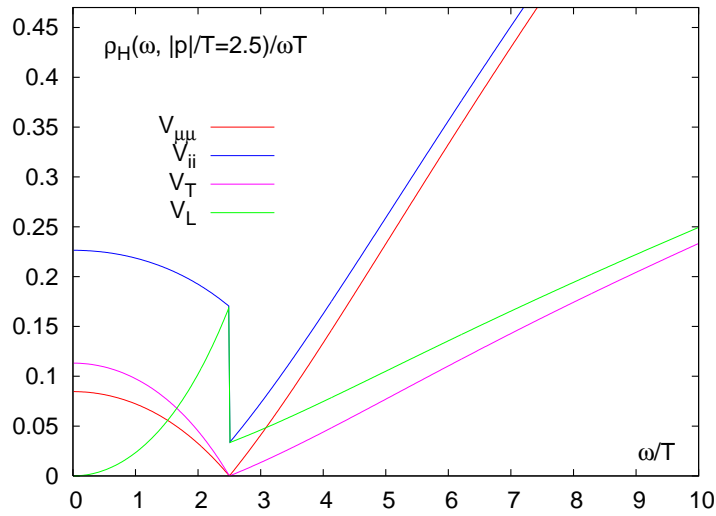


Figure 3.3: *The free  $V_{\mu\mu}$ ,  $V_{ii}$ ,  $V_T$  and  $V_L$  vector current-current spectral functions at  $|p|/T = 2.5$  in the massless limit in units  $1/\omega$ . Clearly the simple form of  $V_{\mu\mu}$  in the free case relies on cancellations of its components.*

show the results divided by  $\omega \rightarrow \rho(\omega)/\omega$ , as then the limit  $\omega \rightarrow 0$  approaches a constant corresponding to a linear behavior in  $\omega$ .

Returning to the  $V_{\mu\mu}$  channel note that the relatively simple shape of the full spectral function in fact finds its origin in the exact cancellation of parts of its components. As such the discontinuity at  $\omega = p$  is taken care of by the time-time and longitudinal components, while the polylogarithmic and momentum dependent parts are canceled by the combination of all three possible components.

In the interacting case these cancellations cannot be a priori assumed as all components are subject to thermal modifications at finite momentum. As a consequence the transversal, longitudinal and time-time spectral functions have to be studied separately. From a physics point of view all three are connected to in part different physics, e.g. the spatial spectral function is still connected to the dilepton rate, see Eq. 1.18, the transversal part on the other hand is directly related to the photon rate, see Eq. 1.17, while still differently the longitudinal and time-time components are linked to the quark diffusion constant, as will be shown below.

### 3.1.3 Free Discretized Spectral Functions

So far we have concentrated on the free continuum spectral function. Next it is instructive to also derive a lattice discretized version of the free spectral function. To do so space-time is discretized as was explained in Chp. 2, the most important thing to keep in mind however is that as a consequence of the lattice discretization also the momenta

### 3.1 Spectral Functions in Non-Interacting Theory

are discrete and confined to the Brillouin zone.

Consequently the lattice momenta in spatial direction are given by the condition:

$$k_i = 2\pi n_i / N_\sigma \quad , \quad \text{where: } n_i = -N_\sigma/2 + 1, -N_\sigma/2 + 1, \dots, N_\sigma/2 - 1, N_\sigma/2 \quad . \quad (3.73)$$

Following the recipe for deriving spectral functions outlined above write the correlation function:

$$G_H(\tau, \vec{p}) = -\frac{N_c}{N_\sigma^3} \sum_{\vec{k}} \text{Tr} \left[ S(\tau, \vec{k}) \Gamma_H S(-\tau, \vec{\tau}) \Gamma_H \right] \quad , \quad (3.74)$$

with the free Wilson lattice fermion propagator

$$S(\tau, \vec{k}) = \frac{-i\gamma_4 \sin(k_4) - iK_{\vec{k}} + 1 - \cos(k_4) + M_{\vec{k}}}{\sin^2(k_4) + K_{\vec{k}}^2 + (1 - \cos(k_4) + M_{\vec{k}})^2} \quad , \quad (3.75)$$

where in turn

$$K_{\vec{k}} = \sum_i \gamma_i \sin(k_i) \quad \text{and} \quad M_{\vec{k}} = \sum_i (1 - \cos(k_i)) + m \quad . \quad (3.76)$$

In the next step the propagator may be decomposed as [76]:

$$S(\tau, \vec{k}) = \gamma_4 S_4(\tau, \vec{k}) + \sum_i \gamma_i S_i(\tau, \vec{k}) + \mathbb{1} S_u(\tau, \vec{k}) \quad . \quad (3.77)$$

In the following we are interested especially in the spectral functions in an equivalent form to Eq. 3.34. To arrive at such an expression it is best to separate away the time dependence, the components of the propagator may then be written as [74]:

$$S_4(\vec{k}) = \frac{\sinh(E_{\vec{k}})}{2\mathcal{E}_{\vec{k}} \cosh(E_{\vec{k}}/2T)} = \frac{S_4(\tau, \vec{k})}{\cosh((\tau - 1/2T)E_{\vec{k}})} \quad (3.78)$$

$$S_i(\vec{k}) = \frac{i \sin(k_i)}{2\mathcal{E}_{\vec{k}} \cosh(E_{\vec{k}}/2T)} = \frac{S_i(\tau, \vec{k})}{\sinh((\tau - 1/2T)E_{\vec{k}})} \quad (3.79)$$

$$S_u(\vec{k}) = -\frac{1 - \cosh(E_{\vec{k}}) + M_{\vec{k}}}{2\mathcal{E}_{\vec{k}} \cosh(E_{\vec{k}}/2T)} = \frac{S_u(\tau, \vec{k})}{\sinh((\tau - 1/2T)E_{\vec{k}})} + \frac{\delta_{\tau 0}}{2(1 + M_{\vec{k}})} \quad , \quad (3.80)$$

here

$$\mathcal{E}_{\vec{k}} = (1 + M_{\vec{k}}) \sinh(E_{\vec{k}}) \quad \text{and} \quad \cosh(E_{\vec{k}}) = 1 + \frac{K_{\vec{k}}^2 + M_{\vec{k}}^2}{2(1 + M_{\vec{k}})} \quad . \quad (3.81)$$

The resulting free spectral function for Wilson fermions corresponding to Eq. 3.34 may

then be shown to read

$$\begin{aligned}
 \rho_H^{\text{latt}}(P) = & \frac{4\pi N_c}{N_\sigma^3} \sum_{\vec{k}} \sinh\left(\frac{\omega}{2T}\right) \cdot \\
 & \left\{ \left[ a_H^{(1)} S_4(\vec{k}) S_4^\dagger(\vec{r}) + a_H^{(2)} \sum_i S_i(\vec{k}) S_i^\dagger(\vec{r}) + a_H^{(3)} S_u(\vec{k}) S_u^\dagger(\vec{r}) \right] \cdot \delta(\omega + E_{\vec{k}} - E_{\vec{r}}) \right. \\
 & + \left[ a_H^{(1)} S_4(\vec{k}) S_4^\dagger(\vec{r}) - a_H^{(2)} \sum_i S_i(\vec{k}) S_i^\dagger(\vec{r}) - a_H^{(3)} S_u(\vec{k}) S_u^\dagger(\vec{r}) \right] \cdot \delta(\omega - E_{\vec{k}} - E_{\vec{r}}) \\
 & \left. + (\omega \rightarrow -\omega) \right\} , \tag{3.82}
 \end{aligned}$$

where the channel constants  $a_H^{(i)}$  are the same as before. This expression may in turn be evaluated numerically and we will do so in the following.

Note at this point that one must be careful taking the massless limit when computing the spectral function from Eq. 3.82. As the mass goes to zero it is also possible for the single particle energies  $E_{\vec{k}}$  to go to zero, when this happens one numerically hits a divergence as  $S(\vec{k}) \sim 1/\mathcal{E}_{\vec{k}} \sim 1/\sinh(E_{\vec{k}}) \rightarrow 1/0$ . This problem is easily circumvented using l'Hopital at  $E_{\vec{k}} = 0$  and setting:

$$S_4(\vec{k}) = 2(1 + M_{\vec{k}})^{-1} \quad \text{and} \quad S_i(\vec{k}) = S_u(\vec{k}) = 0 \quad . \tag{3.83}$$

### Discrete Spectral Functions and the Binning Method

The lattice discretized spectral and correlation functions are made up of the sums over all lattice momenta, in a finite lattice volume these are naturally limited to a finite number by construction. As a consequence the lattice discretized versions of the spectral and correlation functions are made up of a sum of disconnected  $\delta$ -functions in spatial momentum and frequencies.

Making the momenta continuous thus implies taking the thermodynamic limit  $V \rightarrow \infty$ , which in principle entails replacing the sum in Eq. 3.82 by an appropriate integral. In practice however one turns to the so called binning method [75]. In a nutshell this method implies smearing the delta functions of Eq. 3.82:

$$\delta\left(\omega + E^{(\pm)}(\vec{k}, \vec{r})\right) \rightarrow \Theta\left(\omega + E^{(\pm)}(\vec{k}, \vec{r})\right) \cdot \Theta\left([E^{(\pm)}(\vec{k}, \vec{r}) + \Delta\omega] - \omega\right) \quad . \tag{3.84}$$

In this way the  $\delta$ -functions are averaged over an energy region, setting a large number of lattice momenta then effectively gives a spectral function in the thermodynamic limit.

To illustrate the resulting effect we show the free lattice full vector spectral function for  $|p|/T = 2.3562$  in the massless limit in Fig. 3.4. In this figure the free lattice spectral function is shown with a resolution in frequency of  $\Delta\omega = 0.004$  and varying number of spatial sizes and thus inner momenta  $N_\sigma = 128, 256, 512$  and finally  $N_\sigma = 4056$ . The very high resolution in frequency implies very narrow bins, which for most  $N_{k_i}$  effectively constitute  $\delta$ -functions as in the prescription of Eq. 3.82. A smooth encompassing

### 3.1 Spectral Functions in Non-Interacting Theory

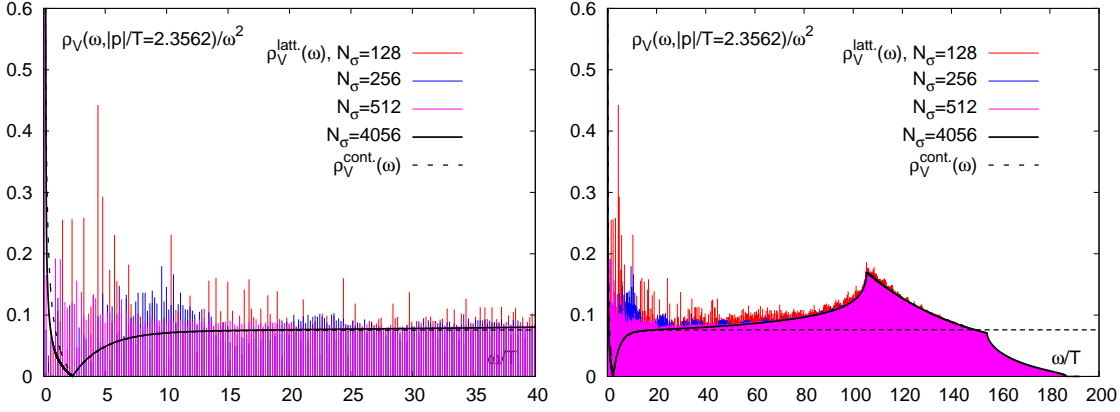


Figure 3.4: *The free lattice full vector spectral function at  $|p|/T = 2.3562$  and vanishing mass with varying spatial sizes  $N_\sigma$ , the black line shows the free continuum result. Only in the thermodynamic limit may we obtain a smooth encompassing function, in practice this is mimicked by the binning method.*

discretized spectral function is only achieved with a very large number of internal momenta. In our example case we take only spectral functions with  $N_\sigma \geq 4056$  to be close enough to the thermodynamic limit and to capture most of the relevant discretization effects at the frequency resolution  $\Delta\omega = 0.004$ .

In practice varying the latter by changing the bin width smoother lattice spectral functions may be computed with smaller  $N_\sigma$ . Nevertheless our fine resolution shows quite clearly that large lattices are necessary when studying spectral functions. Additionally it is advantageous to use a very fine frequency resolution, when supplying the free lattice spectral function as default model for the maximum entropy method, see Chp. 4.3.

Note the most striking difference between the free continuum and free lattice spectral functions as seen in Fig. 3.4 is that the lattice part does not diverge in  $\mathcal{O}(\omega^2)$ . Instead it develops two cusps at large frequencies  $\omega$ , whereby it can be shown that these actually originate from the edges of the Brillouin zone [75].

To see this recall the single particle energy of Eq. 3.81 and write [22, 74, 75]:

$$E_{\vec{k}} = \log \left[ 1 + \frac{K_{\vec{k}}^2 + M_{\vec{k}}^2}{2(1 + M_{\vec{k}})} + \frac{\sqrt{(K_{\vec{k}}^2 + M_{\vec{k}}^2)(K_{\vec{k}}^2 + (M_{\vec{k}} + 2)^2)}}{2(1 + M_{\vec{k}})} \right] . \quad (3.85)$$

At the corners of the Brillouin zone the doublers contribute to the frequency  $\omega$ :

$$\omega = 2E_{\vec{k}} = 2 \log[1 + M_{\vec{k}}] . \quad (3.86)$$

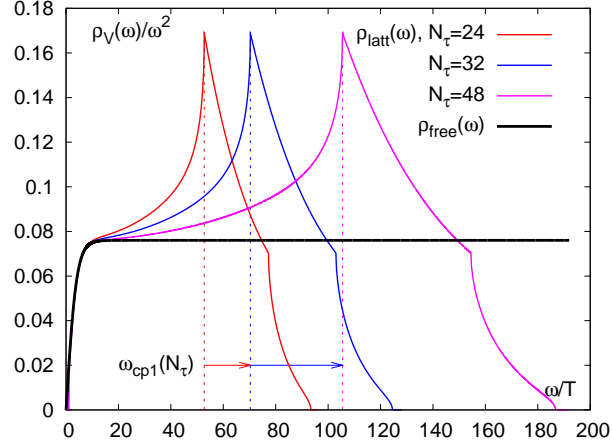


Figure 3.5: *The free lattice vector spectral function  $\rho(\omega)/\omega^2$  with varying  $N_\tau$ , at fixed temperature this corresponds to taking the continuum limit. The free continuum spectral function (black) is given for reference.*

As a consequence the doublers contribute at the frequencies:

$$\omega_{min} = \frac{2}{a} \log[1 + (1 + am)] \quad , \quad \vec{k} = (0, 0, 0) \quad (3.87)$$

$$\omega_{cp1} = \frac{2}{a} \log[1 + (2 + am)] \quad , \quad \vec{k} = \left(\frac{\pi}{a}, 0, 0\right), \dots \quad (3.88)$$

$$\omega_{cp2} = \frac{2}{a} \log[1 + (4 + am)] \quad , \quad \vec{k} = \left(\frac{\pi}{a}, \frac{\pi}{a}, 0\right), \dots \quad (3.89)$$

$$\omega_{max} = \frac{2}{a} \log[1 + (6 + am)] \quad , \quad \vec{k} = \left(\frac{\pi}{a}, \frac{\pi}{a}, \frac{\pi}{a}\right) \quad . \quad (3.90)$$

Thus the closer we are to the continuum, i.e. small lattice spacing, the higher are the frequencies at which the discretization effects become noticeable. In this way for  $a \rightarrow 0$  the continuum spectral function is retrieved in the thermodynamic limit, as such the low frequency behavior closely resembles that of the free continuum at sufficiently small lattice spacings. This is illustrated in Fig. 3.5 as we plot the massless free continuum vector spectral function  $\rho(\omega)/\omega^2$  and its free discretized counterparts at different  $N_\tau$  and vanishing momentum. At fixed temperature the increasing  $N_\tau$  correspond to finer and finer lattice spacings. As the temporal extent is increased the discretization effects encoded in the cusp, e.q. at  $\omega_{cp1}$  move to larger and larger frequencies. Below and especially in the low frequency region the free continuum spectral function is thus retrieved already at finite lattice spacing, even though the full continuum is only reached at  $N_\tau \rightarrow \infty$ .

### 3.2 Expectations for Interacting Theory

To estimate what is to be expected once interactions are introduced a large body of physical understanding of the system is required.

Partly the behavior at finite temperatures may be constrained from certain physics assumptions or general relations of the system. Another useful tool is to apply the theory of linear response in order to get an idea of the reaction of a system to thermal processes. In the following both approaches will be exploited to pin down the behavior of the spectral functions as good as possibly feasible.

First turn to physics arguments and recall the free spectral function of the time-time vector channel:

$$\rho_{00}^{free}(\omega) = 2\pi T^2 \omega \delta(\omega) \quad . \quad (3.91)$$

Indeed the time-time component of the spectral function may be connected to the quark number susceptibility  $\chi_q$ , as it is defined by [77]:

$$\chi_q = -\frac{1}{T} \int d^3x \langle J_0(\tau, \vec{x}) J_0^\dagger(0, \vec{0}) \rangle. \quad (3.92)$$

Physically speaking the integral over the time-time component of the vector current gives the net number of quarks of a given flavor channel. As the net number of quarks is conserved, it explicitly does not depend on Euclidean time. Consequently the time-time vector correlation function  $G_{00}(\tau, \vec{p} = 0)$  is a constant in Euclidean time. This is exactly mirrored by the shape of the spectral function being a  $\delta$ -function.

Introducing the quark number susceptibility the non-interacting and also the interacting time-time spectral function of the vector current reads:

$$\rho_{00}(\omega) = 2\pi \chi_q \omega \delta(\omega) \quad . \quad (3.93)$$

The subsequent correlation function may then be written as a constant contribution proportional to the quark number susceptibility and the temperature

$$G_{00}(\tau, \vec{p} = 0) = -\chi_q T \quad , \quad (3.94)$$

clearly the spatial and full vector correlation functions at vanishing momentum only differ by this constant:

$$G_V(\tau, \vec{p} = 0) = G_{ii}(\tau, \vec{p} = 0) - \chi_q T \quad (3.95)$$

This is an example where physics arguments completely determine the shape of the spectral function and we will see below that the above relations are well motivated and hold for all temperatures evaluated in this work.

In general however only assumptions on the temperature dependence of the spectral function can be made. As such the known free, non-interacting case corresponds to that

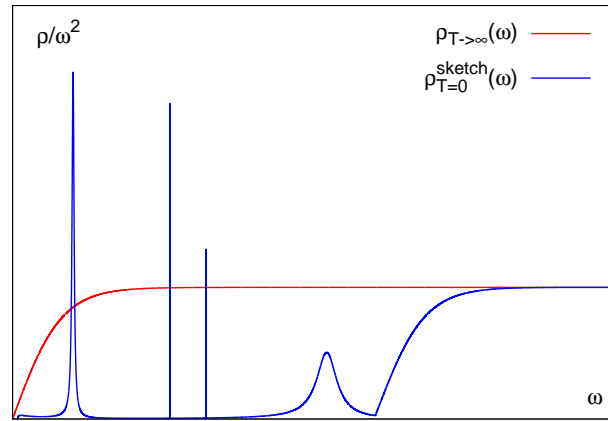


Figure 3.6: *Sketch of the spectral functions in the free ( $T \rightarrow \infty$ ) and confined ( $T \sim 0$ ) case in units of  $1/\omega^2$ . In the intermediate case one expects the peak structure to “melt” and be absorbed into the continuous spectrum while additional transport phenomena might appear.*

in the limit of infinite temperature due to asymptotic freedom. At the same time from spectroscopy and experiments there is good knowledge of the spectral functions at low temperatures, i.e. in the confined phase.

Subsequently being given the two opposite limiting cases of the shape of the spectral functions, it is the intermediate behavior that we have to establish to reach a full understanding. To get an idea how this might look like recall the spectral functions in the case of vanishing momentum at infinite temperature. In Fig. 3.6 the full vector spectral function is once more shown, the characteristic divergence with  $\mathcal{O}(\omega^2)$  immediately entails that the spectrum is given by a continuum of many-particle states.

On the other hand in the confined phase we know that the spectrum is made up of a collection of Breit-Wigner peaks with the continuum of states dominating above a certain mass-threshold, as sketch of a possible spectrum is also given in Fig. 3.6. The width of the peaks is directly connected to the decay with of the particle states and thus varies from very narrow resonances to large bumps in the spectrum.

A reasonable assumption to connect these two regimes is to assume that both known regimes are in fact connected by a smooth change from the one into the other. This would imply that the mass-threshold for the continuum is reduced as the temperature rises, with the Breit-Wigner peaks being swallowed along the way. Simultaneously the Breit-Wigner peaks may melt, i.e. their widths increase, while the amplitudes are reduced, or change their position on the frequency axis.

In addition to these effects also new in-medium phenomena might arise that do not yet exist in the confined phase and vanish at very high temperatures.

### 3.2.1 Linear Response and Transport Coefficients

To get an idea of these in-medium, thermal modifications of the spectral functions in the quark gluon plasma we invoke the linear response formalism, see e.g [30] or [23].

Imagine applying an external field to an equilibrium system, the goal of linear response theory is then to calculate the change of the thermal average of the operator  $O(t)$  caused by this external field to first (i.e. linear) order. The equation of motion of such a system may be generically written as:

$$\frac{\partial}{\partial t} O(t) = i [H_0 + H_{ext}(t), O(t)] \quad , \quad (3.96)$$

where  $H_0$  and  $H_{ext}(t)$  denote the Hamiltonian operators of the equilibrium and the external fields respectively. Given the eigenstates  $|n\rangle$  of the Hamiltonian  $H_0$  in the Heisenberg picture it follows that

$$\frac{\partial}{\partial t} \langle n | O(t) | n \rangle = i \langle n | [H_{ext}(t), O(t)] | n \rangle \quad . \quad (3.97)$$

The above equation, although being exact, cannot be solved in a closed form, so here integrate only to the first order in  $H_{ext}(t)$  as mentioned above:

$$\delta \langle n | O(t) | n \rangle = \langle n | O(t) | n \rangle - \langle n | O(t_0) | n \rangle = i \int_{t_0}^t dt' \langle n | [H_{ext}(t'), O(t)] | n \rangle \quad . \quad (3.98)$$

Finally taking the ensemble average one arrives at an expression that gives the change of the thermal average of the operator  $O(t)$  caused by this external field to first order, exactly as was the aim:

$$\delta \langle O(t) \rangle = i \int_{t_0}^t dt' \text{Tr} [\hat{\rho} [H_{ext}(t'), O(t)]] \quad . \quad (3.99)$$

Without loss of generality now assume a field  $\phi(\vec{x}, t)$  coupling to the external source  $J_{ext}(\vec{x}, t)$  as

$$H_{ext}(t) = \int d^3x J_{ext}(\vec{x}, t) \phi(\vec{x}, t) \quad , \quad (3.100)$$

then Eq. 3.99 may be rewritten in terms of the retarded correlation function introduced in Eq. 3.14 and Eq. 3.19:

$$\begin{aligned} \delta \langle \phi(\vec{x}, t) \rangle &= i \int_{t_0}^t dt' \int d^3x' J_{ext}(\vec{x}', t') \text{Tr} [\hat{\rho} [\phi(\vec{x}', t'), \phi(\vec{x}, t)]] \\ &= \int_{-\infty}^{\infty} dt' \int d^3x' J_{ext}(\vec{x}', t') G^R(\vec{x}', t') \end{aligned} \quad (3.101)$$

$$\delta \langle \phi(t, \vec{p}) \rangle = \int_{-\infty}^{\infty} dt' J_{ext}(t', \vec{p}) G^R(t', \vec{p}) \quad (3.102)$$

$$\delta \langle \phi(\omega, \vec{p}) \rangle = J_{ext}(\omega, \vec{p}) G^R(\omega, \vec{p}) \quad , \quad (3.103)$$

where in Eq. 3.101 we have sent  $t_0 \rightarrow -\infty$  and respecting the  $\Theta$ -function in Eq. 3.19 set  $t = \infty$ . Note in this form the retarded correlation function is also known as the response function, it thus quantifies the response of a system to a small perturbation out of equilibrium due to the external source. Subsequently it yields the opportunity to compute dynamical quantities of a thermal system.

To do so it is an advantage to define the static susceptibility at  $t = 0$ , where the source term is specified to read:

$$J_{ext}(t, \vec{p}) = e^{\epsilon t} \Theta(-t) J_{ext}(0, \vec{p}) \quad , \quad (3.104)$$

this type of external source leads to an adiabatic change in the thermal system. In this setup the static susceptibility is

$$\begin{aligned} \delta \langle \phi(0, \vec{p}) \rangle &= \chi_s(\vec{p}) J_{ext}(0, \vec{p}) = \chi_s(\vec{p}) J_{ext}^0 \\ \Rightarrow \chi_s(\vec{p}) &= \int_{-\infty}^{\infty} dt' e^{-\epsilon t'} G^R(t', \vec{p}) = G^R(i\epsilon, \vec{p}) \quad , \end{aligned} \quad (3.105)$$

as a consequence the zero frequency correlation function is equal to the static susceptibility  $\chi_s$ . Combining the above relations and integrating both sides of Eq. 3.102 by  $\int_0^{\infty} d\omega e^{i\omega t}(\dots)$  one may derive an explicit expression for the response function [23]:

$$G^R(\omega, \vec{p}) \cdot J_{ext}^0 = \chi_s(\vec{p}) \cdot J_{ext}^0 + i\omega \int_0^{\infty} dt e^{i\omega t} \delta \langle \phi(t, \vec{p}) \rangle \quad . \quad (3.106)$$

A good example to see how Eq. 3.106 works is to consider the diffusion of a massive particle in a thermal medium. Specifically the particle density  $n(t, \vec{p})$  is connected with the following correlation function:

$$G_{nn}(t, \vec{p}) = \int d\vec{x} e^{-i\vec{p}\vec{x}} \langle [n(t, \vec{x}), n(0, \vec{x})] \rangle \quad (3.107)$$

and obeys the classical diffusion equation [23]:

$$\partial_t n(t, \vec{x}) + D \Delta n(t, \vec{x}) = 0 \quad , \quad (3.108)$$

where  $D$  is the diffusion constant. After Fourier transformation the solution of the diffusion equation reads

$$n(\omega, \vec{p}) = \frac{n(t=0, \vec{p})}{-i\omega + Dp^2} \quad . \quad (3.109)$$

note due to Eq. 3.105 the initial conditions is given by  $n(t=0, \vec{p}) = \chi_q(\vec{p})$ . Plugging the last expression into Eq. 3.106 one obtains the retarded correlation function

$$G_{nn}^R(\omega, \vec{p}) = \chi_s(\vec{p}) + i\omega \frac{\chi_s(\vec{p})}{-i\omega + Dp^2} \quad . \quad (3.110)$$

As highlighted above the imaginary part of the retarded correlation function immediately gives the spectral function:

$$\rho_{nn}(\omega, \vec{p}) = \frac{1}{\pi} \text{Im} G_{nn}^R(\omega, \vec{p}) = \frac{\chi_s(\vec{p})}{\pi} \frac{\omega D p^2}{\omega^2 + (D p^2)^2} \quad . \quad (3.111)$$

Also in this case the density-density, i.e. time-time, and longitudinally polarized spectral functions are connected by Eq. 3.72, subsequently one writes:

$$\rho_L(\omega, \vec{p}) = \frac{\chi_s(\vec{p})}{\pi} \frac{D \omega^3}{\omega^2 + (D p^2)^2} \quad . \quad (3.112)$$

Using the last expression it is possible to define a Kubo formula. The so called Kubo formula (see e.g. [30]) thereby relate the spectral functions to the transport properties of a system, i.e. the transport coefficients, which is in this case the diffusion constant  $D$ :

$$D \chi_s = \pi \lim_{\omega \rightarrow 0} \lim_{\vec{p} \rightarrow 0} \frac{\rho_L(\omega, \vec{p})}{\omega} \quad . \quad (3.113)$$

For the electrical conductivity defined by  $\vec{J}_{EM} = \sigma \vec{E}$  one may argue similarly to find [28–30]:

$$\sigma = \frac{1}{6} \lim_{\omega \rightarrow 0} \frac{1}{\omega} \int d^4x e^{i\omega t} \left\langle \left[ J_{EM}(x, t), J_{EM}(0, 0) \right] \right\rangle \Theta(t) \quad (3.114)$$

As a result, given the connection of the retarded correlation function to the spectral function, the corresponding transport coefficients may be read off the spectral function once it is computed. In this work this is precisely the electrical conductivity of the quark gluon plasma and the corresponding Kubo formula is:

$$\Rightarrow \sigma = \frac{C_{em}}{6} \lim_{\omega \rightarrow 0} \frac{\rho_{ii}(\omega, \vec{p}=0)}{\omega} = \frac{C_{em}}{6} \lim_{\omega \rightarrow 0} \frac{\rho_V(\omega \neq 0, \vec{p}=0)}{\omega} \quad , \quad (3.115)$$

where  $C_{em} = \sum_f Q_f^2$  is the sum of the electrical charges squared over the number of flavors.

### 3.2.2 Heavy Quark Diffusion from the Langevin Equation

To get an idea of the shape of the spectral function that arises due to transport phenomena in QCD, first look at the diffusion of a heavy quark in the quark gluon plasma. In this setting the time scale for the diffusion of a heavy quark is in fact set by  $M/T^2$ , which is long compared to the thermal time scale  $1/T$  typically obeyed by the light quarks. As a consequence a Langevin formalism may be invoked to appropriately describe the system [78].

Together with the diffusion equation Eq. 3.108 the equations of motion in the Langevin formalism are:

$$\frac{d\vec{x}}{dt} = \frac{P}{M} \quad , \quad \frac{d\vec{p}}{dt} = \xi(t) - \eta \vec{p}(t) \quad , \quad \langle \xi_i(t) \xi_j(t') \rangle = \kappa \delta_{ij} \delta(t - t') \quad . \quad (3.116)$$

The solution may be found to read

$$\vec{p}(t) = e^{-\eta t} \left[ \vec{p}(0) + \int_0^t dt' \xi(t') e^{\eta t'} \right] , \quad (3.117)$$

so that

$$\lim_{t \rightarrow \infty} \langle p_i(t) p_j(t) \rangle = \frac{\kappa}{2\eta} \delta_{ij} . \quad (3.118)$$

Due to the equipartition and fluctuation-dissipation theorems the drag and fluctuation coefficients are directly related

$$\eta = \frac{\kappa}{2MT} . \quad (3.119)$$

For a thermal initial distribution of momenta  $\langle p_i(0) p_j(0) \rangle = MT \delta_{ij}$  one may work out the mean square distance

$$\langle x^2(t) \rangle = \frac{6D}{\eta} (\eta t - (1 - e^{-\eta t})) \quad \text{with} \quad D = \frac{T}{M\eta} , \quad (3.120)$$

where the diffusion constant  $D$  has been introduced. As such the above equation describes both the initial thermal velocity of the heavy quarks and the late time diffusion.

In order to make the connection with linear response theory and especially Eq. 3.106, assume the probability  $P(t, \vec{x})$  of a heavy quark starting at time  $t = 0$  moves a distance  $\vec{x}$  over a time  $t$  is given by a Gaussian distribution where the width is given by the mean square distance:

$$\begin{aligned} N(t, \vec{x}) &= \int d\vec{x}' P(t, \vec{x} - \vec{x}') N(0, \vec{x}') \\ &= \int d\vec{x}' (2\pi \langle x^2(t) \rangle)^{-3/2} \exp \left[ -\frac{(\vec{x} - \vec{x}')^2}{2 \langle x^2(t) \rangle} \right] N(0, \vec{x}') . \end{aligned} \quad (3.121)$$

This expression is equivalent to  $N(t, \vec{p}) = P(t, \vec{p}) N(0, \vec{p})$  and consequently the retarded correlation function from linear response theory is written as

$$G_{00}^R(\omega, \vec{p}) = \chi_s(\vec{p}) + i\omega \int_0^\infty dt e^{i\omega t} P(t, \vec{p}) \quad (3.122)$$

$$= \chi_s(\vec{p}) + Dp^2 \int_0^\infty dt e^{i\omega t} (1 - e^{-\eta t}) \exp \left[ -\frac{Dp^2}{\eta} (\eta t - (1 - e^{-\eta t})) \right]. \quad (3.123)$$

Assuming  $Dp^2 \ll \eta$ , which is equivalent to assuming  $(D\vec{p})^2 \ll T/M$  the last equation may be approximated [22], the subsequent integration yields

$$G_{00}^R(\omega, \vec{p}) = \chi_s(\vec{p}) + Dp^2 \left( \frac{1}{Dp^2 - i\omega} - \frac{1}{\eta - i\omega} \right) . \quad (3.124)$$

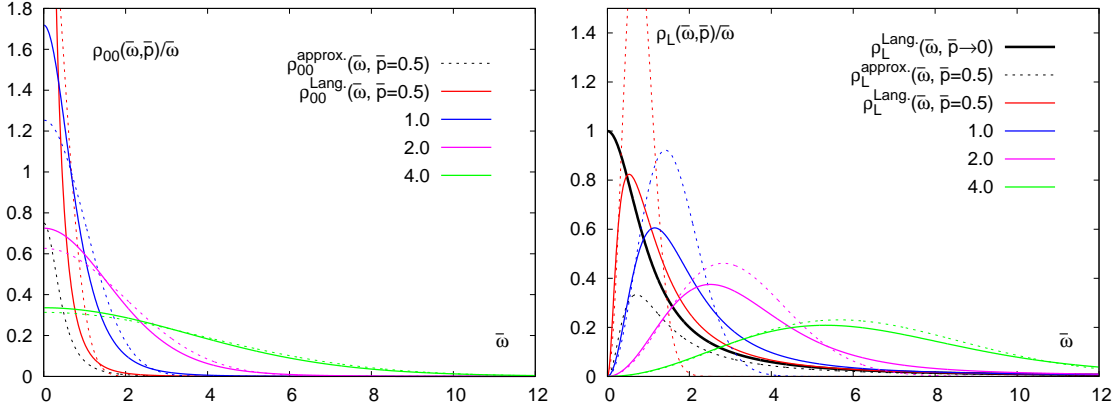


Figure 3.7: The time-time (left) and longitudinal (right) spectral functions divided by frequency from the Langevin approach for diffusive heavy quarks at different momenta (solid lines), the corresponding free results have been included (dashed lines) for comparison, whereby the diffusion constant  $D$  has been set to unity throughout. Note the approximation of Eq. 3.124 (black dashed lines) does not reproduce the full data well even at momentum  $\bar{p} = 0.5$ .

As before the corresponding spectral functions are then obtained from the imaginary part of the retarded correlation function:

$$\rho_{00}(\omega, \vec{p}) = \frac{1}{\pi} \text{Im} G_{00}^R(\omega, \vec{p}) = \frac{\chi_s(\vec{p})}{\pi} \frac{\omega(\eta^2 - (Dp^2)^2) D p^2}{((Dp^2)^2 + \omega^2)(\eta^2 + \omega^2)} \quad (3.125)$$

$$\rho_L(\omega, \vec{p}) = \frac{\omega^2}{p^2} \rho_{00}(\omega, \vec{p}) = \frac{\chi_s(\vec{p})}{\pi} \frac{\omega^3 D(\eta^2 - (Dp^2)^2)}{((Dp^2)^2 + \omega^2)(\eta^2 + \omega^2)} \quad (3.126)$$

The integration of Eq. 3.123 without further assumptions yields the Langevin results on the spectral function of diffusing heavy quarks [78]. This may be done numerically or analytically, whereby it is an advantage to rescale the variables to:

$$\bar{t} = t\eta \quad ; \quad \bar{\omega} = \frac{\omega}{\eta} \quad \text{and} \quad \bar{p}^2 = \frac{Dp^2}{\eta} \quad (3.127)$$

The resulting spectral functions in these rescaled variables are shown in Fig. 3.7. Here the spectral functions are given in units  $1/\omega$  and the approach to the Breit-Wigner peak in the limit  $\bar{p} \rightarrow 0$  can be nicely seen. At the same time the approximation of the integral is clearly only valid for very small momenta and the deviation from the actual result is already very large at  $\bar{p} = 0.5$ .

Note the free theory results also shown in Fig. 3.7 can be derived directly following the scheme of Chp. 3.1.1 in the non-relativistic limit,  $n_f = \exp[-p^2/(2MT)]$ , at very low

momentum  $p \ll T$  [78]:

$$\rho_L(\omega, \vec{p}) = \chi_s(\vec{p}) \frac{\omega^3}{p^2} \cdot \left(2\pi p^2 \langle v^2 \rangle\right)^{-1/2} \cdot \exp \left[ -\frac{\omega^2}{2p^2 \langle v^2 \rangle} \right] , \quad (3.128)$$

here  $\langle v^2/3 \rangle$  is the thermal average of the squared velocity of quarks. As such its value is  $\langle v^2/3 \rangle = 1/3$  for light and  $\langle v^2/3 \rangle = T/M$  for heavy quarks. Note however that the non-relativistic limit is not appropriate for a light quark system.

Beginning from Eq. 3.126 the longitudinally polarized spectral function in the limit of vanishing momentum becomes equivalent to the spatial spectral function  $\rho_L \rightarrow \rho_{ii}/3$ , in this case the spectral function becomes [78]

$$\rho_L(\omega, 0) = \lim_{\vec{p} \rightarrow 0} \frac{\omega^2}{p^2} \rho_{00}(\omega, \vec{p}) = \frac{\chi_s(0)}{\pi} \frac{T}{M} \frac{\omega \eta}{\omega^2 + \eta^2} , \quad (3.129)$$

which in turn yields the expected  $\delta$ -function shape if the drag coefficient vanishes:

$$\lim_{\eta \rightarrow 0} \rho_L(\omega, 0) = \frac{\chi_s(0)}{\pi} \frac{T}{M} \omega \delta(\omega) . \quad (3.130)$$

This result implies that in the limit of vanishing momentum the transport contribution arising in the interacting theory is in fact well described by a Breit-Wigner peak with its maximum at  $\omega = 0$ . Even though this result was derived for massive quarks, it is reasonable to assume that this shape is also realized in the case of massless quarks. In the next step further evidence to substantiate this assumption is given by considering light quarks in a Boltzmann type gas of particles.

### 3.2.3 Light Quarks in a Boltzmann Gas

The Langevin theory that was applied above hinges on the separation of time scales between the diffusing heavy particle  $\sim M/T$  and the thermal medium  $\sim 1/T$ . A priori such a separation cannot be safely assumed for light quark species.

One possibility however to study a thermal system of light quarks is to use the framework laid down in the Boltzmann transport equation. In this kinetic theory the properties of dilute gases are explained by analyzing the elementary collision processes between its constituents. As such the physical interpretation is that of a particle propagating freely until it collides with a constituent of the medium, at which point it consequently changes its properties, e.g. momentum or flavor. The evolution of the transition probabilities of such a particle may then be approximated by the Boltzmann equation for the probability distribution  $f(t, \vec{x}, \vec{p})$ :

$$(\partial_t + v_p \cdot \partial_x) f(t, \vec{x}, \vec{p}) = C[f, \vec{p}] , \quad (3.131)$$

where  $C[f, \vec{p}]$  is the so called collision operator. Generally speaking the Boltzmann equation is linearized in a next step, as it cannot be solved analytically. One possibility to do so is to linearize around the equilibrium distribution with constant temperature [79]:

$$f(t, \vec{x}, \vec{p}) = n_F + \delta f(t, \vec{x}, \vec{p}) . \quad (3.132)$$

In the specific case of light quarks the computation was done by Hong and Teaney in [79] and the most important steps of their treatment are briefly sketched in the following, see also [23] for a review.

Through linear response theory and Eq. 3.103 the aim is to compute the retarded correlator  $G_R^{\mu\nu}(\omega, \vec{k})$ , switching to the notation of [79] Eq. 3.103 becomes:

$$\langle J_\mu(\omega, \vec{k}) \rangle_A = -G_R^{\mu\nu}(\omega, \vec{k}) A_\nu(\omega, \vec{k}), \quad (3.133)$$

where  $\langle J_\mu(\omega, \vec{k}) \rangle_A = \delta\langle\phi(\omega, \vec{p})\rangle$  and the source is  $A_\nu(\omega, \vec{k}) = J_{ext}(\omega, \vec{k})$ . Ultimately it can be shown that  $\langle J_\mu(\omega, \vec{k}) \rangle_A$  is directly accessible from the probability distributions  $\delta f(t, \vec{x}, \vec{p})$ , see below Eq. 3.138.

Treating light quarks using the Boltzmann equation one has to include an external field, this is the Lorentz force acting on a charged particle  $F^i = Q_s F_\mu^i v^\mu$  and it leads to the Boltzmann equation for strangeness excess:

$$\frac{1}{E_{\vec{p}}} \left[ p^\mu \partial_\mu + Q_s F^{\mu\nu} p_\nu \frac{\partial}{\partial p_\mu} \right] f^s(\vec{x}, \vec{p}, t) = C^s[f, \vec{p}] \quad , \quad (3.134)$$

whereby the charge  $Q_s$  is one for strange, minus one for anti-strange and zero for all other quark species. In the next step one applies a weak external gauge field  $A_\mu = (0, \vec{A})$  to disturb the system from equilibrium. In this setting the corresponding linearized Boltzmann equation is:

$$(-i\omega + i\vec{v}_p \cdot \vec{k}) \delta f^{s-\bar{s}}(\omega, \vec{k}) - i\omega n_F(1 - n_F) 2Q_s A_i \frac{p_i}{E_{\vec{p}}} = C^{s-\bar{s}}[\delta f, \vec{p}] \quad , \quad (3.135)$$

where  $C^{s-\bar{s}}[\delta f, \vec{p}]$  is the full collision operator and the gauge field disturbs only the fermionic difference  $\delta f^{s-\bar{s}} = \delta f^s - \delta f^{\bar{s}}$ .

The above equation must be solved for  $\delta f^{s-\bar{s}}$  given the specific collision operator  $C^{s-\bar{s}}[\delta f, \vec{p}]$ :

$$\begin{aligned} (C_{qg}^q - c_{qg}^{\bar{q}}) &= -\frac{2\gamma}{p} n_F(1 + n_B) [\chi^q(\vec{p}) - \chi^q(\vec{p})] \\ &+ \frac{2\gamma}{\xi p} n_F(1 + n_B) \int_{\vec{k}} \frac{1}{k} n_F(1 + n_B) [\chi^q(\vec{p}) - \chi^q(\vec{p})] \quad , \end{aligned} \quad (3.136)$$

where, introducing also the Debye screening mass  $m_D$ ,

$$\gamma = \frac{g^4 C_F^2 \xi}{4\pi} \log\left(\frac{T}{m_D}\right) \quad \text{and} \quad \xi = \int \frac{d\vec{k}}{(2\pi)^3} \frac{1}{k} n_F(1 + n_B) = \frac{T^2}{16} \quad . \quad (3.137)$$

As such the collision operator combines a loss and a gain term due to the quarks and gluons. Once having computed  $\delta f^{s-\bar{s}}(\omega, \vec{k})$  the solution can be directly connected to Eq. 3.133:

$$\langle J_i \rangle_A = Q_s \nu_s \int \frac{d\vec{p}}{(2\pi)^3} \frac{p_i}{E_{\vec{p}}} \delta f^{s-\bar{s}} \quad , \quad (3.138)$$

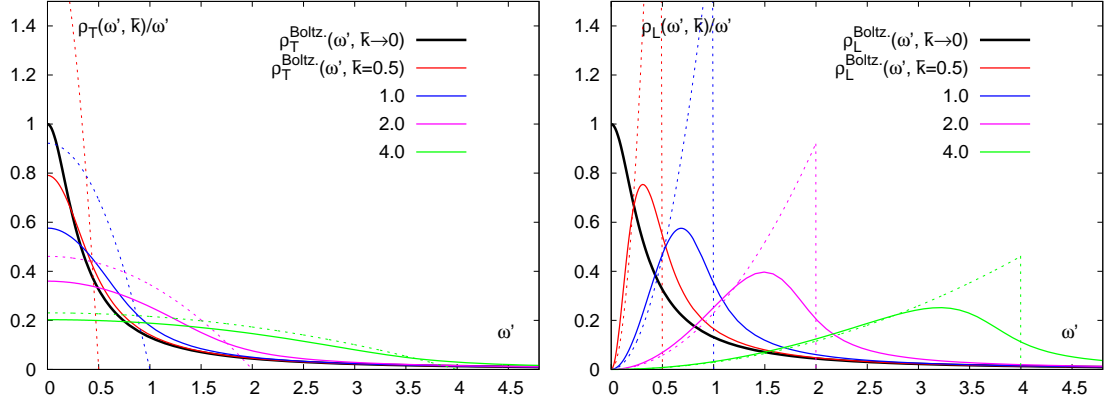


Figure 3.8: *The spectral functions divided by the frequency and normalized to unity at  $\omega' \rightarrow 0$ ,  $\bar{k} \rightarrow 0$  for the transversally (left) and longitudinally (right) polarized vector spectral functions at finite momentum from the Boltzmann equation. The solid lines show the spectral functions given their momentum  $\bar{k}$ , the dashed lines denote the corresponding free curves. The results at vanishing momentum are given by the solid black lines.*

whereby  $\nu_s$  counts the degrees of freedom of the quarks and gluons.

As noted the corresponding calculations were done in [79], where additionally the same procedure was applied to the free Boltzmann equation. In this case it is possible to derive the corresponding spectral functions below the lightcone analytically:

$$\frac{\rho_L(\omega, \vec{p})}{\omega} = c_1 \cdot \frac{\omega^2}{p^3} \Theta(p - \omega) \quad , \quad c_1 = \frac{\pi Q_s^2 \nu_s}{6} \quad (3.139)$$

$$\frac{\rho_T(\omega, \vec{p})}{\omega} = c_2 \cdot \frac{1}{p} \left(1 - \frac{\omega^2}{p^2}\right) \Theta(p - \omega) \quad , \quad c_2 = \frac{\pi Q_s^2 \nu_s}{12} \quad . \quad (3.140)$$

The resulting spectral functions scaled by frequency and normalized to unity in the limits of vanishing frequency and momentum are shown in Fig. 3.8 both in the free and the interacting case. Note here that the parameters are rescaled via

$$\mu_F \equiv \frac{g^2 C_F m_D^2}{8\pi} \log(T/m_D) \quad \text{to} \quad \omega' = \omega T / \mu_F \quad \text{and} \quad \bar{k} = |p| T / \mu_F \quad . \quad (3.141)$$

As such the parameters are not directly compatible with those invoked in the Langevin formalism or those generally used in this work. Nevertheless comparing Fig. 3.8 and Fig. 3.7 note the shape of the curves in the longitudinal channel are in fact very similar for both cases. One particularly encouraging result is that in the case of vanishing momentum all models seem to be well described by a simple Breit-Wigner form. This solidifies the idea that the transport contribution in the vector current-current channel may be modeled by a Breit-Wigner peak.

### 3.3 Hard Thermal Loops and Alternative Approaches

Even though our aim here is the calculation of ultimately non-perturbative effects from ab initio conditions, the above examples have shown the usefulness of model calculations. Additionally perturbative techniques are among the most efficient and highly advanced methods at our disposal and great successes have been made in extending its regime of validity also in QCD. One such effort is given by the hard thermal loop resummation scheme, another by exploiting the gauge/gravity correspondence of string theory.

#### 3.3.1 Dileptons from Hard Thermal Loops

In finite temperature perturbative QCD one has to differentiate between hard momenta of the order of  $\mathcal{O}(T)$  and soft momenta  $\mathcal{O}(gT)$ . It can be shown that if all momenta in a perturbative expansion are hard, ordinary perturbation theory applies and loop corrections are suppressed by two powers in the strong coupling  $\mathcal{O}(g^2)$  [80]. If on the other hand there is a soft momentum involved additional loop corrections at  $\mathcal{O}(g)$  arise and are of the same magnitude as the tree-level amplitudes [30, 31, 80]. The essential ingredient of the hard thermal loop scheme is to resum these hard thermal loop corrections in order to include all leading order effects in  $\mathcal{O}(g)$  [80]. In our case this implies the free propagator introduced in Eq. 3.33 is replaced by a resummed hard thermal loop effective propagator. The rest of the calculation may then follow the general scheme outlined in Chp. 3.1.1.

The effective hard thermal loop propagator reads [35, 80]:

$$\rho_F^{HTL}(K) = \frac{1}{2} \left( \rho_+(K) (\gamma_0 - i \frac{\vec{k}}{|\vec{k}|} \vec{\gamma}) + \rho_-(K) (\gamma_0 + i \frac{\vec{k}}{|\vec{k}|} \vec{\gamma}) \right) , \quad (3.142)$$

where

$$\rho_{\pm}(k_0, k) = \frac{k_0^2 - k^2}{2m_T^2} [\delta(k_0 - \omega_{\pm}) + \delta(k_0 + \omega_{\mp})] + \beta_{\pm}(k_0, k) \Theta(k^2 - k_0^2) , \quad (3.143)$$

and

$$\beta_{\pm}(k_0, k) = -\frac{m_T^2}{2} (\pm k_0 - k) \left( \left[ \frac{\pi m_T^2}{2} \frac{\pm k_0 - k}{k} \right]^2 + \left[ k(-k_0 \pm k) + m_T^2 \left( \pm 1 - \frac{\pm k_0 - k}{2k} \ln \left[ \frac{k + k_0}{k - k_0} \right] \right) \right]^2 \right)^{-1} , \quad (3.144)$$

whereby  $m_T(T) = g(T)T/\sqrt{6}$  denotes the thermal mass. Clearly the spectral density of the fermions is much more complicated in the HTL-scheme compared to the free case, first of all there are two separate dispersion relations [35, 80] in the thermal medium denoted by  $\omega_{\pm}(k)$ . These two branches represent the propagation of quarks in the medium ( $\omega_+(k)$ ) and a propagating collective mode that does not have an analog at zero temperature ( $\omega_-(k)$ ). Additionally however there is a branch cut from below the lightcone, it can be shown that this contribution results from the interaction of valence

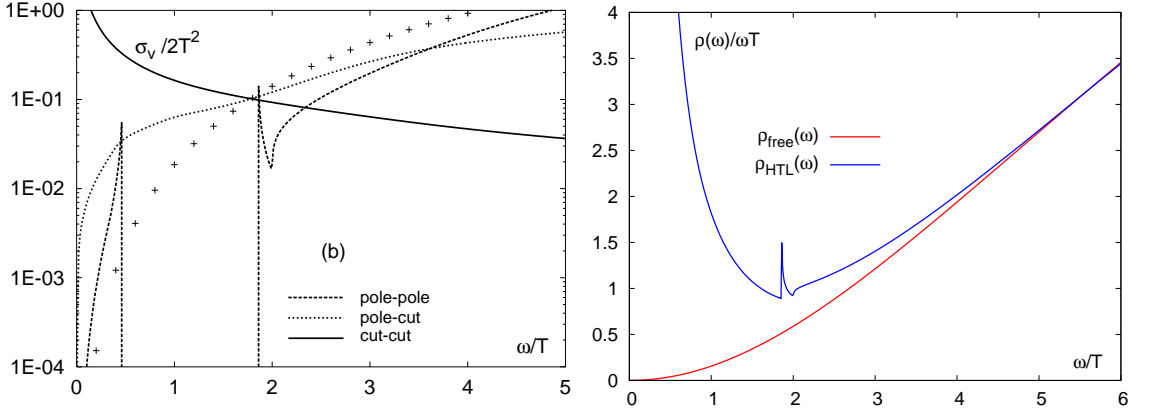


Figure 3.9: *Left: The pole-pole, pole-cut and cut-cut contributions to the vector spectral function ( $\sigma(\omega) = \rho(\omega)$ ) from hard thermal loops at  $m_T/T = 1$ , the free vector spectral function is shown for comparison and given by the crosses. Figure taken from [81]. Right: The full hard thermal loop spectral function in  $1/\omega$  compared to the free continuum at  $m_T/T = 1$ .*

quarks with the thermal gluons and corresponds to Landau damping [30, 35, 80].

As a consequence of these different contributions to the fermion spectral function the desired vector meson spectral function is made up of three distinct contributions:

$$\rho_{HTL}(\omega) = \rho_{\text{pole-pole}}(\omega) + \rho_{\text{pole-cut}}(\omega) + \rho_{\text{cut-cut}}(\omega) \quad . \quad (3.145)$$

Nevertheless the calculation can be done [35] for the dilepton rate and using Eq. 1.21 the spectral function can be computed:

$$\begin{aligned} \rho_{HTL}(\omega) &= \frac{4 \cdot N_c}{\pi^2} (e^{\omega/T} - 1) \int k^2 dk \int dx \int dx' n_F(x) n_F(x') \delta(\omega - x - x') \\ &\times \left[ 4 \left( 1 - \frac{x^2 - x'^2}{2k\omega} \right)^2 \rho_+(x, k) \rho_-(x', k) \right. \\ &\quad + \left( 1 + \frac{x^2 + x'^2 - 2k^2 - 2m^2}{2k\omega} \right)^2 \rho_+(x, k) \rho_+(x', k) \\ &\quad + \left( 1 - \frac{x^2 + x'^2 - 2k^2 - 2m^2}{2k\omega} \right)^2 \rho_-(x, k) \rho_-(x', k) \\ &\quad + \Theta(k^2 - x^2) \frac{m_q^2}{4k\omega^2} \left( 1 - \frac{x^2}{k^2} \right) \\ &\quad \left. \times \left( \left( 1 + \frac{x}{k} \right) \rho_+(x', k) + \left( 1 - \frac{x}{k} \right) \rho_-(x', k) \right) \right] \quad . \quad (3.146) \end{aligned}$$

The resulting contributions to the spectral function and the full result at  $m_T = 1$  are shown in Fig. 3.9. Clearly the pole-pole, pole-cut and cut-cut yield very different contributions to the spectral function and we refer the reader to [35, 80] and [81] for detailed discussions. At this point we are only interested in the full result on the right of

Fig. 3.9. For large frequencies the hard thermal loop result approaches the free continuum one, while it diverges at low frequencies and especially does not yield a finite value at  $\omega \rightarrow 0$ , this phenomenon however has been well studied and is due to the order of accuracy in the hard thermal loop scheme as higher and higher orders in  $\mathcal{O}(g^n T)$  contribute. The peaks visible in the full result are known as van-Hove singularities and it would be interesting to see whether the lattice might confirm the existence of the latter. In this work however we are far away of achieving this.

#### 3.3.2 Spectral Functions from *AdS/CFT* Correspondence

The *AdS/CFT* correspondence is the best understood gauge/gravity correspondence and to date the most successful invocation of the holographic principle.

The idea of the holographic principle was first introduced by 't Hooft [82] and later put into a string theory context by Susskind [83]. Whereby the initial spark to its formulation came from the study of black holes. Here the well known Bekenstein-Hawking entropy formula [84] suggested the entropy of a black hole is in fact proportional to the area  $A$  of its boundary and not its volume:

$$S_{BH} = A \cdot \frac{k_B}{4\sqrt{G\hbar}/c^3} \quad . \quad (3.147)$$

The idea that the information content of a gravity system is not proportional to its volume caused a lot of puzzlement for many years. Ultimately however it led to the formulation of the holographic principle, which states that the gravity description of a volume of space can be thought of as encoded on a boundary to the region by some other theory. So a  $d$ -dimensional gravity theory may be described by a  $d - 1$ -dimensional theory on its boundary.

In type IIB string theory in an  $AdS_5 \times S_5$  background it could be shown [85] that after compactification of the  $S_5$ -spheres, so they do not contribute any more, there is indeed such a boundary theory. Moreover it could be shown that this theory is in fact four dimensional  $\mathcal{N} = 4$  SYM theory [85].

Hereby the parameters of the field theory, i.e. the number of colors  $N_c$  and the coupling  $g^2$ , could be directly related to those of string theory in the *AdS*-space-time. This duality between string theory and field theory can be shown to be strongest when the coupling  $g^2$  is small but the 't Hooft coupling is large  $\lambda = g^2 N_c$ . In this situation the former limit suppresses the loops in string theory and the latter suppresses the stringy effects, effectively reducing string theory to supergravity. As a consequence the weakly coupled supergravity theory may be used to compute strongly coupled  $\mathcal{N} = 4$  SYM theory. Additionally placing the string equivalent of a black hole into the *AdS* space-time it is possible to set the temperature of the system and to naturally study finite temperature effects in  $\mathcal{N} = 4$  SYM theory.

With such a setup in hand it is possible to derive the spectral functions of finite

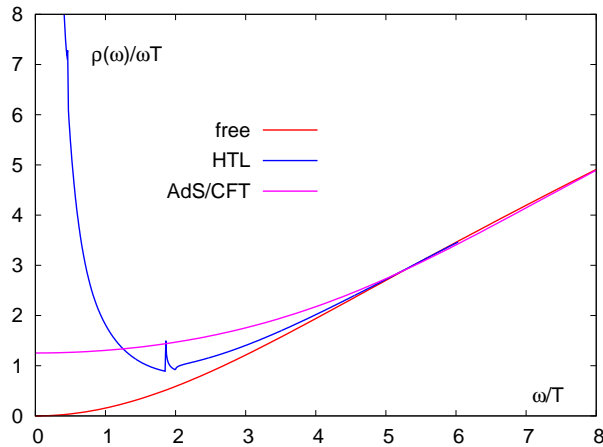


Figure 3.10: *The spectral function from AdS/CFT. Note the shown result is Eq. 3.148 with  $N_c = 3$  and adjusted to match the free continuum result for large frequencies. For comparison the free spectral function and the HTL result at  $m_T/T = 1$  is also given.*

temperature strongly coupled  $\mathcal{N} = 4$  SYM theory in the large  $N_c$  limit explicitly [86]:

$$\rho(\omega) = \frac{N_c^2}{16\pi} \cdot \frac{\omega^2 \sinh(\omega/2T)}{\cosh(\omega/2T) - \cos(\omega/2T)} \quad , \quad (3.148)$$

leading to the conductivity

$$\frac{\sigma}{T} = \frac{N_c^2}{16\pi} \quad . \quad (3.149)$$

Setting  $N_c = 3$  and rescaling to fit the free continuum result this spectral function is shown in Fig. 3.10. Even though the conductivity is not a universal parameter and thus depends on the theory under consideration, it is interesting nevertheless to see what happens to it in a strongly coupled setting [87]. Comparing the lines from hard thermal loops and *AdS/CFT* in Fig. 3.10 the lack of a transport peak in the low frequency region is immediately apparent. The lack of the latter would imply that the strongly coupled theory does not admit a quasiparticle interpretation [88] and it is subsequently interesting to see whether or not strongly coupled QCD shares similar features.

# Lattice Methodology

After these points on the spectral function let us turn to the actual methods on the lattice that are needed to calculate the latter.

From finite temperature quantum field theory and statistical physics it is clear that thermal expectation values of observables are given by [41–47]:

$$\langle \hat{O} \rangle = \frac{1}{\hat{Z}_{QCD}} \int d\hat{A} d\bar{\Psi} d\hat{\Psi} \cdot \hat{O} \cdot \exp[-\hat{S}_{QCD}] \quad (4.1)$$

The observables of interest in this thesis are the vector current-current correlation functions defined in Eq. 3.26 on the lattice, thus write:

$$\begin{aligned} G_{\mu\nu}(\tau, \vec{x}) &= \langle J_\mu(\tau, \vec{x}) J_\nu^\dagger(0, \vec{0}) \rangle \\ &= \frac{1}{\mathcal{Z}} \int DU D\bar{\Psi} D\Psi \left( \bar{\Psi}(\tau, \vec{x}) \gamma_\mu \Psi(\tau, \vec{x}) \right) \left( \bar{\Psi}(0, 0) \gamma_\nu^\dagger \Psi(0, 0) \right) \cdot \exp[-S] \\ &= \frac{1}{\mathcal{Z}} \int DU D\bar{\Psi} D\Psi \left( \text{Tr} \left[ M^{-1}(\tau, \vec{x}; 0, \vec{0}) \gamma_\mu M^{-1}(0, \vec{0}; \tau, \vec{x}) \gamma_\nu^\dagger \right] \right. \\ &\quad \left. - \text{Tr} \left[ \gamma_\nu^\dagger M^{-1}(0, \vec{0}; 0, \vec{0}) \right] \text{Tr} \left[ \gamma_\mu M^{-1}(\tau, \vec{x}; \tau, \vec{x}) \right] \right) \cdot \exp[-S] \quad , \quad (4.2) \end{aligned}$$

whereby the first summand of the above equation corresponds to connected, while the second corresponds to disconnected diagrams in the correlation function.

However the contributions from the disconnected diagrams are parametrically small. This can be argued from high temperature perturbation theory. Here they give rise to the small difference of quark number and isospin susceptibilities, as they occur at  $\mathcal{O}(g^6 \ln 1/g)$  in the perturbative expansion and only show close to the critical temperature  $T_c$  [77, 89].

Additionally the contribution of the disconnected diagrams vanishes for three degenerate quark flavors in the calculation of the electromagnetic current:

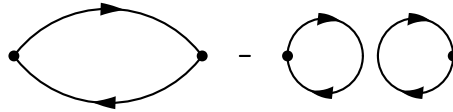


Figure 4.1:  $G(\tau, \vec{x})$  is made up of connected and disconnected diagrams.

$$J_{em} = \sum_q Q_q \bar{\Psi}_q(\tau, \vec{x}) \gamma_\mu \Psi_q(\tau, \vec{x}) \quad , \quad (4.3)$$

here the contribution can be shown [77, 90] to be proportional to  $\sim (\sum_q Q_q)^2$ , while the connected part is proportional to  $C_{em} = \sum_q Q_q^2$ .

As a consequence we will restrict our discussion to the connected diagrams of Eq. 4.2, the path integral in the case of two light quark flavors that is to be evaluated is:

$$G_{\mu\nu}(x_\mu) = \frac{1}{\mathcal{Z}} \int DU \text{Tr} \left[ M[U]^{-1}(x_\mu; 0) \gamma_\mu M[U]^{-1}(0; x_\mu) \gamma_\nu^\dagger \right] \det[M[U]]^2 \exp[-S_G[U]]. \quad (4.4)$$

In the quenched approximation the term  $\det[M[U]]^2 = 1$  as described before. Thus the fermion matrix must be handled solely when computing the fermion propagator.

## 4.1 Lattice Correlation Functions and the Kernel

The connection between the lattice correlation function and the spectral function is given by Eq. 3.30:

$$G(\tau) = \int_0^\infty \frac{d\omega}{2\pi} \rho(\omega) K(\tau, \omega) \quad (4.5)$$

where the kernel  $K(\tau, \omega)$  is given by:

$$K(\tau, \omega) = \frac{\cosh(\omega(\tau - 1/2T))}{\sinh(\omega/2T)} \quad , \quad (4.6)$$

as noted before it may be interpreted as the free boson propagator [29] and the spectral function determines spectral distribution. Consequently the kernel is fixed and it is important to understand its effect on the correlation functions we will compute on the lattice.

To this extent notice the kernel may be rewritten in the limit of very large frequencies:

$$K(\tau, \omega) = \frac{\cosh(\omega(\tau - 1/2T))}{\sinh(\omega/2T)} \xrightarrow{\omega \gg 0} \exp[-\omega\tau] \quad . \quad (4.7)$$

This implies the kernel suppresses the high frequency region of the spectral function in Eq. 4.5 and subsequently the correlator is largely insensitive to the high  $\omega$ -region. For completeness note the same situation arises in the limit  $T \rightarrow 0$ , as there the kernel may be rewritten in the same fashion.

## 4.1 Lattice Correlation Functions and the Kernel

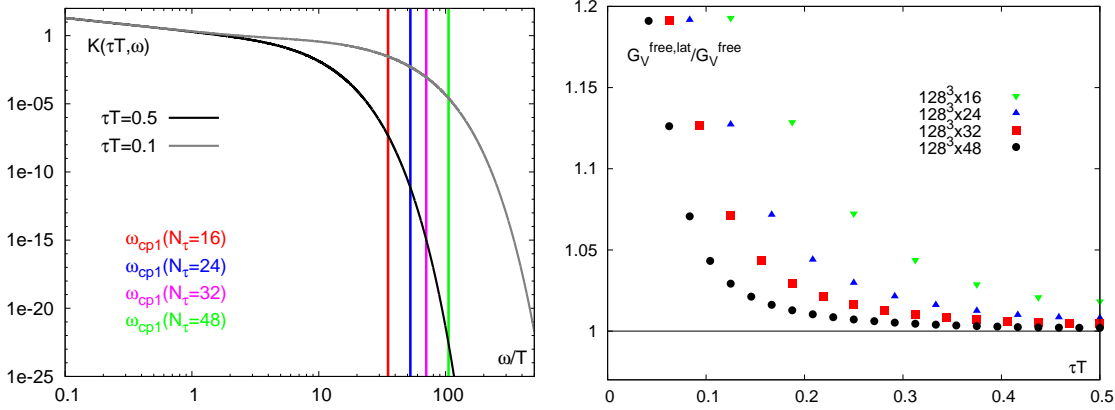


Figure 4.2: Left: The kernel  $K(\tau T, \omega/T)$  at  $\tau T = 0.1$  (grey) and  $\tau T = 0.5$  (black) in a double logarithmic plot. The vertical lines denote the cusp location  $\omega_{cp1}$  of the free lattice spectral function for  $N_\tau = 16, 24, 32$  and  $48$ . Right: The ratio of the free lattice and free continuum correlation functions for the same  $N_\tau$ .

Expanding the kernel in the low frequency region on the other hand gives [94]:

$$K(\tau, \omega) = \frac{2T}{\omega} + \left( \frac{1}{6T} - \tau + T\tau^2 \right) \omega + \mathcal{O}(\omega^3) \quad , \quad (4.8)$$

clearly this expression diverges as  $\mathcal{O}(1/\omega)$ . Then time dependence only goes as  $\tau \cdot \omega$ , as the contribution  $T\tau^2 \cdot \omega$  is suppressed given typical Euclidean times  $\tau T \in [0.1 : 0.5]$ . As such the kernel exhibits only very weak time dependence in the region of low frequencies.

In Fig. 4.2(left) we show the kernel  $K(\tau T, \omega/T)$  in a double logarithmic plot for  $\tau T = 0.1$  (grey) and  $\tau T = 0.5$  (black), as such the two values constitute the edges of the Euclidean time window of a typical correlator. For frequencies  $\omega/T \lesssim 4$  the kernel is seen to be the same over the entire time window, given the scales of the figure. Beyond  $\omega/T \simeq 4$  on the other hand it starts to diverge and fall rapidly, consequently the kernel highly suppresses the high frequency behavior of the spectral function in the correlator computed from Eq. 4.5. To illustrate the effect this has on the full integrand we also show the location of the dominant cusp in the free lattice spectral function  $\omega_{cp1}$ , see also Fig. 3.5. Comparing the strength of the suppression of the kernel and the location of  $\omega_{cp1}$  it becomes apparent that for  $\tau T = 0.5$  the contribution of the spectral function at  $\omega_{cp1}$  on the  $N_\tau = 16$  lattice gets a suppression factor of the order  $\mathcal{O}(10^{-5})$  and even  $\mathcal{O}(10^{-25})$  for  $N_\tau = 48$ . With such large suppression factors we can quite safely conclude that the high frequency behavior of the correlator at  $\tau T = 0.5$  is effectively cut off and all the information originates from the low and intermediate frequency regions.

However this is only the midpoint, at smaller Euclidean times and ultimately  $\tau T = 0.1$  we see that the suppression factor from the kernel weakens and becomes  $\mathcal{O}(10^{-5})$  for  $N_\tau = 48$  and even  $\mathcal{O}(1)$  for  $N_\tau = 16$ . So across the time window the high frequency part and thus the lattice discretization effects gain in importance in the integrand of

Eq.4.5. In the following we will therefore choose carefully the region where we might safely assume the high frequency, discretization effects to be of a subleading order. The above argument is shown once more in Fig.4.2(right), where we show the ratio of the free lattice to free continuum correlation function. The deviation decreases with increasing Euclidean time, however we also see that the  $N_\tau = 16$  lattice is contaminated with discretization effects through the entire time window. Here the large suppression factor from the kernel is not enough to cut off the high frequency contributions.

The large suppression of the high frequency region due to the kernel implies the correlation function is in fact mostly determined by the low to intermediate frequency domain. Even though this is exactly the region we wish to explore this result does not simplify the problem. To see this remember that the correlation function is indeed only dependent on Euclidean time and momentum  $G(\tau, \vec{p})$ , as the frequencies are integrated out. However returning to our discussion of the low frequency behavior of the kernel and its time dependence, we see that in the region  $\omega/T \lesssim 4$  in Fig.4.2(left) the time dependence is not clearly visible as the linear difference  $\omega\tau$  is swallowed by the Euclidean time independent divergence of the kernel, as expected. Consequently the weak time dependence in  $G(\tau, \vec{p})$  makes it difficult to extract details of the contributing spectral function, as the correlator at any  $\tau$  essentially shows the same information, also in the interacting case. As such extracting the detailed shape of the transport peak from the correlator alone is very difficult.

## 4.2 Thermal Moments of the Correlation Function

Given the physics effects we are interested in here contribute at low frequencies and the weak Euclidean time dependence entailing a weak signal of the detailed structure of spectral functions in the correlator, one is prompted to motivate observables that might be more sensitive to the region of low frequencies  $\omega$  that we wish to explore.

One such possibility is the calculation of the thermal moments of the correlation functions defined as:

$$\begin{aligned} G_H^{(n)} &= \frac{1}{n!} \left. \frac{d^n G_H(\tau T)}{d(\tau T)^n} \right|_{\tau T=1/2} \\ &= \frac{1}{n!} \int_0^\infty \frac{d\omega}{2\pi} \left( \frac{\omega}{T} \right)^n \frac{\rho_H(\omega)}{\sinh(\omega/2T)} \quad , \end{aligned} \quad (4.9)$$

where  $H = ii, V, P$  and  $n = \text{even}$ . Note all odd moments vanish as the spectral functions as well as the integration kernel in the spectral representation of the correlators are odd functions of the frequency.

Subsequently the thermal moments define the Taylor expansion coefficients of the expansion of the correlation function around the temporal midpoint of the Euclidean lattice

## 4.2 Thermal Moments of the Correlation Function

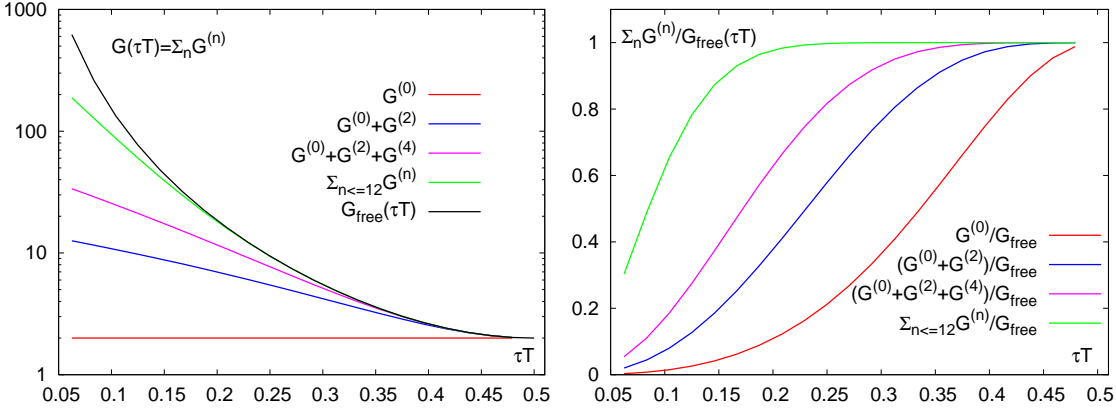


Figure 4.3: *Left: The free correlator made up of the sum of thermal moments to a varying degree in summands. The black curve denotes the full analytic result. Right: The deviation of the thus obtained correlator to the free case.*

correlator:

$$G_H(\tau T) = \sum_{n=0}^{\infty} G_H^{(n)} \left( \frac{1}{2} - \tau T \right)^n . \quad (4.10)$$

When computing the thermal moment defined in Eq. 4.9 the spectral function is weighted by a term with a maximum at  $\tanh(\omega/2T) = \omega/2nT$ . This implies the  $n$ -th order moment is most sensitive to the spectral function in the region where  $\omega/T \simeq 2n$ , contributions from higher order moments should be thus closer to their perturbative counterparts. Furthermore the lowest order moments  $n = 0, 2, 4$  are then expected to be most sensitive to the low  $\omega$ -region of the spectral function. Consequently the corrections due to higher orders should be highly suppressed in the correlator at large Euclidean times.

To illustrate Eq. 4.10 we show the thus obtained correlator partially summing to  $n = 0, 2, 4, 12$  compared to the free correlation function in Fig. 4.3, on the left directly and via the ratio  $G_{\text{partial}}(\tau T) / G_{\text{free}}(\tau T)$  on the right. The dominance of the lowest thermal moments at large distances  $\tau T$  is nicely revealed, as most of the correlation function at  $\tau T \gtrsim 0.38$  is given in terms of the zeroth and second thermal moments.

In the infinite temperature, free field limit the correlation function is known analytically, as was shown in Chp. 3.1.2. For massless quarks recall:

$$\begin{aligned} G_V^{\text{free}}(\tau T) &= 6T^3 \left( \pi(1 - 2\tau T) \frac{1 + \cos^2(2\pi\tau T)}{\sin^3(2\pi\tau T)} + 2 \frac{\cos(2\pi\tau T)}{\sin^2(2\pi\tau T)} \right) \\ G_{ii}^{\text{free}}(\tau T) &= T^3 + G_V^{\text{free}}(\tau T) \\ G_{PS}^{\text{free}}(\tau T) &= \frac{1}{2} G_V^{\text{free}}(\tau T) . \end{aligned} \quad (4.11)$$

Consequently the first three non-vanishing moments become:

$$G_V^{(0),free} = 2G_{PS}^{(0),free} = \frac{2}{3}G_{ii}^{(0),free} = 2T^3 \quad (4.12)$$

$$G_H^{(2),free} = 2G_{PS}^{(2),free} = \frac{28\pi^2}{5}T^3 \quad (4.13)$$

$$G_H^{(4),free} = 2G_{PS}^{(4),free} = \frac{124\pi^4}{21}T^3 \quad (4.14)$$

At this point also define the ratios of moments given by:

$$R_{V,free}^{(2,0)} = \frac{G_V^{(2),free}}{G_V^{(0),free}} = R_{PS,free}^{(2,0)} = \frac{14\pi^2}{5} \simeq 27.635 \quad (4.15)$$

$$R_{ii,free}^{(2,0)} = \frac{2}{3}R_{V,free}^{(2,0)} \simeq 18.423 \quad (4.16)$$

$$R_{H,free}^{(4,2)} = \frac{155\pi^2}{147} \simeq 10.407 \quad (4.17)$$

Note also that  $G_{ii}^{(n)} = G_V^{(n)}$  for all  $n > 0$  at all values of the temperatures as the correlators differ only by the constant contribution originating from the time-time correlator  $G_{00}(\tau T)$  that is connected to the quark number susceptibility  $\chi_q(T)$ , as noted in Chp. 3.2. While in the free case  $G_{ii}(\tau T)$  contains a constant contribution that drops out in the calculation of the higher moments, this is no longer the case at finite values of the temperature. All thermal moments  $G_H^{(n)}$  with  $n \geq 0$  will be sensitive to the thermal modification of the  $\delta$ -function contribution of  $\rho_{ii}(\omega)$ . Following the above reasoning we nevertheless expect this contribution to be more and more suppressed in higher order thermal moments.

The correlation function is dominated by an exponential decay, see e.g. Eq. 3.65. To cancel this contribution we will analyze the ratio of  $G_H(\tau T)$  and the free field correlator  $G_H^{free}(\tau T)$  in the following:

$$\frac{G_H(\tau T)}{G_H^{free}(\tau T)} = \frac{G_H^{(0)}}{G_H^{(0),free}} \left( 1 + (R_H^{(2,0)} - R_{H,free}^{(2,0)}) \left( \frac{1}{2} - \tau T \right)^2 + \dots \right) \quad (4.18)$$

As the thermal moments are defined by derivatives of the correlation function, the ratio of midpoint subtracted correlation functions gives a more direct handle on the second and higher orders:

$$\begin{aligned} \Delta_H(\tau T) &\equiv \frac{G_H(\tau T) - G_H^{(0)}}{G_H^{free}(\tau T) - G_H^{(0),free}} \\ &= \frac{G_H^{(2)}}{G_H^{(2),free}} \left( 1 + (R_H^{(4,2)} - R_{H,free}^{(4,2)}) \left( \frac{1}{2} - \tau T \right)^2 + \dots \right) \quad (4.19) \end{aligned}$$

### 4.3 An Ill Posed Problem and its Bayesian Solution

As a consequence the curvature of these ratios at the midpoint determines the deviation of ratios of the thermal moments from the corresponding free field values. In the subtracted correlation function the additional constant contributing to  $G_V(\tau T)$  drops out and subsequently  $H = ii$  and  $H = V$  degenerate. The ratio of the correlation functions on the other hand differ:

$$\frac{G_V(\tau T)}{G_V^{free}(\tau T)} \neq \frac{G_{ii}(\tau T)}{G_{ii}^{free}(\tau T)}, \quad \Delta_V(\tau T) = \Delta_{ii}(\tau T) \quad \text{and} \quad G_V^{(n)} = G_{ii}^{(n)} \quad \text{for } n > 0 \quad (4.20)$$

These relations and the special sensitivity of the thermal moments on the low frequency region of the spectral function give us a new handle on the expected in-medium modification of the latter. As such they will prove very useful in the following.

### 4.3 An Ill Posed Problem and its Bayesian Solution

Given the correlation function from the lattice the spectral function may be directly computed via inversion of the relation of Eq. 3.30:

$$\begin{aligned} G(\tau) &= \int_0^\infty \frac{d\omega}{2\pi} \rho(\omega) \frac{\cosh(\omega(\tau - 1/2T))}{\sinh(\omega/2T)} \\ &\xrightarrow{T \rightarrow 0} \int_0^\infty \frac{d\omega}{2\pi} \rho(\omega) \exp[-\omega\tau] \\ \Rightarrow \rho(\omega) &= \mathcal{F}^{-1}(G(\tau)) \quad , \end{aligned} \quad (4.21)$$

where  $\mathcal{F}^{-1}$  denotes the inverse transformation. As mentioned before for large frequencies  $\omega \gg 0$  or at zero temperature this is the inverse Laplace transform. Numerically this is an ill-posed problem, which in the case of the inverse Laplace transform is subject of intense mathematical research [23].

Put simply the resulting spectral functions should be continuous with an order of degrees of freedom  $\sim \mathcal{O}(1000)$  but the correlators computed on the lattice only have an order of  $\sim \mathcal{O}(10)$  points that can be used as input. Consequently there is an infinite number of solutions to Eq. 4.21.

However, even if it were feasible to compute the correlation function with  $\sim \mathcal{O}(1000)$  points this does not solve the problem, as the data naturally possess errors. In the case of the inverse Laplace transform it can be shown mathematically [91] that the possible errors in the spectral function resulting from the imprecise correlator data only decrease logarithmically. This implies improving the accuracy of the spectral function is in fact exponentially computationally expensive.

To see this write the data as  $G(\tau) = G_{true}(\tau) + \delta G(\tau)$ , then let the 'error-spectral function'  $\delta\rho(\omega)$  correspond to  $\delta G(\tau)$ . Now let the data satisfy a quality criterion, while also limiting the oscillations of the error-spectral function [23, 91]:

$$\int_0^\infty d\tau |\delta G(\tau)|^2 \leq \epsilon^2 \quad \text{and} \quad \int_0^\infty d\omega \omega |\delta\rho(\omega)|^2 \leq E^2 \quad (4.22)$$

The size of the set of solutions  $S = \{\delta\rho\}$  can then be shown to satisfy the lower bound:

$$\sup_{\delta\rho \in S} \|\delta\rho\| \gtrsim \frac{\pi E}{2|\log(\epsilon/E)|} \quad (4.23)$$

As noted above the accuracy thus only decreases logarithmically in the quality of the correlator data.

Taken together these two statements immediately imply that to compute the spectral function via Eq. 4.5 large lattices and highly accurate data are needed. As such the analysis in this thesis presents results of the largest today feasible quenched lattices with  $N_\sigma = 128$  and  $N_\tau = 48$  with accuracies below the 1%-level. A full dynamical calculation is forbidding at this time also due to these additional constraints.

### 4.3.1 Maximum Entropy Method

One possibility to nevertheless solve Eq. 4.5 given the lattice data with errors is to resort to a Bayesian method [92, 93]. Thus we are satisfied with computing the best solution to Eq. 4.5 given some criterion, for example we could require the best solution to be the most probable or “average” of the latter.

In our specific case Bayes’ theorem states that the most probable spectral function can be found by maximizing the posterior probability defined as [93]:

$$P[\rho|GH] = \frac{P[G|\rho H]P[\rho|H]}{P[G|H]} \quad , \quad (4.24)$$

here  $\rho$  is the desired spectral function, while  $G$  denotes the data with errors and  $H$  prior input information. Generally  $P[\rho|GH]$  is called the posterior probability, as noted above,  $P[G|\rho H]$  the likelihood function,  $P[\rho|H]$  the prior probability and  $P[G|H]$  the evidence. As a consequence the problem of computing the spectral function is reduced to specifying the likelihood function and the prior probability [22, 93].

In the case of the likelihood function this can be done by following the central limit theorem. The functional form of  $P[G|\rho H]$  can be expressed by a standard  $\chi^2$ -distribution when the number of measurements  $N$  becomes large:

$$P[G|\rho H] \sim \exp[-L] = \exp\left[-\frac{\chi^2}{2}\right] \quad , \quad (4.25)$$

with

$$\chi^2 = \sum_{i,j}^{N_\tau/2} \left( \bar{G}(\tau_i) - F(\tau_i) \right) C_{ij}^{-1} \left( \bar{G}(\tau_j) - F(\tau_j) \right) \quad , \quad (4.26)$$

here  $\bar{G}(\tau_i)$  denotes the average over all measurements, while  $C_{ij}$  is given by the covariance matrix:

$$C_{ij} = \frac{1}{N(N-1)} \sum_{n=1}^N [G^n(\tau_i) - \bar{G}(\tau_i)][G^n(\tau_j) - \bar{G}(\tau_j)] \quad , \quad (4.27)$$

### 4.3 An Ill Posed Problem and its Bayesian Solution

$F(\tau_i)$  on the other hand is given in a discretized version by the trial spectral function  $\bar{\rho}(\omega)$  and the predefined kernel  $K(\tau_i, \omega)$ :

$$F(\tau_i) = \int_0^\infty d\omega K(\tau_i, \omega) \bar{\rho}(\omega) \simeq \sum_j \Delta\omega K(\tau_i, \omega_j) \bar{\rho}(\omega_j) \quad (4.28)$$

with  $\omega_j = j \cdot \omega$ . In principle what we described so far is at basis of the standard  $\chi^2$ - or least-squares fit procedure. In the standard approach the next step would be to maximize the likelihood function or equivalently minimize  $\chi^2$ .

However this method fails in our case as the number of input data points must be larger than the parameters to be fitted. The fit parameters here are the degrees of freedom of the spectral function and subsequently we run into the problem illuminated above.

The prior probability on the other hand cannot be derived as cleanly as the likelihood function, it must be motivated and many different possibilities exist in literature. In our case we choose the prior probability to be proportional to an entropy term:

$$P[\rho|H] \sim \exp[\alpha S] \quad , \quad (4.29)$$

where  $\alpha$  denotes a relative weight parameter between the likelihood function and the entropy. The entropy term  $S(\rho)$  is given by the Shannon-Jaynes Entropy:

$$S(\rho) = \int_0^\infty d\omega \left[ \rho(\omega) - m(\omega) - \rho(\omega) \ln \left( \frac{\rho(\omega)}{m(\omega)} \right) \right] \quad . \quad (4.30)$$

At this point  $m(\omega)$ , the so called default model, enters. As such it encodes all the prior information that we are able to specify for the system at hand. One advantage of this type of prior probability is that it enforces the positivity of the result spectral function, at the same time it allows one to specify prior knowledge about the spectrum explicitly through the default model.

As the evidence  $P[G|H]$  is independent of the spectral function, it only implies a normalization factor  $c_{GH}$ . Putting these three pieces of information together one arrives at the posterior probability by utilizing Eq. 4.24:

$$P[\rho|GH] = \exp[-L] \cdot \exp[\alpha S(\rho)] / c_{GH} \sim \exp[\alpha S(\rho) - L] := \exp[Q] \quad . \quad (4.31)$$

Subsequently the most probable spectral function can be found by maximizing  $P[\rho|GH] \sim \exp[Q]$  as function of the spectral function:

$$\alpha \nabla_{\rho_\alpha} S(\rho) - \nabla_{\rho_\alpha} L = 0 \quad (4.32)$$

As such this procedure to solve Eq. 3.30 numerically using Bayes' theorem is called the maximum entropy method (MEM).

Finally to reconstruct the spectral function the dependence on the weight parameter  $\alpha$  has to be specified. To do so once more invoke Bayes' theorem and the identity

$$P[G|m\alpha] = \int [d\rho_\alpha] P[G|\rho_\alpha m\alpha] P[\rho_\alpha|m\alpha] \quad (4.33)$$

and arrive at:

$$\begin{aligned} P[\alpha|Gm] &= \int [d\rho] P[G|\rho m \alpha] P[\alpha|m] P[\rho|m \alpha] / P[G|m] \\ &= \frac{1}{\alpha} \int [d\rho_\alpha] \exp[\alpha S(\rho_\alpha) - L] \end{aligned} \quad (4.34)$$

Using  $P[\rho_\alpha|G\alpha m] = P[\rho_\alpha|GH]$  and integrating over the wight parameter  $\alpha$  the result spectral function can be constructed:

$$\begin{aligned} \rho &= \int d\alpha \int [d\rho_\alpha] \rho_\alpha P[\rho_\alpha|G\alpha m] P[\alpha|Gm] \\ &\simeq \int d\alpha \rho_\alpha P[\alpha|Gm] \\ &= \int \frac{d\alpha}{\alpha} \rho_\alpha \int [d\rho_\alpha] \exp[\alpha S(\rho_\alpha) - L] \quad . \end{aligned} \quad (4.35)$$

As noted above using MEM it becomes possible to compute the most probable spectral function given the data with errors and prior information, parameterized in the default model. It should be noted that MEM is a highly successful procedure with applications in many areas ranging from high energy physics to image processing [93]. Naturally we will be most concerned employing it to compute the current-current spectral functions in lattice QCD and will highlight some of the specific challenges posed in this case below.

### 4.3.2 Remarks on the Bayesian solution

Computing spectral functions from meson correlation functions one is faced with some limitations of the maximum entropy method and we will discuss two of them in the following.

First recall that in the very low frequency region one may expand the integration kernel to read (Eq. 4.8):

$$K(\tau, \omega) = \frac{2T}{\omega} + \left( \frac{1}{6T} - \tau + T\tau^2 \right) \omega + \mathcal{O}(\omega^3) \quad , \quad (4.36)$$

this expression is clearly divergent at  $\omega = 0$  as mentioned before. When applying MEM this must be taken into account, as it will otherwise influence the spectral function one obtains [94, 95].

This divergence can be fairly simply removed by redefining the kernel before applying MEM:

$$\tilde{K}(\tau, \omega) = \tanh\left(\frac{\omega}{2}\right) \cdot K(\tau, \omega) \quad (4.37)$$

$$\tilde{\rho}(\omega) = \coth\left(\frac{\omega}{2}\right) \cdot \rho(\omega) \quad . \quad (4.38)$$

In principle one is free to choose any suitable redefinition as long as the correlator remains unmodified. One advantage of our choice is that it leaves the large frequency

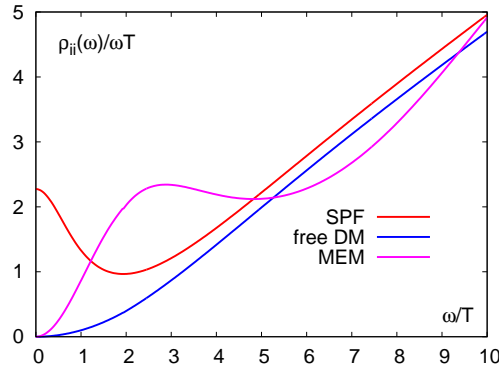


Figure 4.4: *Mockdata test of MEM to highlight its problems. Shown is the spectral function in units of  $1/\omega$ , the blue line shows the default model supplied to MEM, while the red line describes the input data. The magenta line represents the MEM result and deviates strongly from the expected shape.*

behavior of the kernel and the spectral function unchanged [95].

In practice a much more substantial drawback of the method is having to choose the default model itself. Naturally the spectral function should behave as in the free case at large enough frequencies or temperatures, however it is a priori not clear what the input should be in the interesting low frequency region.

Given the data with errors there will be thus dependence on the default model and the solution will not be unique. This is a systematic error introduced by MEM and there is no clear possibility to quantify this error.

To illustrate these issues we show a mocktest of MEM in Fig. 4.4. Here the method is given input data described by the spectral function denoted by SPF and choosing the free spectral function as default model (DM). Clearly the resulting spectral function obtained by MEM does not reproduce the input. In this case this is due to the exact zero at  $\omega = 0$  in the free spectral function and the algorithm behind MEM. Without going into too much detail note the spectral function that is to be computed may be written as [94]:

$$\rho(\omega) = m(\omega) \cdot \exp\left[\sum_j^N c_j u_j(\omega)\right] \quad , \quad (4.39)$$

where the functions  $u_j(\omega)$  are the basis functions of the discretized kernel  $K(\tau_j, \omega_j)$ . So clearly to enable a non-zero intercept at  $\omega = 0$  in the spectral function the default model is explicitly forbidden to vanish at this point. Thus using the free spectral function as input MEM models the result spectral function around this fixed point at  $\omega = 0$  compensating at higher frequencies for the mismatch.

Nevertheless MEM is a very powerful tool, that, given the proper care, can be used very

successfully and efficiently to obtain a feeling for the most dominant contributions to the spectral function from only minimal input knowledge. However the uncertainties induced by e.g the default model dependence lead to very large and undetermined errors on physics results. If one were basing a physics analysis solely on MEM, it is therefore best to put focus more on qualitative than quantitative results. A more qualitative question that one might successfully answer using MEM for example is the dissociation temperature of for instance charmonium, see e.g [22,96].

The direct consequence in this work is however that we will not use MEM as a direct tool to compute the spectral function from lattice a correlator. Instead we will develop an alternative route that does not rely on MEM, but at the same time may be augmented by it as a crosscheck.

## 4.4 An Alternative Route

Due to the insufficiencies of MEM it is desirable to develop and use an alternative approach, preferably one that is more controllable and has understandable systematic errors.

Here we revive and refine an older idea from [97], in a nutshell instead of using MEM it entails using a well motivated fit-Ansatz for the spectral function that is used to compute the correlator. This Ansatz naturally depends on a number of parameters, which are then straightforwardly fitted to the correlator data using a standard  $\chi^2$ -procedure.

As we are free to choose we can construct classes of fit-Ansätze that may be varied to explore the systematic effects induced by the choice of the specific Ansatz. Consequently this gives us maximum control but also maximum bias.

To minimize the bias the Ansatz must be chosen with extreme care. The correlator data must be evaluated very carefully, questions one needs to ask among others are:

- What and how strong are the effects of e.g. cut-off or finite size on the lattice?
- Is it possible to cleanly separate lattice effects from physics?
- Where is the data dominated by the perturbative/ the non-perturbative region?
- How well can the data be explained by known analytical solutions, e.g. the non-interacting case?
- Can second level observables such as the thermal moments contribute additional information that might be missed at first level?
- What are the model predictions in interacting theory? Are they compatible with the data obtained?

Once these questions have been discussed we can motivate an Ansatz and systematically vary it to describe all the data at hand simultaneously, in our case this means we fit the correlator data and the thermal moments in the same fit-routine. The subsequent result parameters give a fit-error and a quality criterion via the  $\chi^2/\text{d.o.f}$  of the fit-routine.

Systematically varying the Ansatz within a suitably defined Ansatz class we can in turn define also a more reliable systematic error. As a result parameters and spectral functions are obtained that contain a small standard error but also a systematic error that realistically encodes our gained knowledge.

In a next step the validity of the Ansatz class can be further confirmed by the maximum entropy method. As such the result spectral functions from the Ansatz method are used as default model for MEM, which will subsequently compute any corrections to the former. In this fashion MEM goes from a black box with difficult to control uncertainties to a tool that quantifies corrections to a systematically obtained result.

In the following analysis we follow the above outlined scheme and ultimately we successfully compute the vector spectral function, see also [1] and [2].



# The Vector Spectral Function at Vanishing Momentum

In the past the vector current correlation function was already calculated, so before turning to our new results we quickly review what has been achieved so far.

One of these past calculations was done using the same non-perturbatively improved clover action as used in this work, however on lattices of size  $64^3 \times 16$  [98]. A pure MEM analysis without improved Kernel was used to determine thermal dilepton rates which suggested a suppression of the spectral weight relative to the free spectral function at small energies.

Additionally the vector correlation functions at finite temperature were analyzed using staggered fermion formulations and a modified kernel was used in the MEM analysis [94, 99]. This modification of the MEM algorithm increased the sensitivity of MEM to the low energy structure of spectral functions and resolved part of the problems observed before. However as was shown above, it is also crucial in a MEM analysis to choose default models which allow for a linear slope of the spectral functions at small energies for MEM to be able to reproduce a realistic spectral function.

Calculations of vector spectral functions using staggered fermions are more involved, as two spectral functions, corresponding to different parity channels [100], need to be determined simultaneously [94, 99]. As such the staggered action is not particularly suited to extract the spectral function from the correlator.

The past studies were performed using lattices with temporal extent up to  $N_\tau = 14$  [99] and  $N_\tau = 24$  [94], respectively. They were performed with unrenormalized currents and primarily aimed at a determination of the (unrenormalized) electrical conductivity. They led, however, to quite different results,  $\sigma/T \simeq 7C_{em}$  [99] and  $\sigma/T \simeq (0.4 \pm 0.1)C_{em}$  [94].

Our aim here is to improve over these studies with staggered fermions as well as the analysis of the thermal dilepton rate performed with improved Wilson fermions. To achieve this goal we compute the desired meson correlation functions using Wilson-Clover fermions with unprecedented accuracy on very large lattices at varying values of the cut-off and volume. Whereby the large lattice sizes enable us to go to very small lattice spacing.

Ultimately we extrapolate the obtained results to the continuum limit, carefully checking the systematics and keeping the lattice errors under tight control and below the 1%-level.

Subsequently we compute the electrical conductivity and dilepton rates in the continuum of quenched QCD at  $T \simeq 1.45T_c$ , taking into account also the systematic errors that might arise from our analysis.

Going into more detail we have calculated the vector correlation function on lattices of size  $N_\sigma^3 \times N_\tau$ , with  $32 \leq N_\sigma \leq 128$  and  $N_\tau = 16, 24, 32$  and  $48$ . For  $N_\tau = 16$  we calculated  $G_H(\tau T)$  on lattices with spatial extent  $N_\sigma = 32, 64, 96$  and  $128$ . For  $N_\tau = 24$  we checked that the quark masses used in our calculations are indeed small enough on the scale of the temperature to be ignored in the analysis of our correlation functions. On the largest spatial lattice,  $N_\sigma = 128$ , we performed calculations for four different values of the lattice cut-off by choosing  $N_\tau = 16, 24, 32$  and  $48$  and at the same time changing the value of the gauge coupling  $\beta$  such that the temperature is kept constant,  $T \simeq 1.45T_c$ . Finally we varied the temperature at  $N_\sigma = 128$  keeping the cut-off scale fixed and varying the temporal extent  $N_\tau = 16, 32$  and  $40$ , corresponding to the respective temperatures  $T \simeq 3.0T_c, 1.45T_c$  and  $1.2T_c$ .

As will be shown in the following it is indeed possible to systematically examine the finite-size effects, as the large range of spatial lattice sizes used in this calculation,  $2 \leq N_\sigma/N_\tau \leq 8$ , allows to quantify finite volume effects at fixed values of the lattice cut-off,  $aT = 1/N_\tau$ . At the same time we are able to reduce the lattice spacing at  $T \simeq 1.45T_c$  to about  $0.01\text{fm}$ . As a result the variation of the cut-off, i.e. lattice spacing by a factor three gives us good control over lattice cut-off effects in our calculation. We are subsequently capable of carrying out the continuum extrapolation both for the correlation function and its thermal moments. As a consequence we are able to compute the electrical conductivity of the quark gluon plasma and the dilepton rate at unprecedented accuracy with secure control over the systematic effects influencing our result.

## 5.1 The Vector SPF and Dilepton Rate in the Continuum at $T \simeq 1.45T_c$

To begin our discussion let us first turn to the full vector correlation function  $G_V(\tau T)$ . In Fig. 5.1 we show the correlation function on the lattices at fixed temperature  $T \simeq 1.45T_c$  and spatial extent  $N_\sigma = 128$  together with their free continuum and free lattice counterparts. Here the open symbols denote the free lattice correlators, while the magenta line gives the free continuum. Clearly the exponential decay of the correlation function dominates and obscures more subtle effects.

Nevertheless a large deviation of the correlator from the free case is naturally possible, as is the case in the confined phase of QCD. Here, however, the correlator is seen to be very close to the free field limit, implying that a spectral description based on or incorporating the free behavior is a good starting point.

In the following therefore it will be useful to cancel the dominant exponential decay of the correlator by normalizing with the free continuum or lattice counterparts. As will be seen such a ratio efficiently reveals the more subtle physics in the correlation functions

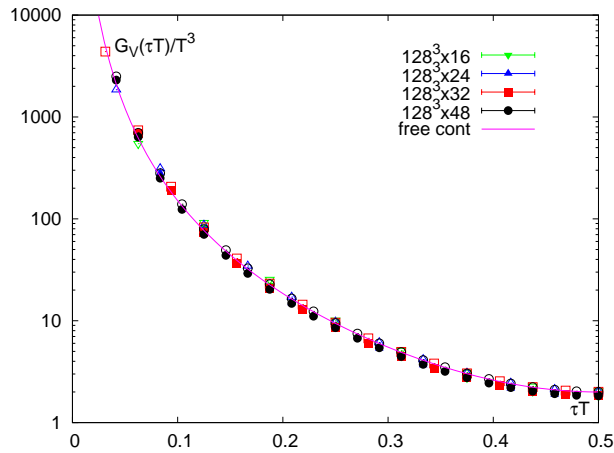


Figure 5.1: The full vector correlation function  $G_V(\tau T)$  at  $T \simeq 1.45T_c$  and varying cut-off scale. The free continuum (magenta lines) and free lattice (open symbols) are given for reference.

and, especially interesting for us, the contribution originating from the transport region of the spectral function.

### 5.1.1 The Spectral Function of the Time-Time Vector Correlator

As was discussed in more detailed in Chp. 3.2 the spectral function of the time-time correlation function  $G_{00}(\tau T)$  can be deduced from rather general arguments.

There it could be shown that the time-time correlation function is connected to the conserved net quark number  $\langle n \rangle = 0$  through the quark number susceptibility [89]. Recall the time-time correlation function of the vector current given by Eq. 3.94 and write

$$-G_{00}(\tau T, \vec{p} = 0)/T^3 = \chi_q/T^2 \quad . \quad (5.1)$$

It is apparent that to verify the shape of the spectral function is to verify  $-G_{00}(\tau, \vec{p} = 0)/T^3$  to be indeed a  $\tau$ -independent constant. In Fig. 5.2 we show the results for  $-G_{00}(\tau, \vec{p} = 0)/T^3$  for all lattices analyzed in this work.

The left hand part of Fig. 5.2 shows results obtained on lattices with different spatial extent at fixed lattice cut-off. Except for the smallest aspect ratio,  $N_\sigma/N_\tau = 2$ , the results agree within statistical errors of about 1%. The right hand part shows results obtained on our largest spatial lattice,  $N_\sigma = 128$ , at four different values of the lattice cut-off. This shows that also cut-off effects are small in the calculation of the time-time component of the vector correlation function, *i.e.* the quark number susceptibility. Apparently the fact that we use a non-conserved local current does not significantly alter the spectral properties of the time-time correlator. Except for short distances it is to a

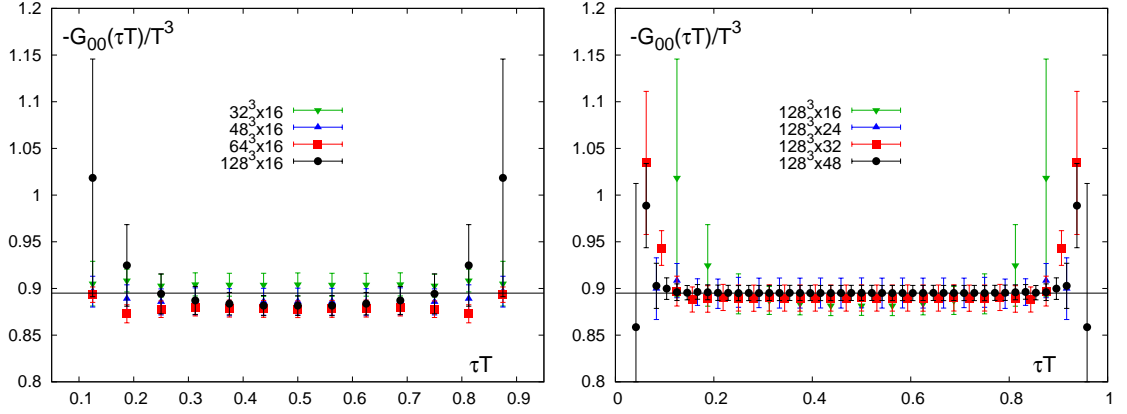


Figure 5.2: *The time-time component of the vector correlation function,  $-G_{00}(\tau T)/T^3$ , calculated at  $T \simeq 1.45T_c$  versus Euclidean time  $\tau T$ . The left hand part of the figure shows the volume dependence of  $-G_{00}(\tau T)/T^3$  for  $N_\tau = 16$  and  $32 \leq N_\sigma \leq 128$ . The right hand figure shows the cut-off dependence of  $-G_{00}(\tau, T)/T^3$  for  $N_\sigma = 128$  and  $16 \leq N_\tau \leq 48$ . In both figures the horizontal line shows a fit to the data obtained on the largest lattice,  $128^3 \times 48$ .*

good degree  $\tau$ -independent.

This implies the spectral function is indeed a  $\delta$ -function and we confirm:

$$\rho_{00}(\omega) = 2\pi\chi_q\omega\delta(\omega) \quad (\checkmark). \quad (5.2)$$

The results for  $\chi_q/T^2 \equiv -G_{00}(\tau T)/T^3$  calculated on the  $128^3 \times N_\tau$  lattices are summarized in Table 5.1.1, here we also include a continuum extrapolation taking into account cut-off errors of  $\mathcal{O}(a^2)$  due to the non-perturbatively improved Wilson-Clover action. As a side remark note that at  $T \simeq 1.45T_c$  the quark number susceptibility,  $\chi_q/T^2$ , is about 10% smaller than the free field value  $\chi_q^{free}/T^2 = 1$  which is in accordance with calculations performed with staggered fermions [101–104].

$N_\tau$	16	24	32	48	$\infty$
$\chi_q/T^2$	0.882(10)	0.895(16)	0.890(14)	0.895(8)	0.897(3)

Table 5.1: *Quark number susceptibility ( $\chi_q/T^2$ ) calculated on lattices of size  $128^3 \times N_\tau$ . The quark number susceptibilities have been renormalized using the renormalization constants listed in Tab. 5.1.1. The last column gives the result of a continuum extrapolation taking into account cut-off errors of  $\mathcal{O}(a^2)$ .*

## 5.1 The Vector SPF and Dilepton Rate in the Continuum at $T \simeq 1.45T_c$

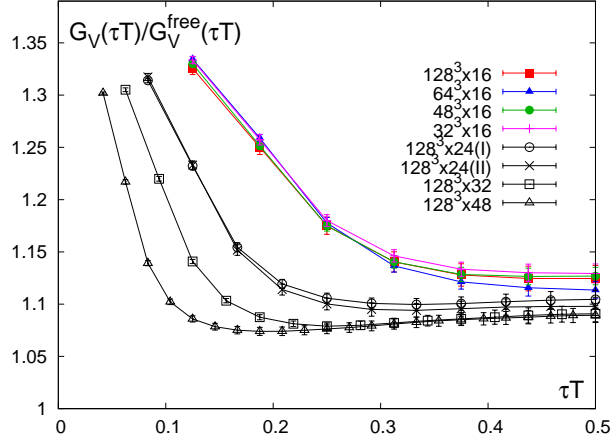


Figure 5.3: The vector correlation function,  $G_V(\tau T)$ , calculated on lattices of size  $N_\sigma^3 \times N_\tau$  at  $T \simeq 1.45T_c$ . The correlation functions are normalized to the free vector correlation function  $G_V^{\text{free}}(\tau T)$  in the continuum. Shown are data for  $\tau T > 1/N_\tau$  only. Label I and II refer to data sets generated with two different values of the quark mass (see Tab. 2.5 or Tab. 2.5).

Moreover, these results encourage us to normalize the correlation functions with the quark number susceptibility  $\chi_q/T^2$  to avoid the usage of renormalization constants. This is a property we may exploit here as the components of the vector current correlation functions are subject to the same renormalization constant, see Chp. 2.4.1.

### 5.1.2 Spatial and Full Vector Correlation Functions

Turning to the main objectives of this work, i.e. the spatial and full vector correlation and ultimately spectral functions, recall that Fig. 5.1 showed the thermal in-medium effects to be obscured by the exponential decay of the correlation function. To alleviate this issue we forthwith eliminate this decay by normalizing with the free correlation functions as obtained from the free continuum and free discretized formulations. This procedure is based on the observation that the dependence of the correlation function on Euclidean time is in fact very similar to the free case. Additionally asymptotic freedom guarantees that the non-interacting case is reproduced at  $\tau T = 0$  in the continuum limit.

In Fig. 5.3 we show results for the ratio of the vector correlation function normalized by its free continuum counterpart for  $H = V$  for all available lattice sizes. Data sets with fixed spatial size at  $N_\sigma = 128$  while varying the cut-off  $N_\tau$  are shown in black. Data sets with fixed cut-off ( $N_\tau = 16$ ) and varying volume are shown in color. Recall for  $N_\tau = 24$  we performed calculations for two different values of the quark mass. We find that finite quark mass effects are small and well within 2%. From the fixed cut-

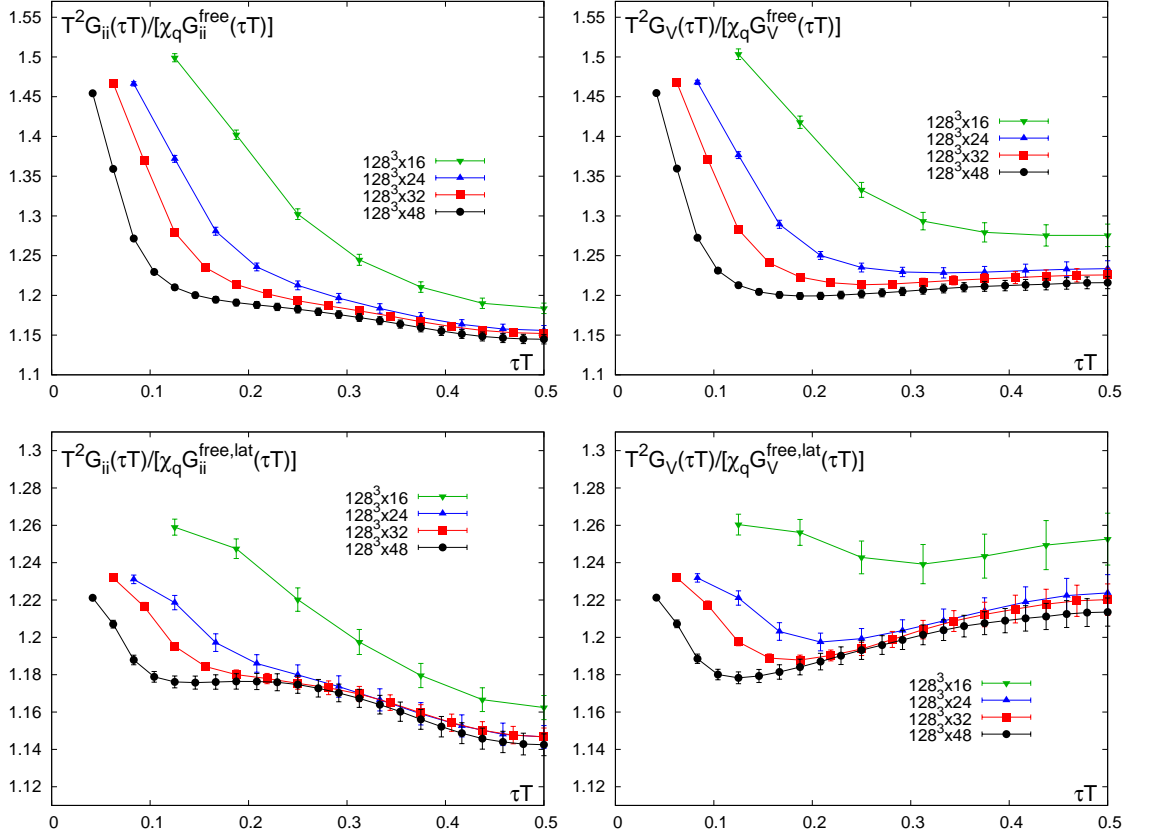


Figure 5.4: *The spatial component of the vector correlation function,  $G_{ii}(\tau T)/T^3$ , calculated at  $T \simeq 1.45T_c$  on lattices of size  $128^3 \times N_\tau$  versus Euclidean time  $\tau T$  (left) and the full vector correlator  $G_V(\tau T)/T^3$  (right). Both correlators have been normalized by the continuum version of the corresponding free vector correlation function (top) and its discretized version calculated on infinite spatial volumes with fixed  $N_\tau$  (bottom), respectively.*

off (colored)  $N_\tau = 16$  results finite volume effects for  $\tau T \geq 0.3$  are seen to remain within below the 0.5% percent level even for the largest Euclidean time separation at  $\tau T = 0.5$ . As a consequence these results show that finite volume effects are under control. Focusing on cut-off effects it is immediately apparent that cut-off effects become large and dominate the ratio below a certain Euclidean time distance, as all results rise rapidly in the small distance region. In fact, the cut-off effects strongly influence the behavior of  $G_V(\tau T)$  at short distances for the first 6 to 8 Euclidean time units, where  $1/N_\tau \leq \tau T \lesssim 8/N_\tau$ . As such for  $N_\tau = 48$  the cut-off effects dominate the ratio below  $\tau T \lesssim 0.15$ , whereby this upper value increases with decreasing  $N_\tau$  from  $\tau T \lesssim 0.2$  at  $N_\tau = 32$  via  $\tau T \lesssim 0.25$  at  $N_\tau = 24$  to  $\tau T \lesssim 0.35$  at  $N_\tau = 16$ .

In Fig. 5.4 we show separately results for the spatial component of the vector current

5.1 The Vector SPF and Dilepton Rate in the Continuum at  $T \simeq 1.45T_c$

$N_\tau$	16	24	32	48	$\infty$
$G_V(1/2)/(\tilde{\chi}_q G_V^{free}(1/2))$	1.276(14)	1.234(10)	1.226(10)	1.216(8)	1.211(9)
$G_V(1/4)/(\tilde{\chi}_q G_V^{free}(1/4))$	1.333(9)	1.235(6)	1.213(4)	1.202(5)	1.190(7)
$G_{ii}(1/2)/(\tilde{\chi}_q G_{ii}^{free}(1/2))$	1.184(7)	1.156(6)	1.152(5)	1.145(6)	1.142(9)
$G_{ii}(1/4)/(\tilde{\chi}_q G_{ii}^{free}(1/4))$	1.302(7)	1.213(6)	1.193(3)	1.183(5)	1.172(7)

Table 5.2: *Several values of the vector correlation functions expressed in units of the corresponding free field values and normalized with the quark number susceptibility. Results are from calculations on lattices of size  $128^3 \times N_\tau$ . The last column gives the continuum extrapolated results (see below). Note in these ratios the renormalization constants drop out.*

correlation function  $G_{ii}(\tau T)/T^3$  and the combined vector correlator  $G_V(\tau T)/T^3$ . In both cases the correlation function has been normalized to its respective free correlator  $G_H^{free}(\tau T)/T^3$ . Recall however, that ratios for  $H = V$  and  $H = ii$  are related through Eq. 3.95 and provide identical information on the vector spectral function representing these correlators.

As discussed above it is apparent that the short distance ( $\tau \lesssim (6 - 8)$ ) part of the vector correlation functions is strongly influenced by lattice cut-off effects. To some extent one can eliminate this dominant contribution by calculating the free field correlation functions on lattices with finite temporal extent, as was shown in Chp. 3, and considering the ratio  $G_V/G_V^{free,lat}$  rather than the ratio obtained by normalizing with the free vector correlator in the continuum limit. Naturally one expects the free lattice correlator to capture much of the cut-off dependence and thus describe the data somewhat better. A comparison between the lower and upper panels of Fig. 5.4 indeed shows a reduction of cut-off effects across all available datasets, although the short distance part  $\tau T \lesssim 0.15$  at  $N_\tau = 48$  or  $\tau T \lesssim 0.35$  at  $N_\tau = 16$  still deviates substantially from the free field values. However, in the entire Euclidean time interval, where cut-off effects are under control, a continuum extrapolation should be possible. Restricting ourselves to calculations with comparable quark mass, i.e.  $N_\tau = 48, 32$  and  $24$  this is seen to be the case for the Euclidean time window  $\tau T \in [0.2 : 0.5]$ . In this interval  $G_V(\tau T)$  as well as  $G_{ii}(\tau T)$  stay close to the corresponding free field correlation functions.

Moreover, note that the data shown in Fig. 5.4 have been divided by the quark number susceptibility  $\chi_q/T^2$  to avoid the usage of any renormalization constants as was discussed above and are in fact renormalization independent results.

The corresponding data normalized by the free continuum correlation function and the quark number susceptibility at  $\tau T = 0.5$  and  $\tau T = 0.25$  is summarized in Tab. 5.1.2. Naturally multiplying the data shown in Fig. 5.4 by the quark number susceptibility given in Tab. 5.1.1 gives the ratio of the vector correlation functions and the free vector

correlator. These values are about 10% smaller than those shown in Fig. 5.4. We therefore expect that in the continuum limit deviations of the vector correlation function as well as its spatial component from the corresponding free correlator remain smaller than 9% for all  $\tau T \geq 0.2$ .

### 5.1.3 Continuum Extrapolation of the Vector Correlation Function

As the ratios for  $H = V$  and  $H = ii$  are related through Eq. 3.95 and provide identical information on the vector spectral function representing these correlators, we will concentrate on the full vector correlation function in the following.

With the above results we are in a position to extrapolate to the continuum in the region where the cut-off effects are under control.

This can be done directly for three values of Euclidean time,  $\tau T = 1/4, 3/8, 1/2$ , where we have numerical results from calculations at all four values of the lattice cut-off. In these cases we perform the continuum extrapolation of the correlation functions using the data from lattices with temporal extent  $N_\tau = 24, 32$  and  $48$ , as we ensure maximum comparability on these lattices due to the almost equal quark masses.

Specifically, we extrapolated the ratio of correlation functions  $G_H(\tau T)/(\tilde{\chi}_q G_V^{free}(\tau T))$ , where  $\tilde{\chi}_q/T^2$  by using a quadratic Ansatz in  $aT = 1/N_\tau$ . Whereby the quadratic Ansatz owes up to the fact that Wilson-Clover fermions, as used in this work have errors of order  $\mathcal{O}(a^2)$ . At other values of  $\tau T$  on the  $N_\tau = 48$  lattice we use spline interpolations of the data sets on the  $N_\tau = 24$  and  $32$  lattices to perform continuum extrapolations, i.e. we do the continuum extrapolations on all points  $\tau T = k/48$  for  $9 \leq k \leq 24$ . The resulting continuum extrapolations at the Euclidean time separations  $\tau T = 0.1875, 0.25, 0.3125, 0.375$  and  $0.5$  are shown in Fig. 5.5. Note here that the results obtained from the continuum extrapolation of correlators normalized with the free lattice and continuum correlation functions agree within errors. The resulting continuum extrapolation of the vector correlation function obtained in this way is shown in Fig. 5.6. Data for  $\tau T = 1/4$  and  $1/2$  are also summarized in Table 5.1.2.

From Fig. 5.6 we conclude that in the continuum limit the largest deviation of  $G_V(\tau T)$  from the free vector correlation function occurs at  $\tau T = 1/2$ . Taking into account the normalization with  $\tilde{\chi}_q$  we obtain from Tab. 5.1.1

$$\begin{aligned} \frac{G_V(1/2)}{G_V^{free}(1/2)} &= 1.086 \pm 0.008, \\ \frac{G_V(1/4)}{G_V^{free}(1/4)} &= (0.982 \pm 0.005) \frac{G_V(1/2)}{G_V^{free}(1/2)} \end{aligned} \quad (5.3)$$

where the second relation has been obtained from a jackknife analysis of the ratio  $G_V(1/4)/G_V(1/2)$ .

We note that the increase of  $G_V(\tau T)/G_V^{free}(\tau T)$  with  $\tau T$  is significant. It becomes apparent only for sufficiently small lattice spacing, i.e. for large  $N_\tau$ , in particular in the

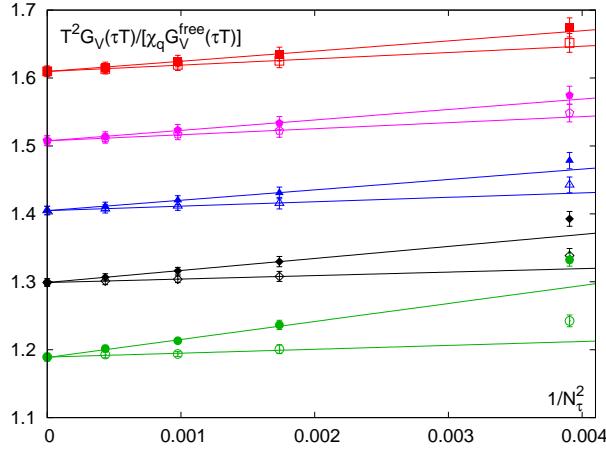


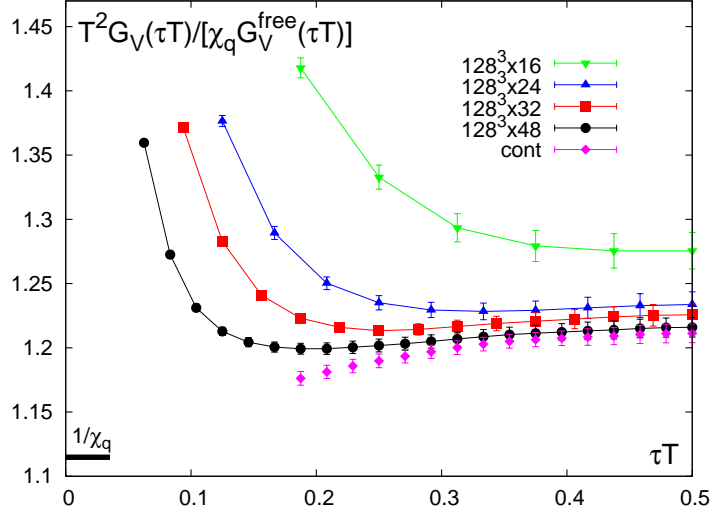
Figure 5.5: The ratio of the vector correlation function,  $G_V(\tau, T)$ , normalized with the quark number susceptibility and the free vector correlation function calculated in the continuum (full symbols) and on lattices with temporal extent  $N_\tau$  (open symbols). Shown are results for five values of Euclidean time,  $\tau T = 0.1875, 0.25, 0.3125, 0.375$  and  $0.5$  (bottom to top), on lattices with temporal extent  $N_\tau = 16, 24, 32$  and  $48$ . For distances larger than  $\tau T = 0.1875$  data have been shifted in steps of  $0.1$  for better visibility. For  $\tau T = 0.1875$ , and  $0.3125$  spline interpolations have been used on the  $N_\tau = 24$  lattice to estimate results at these Euclidean time separations. Note that the far most right data set, corresponding to  $N_\sigma = 16$ , has not been included in the extrapolation.

normalization with the free continuum vector correlator. The rise with  $\tau T$  is a direct indicator that the vector spectral function in the low- $\omega$  region is different from the free case. As such it is absolutely mandatory to go to very fine lattice spacing, as was done in this work, if one wants the chance to resolve the interesting thermal effects. Consequently past calculations on lattices with small temporal extent are subject to large systematic effects from the finite size but especially the cut-off.

Finally note that the monotonic increase of the continuum extrapolated ratio with increasing Euclidean time once more indicates that the rapid drop observed in the lattice data at small distances is governed by cut-off effects. Due to asymptotic freedom the ratio must approach  $1/\chi_q$  in the limit  $\tau T \rightarrow 0$ , as indicated also in Fig. 5.6. Even though our result is still far away from this limit the continuum extrapolated result and its monotonic increase is seen to fit well with such a behavior.

#### 5.1.4 Computation of Thermal Moments

In the preceding chapter our careful analysis of the vector current at the correlator level enabled us to establish that the low- $\omega$ , i.e. low-frequency, region is in fact modified in the


 Figure 5.6: *Continuum extrapolation of the vector correlation function.*

high temperature phase of QCD compared to the non-interacting case. In Chp. 4.2 we introduced the notion of the thermal moment specifically as an observable that should be especially sensitive to this regime.

Looking once more at Fig. 5.3 or Fig. 5.4 and recalling Eq. 4.18, we can already deduce some basic results for the thermal moments. For one part it is obvious that the deviation of the data from the free field correlation function change qualitatively when the lattice spacing is reduced. For  $N_\tau \geq 24$  the ratio  $G_V(\tau T)/G_V^{free}(\tau T)$  increases close to  $\tau T = 1/2$  indicating that the ratio of thermal moments  $R_V^{(2,0)}$  actually is smaller than the corresponding free field value. Consequently we expect  $R_V^{(2,0)} < R_{V,free}^{(2,0)}$ .

The spatial part alone on the other hand drops when approaching  $\tau T = 1/2$ , as can be seen in Fig. 5.4. This suggests  $R_{ii}^{(2,0)} > R_{ii,free}^{(2,0)}$ .

To get a more direct handle on the thermal moment we analyze the ratio of the mid-point subtracted correlation function  $\Delta_V(\tau T)$  introduced in Eq. 4.19. Results for  $\Delta_V(\tau T)$  calculated at the four different values of the lattice cut-off are shown in Fig. 5.7.

As before in the case of the correlation function we perform spline interpolations of the results obtained on lattices with temporal extent  $N_\tau = 24$  and  $32$ . These interpolated data together with the results obtained on the  $N_\tau = 48$  lattices are then extrapolated to the continuum limit taking into account corrections of  $\mathcal{O}((aT)^2)$ . As such the extrapolated data at all distances  $\tau T = \tau/48$  are shown also in Fig. 5.7. These extrapolated data have been fitted to a quartic polynomial as indicated by the Taylor expansion given in Eq. 4.19. From this fit we obtain

$$\frac{G_V^{(2)}}{G_V^{(2),free}} = 1.067 \pm 0.012 \quad . \quad (5.4)$$

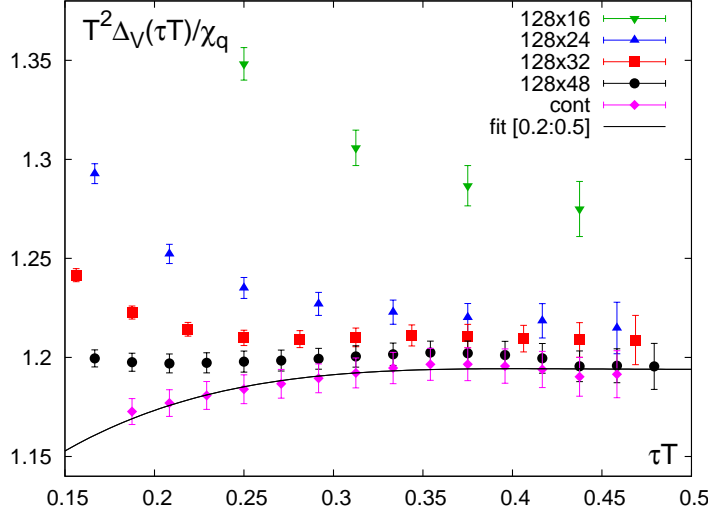


Figure 5.7: The mid-point subtracted vector correlation function normalized to the corresponding difference for the free vector correlation function. Shown is the ratio as defined in Eq. 4.19 but normalized by the quark number susceptibility. The continuum extrapolation is achieved as for the correlator.

Fits of the vector correlation function and the mid-point subtracted correlator are correlated, as they are calculated from each other. We made use of this and also computed the ratio of the second thermal moment and the correlation function at the mid-point employing an additional jackknife analysis. We find

$$\begin{aligned} \frac{G_V^{(2)}}{G_V^{(0)}} &= (0.982 \pm 0.012) \frac{G_V^{(2),free}}{G_V^{(0),free}}, \\ \frac{G_{ii}^{(2)}}{G_{ii}^{(0)}} &= (1.043 \pm 0.010) \frac{G_{ii}^{(2),free}}{G_{ii}^{(0),free}}. \end{aligned} \quad (5.5)$$

Although the deviation of  $G_V^{(2)}/G_V^{(0)}$  from the non-interacting limit is marginal, the small difference from unity is consistent with the behavior of  $G(\tau T)/G^{free}(\tau T)$  close to  $\tau T = 1/2$  shown in Fig. 5.6. At large enough  $\tau T$  the latter has a positive slope in  $\tau T$ , which approaches zero from above when  $\tau T$  reaches  $1/2$ , and a small negative curvature that is in the limit of  $\tau T$  going to  $1/2$  proportional to  $R_V^{(2,0)} - R_{V,free}^{(2,0)}$ , as shown in Eq. 4.18.

Note we also tried to look at the fourth thermal moment, which implied using the quartic polynomial Ansatz. Unfortunately this moment could not be obtained as of this time, as the numerical accuracy of our data does not allow to draw a firm conclusion about its value. This and the small but significant and important deviation from unity in Eq. 5.5 shows the need of very high precision data and a proper continuum limit.

$N_\tau$	16	24	32	48	$\infty$
$G_V^{(2)}/(\tilde{\chi}_q G_V^{(2),free})$	1.273(4)	1.214(2)	1.207(1)	1.193(1)	1.189(13)

Table 5.3: *The ratio of the second thermal moment and its corresponding free value for our lattices  $128^3 \times N_\tau$ . The last column gives the continuum extrapolated results taking into account corrections of  $\mathcal{O}((aT)^2)$ .*

Nonetheless the above results put stringent bounds on the magnitude of any contribution to the vector correlation function that may arise from a peak in the vector spectral function at small energies.

The results from Eq. 5.4 modulo the quark number susceptibility  $\tilde{\chi}_q$  on the individual lattices and the continuum are summarized in Tab. 5.1.4.

### 5.1.5 Analyzing the Vector Correlator and computing the SPF

With all these results in hand, what can we say about the vector spectral function? First of all we could establish the time-time vector spectral function, with this knowledge we can intimately relate the spatial and full vector spectral functions at vanishing momentum. As such the spatial component misses the the  $\delta$ -function contribution of the time-time part, it is subsequently somewhat clearer to switch to  $G_{ii}(\tau T)$  and  $\rho_{ii}(\omega)$  in the following. To summarize our most important findings recall:

- The correlation function at  $\tau T = 1/2$  is about 2% larger than the corresponding free field value,  $G_{ii}(1/2)/G_{ii}^{free}(1/2) = 1.024(8)$ .
- The deviation from the free field value increases with decreasing Euclidean time. At  $\tau T = 1/4$  the ratio is  $G_{ii}(1/4)/G_{ii}^{free}(1/4) = 1.051(7)$ .
- The second moment of the vector spectral function deviates from the free field value by about 7%,  $G_V^{(2)}/G_V^{(2),free} = G_{ii}^{(2)}/G_{ii}^{(2),free} = 1.067(12)$ .

In view of these results and also Fig. 5.3-5.7 suggest the starting point for our “alternative route”, outlined in Chp. 4.4, is in fact the non-interacting, i.e.  $T \rightarrow \infty$ , theory.

Given the extensive knowledge gathered in Chp. 3 on the non-interacting spectral functions and our expectations in the interacting case, we may immediately motivate the desired Ansatz.

First of all, as stated above, the basis of the Ansatz should be formed by the free continuum spectral function. At intermediate temperatures this contribution clearly may be subject to perturbative corrections and we write:

$$\rho_{ii}^{\text{base}}(\omega) = \frac{3}{2\pi} (1 + k(T)) \omega^2 \tanh(\omega/4T) \quad , \quad (5.6)$$

### 5.1 The Vector SPF and Dilepton Rate in the Continuum at $T \simeq 1.45T_c$

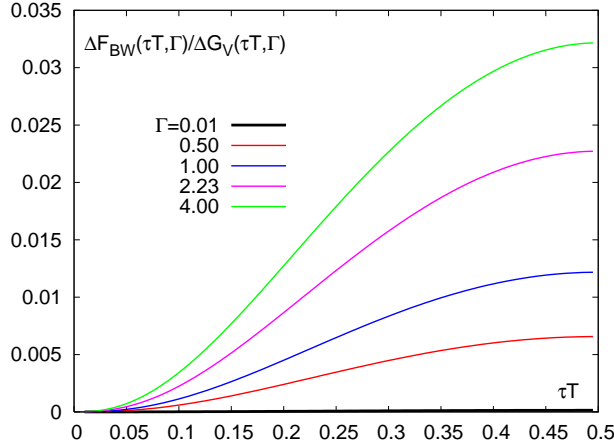


Figure 5.8: The reduced version of Eq. 5.13 for a number of widths over Euclidean time shows the monotonic rise of our Ansatz.

where the parameter  $k(T)$  parametrizes deviations from a free spectral function at large energies as suggested above. At high temperature and for large energies,  $\omega/T \gg 1$ , we expect to find  $k(T) \simeq \alpha_s/\pi$  [105]. Note that  $k(T)$  will also depend on  $\omega$  and actually will vanish for  $\omega \rightarrow \infty$  at fixed  $T$ . Here we will treat  $k(T)$  as a constant and will not take into account any running of  $\alpha_s$ .

This takes care of the basic shape of the spectral function and its large frequency behavior. In the next step recall our gained knowledge of interacting theory via linear response already showed us the prime candidate for the transport contribution. All computations in Chp. 3 with interactions at vanishing momentum point to a Breit-Wigner shape as most possible contribution:

$$\rho_{ii}^{\text{BW}}(\omega) = 2\chi_q c_{BW} \frac{\omega\Gamma/2}{\omega^2 + (\Gamma/2)^2} \quad . \quad (5.7)$$

Indeed this shape as the attractive feature that it retrieves the  $\delta$ -peak necessary for free theory as the width  $\Gamma \rightarrow 0$ , it thus satisfies our assumption of smoothness.

In total we thus motivate the Ansatz:

$$\begin{aligned} \rho_{ii}(\omega) &= \rho_{ii}^{\text{BW}}(\omega) + \rho_{ii}^{\text{base}}(\omega) \\ &= 2\chi_q c_{BW} \frac{\omega\Gamma/2}{\omega^2 + (\Gamma/2)^2} + \frac{3}{2\pi} (1+k) \omega^2 \tanh(\omega/4T) \quad , \end{aligned} \quad (5.8)$$

as such this Ansatz depends on four temperature dependent parameters; the quark number susceptibility  $\chi_q(T)$ , the strength  $c_{BW}(T)$  and width  $\Gamma(T)$  of the Breit-Wigner peak and the free parameter  $k(T)$ , as explained above.

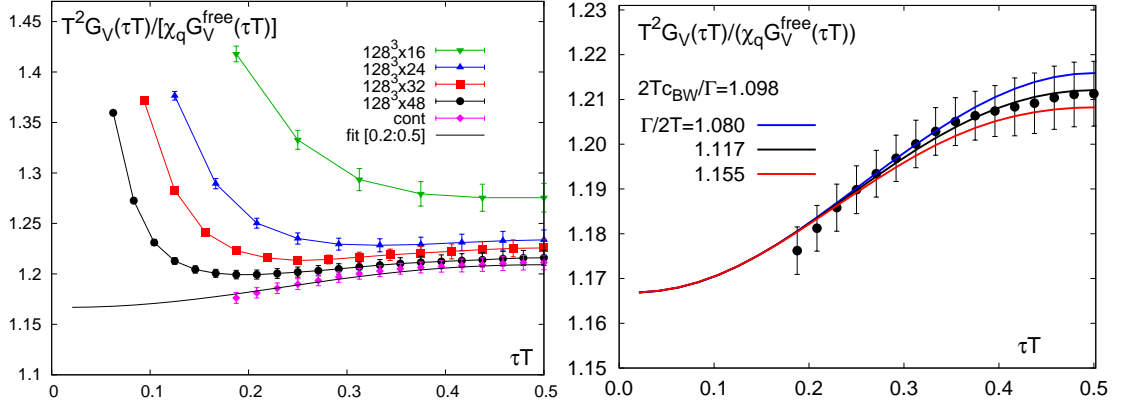


Figure 5.9: *Fit and continuum extrapolation of the vector correlation function. Left: The resulting fit is shown. Right: The data for the continuum extrapolation of  $T^2 G_V(\tau T)/(\chi_q G_V^{free}(\tau T))$  is shown and an error band varying the width  $\tilde{\Gamma}$  within its errors obtained from the fit is given.*

With this Ansatz and introducing  $\tilde{\Gamma} = \Gamma/T$  as well as  $\tilde{\chi}_q = \chi_q/T^2$  the corresponding correlation function reads:

$$\tilde{G}_{ii}(\tau T) = (1 + k(T)) \tilde{G}_V^{free}(\tau T) + c_{BW} \tilde{\chi}_q F_{BW}(\tau T, \tilde{\Gamma}) \quad , \quad (5.9)$$

where

$$F_{BW}(\tau T, \tilde{\Gamma}) = \frac{\tilde{\Gamma}}{2\pi} \int_0^\infty d\tilde{\omega} \frac{\tilde{\omega}}{(\tilde{\Gamma}/2)^2 + \tilde{\omega}^2} \frac{\cosh(\tilde{\omega}(\tau T - 1/2))}{\sinh(\tilde{\omega}/2)} \quad . \quad (5.10)$$

Once more this Ansatz shows the desirable properties (for  $k(T)=1$ ):

$$\lim_{\tilde{\Gamma} \rightarrow 0} F_{BW}(\tau T, \tilde{\Gamma}) = 1 \quad \Rightarrow \quad \tilde{G}_{ii}(\tau T) \rightarrow G_{ii}^{free}(\tau T) \quad (5.11)$$

$$\lim_{\tilde{\Gamma} \rightarrow \infty} F_{BW}(\tau T, \tilde{\Gamma}) = 0 \quad \Rightarrow \quad \tilde{G}_{ii}(\tau T) \rightarrow G_V^{free}(\tau T) \quad . \quad (5.12)$$

In the next step this Ansatz allows a straight forward definition of the midpoint subtracted correlation function, as introduced in Eq. 4.19:

$$\Delta_V(\tau T) = 1 + k(T) + c_{BW} \tilde{\chi}_q \frac{F_{BW}(\tau T, \tilde{\Gamma}) - F_{BW}(1/2, \tilde{\Gamma})}{\tilde{G}_V^{free}(\tau T) - \tilde{G}_V^{free}(1/2)} \quad . \quad (5.13)$$

Extrapolating to  $\tau T = 1/2$  this fit Ansatz yields results for the zeroth and second moment of the spectral function as introduced in Eq. 4.9 and Eq. 4.19,

$$\begin{aligned} \tilde{G}_{ii}(1/2) &= 2(1 + k(T)) + c_{BW} \tilde{\chi}_q F_{BW}^{(0)}(\tilde{\Gamma}) \quad , \\ \Delta_V(1/2) &= 1 + k(T) + c_{BW} \tilde{\chi}_q \frac{F_{BW}^{(2)}(\tilde{\Gamma})}{\tilde{G}_V^{(2),free}} \quad , \end{aligned} \quad (5.14)$$

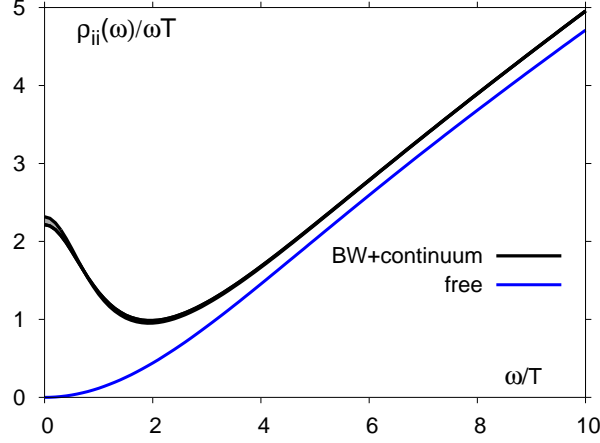


Figure 5.10: The vector spectral function obtained from the fit compared to its free continuum counterpart, the shaded area gives the error band fixed by the error of the fit.

with

$$F_{BW}^{(2n)}(\tilde{\Gamma}) = \frac{1}{(2n)!} \frac{\tilde{\Gamma}}{2\pi} \int_0^\infty d\tilde{\omega} \frac{\tilde{\omega}^{2n+1}}{\left(\left(\frac{\tilde{\Gamma}}{2}\right)^2 + \tilde{\omega}^2\right) \sinh(\tilde{\omega}/2)}. \quad (5.15)$$

In the limit  $\tilde{\Gamma} \rightarrow 0$  the thermal moments  $F_{BW}^{(2n)}$  vanish for all  $n > 0$  and the fit Ansatz for  $\Delta_V(\tau T)$  becomes a constant which relates to the deviations of the vector correlation function from the free field correlator at short distances. For all  $\tilde{\Gamma} > 0$ , however, the right hand side of Eq. 5.13 is a monotonically increasing function of  $\tau T$ . This behavior is illustrated in Fig. 5.8 where we show a reduced version Eq. 5.13:

$$\frac{\Delta F_{BW}(\tau T, \tilde{\Gamma})}{\Delta \tilde{G}_V^{free}(\tau T)} = \frac{F_{BW}(\tau T, \tilde{\Gamma}) - F_{BW}(1/2, \tilde{\Gamma})}{\tilde{G}_V^{free}(\tau T) - \tilde{G}_V^{free}(1/2)}, \quad (5.16)$$

clearly only multiplicative factors and constant contributions have been omitted and the resulting ratio is shown in Fig. 5.8 for a number of widths over Euclidean time.

In the next step we fit the continuum extrapolated correlation function  $G_{ii}(\tau T)$  with the Ansatz  $\tilde{G}_{ii}(\tau T)$  together with the zeroth and second moments  $G_{ii}^{(0)}$  and  $G_{ii}^{(2)} = G_V^{(2)}$  via  $\tilde{G}_{ii}(1/2)$  and  $\Delta_V(\tau T)$ . Note here the first thermal moment is taken into account trivially as it is given by the midpoint of the correlation function. The parameters obtained in the fit window  $[0.2 : 0.5]$  are:

$$k = 0.1465(30) \quad , \quad \tilde{\Gamma} = 2.235(75) \quad \text{and} \quad 2c_{BW}\tilde{\chi}_q/\tilde{\Gamma} = 1.098(27) \quad . \quad (5.17)$$

This three parameter fit has a  $\chi^2/d.o.f. = 0.06$  for 12 degrees of freedom. Even though this small  $\chi^2/d.o.f$  shows that the data is strongly correlated also after continuum extrapolation, the fit provides an excellent description of the data.

Using Eq. 3.95 it is straightforward to calculate  $G_V(\tau T)$  and to cross check the fit results, they indeed agree. On the left of Fig. 5.9 the resulting line is shown together with the lattice data and the continuum extrapolation. On the right we show the data for the continuum extrapolation of  $T^2 G_V(\tau T)/(\chi_q G_V^{free}(\tau T))$  and give an error band varying the width  $\tilde{\Gamma}$  within its errors obtained from the fit.

The corresponding spatial vector spectral function can be easily obtained plugging in the fit values and their errors. In Fig. 5.10 we show the corresponding spectral function including also the resulting error band arising from the errors of the fit. These results show that the vector correlation function is indeed sensitive to the low energy Breit-Wigner shaped transport contribution only for Euclidean times  $\tau T \gtrsim 0.25$ . However taking into account the second thermal moment the fit parameters are well constrained and the large distance behavior of the correlator and the low frequency spectral function is excellently reproduced.

Using the Kubo-formula Eq. 3.115 we thus retrieve a significant result for the electrical conductivity of the quark gluon plasma from quenched QCD at  $T \simeq 1.45T_c$ :

$$\frac{\sigma}{T} = \frac{C_{em}}{6} \lim_{\omega \rightarrow 0} \frac{\rho_{ii}(\omega)}{\omega T} = \frac{2C_{em}}{3} \frac{c_{BW} \tilde{\chi}_q}{\tilde{\Gamma}} = (0.37 \pm 0.01) C_{em} \quad . \quad (5.18)$$

This result is close to the past result found in [94] from staggered fermion calculations and deviates somewhat of that found in [99]. Note also that its value is more than an order of magnitude larger than the electrical conductivity of a pion gas above  $T_c$  [106]. At the same time the value determined for the correction to the free field behavior at large energies  $k \simeq 0.05$  at  $T \simeq 1.45T_c$  is quite reasonable. Using the relation to the perturbative result  $k = \alpha_s/\pi$  yields for the temperature dependent running coupling  $g^2(T) = 4\pi\alpha_s \simeq 2$  which is in good agreement with other determinations of temperature dependent running couplings at high energies or short distances [107].

Note at this point that the error quoted above is the fit error. Subsequently we will estimate a systematic error in the following.

### Systematics of the Breit-Wigner Ansatz

Naturally the above determination of the electrical conductivity is sensitive to the Ansatz we chose for our Analysis. Even though we obtain excellent fit results for the vector correlation function with the simple Ansatz given in Eq. 5.9, other Ansätze might yield equally good results. An additional analysis of the systematic errors introduced by our choice is therefore desirable.

Beginning such an analysis we observe that the free continuum part of the Ansatz contributes to the spectral function for all frequencies  $\omega$ . This means especially the highly non-perturbative low frequency region where the continuum part of the Ansatz contributes a term proportional to  $\omega^3/T$ . To analyze the systematics introduced by this

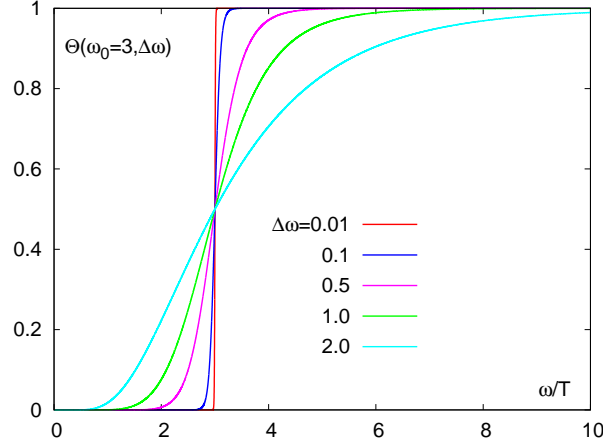


Figure 5.11: The truncation factor for the Ansatz of Eq. 5.9 at  $\omega_0 = 3$  and several values of  $\Delta\omega$ .

contribution we add a smooth truncation to our Ansatz:

$$\rho_{ii}(\omega) = 2\chi_q c_{BW} \frac{\omega\Gamma/2}{\omega^2 + (\Gamma/2)^2} + \frac{3}{2\pi} (1+k) \omega^2 \tanh(\omega/4T) \cdot \Theta(\omega_0, \Delta\omega)$$

$$\Theta(\omega_0, \Delta\omega) = \left(1 + e^{(\omega_0^2 - \omega^2)/\omega\Delta\omega}\right)^{-1} . \quad (5.19)$$

Hereby the truncation factor  $\Theta(\omega_0, \Delta\omega)$  depends on a width  $\Delta\omega$  and a cut-position  $\omega_0$  parameter and mimics a smeared  $\Theta$ -function. For illustration we show  $\Theta(\omega_0, \Delta\omega)$  for a number of widths  $\Delta\omega$  in Fig. 5.11. Clearly in the limit  $\Delta\omega \rightarrow 0$  the  $\Theta$ -function with discontinuity at  $\omega_0$  is achieved as desired, while at the same time ensures the continuum contribution to vanish exponentially at  $\omega = 0$ .

Now we perform three parameter fits with  $c_{BW}$ ,  $\Gamma$  and  $k$  as free parameters for several values of  $\omega_0$  and  $\Delta\omega$ . With increasing  $\omega_0$  and/or increasing  $\Delta\omega$  the  $\chi^2$  of the fit also rises, implying the data can no longer be described well by the truncated Ansatz. This implies that in both cases eventually too much of the continuum part at high energies is suppressed. For small values of  $\omega_0$  and  $\Delta\omega$  the Breit-Wigner term compensates for the continuum contribution that has been cut off by increasing the low energy contribution and the intercept at  $\omega = 0$  (electrical conductivity) rises. At large values of  $\omega_0$  and  $\Delta\omega$  the Breit-Wigner term however fails to compensate the missing continuum contribution and the fit cannot describe the data well anymore.

Results from fits which all lead to  $\chi^2/d.o.f.$  smaller than unity are shown in Fig. 5.12. As  $\omega_0$  and  $\Delta\omega$  increase the  $\chi^2/d.o.f.$  of the fits shown in this figure rises from its minimal value of about 0.06, obtained for  $\omega_0/T = \Delta\omega/T = 0$  to unity. All fit parameters corresponding to the curves shown in Fig. 5.12 are summarized in Tab. 5.4.

In particular the second moment of the correlation function normalized by the correlation function at the mid-point of Eq. 4.18  $R_{ii}^{(2,0)}$  reacts quite sensitive to the truncation

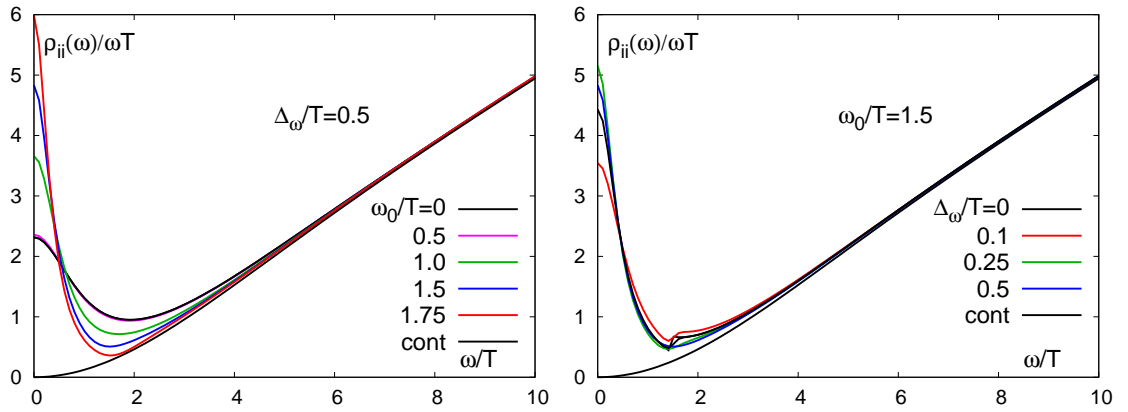


Figure 5.12: Spectral functions obtained from fits to the vector correlation function using the Ansatz given in Eq. 5.19. For comparison we also show only the continuum part of the spectral function. The left hand figure shows results for different values of the cut-off ( $\omega_0$ ) and fixed width ( $\Delta_\omega$ ). The right hand figure shows results for fixed  $\omega_0/T = 1.5$  and several values of  $\Delta_\omega$ . The curve labeled 'cont' is the continuum contribution to the fit described in Eq. 5.9.

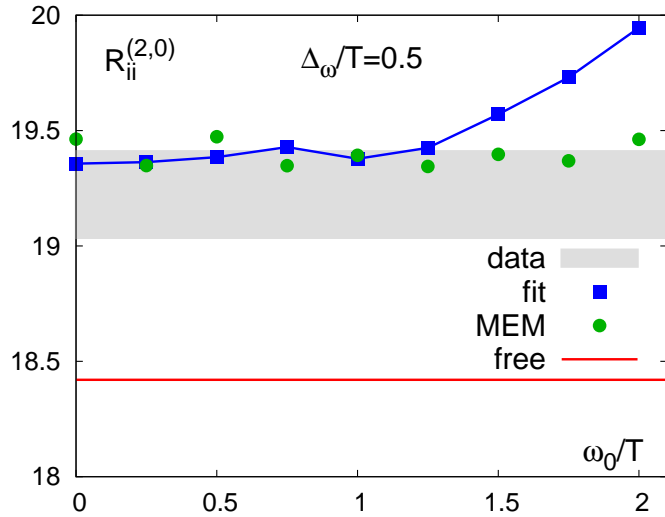


Figure 5.13: The ratio of second and zeroth thermal moment of the correlation function  $G_{ii}(\tau T)$  obtained from fits with different values for the continuum cut-off parameter  $\omega_0/T$  and fixed  $\Delta_\omega$ . Circles show results of a MEM analysis where the fits have been used as default model. The band gives the result extracted from the continuum extrapolated correlation function. The lower curve shows the corresponding free field (infinite temperature) value, which is about 5% smaller than the value obtained at  $T \simeq 1.45T_c$ .

### 5.1 The Vector SPF and Dilepton Rate in the Continuum at $T \simeq 1.45T_c$

$\omega_0/T$	$\Delta_\omega/T$	$2c_{BW}\tilde{\chi}_q/\tilde{\Gamma}$	$\tilde{\Gamma}$	$k/\tilde{\chi}_q$	$\chi^2/dof$
0.0	0.5	1.290(46)	2.091(112)	0.1677(42)	0.08
0.5	0.5	1.315(43)	2.038(114)	0.1683(41)	0.11
1.0	0.5	2.039(22)	1.198(25)	0.1739(4)	0.19
1.5	0.5	2.694(19)	0.866(15)	0.1760(4)	0.56
1.75	0.5	3.338(18)	0.679(15)	0.1774(4)	1.00
1.5	0.0	2.471(20)	0.947(17)	0.1778(4)	0.32
1.5	0.1	1.976(23)	1.232(27)	0.1741(4)	0.36
1.5	0.25	2.873(19)	0.808(13)	0.1773(4)	0.39
1.5	0.5	2.694(19)	0.866(15)	0.1760(4)	0.56

Table 5.4: Parameters for the fits shown in Fig. 5.12 left (top) and right (bottom). The last column gives the  $\chi^2/dof$  of these fits.

of the continuum part of the spectral function. This is shown in Fig. 5.13, where we compare the ratio  $R_{ii}^{(2,0)}$  extracted from our continuum extrapolated data (error band) with fit results obtained for different values of  $\omega_0$ . The dependence on  $\Delta_\omega$  on the other hand is less pronounced.

It can be seen that the results from the truncated Ansatz below  $\omega_0/T \lesssim 1.5$  stay within the upper edge the error band given by the data, while the truncated Ansatz has difficulties to reproduce the data at  $\omega_0/T \geq 1.5$  and fails to do so above  $\omega_0/T \geq 1.75$ . This is in accordance with the same observation made above based on the  $\chi^2$ -values. Note at this point once more the clear and significant separation between the free ratio  $R_{ii,free}^{(2,0)}$  and the interacting result obtained in this work.

The overall conclusion of this analysis is that for  $\omega/T \gtrsim (2-4)$  acceptable spectral functions do in fact not deviate from the free field-like behavior modulo the perturbative factor  $k(T)$ . Even more, we see the structure of the spectral function below  $\omega/T \lesssim (2-4)$  is sensitive to the form of the fit Ansatz. The class of functions analyzed here in this fashion however clearly favor small values for the cut-position  $\omega_0$  and a small value for the intercept of  $\rho_{ii}(\omega)/\omega$  at  $\omega = 0$ .

#### Analysis using the Maximum Entropy Method

In the next step we confront our results with the maximum entropy method. As such we discuss if and to what extent a MEM analysis can improve over our analysis so far and whether or not it can reproduce our findings.

To this extent we performed a MEM analysis of the renormalized vector correlation function on the  $128^3 \times 48$  lattice using the improved Kernel introduced in Chp. 4.3.2.

In light of the discussion of Chp. 4.3.2 it seems ill advised to choose the free continuum

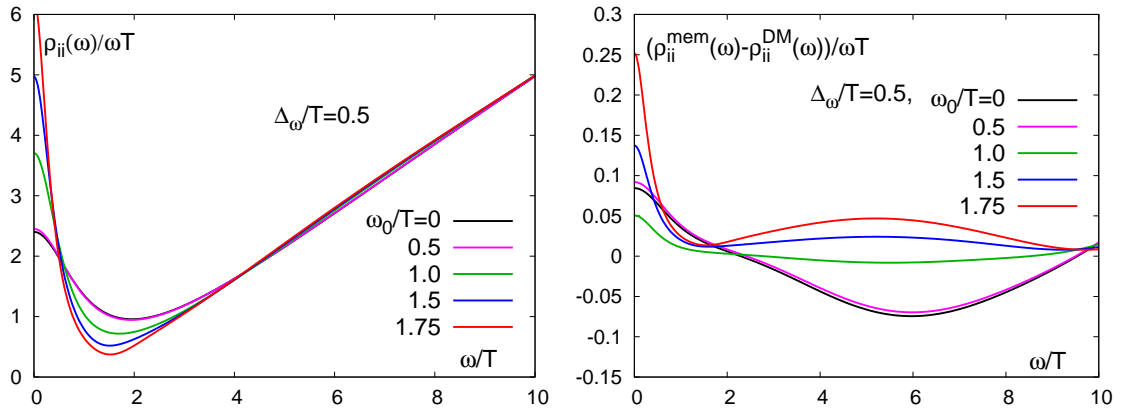


Figure 5.14: *Spectral functions obtained from a maximum entropy analysis using for the default model the spectral functions shown in Fig. 5.12(left). The right hand figure shows the difference between the output spectral function obtained from the MEM analysis and the input spectral function used in each case.*

spectral function as default model. We already know that the MEM algorithm cannot produce a finite intercept in  $\rho(\omega)/\omega$ , if the default model does not contain such a feature, recall Fig. 4.4.

Clearly the best knowledge we have on the spectral function originates from our analysis using the fit Ansatz. It thus seems reasonable to use the results of the above analysis as input for MEM. At this stage one however needs to acknowledge that also MEM can be over-constrained if the input information is too restrictive. In such case the probability peak  $P(\alpha)$  disintegrates and becomes a continuously rising function.

This was checked in all MEM runs and only the result spectral functions that preserve the  $\alpha$ -peak are shown in Fig. 5.14(left). Here the input information is given by the spectral functions shown in Fig. 5.12(left), while the error on the output spectral functions was controlled by performing the MEM analysis within a jackknife analysis.

As a consequence of Fig. 5.14(left) we may judge the stability of the spectral functions obtained by the fit Ansatz using the maximum entropy method. To see this we show the difference between the default models, i.e. our fit Ansatz results, and the output spectral functions obtained by MEM in Fig. 5.14(right). The deviations thereby correspond to unconstrained changes in the spectral functions from MEM and are generally seen to be smaller than  $< 5\%$ . These deviations on the other hand increase for small frequencies  $\omega$  as the  $\chi^2/d.o.f.$  of the default model gets worse. This observation in turn solidifies our Ansatz method.

As a side remark note that the MEM analysis reproduces the calculated ratio of thermal moments as well or even better than the fits used as a default model, although the value of the thermal moments itself did not directly enter the MEM analysis. This can be seen from Fig. 5.13 where the MEM results are also given.

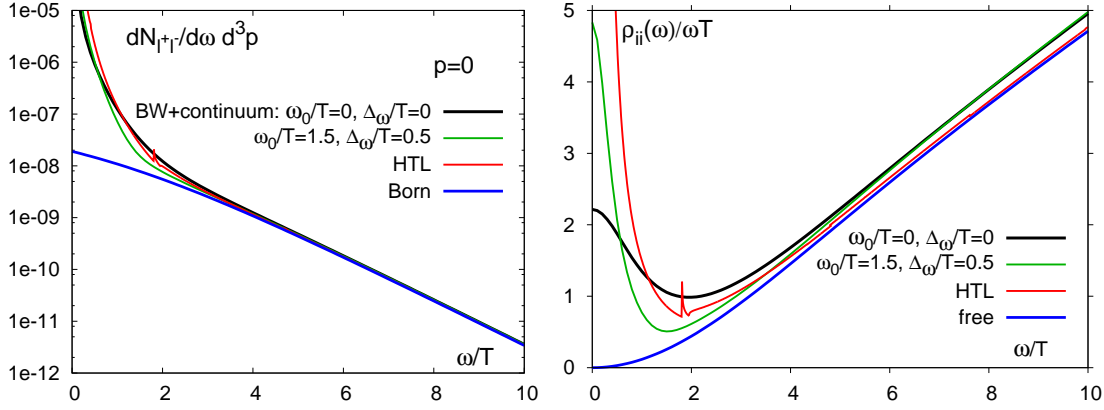


Figure 5.15: Thermal dilepton rate in 2-flavor QCD (left). Shown are results from fits without a cut-off on the continuum contribution ( $\omega_0/T = 0$ ) and with the largest cut-off tolerable in our fit Ansatz ( $\omega_0/T = 1.5$ ). The HTL curve is for a thermal quark mass  $m_T/T = 1$  and the Born rate is obtained by using the free spectral function. The right hand part of the figure shows the spectral functions that entered the calculation of the dilepton rate.

### 5.1.6 The Thermal Dilepton Rate and Electrical Conductivity

The extensive analysis and discussion of our results of the vector correlation function permitted the computation of the vector spectral function at vanishing momentum in the continuum at  $T \simeq 1.45T_c$ .

With these results we may now discuss the consequences and impact have on the thermal production rate of dileptons, the electrical conductivity of the quark gluon plasma and the related soft photon production rate.

First the systematic analysis of the fit Ansatz enables us to put a systematic error on our spectral function result. To do so we choose the result obtained from the simple un-truncated Ansatz as lower bound, while the upper bound is given by the truncated Ansatz spectral function with parameters  $\omega_0/T = 1.5$  and  $\Delta_\omega/T = 0.5$ . The latter spectral function gave a  $\chi^2/d.o.f. \sim 1$  and is thus on the outer rim of what we consider a fit that describes the data well.

In Fig. 5.15 we show the thermal dilepton rate calculated from the vector spectral function via Eq. 1.21 for two massless (u,d) quark flavors. These results are compared to the dilepton spectrum calculated within the hard thermal loop approximation Eq. 3.146 using a thermal quark mass  $m_T/T = 1$ . Clearly the results are in good agreement for all  $\omega/T \gtrsim 2$ . For  $1 \lesssim \omega/T \lesssim 2$  differences between the HTL spectral function and our numerical results is about a factor two, which also is the intrinsic uncertainty in our spectral analysis. At energies  $\omega/T \lesssim 1$  the HTL results grow too rapidly, as was described in Chp. 3.3.

Via the Kubo relation Eq. 3.115 we may calculate the electrical conductivity of the

quark gluon plasma from  $\rho_{ii}(\omega)/\omega$  in the limit  $\omega \rightarrow 0$ . These results are sensitive to the choice of fit Ansatz, however in our class of Ansätze we obtain a small value for the intercept. As such our analysis suggests:

$$2 \lesssim \lim_{\omega \rightarrow 0} \frac{\rho_{ii}(\omega)}{\omega T} \lesssim 6 \quad \text{at} \quad T \simeq 1.45 T_c \quad . \quad (5.20)$$

The electrical conductivity therefore becomes:

$$1/3 \lesssim \frac{1}{C_{em}} \frac{\sigma}{T} \lesssim 1 \quad \text{at} \quad T \simeq 1.45 T_c \quad . \quad (5.21)$$

Via Eq. 1.20 this result translates into an estimate for the production rate of soft photons:

$$\lim_{\omega \rightarrow 0} \omega \frac{dR_\gamma}{d^3p} = (0.0004 - 0.0013) T_c^2 \simeq (1 - 3) \cdot 10^{-5} \text{ GeV}^2 \quad \text{at} \quad T \simeq 1.45 T_c \quad , \quad (5.22)$$

where instead of  $T_c \simeq 270\text{MeV}$  of the quenched theory, we used  $T_c \simeq 165\text{MeV}$ , which is the relevant value for QCD with two light quarks.

## 5.2 Temperature Dependence of the Vector SPF on the Lattice

In the preceding section we could successfully calculate the dilepton rate at  $T \simeq 1.45T_c$  in the continuum limit of quenched QCD. This however is just a snapshot of a single temperature in what should be the full evolution over all temperatures starting from the initial collision, as in the end one is interested in reproducing the experimental figure Fig. 1.8.

As such a single temperature is not yet enough to establish a route that might be followed by an effective hydrodynamics evolution, even though it might be used as starting point [108, 109]. Consequently more temperatures have to be studied in order to pin down the temperature evolution.

In this section we try to close this gap a little by examining also the temperatures  $T \simeq 1.2T_c$  and  $T \simeq 3.0T_c$  at  $\beta = 7.457$ . Here we do not have the data to make a continuum extrapolation and we can only compute the spectral functions at finite lattice spacing. Nevertheless the datasets at  $T \simeq 1.45T_c$  and  $\beta = 7.457$  were seen to be close to the continuum at  $\tau T \gtrsim 0.35$  and we believe that most of the relevant physics effects can indeed be already captured at this lattice spacing.

Let us therefore turn to the ratios of the correlator data to the free continuum in Fig. 5.16. Here we show the ratio of the  $\beta = 7.457$  and the  $\beta = 7.793$  lattices for the  $G_{ii}$  and  $G_V$  channels once as before in Euclidean temperature units (top) and once in physical distance (bottom).

In the bottom panel of Fig. 5.16 we see that the  $\beta = 7.457$  lattices lie on top of each other for  $\tau \lesssim 0.06\text{fm}$  and then deviate from one another. The behavior at  $\tau \lesssim 0.06\text{fm}$  can be immediately understood in light of the analysis of cut-off effects in Chp. 5.1. As such the cut-off effects were shown to dominate the low distance region of the correlation functions. In this work the temperature is varied by varying  $N_\tau = 16, 32, 40$  while keeping  $\beta = 7.457$  fixed, consequently also the lattice cut-off is kept fixed. As a result the cut-off effects should remain the same and this is indeed what is seen in the bottom panel of Fig. 5.16 in the low distance region.

At  $\tau \gtrsim 0.06\text{fm}$  the deviations of the results should subsequently be due to temperature effects. Notice however that the  $N_\tau = 16$  results drop throughout the entire Euclidean time interval, just as before at  $T \simeq 1.45T_c$ . With the  $x$ -axis scaled also in physical distance these results are seen to follow the low distance behavior at almost all available points. This is especially clear e.g. in  $G_V/G_{V,free}$  case on the bottom right in Fig. 5.16. As such the  $N_\tau = 16$  results are more affected by the cut-off effects throughout the Euclidean time interval, as noted before, and it is more difficult to destill the temperature effects from these results.

Nevertheless the  $N_\tau = 16$  results seem to level out at the last few available distances, in the top of Fig. 5.16 in the regime  $\tau T \gtrsim 0.4$ , they are then seen to follow the results of the  $N_\tau = 32$ , i.e.  $T \simeq 1.45T_c$ , calculations.

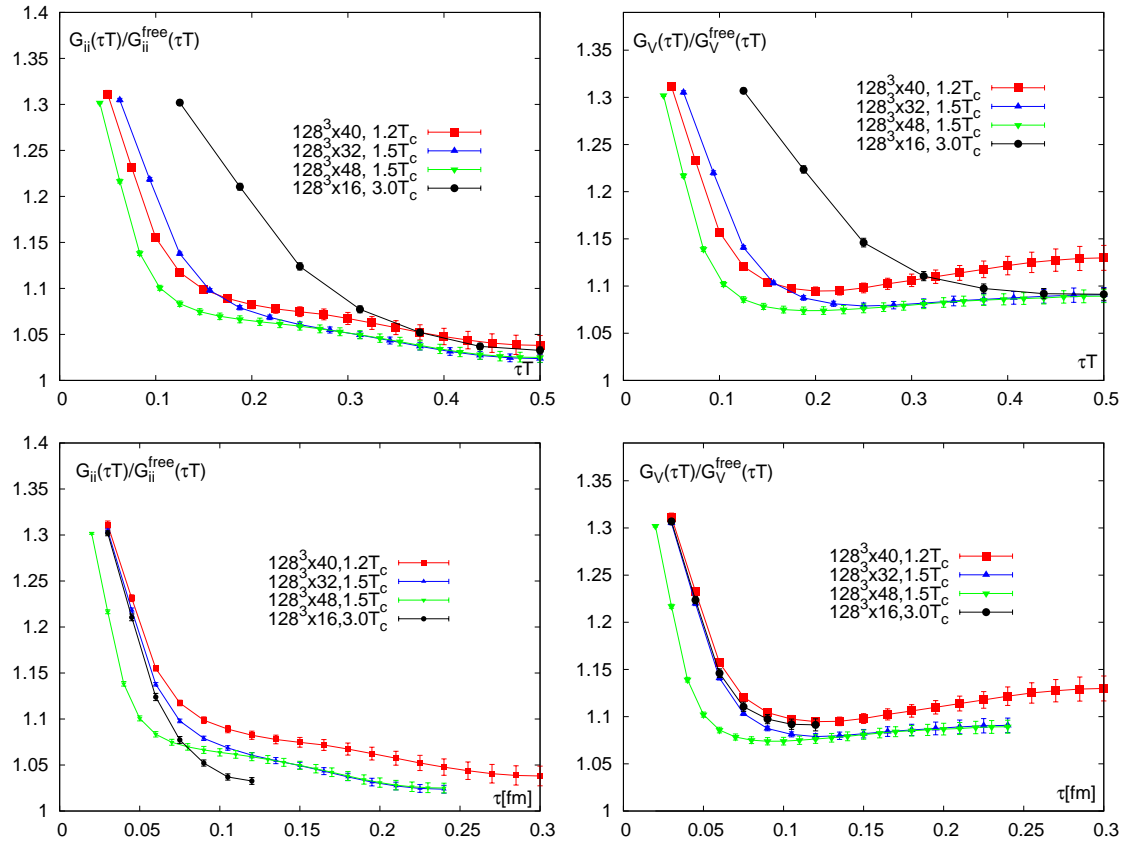


Figure 5.16: *The full (right) and spatial (left) vector correlation functions normalized by their free continuum counterparts at varying temperature. For comparison the results both from the  $N_\tau = 32$  and  $N_\tau = 48$  lattices at  $T \simeq 1.45T_c$  are shown. Results for  $T \simeq 1.2T_c$  and  $T \simeq 3.0T_c$  are obtained at  $\beta = 7.457$  and varying  $N_\tau$ , as such the lattices sized  $N_\tau = 16, 32$  and  $40$  have the same cut-off.*

The correlator ratio from the  $T \simeq 1.2T_c$  lattice on the other hand exhibits a visibly larger value for all Euclidean times, even though its trend is similar to that at  $T \simeq 1.45T_c$ . This could originate from a much broader transport peak that subsequently leaves a larger imprint on the correlator at large distances or it could be a combination of both the transport peak and a possible  $\rho$ -resonance contribution.

### The Temperature Evolution of the Quark Number Susceptibility

The temperature evolution of the quark number susceptibility has been studied quite extensively, see e.g. [101–104]. This is due to the notion that the fluctuations of conserved charges, like the quark number susceptibility in our case, are expected to be sensitive

## 5.2 Temperature Dependence of the Vector SPF on the Lattice

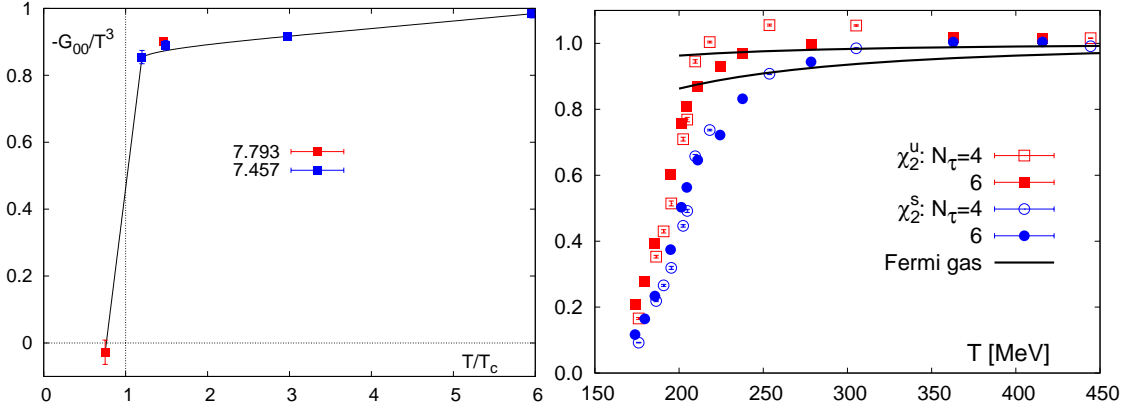


Figure 5.17: *Left: The quark number susceptibility over temperature  $T/T_c$  for the two cut-off values corresponding to  $\beta = 7.457$  and  $\beta = 7.793$ . Note here we also show preliminary light quark results from a  $128^3 \times 96$  lattice at  $T \simeq 0.75T_c$ . Right: The light and strange quark number susceptibilities versus temperature from [104]. The solid lines show results for an ideal Fermi gas with mass  $m = 100$  MeV and  $200$  MeV, respectively (top to bottom). Note to compare with units  $T/T_c$  one needs to identify  $T_c \simeq 200$  MeV.*

to the structure of a thermal medium produced in HIC-events. As such it could be argued that quark number and electric charge in the QGP are in fact carried mostly by quasi-particles with quark quantum numbers, see [103].

The quark number susceptibility and its temperature evolution based on the calculations in this work is shown in Fig. 5.17(left). Here we show the values of the  $\beta = 7.457$  and the  $\beta = 7.793$  lattices over temperature  $T/T_c$ . Whereby we also used added data from a preliminary  $N_\tau = 96$  lattice at  $\beta = 7.793$  and an older  $N_\tau = 8$  lattice at  $\beta = 7.457$ , already evaluated in [110].

To compare the results from this work and results in literature we show the light and

$\beta$	$N_\tau$	$T/T_c$	$\chi_q/T^2$
7.457	8	5.96	0.984(13)
	16	2.98	0.915(11)
	32	1.49	0.890(14)
	40	1.16	0.854(20)
7.793	48	1.43	0.902(8)
	96	0.72	-0.028(36)

Table 5.5: *Table of results for the quark number susceptibility over temperature  $T/T_c$ .*

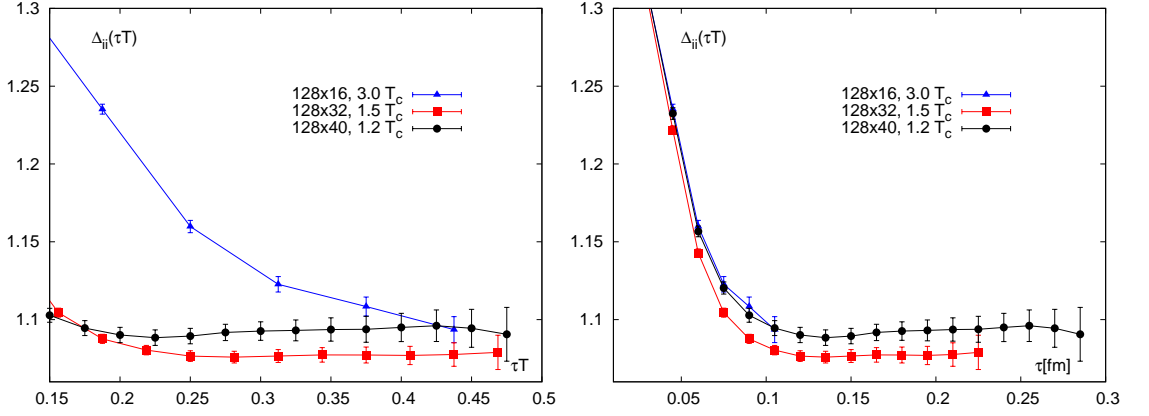


Figure 5.18: *The midpoint subtracted correlator normalized to the corresponding result in the free continuum theory,  $\Delta_{ii}(\tau T)$ , for  $T \simeq 1.2, 1.45$  and  $3.0T_c$  on lattices sized  $128^3 \times 40, 32$  and  $16$ .*

strange quark number susceptibility from [104] on the right of Fig. 5.17. These results were obtained on fully dynamical  $N_f = 2 + 1$  configurations invoking an improved staggered action (p4-action), whereby the quark masses were set to almost physical values for the light quarks and the physical value for the strange quark. Note at this point that the  $x$ -axis in Fig. 5.17(right) is given in energy units instead of  $T/T_c$ . To nevertheless compare both sides identify  $T_c \simeq 200\text{MeV}$ , consequently  $1.5T_c \simeq 300\text{MeV}$ ,  $0.75T_c \simeq 150\text{MeV}$  and so forth. Whereby it should be noted that our calculation does not include the disconnected part of the correlator, as noted in Chp. 4.

Nevertheless we observe similar behavior in both figures. Starting with a very low value clearly both figures show a rapid rise of the quark number susceptibility at  $T \simeq T_c$ . This rise then begins to level off at about  $T \simeq 1.2T_c$  and then slowly approaches the free limit. In our case the free case is approached somewhat slower, this however might be due to the quenched nature of our calculations. For reference the results of our calculation are summarized in Tab. 5.5

### 5.2.1 Temperature Evolution of the Thermal Moments

Next we turn to calculating the temperature dependence of the thermal moments, as before we calculate the quantity  $\Delta_H(\tau T)$ , omitting the normalization by the quark number susceptibility for the time being, and then fit to a quartic Ansatz.

The corresponding results for the spatial component of the vector correlation function  $\Delta_{ii}(\tau T)$ , once in Euclidean temperature units (left) and once in physical distance (right) are given in Fig. 5.18.

On the whole both figures show very similar behavior to the results for the correlator ratio. Just as we would expect from the preceding analysis, e.g. the  $N_\tau = 16$  data is dominated by large cut-off effects. At the same time the  $N_\tau = 40$  results lie somewhat above those of the  $N_\tau = 32$  lattice.

## 5.2 Temperature Dependence of the Vector SPF on the Lattice

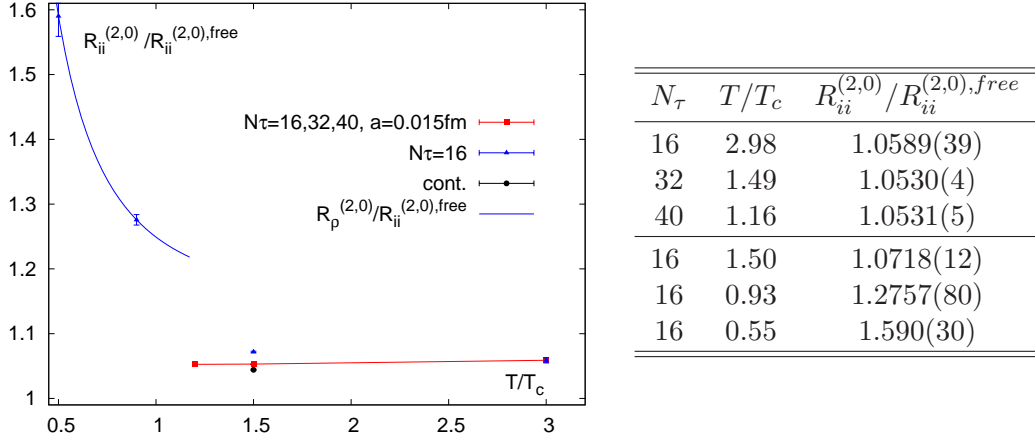


Figure 5.19: *Left: The ratio  $R_{ii}^{(2,0)}/R_{ii}^{(2,0),free}$  over  $T/T_c$  above and below  $T_c$ . Shown are the results for  $\beta = 7.457$  (red) and the continuum extrapolation at  $T \simeq 1.45T_c$  (black). Additionally a number of results from  $N_\tau = 16$  lattices at varying temperatures (blue) are given, including also results that have been obtained using data from [110]. Right: Table of results for  $R_{ii}^{(2,0)}/R_{ii}^{(2,0),free}$ .*

As the extrapolation of  $\Delta_{ii}(\tau T)$  to  $\tau T = 0.5$  yields the ratio  $G_{ii}^{(2)}/G_{ii}^{(2),free}$ , it should be noted that all results point to a slight increase of the second moment compared to the free case. Nevertheless all results lie in the vicinity of  $\sim 1.1$ , which implies that the change in the second thermal moment due to temperature effects is in fact quite small.

In Fig. 5.19 we show the results for the ratio  $R_{ii}^{(2,0)}/R_{ii}^{(2,0),free}$  over  $T/T_c$  from our calculations with  $\beta = 7.457$ , whereby we also give the  $N_\tau = 16$  and continuum extrapolated results at  $T \simeq 1.45T_c$  for comparison. Note here we added points also below  $T_c$  from calculations done by the Bielefeld lattice group that have already been extensively examined in [110].

Above  $T_c$ , i.e. temperature region evaluated here  $1.2T_c \lesssim T \lesssim 3.0T_c$ , the data are seen to be almost constant in  $T/T_c$ . Turning to the table on the right of Fig. 5.19 we identify a slight rise of the ratio within 0.5% going from  $\simeq 1.45T_c$  and  $N_\tau = 32$  to  $\simeq 3.0T_c$  and  $N_\tau = 16$ , this however may be accounted for as the latter results are much more affected by the cut-off effects due to the limited number of points in the time direction in the latter, see also Fig. 5.18(right).

Below  $T_c$  on the other hand we immediately identify a clear temperature dependence of the ratio  $R_{ii}^{(2,0)}/R_{ii}^{(2,0),free}$ . As such there is a 30% difference between the results at  $T \simeq 0.55T_c$  and  $T \simeq 0.93T_c$ . At the same time the result at  $T \simeq 0.93T_c$  is roughly 20% larger than that above  $T_c$ .

Together the drop below and the constant behavior above  $T_c$  are very interesting from the point of view of a possible  $\rho$ -resonance in the spectrum. As such we estimate the impact of a  $\rho$ -resonance on the ratio of thermal moments  $R_{ii}^{(2,0)}/R_{ii}^{(2,0),free}$ .

To do so we assume the  $\rho$ -resonance to contribute a single cosh in the correlator:

$$G_\rho(\tau) = A \cdot \cosh \left[ \frac{m_\rho}{T} \cdot \tau T \right] \quad , \quad (5.23)$$

taking the second derivative in  $\tau T$  of  $G_\rho(\tau)$  would then give the second thermal moment, thus we find:

$$R_\rho^{(2,0)} = \left( \frac{m_\rho}{T} \right)^2 = \left( \frac{m_\rho}{T_c} \right)^2 \cdot \left( \frac{T_c}{T} \right)^2 \quad . \quad (5.24)$$

As a consequence we expect the ratio  $R_\rho^{(2,0)}$  to go like  $\sim 1/T^2$ . Adding also a continuous contribution to this model ratio we arrive at the following estimate for the temperature dependence below  $T_c$ :

$$R_{T < T_c}^{(2,0)} = c_{cont} + \left( \frac{c_\rho m_\rho}{T_c} \right)^2 \cdot \left( \frac{T_c}{T} \right)^2 \quad . \quad (5.25)$$

Even though we have only two points below  $T_c$  we can nevertheless fit this estimate to the data and the result is shown as blue line in Fig. 5.18. The mass contribution of the  $\rho$ -resonance calculated in this way is  $c_\rho m_\rho(T < T_c) \simeq 1.67\text{GeV}$ .

This and the qualitatively very different behavior above and below  $T_c$  observed in Fig. 5.19, subsequently leads us to conclude that the drop of the ratio  $R_{ii}^{(2,0)}/R_{ii}^{(2,0),free}$  below  $T_c$  is in fact mostly due to a particle contribution. At the same time the constant behavior of the ratio above  $T_c$  suggests that the  $\rho$ -resonance does not contribute to  $R_{ii}^{(2,0)}/R_{ii}^{(2,0),free}$  and thus the correlator anymore.

### 5.2.2 Consequences for the Spectral Functions

With the above results in hand we now turn to discussing their consequences on the vector spectral function.

To do so we once more invoke the Breit-Wigner+continuum Ansatz and fit to the  $T \simeq 1.2T_c$ ,  $1.45T_c$  and  $T \simeq 3.0T_c$  data. Unfortunately we cannot fall back on a continuum extrapolation and the data is contaminated by lattice effects.

Because of this we abandon the systematic calculation using the Breit-Wigner+truncated Ansatz, as explained in Chp. 5.1, for the time being. Instead we analyze the dependence of the fit parameters on  $\tau_{min}T$ , as, with the data being subject to potentially large lattice effects, especially in the  $N_\tau = 16$  case, our greatest source of error originates from the fit-window we choose. The results obtained from this analysis are summarized in Tab. 5.6.

From Tab. 5.6 it can be seen that the results at  $\tau_{min}T = 0.396$  and  $\tau_{min}T = 0.354$  have the largest errors, this is understandable, as only very few points are actually passed to the fit. Nevertheless these results should be closest to those in the continuum as only the furthest distance points are comparatively free of lattice effects. Without a continuum

## 5.2 Temperature Dependence of the Vector SPF on the Lattice

$T/T_c$	$\tau_{min}T$	$2c_{BW}\tilde{\chi}_q/\tilde{\Gamma}$	$\tilde{\Gamma}$	$k/\tilde{\chi}_q$	$\chi^2/dof$	$1/C_{em} \cdot \sigma/T$	$R_{sum}$
2.98	0.396	0.93(19)	3.07(70)	0.160(19)	0.54	0.31(7)	4.0(7)
	0.354	0.91(11)	2.93(78)	0.166(11)	0.72	0.30(4)	3.9(8)
	0.3125	0.90(8)	3.08(36)	0.189(6)	1.37	0.30(3)	3.7(7)
	0.25	0.71(2)	3.75(14)	0.122(4)	2.07	0.24(1)	4.4(9)
1.49	0.396	0.98(23)	3.14(80)	0.165(23)	0.01	0.33(8)	4.4(9)
	0.354	0.97(11)	3.16(40)	0.166(11)	0.07	0.32(4)	4.4(12)
	0.3125	0.92(4)	3.47(16)	0.164(7)	0.26	0.31(1)	4.9(17)
	0.25	0.90(2)	3.53(10)	0.170(4)	1.16	0.30(1)	5.0(18)
1.16	0.396	1.00(34)	3.25(12)	0.235(38)	0.01	0.33(11)	4.7(9)
	0.354	0.99(17)	3.30(62)	0.236(18)	0.01	0.33(6)	4.8(14)
	0.3125	0.88(6)	3.89(20)	0.233(12)	0.05	0.29(7)	5.8(23)
	0.25	0.87(4)	3.89(18)	0.242(6)	0.14	0.29(1)	5.7(22)

Table 5.6: *The fit parameters of the simple Breit-Wigner+continuum Ansatz for  $T \simeq 1.45T_c$ ,  $1.2T_c$  and  $T \simeq 3.0T_c$  on lattices with temporal extent  $N_\tau = 16, 32$  and  $40$ . Here the fit window was varied between  $\tau_{min}T = 0.25$  and  $\tau_{min}T = 0.396$ . When the corresponding point was not available on the lattice at hand a spline interpolation combined with a jackknife analysis was used to provide it. Note the right hand column,  $R_{sum}$ , is explained around Eq. 5.31.*

extrapolation however it is at this point not possible to discern the residual deviation due to the lattice cut-off.

Decreasing  $\tau_{min}T$  on the other hand leads to visible systematic trends in the parameters, as such the electrical conductivity and the correction term  $k/\tilde{\chi}_q$  decrease with increasing  $\tau_{min}T$ , while the width  $\tilde{\Gamma}$  increases. Additionally the  $\chi^2/dof$  increases with decreasing  $\tau_{min}T$  implying a lower quality fit with lower  $\tau_{min}T$ . In light of the argument above these results show that indeed the lattice effects influence the fit more strongly with smaller  $\tau_{min}T$ , as they cannot be taken care of by the employed Ansatz. Consequently we attribute the largest part of the systematic trends observed above to the lattice effects.

Focusing on the parameters themselves note that the correction factor  $k(T)$  is the most accurately determined, as before. Clearly it shows an increasing trend with decreasing temperature differing by a factor  $\sim 1.5$  between  $T \simeq 3.0T_c$  and  $T \simeq 1.2T_c$ . However as  $k(T)$  is coupled to the strong coupling via  $k(T) \simeq \alpha_s/\pi$  [105], this behavior is expected. The same can be seen for the width  $\tilde{\Gamma}$  and the parameter  $2c_{BW}\tilde{\chi}_q/\tilde{\Gamma}$ , they also slightly increase with decreasing temperature. However here, they remain within errors of each other and the increase between  $T \simeq 3.0T_c$  and  $T \simeq 1.2T_c$  is only roughly  $\simeq 7\%$ .

Naturally this leads also to at maximum  $\simeq 7\%$  deviations of the absolute values of the electrical conductivity. Note however that the  $N_\tau = 16$  differs by  $\simeq 5\%$  from the  $N_\tau = 32$  results, while this deviation is only  $\simeq 2\%$  for  $N_\tau = 40$ . With the  $N_\tau = 16$  lattice being

most affected by the systematics of the fit, we assume the largest part of this deviation to find its origins there. Even so we find the electrical conductivity to be to a good degree constant and within  $\simeq 7\%$  across the temperature region evaluated here, whereby the values at the individual temperatures have fit errors around  $\simeq (7 - 11)\%$ .

In the next step these results are now confronted with the expectations of the temperature dependence of the electrical conductivity in a pion gas [106] and from perturbation theory [111]:

$$\sigma \sim \sqrt{m_\pi/T} \quad \text{in a pion gas at } T \ll m_\pi \quad , \quad (5.26)$$

$$\sigma \sim (m_\pi/T)^2 \quad \text{in a pion gas at } T \leq m_\pi \quad , \quad (5.27)$$

$$\sigma \sim T \quad \text{from weak coupling perturbation theory, i.e. at } T \gg T_c \quad . \quad (5.28)$$

As the electrical conductivity is given in units of temperature above, the results from this work at  $\beta = 7.457$  imply:

$$\sigma = (0.33 \pm 0.02 \pm 0.04) \cdot C_{em} \cdot T \quad , \quad (5.29)$$

whereby the first error quoted corresponds to the temperature effects and the second to the fit errors. Consequently the results indicate that the electrical conductivity indeed goes linear in temperature above  $T_c$ .

Using Eq. 1.20 this result implies the production rate of soft photons goes as:

$$\lim_{\omega \rightarrow 0} \omega \frac{dR_\gamma}{d^3p} = \frac{3\alpha_{em}}{2\pi^2} C_{em} \cdot (0.33 \pm 0.02 \pm 0.04) \cdot T^2 \quad (5.30)$$

and therefore increases quadratically in temperature.

In addition to the temperature dependence of the electrical conductivity it can be shown in perturbation theory that the area of the low frequency peak in the vector spectral function satisfies a sum rule [112]:

$$R_{sum} = \int_{\text{peak}} d\omega \frac{\rho(\omega)}{\omega} = \frac{2\pi}{3} \cdot N_c \cdot C_{em} \quad , \quad (5.31)$$

whereby inserting  $C_{em}$  for  $N_F = 2$  and  $N_F = 3$  we obtain  $R_{sum}(N_F = 2) = 3.49$  and  $R_{sum}(N_F = 3) = 4.19$ .

With the results obtained above we can immediately check the integral over the low frequency peak as required and the results are given on the far right of Tab. 5.6. At large  $\tau_{min}T$  we clearly observe an increasing trend with decreasing temperature. Nevertheless the results agree within errors and as before the largest deviation manifests itself in the  $N_\tau = 16$  results. However, as  $\tau_{min}T$  is decreased there is a large increase in the integral of the order of  $10\% - 20\%$  for the  $N_\tau = 16$  and the  $N_\tau = 40$  results, respectively. It consequently seems that the integral over the peak is far more sensitive to the systematic uncertainties inherent in the data. As a result we cannot firmly exclude or establish the above sum rule with the current status of our data, nevertheless our current results do lean towards confirming it.

# The Vector Spectral Function at Finite Momentum

So far we have concentrated on the case of vanishing momentum. The study of free spectral functions in Chp. 3 however revealed a particularly rich structure at finite momentum.

Here we present a first level analysis of the properties of the finite momentum correlation functions at  $T \simeq 1.45T_c$  and examine the possible consequences of our results for the finite momentum spectral functions.

To this extent we generated also meson correlators at finite lattice momentum which may be connected to the physical scale  $|p|/T$  via:

$$\frac{|p|}{T} = 2\pi \cdot |\vec{k}| \cdot \frac{N_\tau}{N_\sigma} \quad . \quad (6.1)$$

In our calculation we restrict ourselves to integer components of the momentum vector, i.e.  $\vec{k} = (i, i, i)$  where  $i \in \mathbb{N}$ , consequently the aspect ratio  $N_\sigma/N_\tau$  puts a hard limit on the available momenta on our lattices \*.

$\vec{k} = (x, y, z)$	$ p /T(N_\tau = 16)$	$ p /T(N_\tau = 24)$	$ p /T(N_\tau = 32)$	$ p /T(N_\tau = 48)$
(0,0,1);(1,0,0)	0.7854	1.1781	1.5708	2.3562
(0,0,2);(2,0,0)	1.5708	2.3562	3.1416	4.7124
(0,0,3);(3,0,0)	2.3562	3.5343	4.7124	7.0686
(1,1,0)	1.1107	1.6661	2.2214	3.3322
(2,1,0)	1.7562	2.6343	3.5124	5.2686
(2,2,0)	2.2214	3.3322	4.4429	6.6643
(3,1,0)		3.7255	4.9673	7.4509
(3,2,0)		4.2487	5.6636	8.4954
(3,3,0)		4.9982	6.6643	9.9965

Table 6.1: *Table of available momenta in  $|p|/T$  at  $T \simeq 1.45T_c$  on lattices sized  $128^3 \times 48, 32, 24$  and  $16$ .*

\*In the future it would be interesting to extend our study also to (smaller) non-integer momenta using twisted boundary conditions [113].

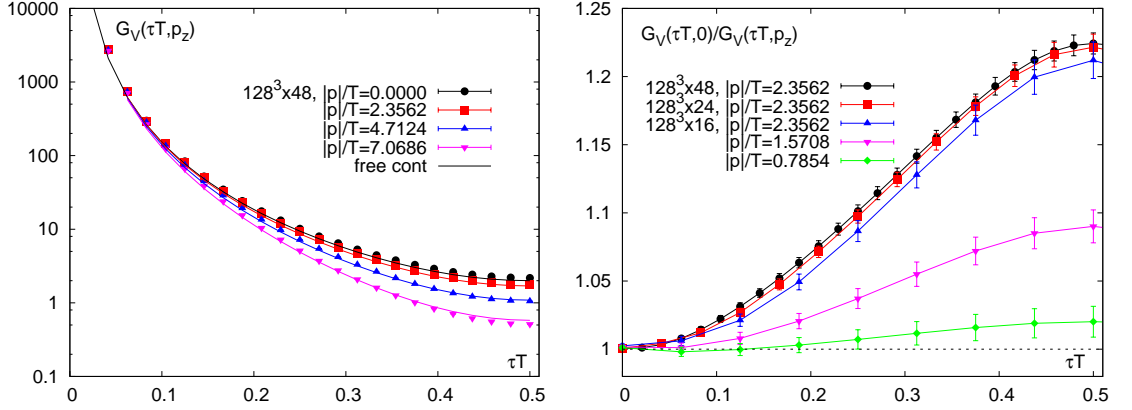


Figure 6.1: *Left: The full vector correlator at  $N_\tau = 48$  with increasing momentum, shown are the results for momenta  $\vec{k} = (0, 0, p_z)$  where  $p_z = 0, 1, 2, 3$ . The colored solid lines hereby denote the corresponding free continuum correlation functions. Right: The ratio of the vector correlation function at varying momenta and the vanishing momentum case. The lower  $N_\tau = 16$  momenta approach the  $N_\tau = 48$  results, however due to cut-off effects do not lie on top of each other at  $|p|/T = 2.3562$ . For comparison at this momentum the results of the  $N_\tau = 24$  lattice are shown, these are seen to be closer to those of  $N_\tau = 48$ .*

The momenta that we could compute in this way are listed in Tab. 6. Without including the  $N_\tau = 16$  there are never more than two matching momenta across the examined lattice sizes, subsequently a continuum extrapolation as was done in the case of vanishing momentum is not possible. Fortunately, recalling Fig. 5.9, the  $N_\tau = 48$  results are seen to be very close to the continuum extrapolation for Euclidean times as low as  $\tau T \simeq 0.25$ , this carries over to finite momentum, as we will see shortly, and in the following we will subsequently mostly examine the results from the  $N_\sigma = 128 \times N_\tau = 48$  lattice.

First look at the difference of the finite momentum case compared to that at vanishing momentum. In Fig. 6.1(left) we show the full vector correlation function at  $N_\tau = 48$  for the momentum in  $\vec{z}$ -direction. We gather that with increasing momentum the correlation function decreases and clearly deviates from the vanishing momentum case at Euclidean times as early as  $\tau T \gtrsim 0.05$ , at the midpoint we make out a difference of a factor  $\sim 3$  between the  $|\vec{k}| = 0$  and  $|\vec{k}| = 3$  case.

As before however the exponential decay dominates the correlator and we take the ratio  $G_V(\tau T, 0)$  and  $G_V(\tau T, \vec{p})$  to examine the momentum induced deviation more closely. From Tab. 6 it is apparent that the lowest physical momenta are achieved by the  $N_\tau = 16$  lattice while the highest are reached for  $N_\tau = 48$ . As such the results from  $N_\tau = 16$  to  $N_\tau = 48$  give a connected line of physical momenta as both contain  $|p|/T = 2.356$ . In Fig. 6.1(right) we therefore show the ratio  $G_V(\tau T, 0)/G_V(\tau T, \vec{p})$  for momentum in  $\vec{z}$ -

direction for the  $N_\tau = 16$  lattice and the first momentum in  $\vec{z}$ -direction for  $N_\tau = 48$ . The figure shows the consequences drawn from the left hand figure on a more firmly basis. Interestingly the momentum  $|p|/T = 2.356$  does not match up between the  $N_\tau = 16$  and  $N_\tau = 48$  lattices, this mirrors the results at vanishing momentum, see e.g. Fig. 5.9. Recall that there the  $N_\tau = 16$  lattice was seen to be highly contaminated with lattice effects, as a consequence it was neglected in the continuum extrapolation. From Fig. 6.1(right) at  $|p|/T = 2.356$  we conclude that this behavior indeed carries over to finite momentum. For comparison also the  $N_\tau = 24$  results at the quark mass  $m/T \simeq 0.1$  and momentum  $|p|/T = 2.356$  are shown in Fig. 6.1(right), these results match up much more nicely with those of  $N_\tau = 48$  as expected.

## 6.1 Analyzing the Vector Correlation Function at Finite Momentum

In Chp. 3 the finite momentum spectral functions were discussed at length, one of the consequences shown in this context was the splitting of the spatial vector correlator into transversally and longitudinally polarized parts:

$$G_{ii}(\tau T, \vec{p}) = 2 \cdot G_T(\tau T, \vec{p}) + G_L(\tau T, \vec{p}) \quad . \quad (6.2)$$

As result five different components or versions of the vector correlation function can be studied, which of course are not independent of each other:

- $G_T(\tau T, \vec{p})$ ,
- $G_V(\tau T, \vec{p})$ ,
- $G_{00}(\tau T, \vec{p})$ ,
- $G_{ii}(\tau T, \vec{p})$ .
- $G_L(\tau T, \vec{p})$ ,

As discussed in Chp. 3 some of these correlators are more difficult to analyses because the underlying interacting spectral functions contain superpositions of a number of different effects, e.g.  $G_V(\tau T, \vec{p})$ . While others are theoretically simpler to understand, e.g. due to a direct connection as in the case of  $G_{00}(\tau T, \vec{p})$  and  $G_L(\tau T, \vec{p})$ . The transversal correlator  $G_T(\tau T, \vec{p})$  hereby takes the middle ground, while phenomenologically speaking it is highly interesting as it directly connects to the photon rate, see Eq. 1.17.

Note at this point that the evaluation of the time-time correlator is postponed to a later section, it will prove useful to examine it directly through its thermal moments and the connection to the longitudinal channel below.

In Fig. 6.2 we give the ratio of the correlation function and its free continuum counterpart in the  $G_V(\tau T, \vec{p})$ ,  $G_{ii}(\tau T, \vec{p})$ ,  $G_T(\tau T, \vec{p})$  and  $G_L(\tau T, \vec{p})$  channels for the momenta  $\vec{k} = (0, 0, p_z)$  where  $p_z = 0, 1, 2, 3$ . Here we only show the results from the  $N_\tau = 48$ ,  $T \simeq 1.45T_c$ , as noted above, subsequently the physical momenta evaluated are  $|p|/T = 0.0, 2.3562, 4.7124$  and  $7.0686$ . Note the  $|p|/T = 0$  lines are identical to

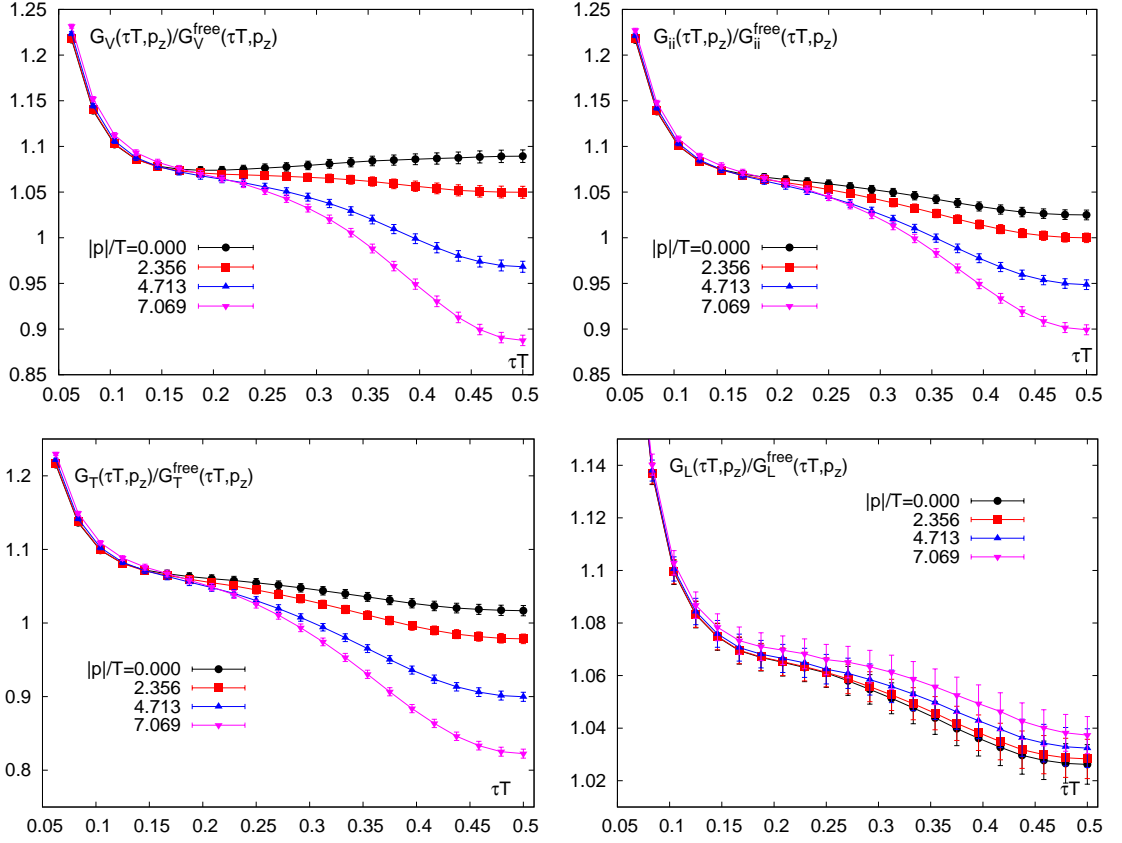


Figure 6.2: *The vector correlation functions at finite momentum normalized by its free continuum counterparts over Euclidean time. Shown are from top left to bottom left in clockwise order the full, spatial, longitudinal and transverse results for momenta  $\vec{k} = (0, 0, p_z)$  where  $p_z = 0, 1, 2, 3$  on the  $N_\tau = 48$  lattice. These momenta correspond to the physical momenta  $|p|/T = 2.3562, 4.7124$  and  $7.0686$  respectively.*

those shown in Chp. 5.1. Whereby the vanishing momentum free continuum correlator in the transversal and longitudinal channels is given by one third of the spatial vector correlator due to Eq. 6.2, as the transverse and longitudinal channels degenerate in the limit  $p \rightarrow 0$ .

In the low distance part  $\tau T \lesssim 0.15$  we expect a dominant cut-off contribution, as in the case of vanishing momentum, to carry over to the case of finite momentum. Indeed the characteristic rapid drop can be seen in all channels and at all momenta. Going further the datasets are seen to lie almost on top of each other at these distances, implying a negligible momentum dependence of this part of the correlator.

Note here that the correction factor introduced in Chp. 5.1 due to the strong coupling  $k(T) \simeq \alpha_s/\pi$  in principle admits also a momentum dependence  $k(T) \rightarrow k(T, \vec{p})$ . How-

## 6.1 Analyzing the Vector Correlation Function at Finite Momentum

ever, the observed negligible momentum dependence in the region  $\tau T \lesssim 0.15$  implies that  $k(T)$  is in fact momentum independent. As both the longitudinal and transverse channels degenerate in the limit of vanishing momentum, this statement also implies that both channels are subject to the same  $k(T)$ .

A weak momentum dependence can also be seen in the longitudinal channel for  $\tau T \gtrsim 0.15$ . Here the ratio decreases with increasing distance for all momenta, however, all results remain within errors throughout the momentum region evaluated. As such the ratio at vanishing momentum drops from about  $\sim 1.07$  at  $\tau T = 0.2$  to  $\sim 1.02$  at  $\tau T = 0.5$ , whereby all momenta evaluated remain above and within  $< 2\%$  of this value. At the same time the ratio shows a milder decrease with increasing momentum, e.g. the  $p_z = 3$  result drops only from  $\sim 1.075$  at  $\tau T = 0.2$  to  $\sim 1.04$  at  $\tau T = 0.5$ .

These observations are in stark contrast to those of the transverse and as a result the spatial and full ratios. Concentrating on the transverse channel at  $\tau T \gtrsim 0.15$ , we also see a decreasing trend of the ratio with increasing Euclidean time. Here however the ratio is seen to drop by  $\sim 20\%$  between the vanishing momentum and the  $|p|/T = 7.0686$  case. So where in the longitudinal channel the vanishing momentum case set a lower bound and larger momenta only deviated marginally, in the transverse the vanishing momentum results sets an upper bound and the larger momenta deviate quite drastically.

This strong momentum dependence consequently sets the behavior of the composite spatial and full vector correlator ratio, as the drop originating in the transverse channel at  $\tau T \gtrsim 0.15$  dominates the result.

In the region where cut-off effects are under control all correlator ratios are seen to show a decreasing trend with increasing distance. Taking into account the correction factor  $k(T)$  this implies that the free correlation function in this distance region is larger than the corresponding data, subsequently the ratio of the two tends to smaller values. Note the smallest values are thereby reached at and around the midpoint.

As this is the region where the low frequency region of the spectral function has its largest impact, on the level of the spectral functions this behavior entails that the free spectral function in the low frequency regime is in fact larger than its interacting counterpart. So the contribution of the interacting low frequency spectral function is smaller than the non-interacting limit.

Consequently the latter puts an upper bound on the contributions that we would model in an Ansatz. Such a behavior also seems to be in accordance with the results of the Langevin and Boltzmann approaches discussed in Chp. 3.2, as here also the free spectral functions were seen to be somewhat larger than those of the interacting results.

### 6.1.1 Thermal Moments of the Finite Momentum Correlators

As the zeroth thermal moment of the correlation functions is given by the midpoint of the correlator itself, the observed trends in Fig. 6.2 already show that the zeroth moment is significantly reduced in the transverse and only lightly in the longitudinal channels compared to their free counterparts. Clearly this mirrors the discussion above that the corresponding free results are larger than those in the interacting case and are

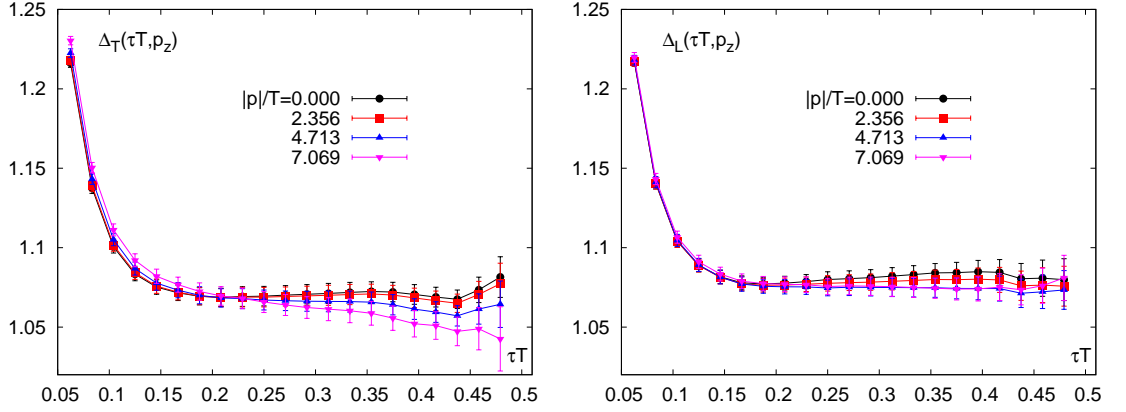


Figure 6.3: *The midpoint subtracted correlator normalized by its corresponding free counterpart  $\Delta_H(\tau T)$  at finite momentum. Shown are the results for  $N_\tau = 48$  and the momenta  $\vec{k} = (0, 0, p_z)$  where  $p_z = 0, 1, 2, 3$  in the full, spatial, transverse and longitudinal vector channels.*

approached from below. In the next step it is interesting to see what happens to the second order thermal moments.

The latter are once more evaluated via the midpoint subtracted correlator normalized by its free continuum counterpart, as defined in Eq. 4.19 and the results for  $N_\tau = 48$  at momenta  $\vec{k} = (0, 0, p_z)$  where  $p_z = 0, 1, 2, 3$  are shown in Fig. 6.3. Note in this figure only the results for the transverse and longitudinal channels are given, as the full and spatial channels are made up of these two, bar the time-time contribution in the former. Turning first to the longitudinal channel on the right of Fig. 6.3 the momentum dependence is seen to be even weaker than in the correlator ratio. The cut-off contribution once more dominates the results at  $\tau T \lesssim 0.15$ , as expected, above however all results lie within a band of roughly  $\sim 0.5\%$  and no clear trend can be identified.

Also in the transverse case the momentum dependence in the midpoint subtracted correlator normalized by the free continuum is not as clear and strong as in the ratio of the correlation functions. Nevertheless at  $\tau T \gtrsim 0.15$  a momentum dependence can be clearly identified as the large momentum results show a decreasing trend with increasing distance, especially for  $|p|/T = 7.0686$ , while the vanishing momentum and  $|p|/T = 2.3562$  results are almost flat.

In the next step the data is fitted by a quartic polynomial Ansatz, as was done in Chp. 5.1, and the ratio of the second to the second free thermal moments is extracted. Augmenting these results with those of the zeroth moment given by the midpoint of the correlation functions, we list the ratios  $G_H^{(2)}/G_H^{(2),free}$  and  $R_H^{(2,0)}/R_H^{(2,0),free}$  for the longitudinal and transverse channels in Tab. 6.2.

As one would expect the values obtained from the longitudinal results show only little change with increasing momentum. Even though a slight trend towards smaller values

## 6.1 Analyzing the Vector Correlation Function at Finite Momentum

$ p /T$	$G_T^{(2)}/G_T^{(2),free}$	$R_T^{(2,0)}/R_T^{(2,0),free}$	$G_L^{(2)}/G_L^{(2),free}$	$R_L^{(2,0)}/R_L^{(2,0),free}$
0.0000	1.073(4)	1.043(9)	1.074(2)	1.043(8)
2.3562	1.068(3)	1.095(29)	1.070(1)	1.040(7)
4.7124	1.058(2)	1.178(21)	1.066(4)	1.033(9)
7.0686	1.045(2)	1.268(18)	1.071(3)	1.033(14)

Table 6.2: *The ratio  $R_H^{(2,0)}/R_H^{(2,0),free}$  for the full, spatial, transverse and longitudinal vector channels. All results have been obtained at  $N_\tau = 48$  and  $T \simeq 1.45T_c$  using the procedure described in Chp. 5.1.*

with increasing momentum in  $R_L^{(2,0)}/R_L^{(2,0),free}$  might be identified, it should be noted that all values match within errors. In addition to this the ratio of second thermal moments  $G_L^{(2)}/G_L^{(2),free}$  is also seen to be constant within errors throughout the momentum range evaluated.

The transverse channel on the other hand exhibits a clear rise in  $R_T^{(2,0)}/R_T^{(2,0),free}$  as the momentum increases. This should be contrasted with the observation that the ratio of second thermal moments  $G_T^{(2)}/G_T^{(2),free}$  on the other hand decreases with increasing momentum. As a result the curvature of the correlator moves further towards the free case as the momentum increases, the ratio of the curvature and the midpoint on the other hand increases, implying the midpoint to drop further with increasing momentum, in accordance with the preceding results.

It will be very interesting to see in a further step whether and in what fashion these results are able to constrain the low frequency modification of the spectral function at finite momentum.

### 6.1.2 Toy Models of the Correlation Function

To get an idea if and in what fashion the data discussed above is in fact accurate enough to constrain and compute the spectral functions at finite momentum, we invoke two sets of toy models that comprise two extreme possibilities for the momentum dependence that might be at work.

Both models use the respective free continuum correlation functions as a starting point. Whereby we introduce the correction factor  $k$  as before.

In the first model we assume the momentum dependence of the low frequency contribution to be modeled by a constant contribution in the correlator, i.e. a Euclidean time-independent part. As it was seen above that the free case is larger than the interacting this contribution should be subtracted. Subsequently in the language of spectral functions this would correspond to a  $\delta$ -function with negative sign.

The second assumes the smearing of the free spectral function at  $\omega \lesssim p$  to be very weak, as to the extent that it suffices to multiply the spectral function below the lightcone only by an additional factor. This possibility thereby includes the Euclidean time-dependence

	$ p /T$	$k$	$c_{const}$	$c_{\omega < p}$
$\rho_T(\omega, \vec{p})$	2.3562	1.070	0.077	0.861
	4.7124		0.092	0.770
	7.0686		0.072	0.690
$\rho_L(\omega, \vec{p})$	2.3562	1.075	0.032	0.941
	4.7124		0.018	0.914
	7.0686		0.008	0.903

Table 6.3: *The parameters of the toy models used to generate the data in Fig. 6.4. Here  $c_{const}$  denotes the constant factor of toy model (I), Eq. 6.3, and  $c_{\omega < p}$  the factor for the low frequency part of the correlation function in toy model (II), Eq. 6.4.*

of the free case, only at a different strength. Both toy models may be written as:

$$(I) \quad G_H(\tau T, \vec{p}) = k \cdot G_H^{free}(\tau T, \vec{p}) - G_{const}$$

$$\longrightarrow \rho_H(\omega, \vec{p}) = k \cdot \rho_H^{free}(\omega, \vec{p}) - c(\vec{p})\delta(\omega) \quad (6.3)$$

$$(II) \quad G_H(\tau T, \vec{p}) = k \cdot G_{H, \omega > p}^{free}(\tau T, \vec{p}) + c(\vec{p}) \cdot G_{H, \omega < p}^{free}(\tau T, \vec{p})$$

$$\longrightarrow \rho_H(\omega, \vec{p}) = k \cdot \rho_{H, \omega > p}^{free}(\omega, \vec{p}) + c(\vec{p}) \cdot \rho_{H, \omega < p}^{free}(\omega, \vec{p}) \quad (6.4)$$

These models are now tested on the data by taking the ratio  $G_H(\tau T, \vec{p})/G_H^{toy}(\tau T, \vec{p})$ , whereby in the next step the model parameters are tuned until this ratio gives unity at least at  $\tau T = 0.5$ . The primary aim here is to compare the two toy models and to see which of the two can better describe the data, so we do not expect to achieve a perfect match throughout the Euclidean time interval. Nevertheless requiring at least the midpoint to fit we can estimate where the assumptions made in the toy models are too strong or too weak.

Following this procedure we obtain the results shown in Fig. 6.4, whereby the corresponding parameters are given in Tab. 6.3. As before we restrict ourselves to the longitudinal and transverse correlators at momentum  $p_z = 1, 2, 3$ , corresponding to the physical momenta  $|p|/T = 2.3562, 4.7124$  and  $7.0686$ . Note here that throughout we have also given the ratio of the data and the free correlation function multiplied by  $k$  for comparison in the figure.

At first glance both models are seen to be able to describe the data astonishingly well. Turning first to the transversal channel the lowest momentum results are hardly distinguishable from one for distances  $\tau T \gtrsim 0.15$ , whereby below this value we once encounter the rapid rise of the ratio due to cut-off effects, see Chp. 5.1. At this momentum both models match very closely and it is not possible to tell if one describes the data better than the other.

## 6.1 Analyzing the Vector Correlation Function at Finite Momentum

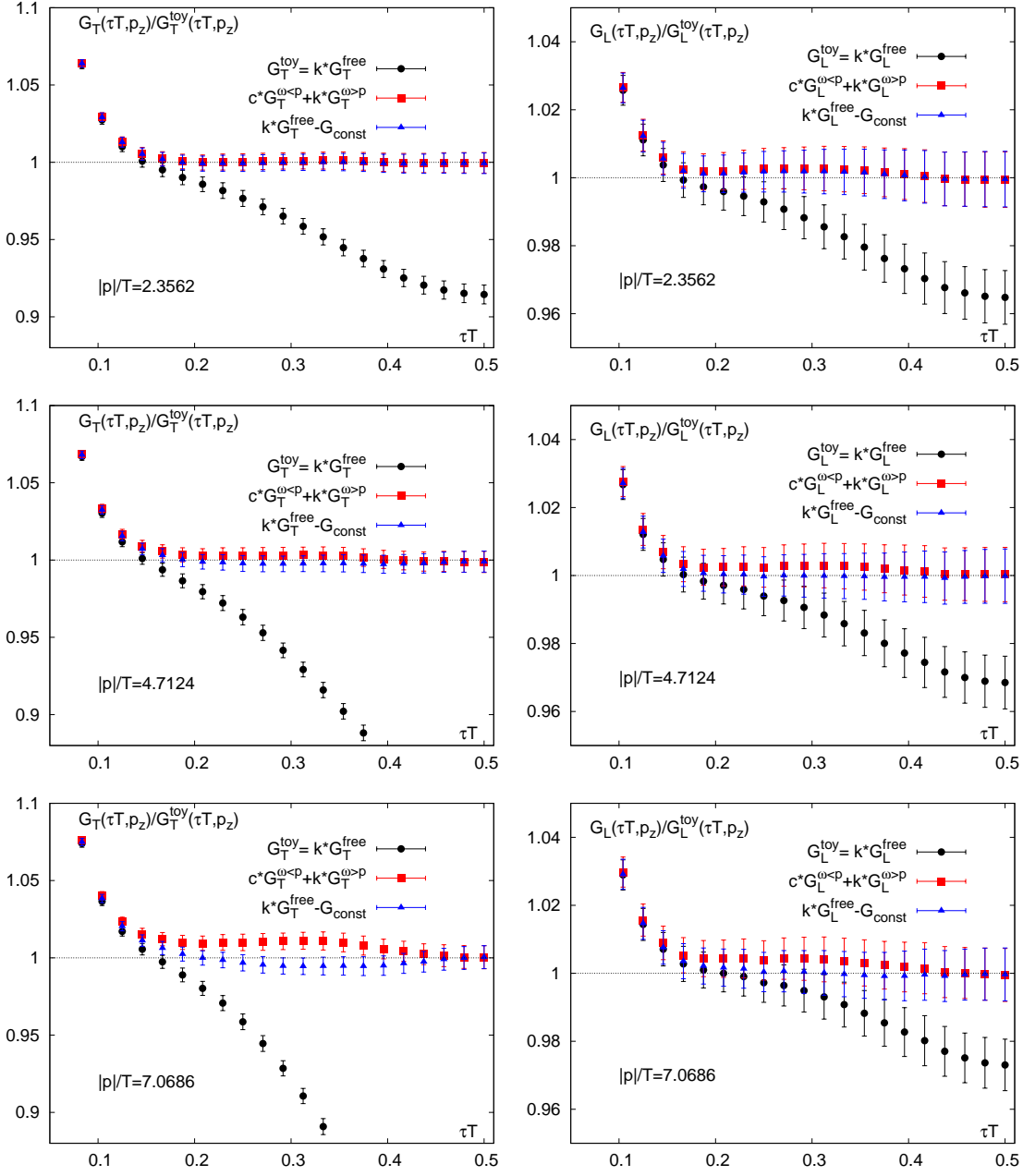


Figure 6.4: Comparison of the transverse (left) and longitudinal (right) data to results obtained by toy models at  $p_z = 1, 2, 3$ . Including a correction due to the running of the coupling via the coefficient  $k$  as before, the coefficients of the toy models are tuned to produce unity in the ratio of the data to the toy model  $G_H(\tau T, \vec{p}) / G_H^{toy}(\tau T, \vec{p})$ . The deviation from unity by the toy models gives a measure of how well they describe the data.

Increasing the momentum however, this is no longer the case. While both models can still reproduce the midpoint and the largest two or three distances, they have problems describing the intermediate distance range  $0.2 \lesssim \tau T \lesssim 0.4$ . As such toy model (II) deviates above one already at  $|p|/T = 4.7124$ , with this deviation increasing at  $|p|/T = 7.0686$ . At the same time toy model (I) can still fairly well describe the data at  $|p|/T = 4.7124$  even though a tendency to deviate below one already emerges. However at  $|p|/T = 7.0686$  this model also begins to visibly deviate.

In the longitudinal channel the situation is a little more subtle. First of all the scale of the momentum dependence is much smaller in this channel, as noted above. Secondly however both toy models deviate only within the errors of each other and we have to rely on the absolute values to draw some conclusions. As before both models are almost degenerate at  $|p|/T = 2.3562$ , at larger momenta however toy model (II) exhibits a deviation from one in the same way it did in the transverse channel. As such the ratio rises above one in the region  $0.2 \lesssim \tau T \lesssim 0.4$ . Model (I) with its constant contribution fares much better in this channel and the ratio remains very close to unity throughout all momenta evaluated.

Turning to the parameters in Tab. 6.3 note that the tuning was done by hand, as such no errors are available. Nevertheless it is interesting to note that  $k$  is identical for all momenta, as was already seen above, but it is also within 0.5% of the longitudinal and the transverse channels, whereby this discrepancy might easily arise from the errors of the data and the somewhat crude tuning technique. The model parameters  $c_{const}$  and  $c_{\omega < p}$  on the other hand both exhibit a decreasing trend with increasing momentum. There is however an exception to this trend at  $|p|/T = 4.7124$  in the transverse channel for  $c_{const}$ , here the value exceeds both those at  $|p|/T = 2.3562$  and  $|p|/T = 7.0686$ . The reason for this is unclear at the time being.

Comparing the model parameters for the longitudinal and transverse channels, notice that the constant  $c_{const}$  is significantly smaller in the longitudinal case than in the transverse case, whereby at the same time the factor  $c_{\omega < p}$  is much larger in the former than the latter. This mirrors the observation that the momentum dependence of the deviation from the free case in the longitudinal channel is much weaker than that of the transverse. With the toy models being based on the free case, with  $c_{const} = 0$  and  $c_{\omega < p} = 1$  implying no deviation from the latter, we would indeed expect a smaller modification of the free case in the longitudinal channel than the transverse.

With these results in hand we can immediately compute the thermal moments encoded in  $\Delta_H(\tau T, \vec{p})$ , Eq. 4.19, also for the toy models and directly compare them with those obtained from the data. The corresponding results are shown in Fig. 6.5, whereby we only show results with  $|p|/T \geq 4.7124$ , because the results from the lowest momentum are indistinguishable, just as was seen in the correlator ratio above. Note at this point that both models are built from the free continuum correlation functions, therefore we do not expect them to reproduce  $\Delta_H(\tau T, \vec{p})$  below  $\tau T \simeq 0.15$ .

Turning to the transverse channel and the left of Fig. 6.5 we notice that as before the shortcomings of the two models reveal themselves most clearly at  $|p|/T = 7.0686$ . However both momenta shown indicate that neither the constant contribution nor the simple free form capture the effects that are encoded in the data. As such the data occupies

## 6.2 The Time-Time Vector Channel and its Thermal Moments

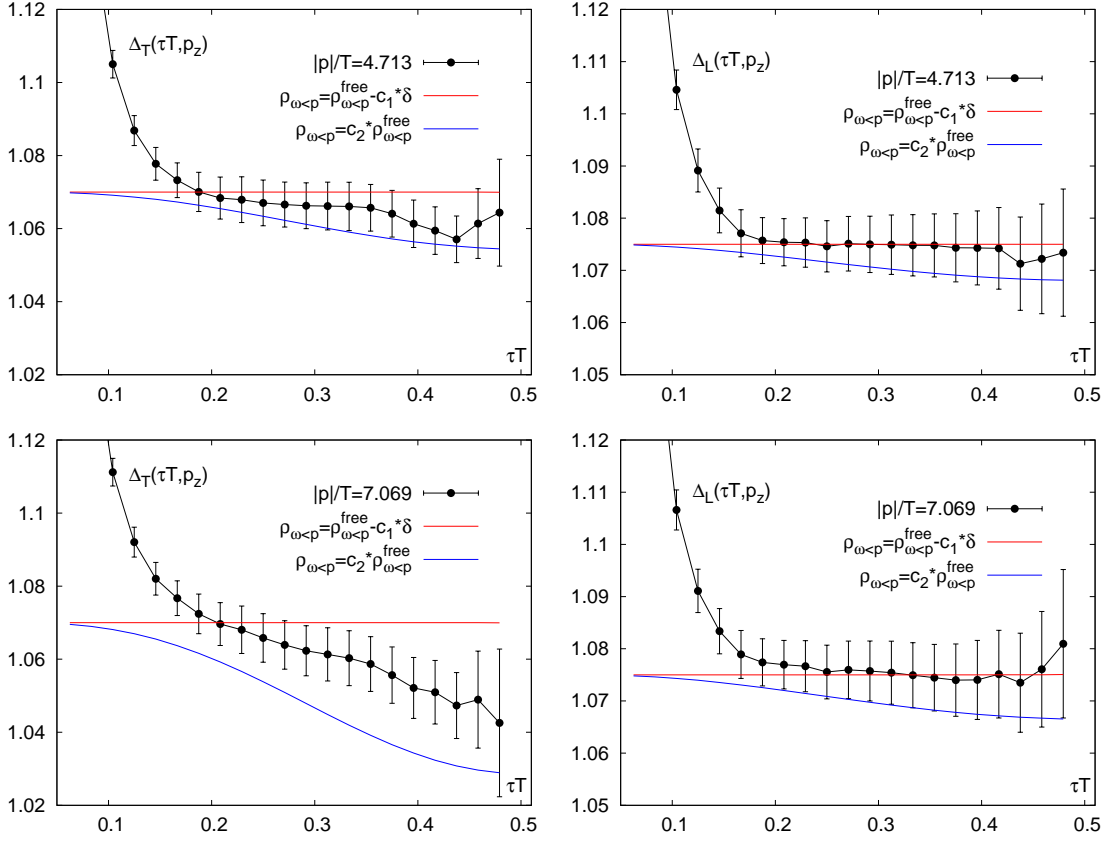


Figure 6.5: Comparison of the thermal moments encoded in  $\Delta_H(\tau T, \vec{p})$  in the transverse (left) and longitudinal (right) channels where  $\vec{k} = (0, 0, p_z)$  for  $p_z = 2, 3$  and the corresponding results from the toy models.

a middle ground between the two limiting assumptions, on which the toy models are based.

Even though the situation is again a little more subtle in the longitudinal channel, as both model predictions are within the errors of the data. The absolute values on the other hand clearly favor the first toy model for both momenta.

Summarizing both the correlator ratio and the thermal moments have shown to be better described by a constant contribution in the longitudinal channel. While both models in the transverse channel, although working well at  $|p|/T = 2.3562$ , fail to describe the data for larger momenta.

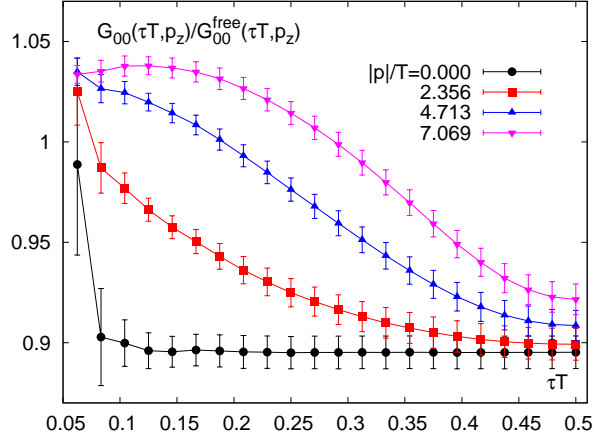


Figure 6.6: *The time-time correlation function normalized by its free continuum counterparts at finite momentum.*

## 6.2 The Time-Time Vector Channel and its Thermal Moments

So far the analysis focused on the transverse and longitudinal vector correlators at finite momentum, however also the time-time component obtains a non-trivial momentum dependence.

Subsequently the ratio of the data to the corresponding free continuum case for the momenta  $|p|/T = 0.0000, 2.3562, 4.7124$  and  $7.0686$  is shown in Fig. 6.6. Note here that the free continuum function at  $|p|/T = 0.0$  is simply  $G_{00}^{free}(\tau T, 0) = 1$  due to the structure of the time-time spectral function highlighted in Chp. 3.

As before the ratio quantifies the deviation of the data from the free case by differing from unity. Whereby in the case of vanishing momentum the quark number susceptibility emerges, as we already saw in Chp. 5.1. Going to finite momentum we can see how this limit is approached.

Indeed we observe a smooth trend towards the vanishing momentum result as the momentum is decreased. Note the limit of vanishing momentum seems to be achieved from the midpoint downwards, with the last four or six Euclidean times being already very close to the vanishing momentum case especially at  $|p|/T = 2.3562$  and then rising with decreasing distance.

Interestingly there seems to be a qualitative difference between the results at  $|p|/T = 2.3562$  and those at larger momenta, as the latter results exhibit an inflexion point around  $\tau T \simeq (0.2 - 0.25)$  that is absent in the former. Nevertheless in general the ratio drops throughout the Euclidean time interval at all momenta evaluated, starting from slightly above one and going to slightly above the vanishing momentum result at the midpoint.

## 6.2 The Time-Time Vector Channel and its Thermal Moments

Recall at this point that the behavior of the longitudinal and time-time correlators is in fact linked by the direct connection between the time-time and the longitudinal components of the vector channel shown in Eq. 3.72. As such it gives rise to a special connection between the two cases in terms of the thermal moments of the time-time channel. Consequently recall Eq. 3.72 and write:

$$p^2 \rho_L(\omega, \vec{p}) = \omega^2 \rho_{00}(\omega, \vec{p}) \quad , \quad (6.5)$$

comparing this relation with the definition of the thermal moments in Eq. 4.9 and Eq. 4.10, we may immediately write the second thermal moment of the time-time vector channel in terms of the longitudinal component:

$$G_{00}(\tau T, \vec{p}) = G_{00}^{(0)}(\vec{p}) + G_{00}^{(2)}(\vec{p}) \left( \frac{1}{2} - \tau T \right)^2 + \dots \quad (6.6)$$

$$G_{00}^{(0)}(\vec{p}) = G_{00}(\tau T = 1/2, \vec{p}) \quad (6.7)$$

$$G_{00}^{(2)}(\vec{p}) = \frac{1}{2} \left( \frac{p}{T} \right)^2 G_L(\tau T = 1/2, \vec{p}) = \frac{1}{2} \left( \frac{p}{T} \right)^2 G_L^{(0)}(\vec{p}) \quad , \quad (6.8)$$

In fact bar the zeroth order the thermal moments of the time-time correlator may be identified order by order by a corresponding moment of the longitudinal channel. To see this write:

$$\begin{aligned} G_{00}^{(2)}(\vec{p}) &\equiv \frac{1}{2} \left( \frac{p}{T} \right)^2 \int_0^\infty \frac{d\omega}{2\pi} \frac{\rho_L(\omega)}{\sinh(\omega/2T)} = \frac{1}{2} \left( \frac{p}{T} \right)^2 G_L^{(0)}(\vec{p}) \\ G_{00}^{(4)}(\vec{p}) &\equiv \frac{1}{24} \left( \frac{p}{T} \right)^2 \int_0^\infty \frac{d\omega}{2\pi} \frac{(\omega)^2}{\sinh(\omega/2T)} \frac{\rho_L(\omega)}{\sinh(\omega/2T)} = \frac{1}{12} \left( \frac{p}{T} \right)^2 G_L^{(2)}(\vec{p}) \\ G_{00}^{(n)}(\vec{p}) &\equiv \frac{1}{n!} \left( \frac{p}{T} \right)^2 \int_0^\infty \frac{d\omega}{2\pi} \frac{(\omega)^{n-2}}{\sinh(\omega/2T)} \frac{\rho_L(\omega)}{\sinh(\omega/2T)} = \frac{(n-2)!}{n!} \left( \frac{p}{T} \right)^2 G_L^{(n-2)}(\vec{p}) \quad . \end{aligned} \quad (6.9)$$

The expansion in thermal moments then becomes:

$$\begin{aligned} G_{00}(\tau T, \vec{p}) &= G_{00}^{(0)}(\vec{p}) + \left( \frac{1}{2} - \tau T \right)^2 \left( \frac{p}{T} \right)^2 \left[ \frac{1}{2} G_L^{(0)}(\vec{p}) + \frac{1}{12} \left( \frac{1}{2} - \tau T \right)^2 G_L^{(2)}(\vec{p}) + \dots \right] \\ &= G_{00}^{(0)}(\vec{p}) + \left( \frac{1}{2} - \tau T \right)^2 \left( \frac{p}{T} \right)^2 \left[ \sum_{n=0}^{\infty} \frac{n!}{(n+2)!} G_L^{(n)} \left( \frac{1}{2} - \tau T \right)^n \right] \quad , \end{aligned} \quad (6.10)$$

thus establishing a direct connection between the time-time correlator and the thermal moments of the longitudinal correlator. Incidentally note here that the additional factor  $\sim (n!(n+2)!)^{-1}$  rapidly suppresses the contribution from thermal moments with increasing order  $n$ .

A straightforward test whether the exact relation and our approximation by thermal moments holds can be done by restricting oneself to the lowest two thermal moments, write

$$\Delta_0(\tau T) = \frac{G_{00}(\tau T, \vec{p})}{G_{00}^{(0)}(\vec{p}) + \frac{p^2}{2} G_L^{(0)}(\vec{p}) \left( \frac{1}{2} - \tau T \right)^2} \quad . \quad (6.11)$$

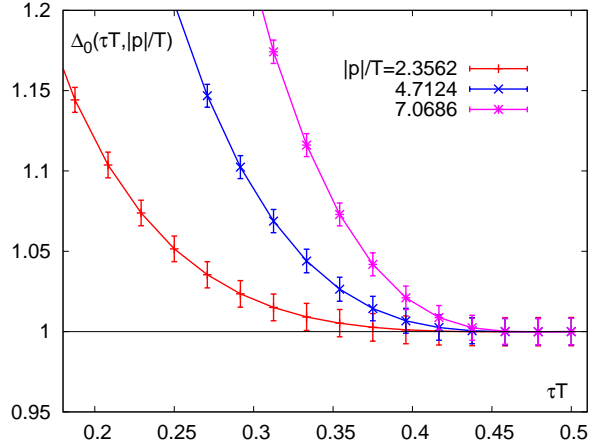


Figure 6.7: *The ratio  $\Delta_0(\tau T, \vec{p})$  defined in Eq. 6.11 for the momenta  $|p|/T = 2.3562, 4.7124$  and  $7.0686$ . The longitudinal channel hereby takes over the role of the second thermal moment of the time-time correlator. In the region where the first two moments are expected to describe the full correlator, the direct connection between the longitudinal and time-time correlators is seen to be excellently confirmed.*

In essence this definition is similar to what was done in Fig. 4.3(right), there we saw that the description of the correlator with only the first two moments worked very well for Euclidean times  $\tau T \gtrsim 0.4$  and is almost exact at  $\tau T \gtrsim 0.45$ .

In Fig. 6.7 we show the resulting  $\Delta_0(\tau T)$  on the  $N_\tau = 48$  lattice with momentum in  $\vec{z}$ -direction. Clearly for  $\tau T \gtrsim 0.45$  the results are almost equal to unity for all momenta shown, while they remain unity within errors down to Euclidean times  $\tau T \gtrsim 0.4$ . This implies the exact relation, Eq. 3.72, between the time-time and longitudinal vector correlation functions is indeed satisfied.

So far we have concentrated on expressing the time-time correlation function with its longitudinal counterpart. This however also works the other way round. To see this consider the longitudinal correlator expressed in terms of the time-time spectral function using Eq. 6.5:

$$\begin{aligned}
 p^2 G_L(\tau, \vec{p}) &\equiv \int_0^\infty \frac{d\omega}{2\pi} \rho_{00}(\omega, \vec{p}) \omega^2 \frac{\cosh(\omega(\tau - 1/2T))}{\sinh(\omega/2T)} \\
 &= \int_0^\infty \frac{d\omega}{2\pi} \rho_{00}(\omega, \vec{p}) \partial_\tau^2 K(\omega, \tau, T) \\
 &= \partial_\tau^2 \int_0^\infty \frac{d\omega}{2\pi} \rho_{00}(\omega, \vec{p}) K(\omega, \tau, T)
 \end{aligned} \tag{6.12}$$

$$\Rightarrow p^2 G_L(\tau, \vec{p}) \equiv \partial_\tau^2 G_{00}(\tau, \vec{p}) \quad . \tag{6.13}$$

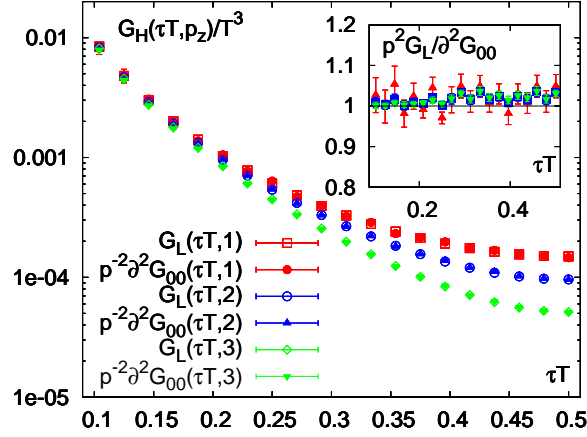


Figure 6.8: The longitudinal correlator (open symbols) and the second derivative of the time-time correlation function divided by momentum squared (closed symbols) for the momenta  $|p|/T = 2.3562$  (red),  $4.7124$  (blue) and  $7.0686$  (green), whereby  $\vec{k} = (0, 0, p_z)$  with  $p_z = 1, 2, 3$ . The insertion shows the ratio of the two, whereby the color coding is the same as in the main figure.

Consequently the second derivative with respect to time of the time-time correlation function is identical to the longitudinal correlator times momentum squared.

To check this relation we discretize the second derivative and compute it numerically given the time-time correlator data. The results are then immediately compared to the longitudinal results in Fig. 6.8. Whereby the insertion shows the ratio  $p^2 G_L/\partial^2 G_{00}$  over Euclidean time. Clearly the relation of Eq. 6.13 holds very well, as the results lie on top of each other and the ratio of the insertion is almost unity throughout the Euclidean time intervall.

All of the above results are due to the exact relation of Eq. 6.5 and as such are expected. Nevertheless it is a valuable cross check of the accuracy of the numerical data to see the equivalence of the correlators of the time-time channel and a sum of thermal moments of the longitudinal, or likewise the longitudinal correlator and the second derivative of the time-time case, emerge also in the data.

### 6.2.1 On a Non-Zero Intercept in the Longitudinal Channel

Recently it was suggested in [114], that contrary to the model predictions of [79], see also Fig. 3.8, there might be a non-zero intercept at  $\omega = 0$  in  $\rho_L(\omega, \vec{p})/\omega$ .

In the study of [114] the authors invoked the staggered formulation and studied lattices of temporal size  $N_\tau = 24$  at two different quark masses  $am_q = 0.01$  and  $am_q = 0.05$ .

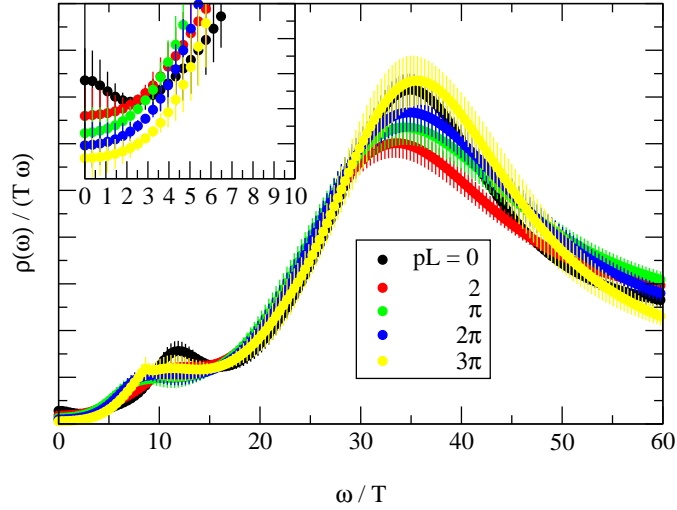


Figure 6.9: Longitudinal vector spectral function for various momenta in the hot case for  $ma = 0.01$  from [114].

Using MEM with an improved kernel the longitudinal spectral function was extracted from the corresponding correlator data at varying momenta and the resulting spectral function is shown scaled with frequency in Fig. 6.9. These results exhibit a non-zero intercept at  $\omega = 0$ , suggesting a contribution linear in  $\omega$  in the low frequency domain.

Having firmly established the link between the longitudinal and time-time vector correlators it is consequently interesting to explore the consequences such an intercept has on the time-time component.

To do this assume that the longitudinal spectral function may be split up into an intercept component linear in the frequency  $c_L \cdot \omega$  and an unspecified high frequency part  $\rho'_L(\omega)$ , then write:

$$\begin{aligned}
 \rho_{00}(\omega, \vec{p}) &= \frac{p^2}{\omega^2} \cdot \rho_L(\omega) \\
 &= \frac{p^2}{\omega^2} \cdot (c_L \omega + \rho'_L(\omega)) \\
 &= \rho_{00}^{low}(\omega, \vec{p}) + \rho_{00}^{high}(\omega, \vec{p}) \quad .
 \end{aligned} \tag{6.14}$$

Then the low frequency part of the time-time correlator may be written as:

$$\begin{aligned}
 G_{00}^{low}(\tau T, \vec{p}) &= \int_0^{\omega'} d\omega \rho_{00}^{low}(\omega, \vec{p}) \cdot K(\tau, \omega) \\
 &= \int_0^{\omega'} d\omega \frac{p^2 \cdot c_L}{\omega} \cdot \frac{\cosh(\omega(\tau - 1/2T))}{\sinh(\omega/2T)} \quad ,
 \end{aligned} \tag{6.15}$$

### 6.3 Consequences for the Spectral Functions at Finite Momentum

Notice here that in the integration:

$$\begin{aligned} \cosh(\omega(\tau - 1/2T)) &\geq 1 && \forall \omega \in [0, \omega'] \\ \sinh(\omega/2T) &< \sinh(\omega'/2T) && \forall \omega < \omega' \end{aligned} \quad (6.16)$$

as a result we can estimate the integral in Eq. 6.15 to obey the lower bound:

$$\int_0^{\omega'} d\omega \frac{p^2 \cdot c_L}{\omega} \cdot \frac{\cosh(\omega(\tau - 1/2T))}{\sinh(\omega/2T)} \geq \frac{1}{\sinh(\omega'/2T)} \int_0^{\omega'} d\omega \frac{p^2 \cdot c_L}{\omega} \rightarrow \infty \forall \tau. \quad (6.17)$$

Consequently a non-zero intercept, linear in frequency in the longitudinal channel leads to a diverging contribution in the time-time channel. Such a behavior is not only not supported by our data but also unphysical and it is therefore excluded.

## 6.3 Consequences for the Spectral Functions at Finite Momentum

Our preliminary analysis of the different vector correlation functions at finite momentum leads to a number of results we will quickly summarize here:

- Focusing on the transverse and longitudinal channels the ratio of the correlators to their corresponding free continuum counterparts reveals only very little momentum dependence in the longitudinal channel. While the momentum dependence in the transverse channel is seen to be quite strong.
- The correlator ratios are seen to exhibit only negligible momentum dependence at  $\tau T \lesssim 0.15$ . Linking this behavior to the correction due to the strong coupling the correction factor  $k(T)$  is indeed only temperature dependent and should be the same for all vector channels.
- All correlator ratios show a decreasing trend with increasing Euclidean time, implying the low frequency free continuum results to be larger than those in the interacting case. This means the contribution due to the low frequency free spectral function is in fact approached from below, in accordance with the Langevin and Boltzmann approaches.
- The ratio  $R_H^{(2,0)}/R_H^{(2,0),free}$  of the longitudinal channel shows hardly any momentum dependence, while that of the transverse is seen to increase with increasing momentum. Nevertheless in the latter case the ratio of second thermal moments  $G_H^{(2)}/G_H^{(2),free}$  slowly decreases towards the free result with increasing momentum.
- We invoked two simple toy models in order to explore what kind of contribution to expect in the interacting spectral functions of the longitudinal and transverse channels. As such a modified low frequency free behavior in the spectral function and a constant contribution in the correlator are tested. Both are seen to describe the data well at low momentum, at larger momenta on the other hand both models

fail to accurately describe the transverse channel both in the correlator and the thermal moments. At the same time a constant contribution in the correlator is seen to model the longitudinal correlator and the corresponding thermal moments very well, while the modified low frequency spectral function fails to do so at larger momenta.

- Additionally it could be shown that the data obeys the direct connection between the time-time and longitudinal correlators. This is done first by using the definition of the thermal moments directly and rewriting the time-time correlator in terms of the thermal moments of its longitudinal counterpart. Secondly the longitudinal correlator is directly connected to the second derivative of the time-time correlator. The subsequent analysis shows excellent agreement with these relations in our data.
- With the relation between time-time and longitudinal correlators firmly established, we estimate the subsequent contribution to the time-time correlator from a non-zero intercept linear in frequency in the longitudinal spectral function. This contribution is seen to be divergent. However, as such a contribution in the time-time correlator is unphysical, a non-zero intercept linear in frequency in the longitudinal spectral function must be excluded.

Note these results are of a more exploratory nature than those obtained at vanishing momentum in the continuum limit at  $T \simeq 1.45T_c$ . However they are nevertheless very encouraging in a sense that more quantitative results may be found in the near future.

# Notes on the Pseudo Scalar and Other Spectral Functions

After having explored the vector channel quite extensively now turn to what may be said on the other channels. To this extent we will show results of the pseudo scalar correlator and its thermal moments at varying temperatures but vanishing momentum.

Additionally the possible degeneracy of the pseudo scalar and scalar, as well as the vector and axial vector correlation functions at the midpoint will be examined.

## 7.1 The Pseudo Scalar Correlator and its Thermal Moments

To open the discussion have a look at the pseudo scalar correlation function at  $T \simeq 1.45T_c$ . Whereby we employ the tadpole-improved renormalization constants of Tab. 2.4.1 if not stated explicitly otherwise In Fig. 7.1(left) we show the correlation function on the available lattices, as before, with their free continuum and free lattice counterparts. The insertion gives the ratio of the free lattice and free continuum correlators. The latter ratio is again seen to differ only in the short distance regime, where the cut-off effects are expected to dominate.

Even though the exponential decay might obscure more subtle effects, in case of the pseudo scalar channel there is a clearly visible deviation from the free behavior. At the midpoint the intercept between the free lines and the data is in fact close to a factor two. Still the correlation function itself is very round, so to explain the effect with a single particle state is ill-advised, as such a state would show as a straight line in this plot.

In Fig. 7.1(right) we immediately show the temperature dependence of the correlator at  $\beta = 7.457$  in order to see what happens to this deviation as the temperature is de- or increased. As before the correlation function together with its free counterparts is shown. Whereby the insertion shows the data with the  $x$ -axis rescaled to physical distance units. We see that the result at  $T \sim 1.2T_c$  given by the  $128^3 \times 40$  lattice lies above that at  $1.45T_c$ , while the  $T \sim 3.0T_c$  result of the  $128^3 \times 16$  lattice is roughly a factor two closer to the free limit. Note however that it still visibly differs from the latter. These results imply the pseudo scalar channel is subject to rather large non-perturbative effects. With the results tending farther towards the free limit as the temperature is increased, we observe

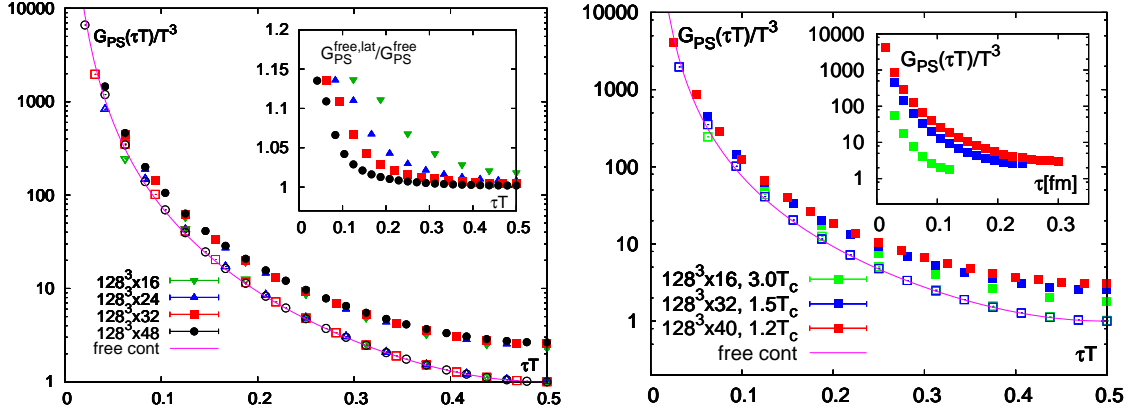


Figure 7.1: The pseudo scalar correlation function, (left) at  $T \simeq 1.45T_c$  and varying cut-off scale and (right) at fixed cut-off while varying the temperature via  $N_\tau$ . As before the free continuum (magenta lines) and free lattice (open symbols) are given for reference. The insertion on the left shows the ratio of the free lattice and free continuum correlation functions, while the insertion on the right shows the correlator data with the x-axis rescaled to physical distance units.

a decreasing trend of the non-perturbative effects as we go closer to the non-interacting regime, as one would expect.

### 7.1.1 The Correlator Ratio at $T \simeq 1.45T_c$

Next it is interesting to also examine the ratios of the correlation functions divided by their free counterparts, as in the vector case. The result is given in Fig. 7.2(top) both with the free continuum (left) and the free discretized (right) correlation function. As before data sets with fixed spatial size at  $N_\sigma = 128$  while varying the cut-off  $N_\tau$  are shown in black. Data sets with fixed cut-off ( $N_\tau = 16$ ) and varying volume are shown in color. For one value of the cut-off ( $N_\tau = 24$ ) we performed calculations for two different values of the quark masses. We find once more that finite quark mass effects are small and well within 2%. From the fixed cut-off (colored)  $N_\tau = 16$  results in both plots finite volume effects for  $\tau T \geq 0.3$  are seen to remain within one percent even for the largest Euclidean time separation at  $\tau T = 0.5$ . As a consequence these results show that finite volume effects are under control.

In the pseudo scalar case the situation concerning cut-off effects is not as immediately evident as in the vector channel. The ratio shown in Fig. 7.2(top) shows large deviations from the free field behavior even at short distances as expected from the analysis of the correlator itself in Fig. 7.1. At all distances the correlator thus seems to be controlled by large non-perturbative effects. Moreover, the analysis of cut-off effects is obscured by the fact that the renormalization constants are known only perturbatively, see Tab. 2.4.1.

## 7.1 The Pseudo Scalar Correlator and its Thermal Moments

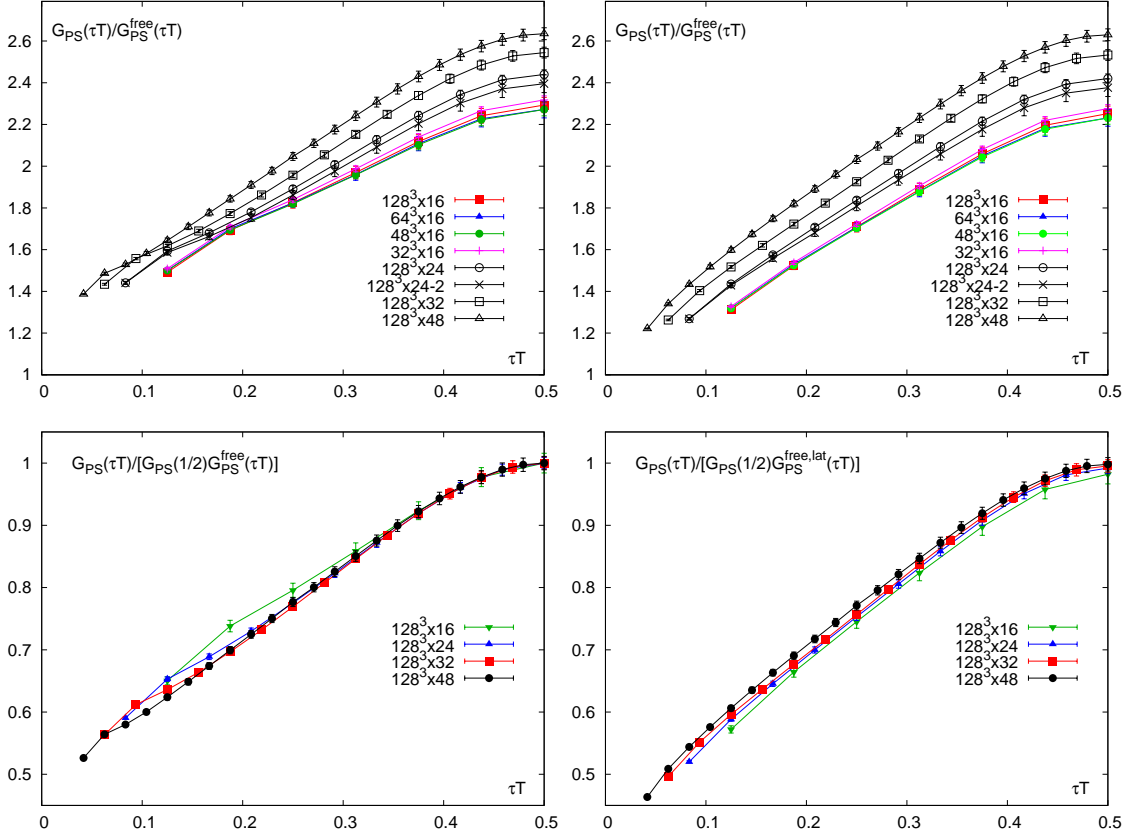


Figure 7.2: The pseudo scalar correlation functions normalized by the free continuum (left) and free lattice (right) correlation functions, calculated on lattices sized  $N_\sigma^3 \times N_\tau$  at  $T \simeq 1.45T_c$ . Note the index “ $128^3 \times 24 - 2$ ” denotes the lighter quark mass on this lattice. Bottom left and right: As top with both additionally rescaled by the correlator at  $\tau T = 1/2$ ,  $G_{PS}(\tau T = 0.5)$ , here only the results with varying cut-off are shown.

To eliminate at least these uncertainties we show in Fig. 7.2(bottom) the pseudo scalar correlation function normalized by the pseudo scalar correlation function at  $\tau T = 0.5$ . As we focus on the cut-off dependence we only show equal quark mass  $N_\sigma = 128$  results. The left hand figure shows the pseudo scalar correlator normalized by the free continuum correlator and in the right hand figure the free lattice correlation function has been used. From the left hand plot it is now possible to get an idea of the cut-off dependence, as a marginal rise in the short distance region becomes visible. We conclude that, similarly to the vector case, cut-off effects above a certain  $\tau T$  are small and increase with decreasing Euclidean time. For the  $N_\tau = 48$  lattice this value is, as before,  $\tau T \simeq 0.15$ , while it increases with smaller  $N_\tau$  and reaches  $\tau T \simeq 0.3$  for  $N_\tau = 16$ . Even though the

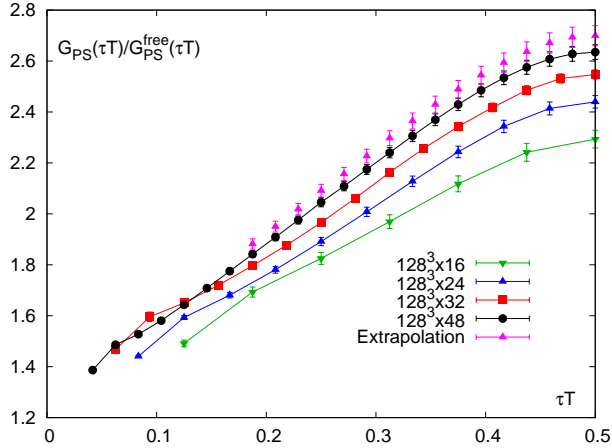


Figure 7.3: *The ratio of the pseudo scalar correlator without normalization by  $G_{PS}(\tau T = 0.5)$  and its free counterparts  $R_{PS}(\tau T)$  including its continuum extrapolation. In both cases the extrapolation was done as described in Chp. 5.1, filling in spline interpolations when necessary. Unfortunately in the pseudo scalar case it is not possible to form renormalization independent ratios and the extrapolation is subject to the subsequent uncertainty.*

cut-off effects become apparent below these values, they do not dominate the behavior of the correlation function as in the vector channel. Actually the right hand side of Fig. 7.2(bottom) indicates that the  $\tau$ -dependence of the cut-off effects is similar to that of the free lattice correlation functions, as hardly any cut-off effect is visible throughout the Euclidean time interval.

### 7.1.2 The Continuum Extrapolation

Following the prescription outlined in the vector case Chp. 5.1.3, we nevertheless attempt a continuum extrapolation. In Fig. 7.3 the corresponding result for the pseudo scalar correlation function is shown. Here it is not possible to eliminate the renormalization effects using suitable ratios of correlation functions. The extrapolation necessarily also includes this ambiguity. As the correlator normalized by its value at the midpoint was found to be almost cut-off independent and as finite volume effects were seen to be small renormalization effects dominate the uncertainty of the extrapolation.

### 7.1.3 Thermal Moments of the Pseudo Scalar Correlator

Naturally we may also compute the thermal moment following the procedure developed in the vector channel and presented in Chp. 5.1.4, as before they are especially interesting as they are obtained at the largest Euclidean time separation where the correlation functions are most sensitive to the low frequency region of the spectral function. In particular, the lower orders of the thermal moments restrict the magnitude of the low

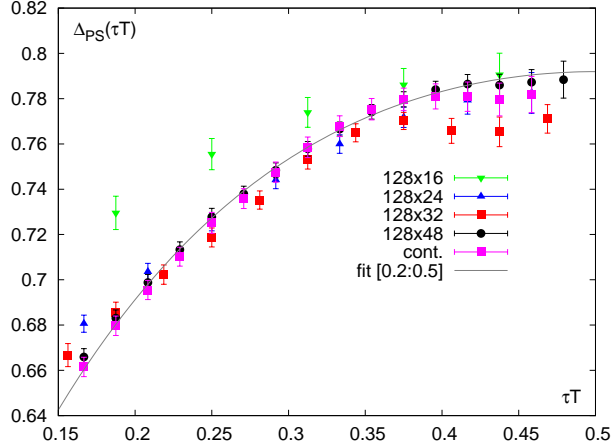


Figure 7.4: The pseudo scalar quantity  $\Delta_{PS}(\tau T)$  normalized by  $G_{PS}^{(0)}$ . The fit obeys a quartic Ansatz as indicated by the definition of  $\Delta_H(\tau T)$  and is shown within the interval  $\tau T \in [0.2 : 0.5]$ .

frequency contribution to the spectral function and thus to the correlation function.

In order to extract thermal moments we once more examine the quantity  $\Delta_H(\tau T)$ , this time in the pseudo scalar case  $\Delta_{PS}(\tau T)$ , as defined in Eq. 4.19. As for the correlation functions the resulting data is extrapolated to the continuum and extrapolated data is subsequently fitted to a quartic polynomial. During this procedure the data is once more rescaled by  $G_{PS}(\tau T = 1/2) = G_{PS}^{(0)}$  in order to suppress the effects from the renormalization constants, the corresponding results are shown in Fig. 7.4.

The resulting fit parameters yield for the second thermal moment:

$$\frac{T^3 G_{PS}^{(2)}}{G_{PS}^{(0)} G_{PS}^{(2),free}} = 0.7912 \pm 0.0012 \quad , \text{ thus } \quad R_{PS}^{(2,0)} = 10.932 \pm 0.017 < R_{PS,free}^{(2,0)} \quad . \quad (7.1)$$

From Fig. 7.3 it is clear that  $G_{PS}^{(0)}/G_{PS}^{(0),free}$  is larger than 1, as a consequence we can conclude the second thermal moment must be closer to the free field limit than the zeroth, even though the renormalization effects cannot be systematically controlled.

#### 7.1.4 MEM analysis of the Pseudo Scalar Channel

In lack of alternatives we turn to a MEM analysis to shed some light on the possible shape of the pseudo scalar spectral function. Specifically we do the analysis at  $T \simeq 1.45T_c$  on the  $128^3 \times 48$  lattice.

For the analysis we employ two default models, the first is given simply by the free lattice pseudo scalar spectral function, the second is a combination of the free lattice

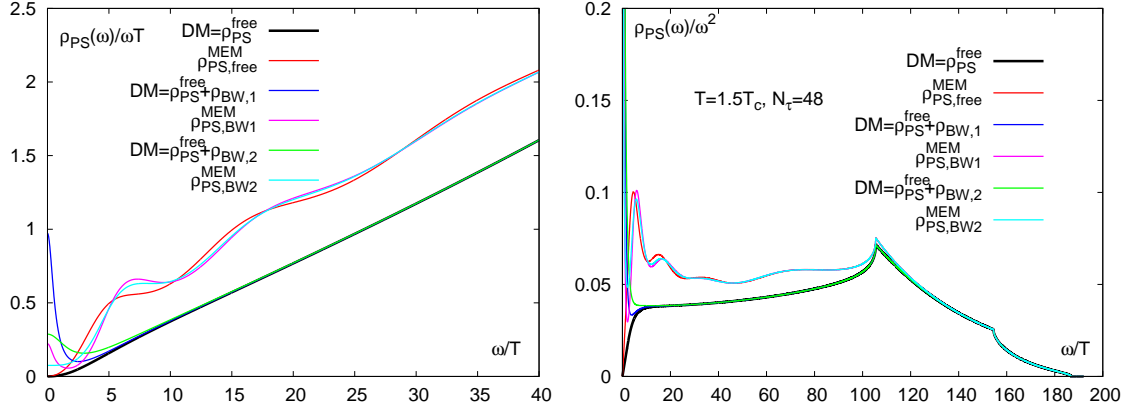


Figure 7.5: Results of a MEM analysis on the pseudo scalar correlator. Left: The low frequency region of  $\rho(\omega)/\omega T$  is shown. Right: The full spectral function is given in units  $1/\omega^2$ . Note the index in  $\rho_{PS,index}^{MEM}$  shows which default model was used as input.

spectral function and a Breit-Wigner type contribution. Here we choose the free lattice spectral functions in order to minimize any effects originating from the large frequency region of the spectral function.

In Fig. 7.5 we show the default models and their respective results, whereby the input parameters of the Breit-Wigner were also varied in order to test default models with peaks ranging from very broad to very narrow\*. On the left of the figure we show the spectral functions scaled by frequency and temperature in the low frequency regime, while on the right the spectral functions by frequency squared is given.

With both types of default model the intermediate and high frequency region exhibit essentially the same form, especially in the frequency region  $\omega/T \simeq (5 - 20)$  the result spectral functions possess a similar peak structure, regardless of the default model. Indeed this peak structure is seen to dominate the low to intermediate shape of the spectral function.

Note however that this peak structure from the Breit-Wigner default models seems to be slightly shifted. This shift can be accounted for by noticing that throughout all Breit-Wigner default models the transport contribution is highly suppressed, if not entirely deleted from the result. The remnant peak in some default models cannot be further canceled by MEM due to the accuracy of the data and subsequently it compensates for the existence of the peak in the higher frequency regions. Even so MEM suppresses the Breit Wigner contribution of the default models by more than 75% throughout all Breit-Wigner default models tested. Within the resolution of MEM this is a clear and significant sign that a peak contribution at low frequencies is absent.

\*Only a representative selection is shown in Fig. 7.5

## 7.2 Midpoints of the Current Correlators at Finite Temperature

At finite temperature many correlation functions are expected to degenerate as signals of symmetry restoration [15,115] and in this section we will briefly examine the situation encountered in this work.

A clear observable to examine these degeneracies is the midpoint of the correlation function. Recalling Eq. 3.80 the free lattice propagator contributions read:

$$S_4(\tau, \vec{k}) = S_4(\vec{k}) \cdot \cosh((\tau - 1/2T)E_{\vec{k}}) \quad (7.2)$$

$$S_i(\tau, \vec{k}) = S_i(\vec{k}) \cdot \sinh((\tau - 1/2T)E_{\vec{k}}) \quad (7.3)$$

$$S_u(\tau, \vec{k}) = S_u(\vec{k}) \cdot \sinh((\tau - 1/2T)E_{\vec{k}}) + \frac{\delta_{\tau 0}}{2(1 + M_{\vec{k}})} \quad (7.4)$$

Using the above relation one realizes that at the midpoint  $\tau = 1/2T$  the decomposition of the correlation function becomes simpler and one may immediately write [74]:

$$G_H(\tau = 1/2T, \vec{p}) = \frac{4N_c}{N_\sigma^3} \sum_{\vec{k}} a_H^{(1)} S_4(\vec{k}) S_4^\dagger(\vec{r}) \quad (7.5)$$

This implies that the midpoints of the scalar and pseudoscalar as well as the vector and axialvector degenerate in the free case:

$$G_{PS}(\tau = 1/2T, \vec{p}) = G_S(\tau = 1/2T, \vec{p}) \quad (7.6)$$

$$G_V(\tau = 1/2T, \vec{p}) = G_A(\tau = 1/2T, \vec{p}) \quad (7.7)$$

This is clear from the channel constant  $a_H^{(1)}$  and Tab. 3.1.1. However, the above particle channels may also degenerate away from the non-interacting limit when symmetries of the vacuum are restored, see e.g. [115].

As such the degeneration of the correlation functions for the vector and axial vector currents is associated with the restoration of chiral symmetry. The degeneracy of the pseudo scalar and scalar channels on the other hand can be shown to be sensitive to the effective restoration of the axial  $U_A(1)$  anomaly.

It is interesting to note at this point that the ratios of the vector to axial vector and pseudo scalar to scalar channels are very sensitive to the uncertainties of the renormalization constants, as:

$$\frac{G_1}{G_2}(\tau = 1/2T, \vec{p}) = \frac{Z_1}{Z_2} \cdot \frac{G_1^{data}}{G_2^{data}}(\tau = 1/2T, \vec{p}) \quad (7.8)$$

In the symmetric phase this implies a deviation from  $\frac{G_1}{G_2}(\tau = 1/2T, \vec{p}) = 1$  in the continuum limit may be attributed to the uncertainties in the renormalization constants.

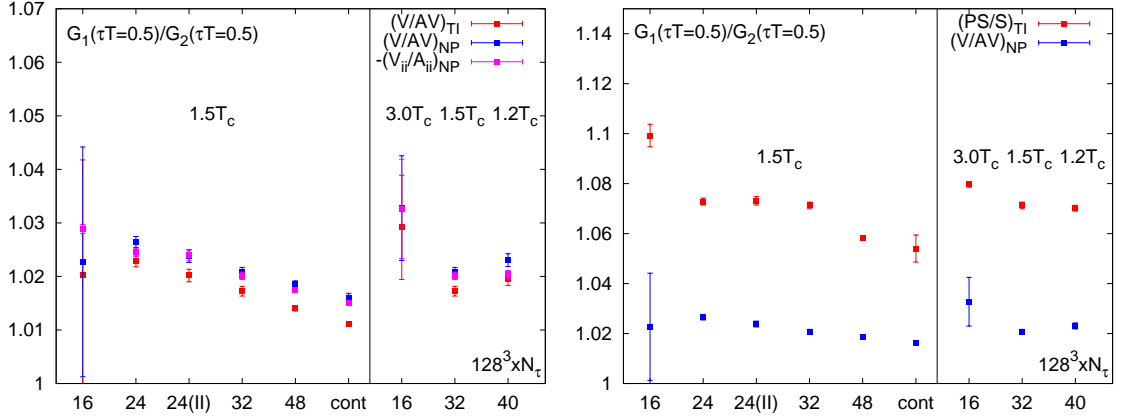


Figure 7.6: *Left: The ratio of the midpoints of the vector and axial vector channel renormalized with non-perturbative and tadpole improved renormalization constants. Right: A comparison of the non-perturbative vector to axial vector ratio and the tadpole improved pseudo scalar to scalar.*

To study these effects we show the ratio of the midpoints of the vector to axial vector and the pseudo scalar to scalar correlation functions for the available lattices with  $N_\sigma = 128$  in Fig. 7.6. In addition the data at  $T \simeq 1.45T_c$  is used to extrapolate the ratio to the continuum. Whereby only the results with approximately the same quark mass were used for the extrapolation, i.e.  $N_\tau = 24, 32$  and  $48$ . Note that in order to check for finite mass effects we show the results for both available quark masses on the  $N_\tau = 24$  lattice.

On the left of Fig. 7.6 we focus on the vector to axial vector ratio and show the full vector to full axial vector ratio once using the non-perturbative and once the tadpole improved renormalization constants given in Tab. 2.4.1. Additionally we give the non-perturbatively renormalized ratio of the spatial components of the vector and axial vector channels. Clearly the results are very much compatible and we observe a systematic decreasing trend with increasing cut-off. However, all our results can be approximately contained in a region deviating in around 1% or 3% across our calculations and the continuum extrapolation.

On the right of Fig. 7.6 we compare the non-perturbative full vector to axial vector ratio with the tadpole improved pseudo scalar to scalar. We observe a strong cut-off dependence and a deviation from unity of something between 10% and 6% in the pseudo scalar by scalar case.

Comparing the two quark masses at  $N_\tau = 24$  in both figures finite mass effects are seen to be small as they deviate from one another only on the level of 0.5%. As such they are not strong enough to explain the deviation from unity of the results in the vector/axial vector and the pseudo scalar/scalar ratios.

With finite mass effects small and a visible deviation from unity also in the continuum

## 7.2 Midpoints of the Current Correlators at Finite Temperature

limit we identify two sources for the apparent mismatch. As such one possibility is that the observed deviation indeed arises from the errors of the renormalization constants. The other possibility is that the corresponding symmetries are not yet restored in the available temperature range.

Fortunately we can turn to a number of studies to get a feeling which of the two scenarios might be applicable, see e.g. [115,116] and references therein. As such using an improved staggered fermion formulation on dynamical  $N_f = 2 + 1$  configurations the recent calculation of [116] could show that in the intermediate temperature region  $1.2T_c \lesssim T \lesssim 1.5T_c$  both chiral symmetry and the anomalous  $U_A(1)$  exhibit signs of restoration.

If we assume this to be the case in our study the deviation from unity would be mostly due to the uncertainties of the renormalization constants.

If this is indeed so we can estimate the error induced by these uncertainties especially in the pseudo scalar/scalar case. As here it is not possible to take renormalization independent ratios, as was done in the vector channel, when examining the correlation functions. In the pseudo scalar channel additional error bands on the correlator data, in e.g. Fig. 7.2, of the order of 5 – 10% due to renormalization could explain the offset of the individual lattice results. Subsequently the discrepancies would not be due to lattice effects.



# Summary and Concluding Remarks

In this thesis we computed meson correlation functions in the deconfined phase of quenched QCD. For the calculation we invoked the framework of  $\mathcal{O}(a^2)$ -improved Wilson-Clover fermions at light quark masses. We computed the vector correlation function on lattices of size  $N_\sigma^3 \times N_\tau$ , with  $32 \leq N_\sigma \leq 128$  and  $N_\tau = 16, 24, 32$  and  $48$ . For  $N_\tau = 16$  we calculated  $G_H(\tau T)$  on lattices with spatial extent  $N_\sigma = 32, 64, 96$  and  $128$ , in order to quantify finite volume effects at fixed values of the lattice cut-off. For  $N_\tau = 24$  we checked that the quark masses used in our calculations are indeed small enough on the scale of the temperature to be ignored in the analysis of our correlation functions. On the largest spatial lattice,  $N_\sigma = 128$ , we performed calculations for four different values of the lattice cut-off by choosing  $N_\tau = 16, 24, 32$  and  $48$  and at the same time changing the value of the gauge coupling  $\beta$  such that the temperature is kept constant,  $T \simeq 1.45T_c$ . Finally we varied the temperature at  $N_\sigma = 128$  keeping the cut-off scale fixed and varying the temporal extent  $N_\tau = 16, 32$  and  $40$ , corresponding to the respective temperatures  $T \simeq 3.0T_c, 1.45T_c$  and  $1.2T_c$ .

With these datasets we were able to undertake physics analysis at an unprecedented precision and our main results are summarized in the following.

## The Light Quark Vector Spectral Function at Vanishing Momentum in the Continuum Limit of Quenched QCD

At the fixed value of temperature  $T \simeq 1.45T_c$  we performed a systematic and detailed analysis of the vector correlation functions at vanishing momentum. Analyzing different lattice cut-off values combined with an analysis of finite volume and quark mass effects allowed us to extrapolate the vector correlation function to the continuum limit for the first time in a renormalization independent fashion for a large interval of Euclidean times, spanning from the midpoint  $\tau T = 0,5$  to  $\tau T \simeq 0.2$ . In this interval we determined the correlation function to an unprecedented accuracy at the 1% level. Additionally we computed the first two thermal moments of the correlation functions, the second being equivalent to the curvature of the correlator at the midpoint of the finite temperature Euclidean time interval.

Subsequently we analyzed the continuum extrapolated correlation functions invoking several fit Ansätze that differ in their low frequency structure. As a result we find the vector correlator to be best fitted by a simple Ansatz of the free spectral function times a perturbatively motivated correction factor  $k(T)$  plus a phenomenologically inspired Breit-Wigner term centered at  $\omega = 0$ .

This Ansatz already gives small  $\chi^2/d.o.f.$  and describes the data well. Systematically

## Summary and Concluding Remarks

changing the low frequency structure of the Ansatz spectral function, we are able to estimate the systematic uncertainty of the low energy structure of the spectral function. Some features of the spectral functions are robust, as such the spectral function for frequencies  $\omega/T \gtrsim (2 - 4)$  is close to its free form. In this regime it would be interesting to replace the component proportional to the free continuum spectral function in our Ansatz by the hard thermal loop spectral function. This is easily possible and will be done in the near future.

For energies in the region  $\omega/T \lesssim (1 - 2)$  the spectral function is significantly larger than the free result, but smaller than the HTL spectral function, which diverges at small energies. As a result the the resulting thermal dilepton rate is an order of magnitude larger than the leading order Born rate at energies  $\omega/T \simeq 1$ .

Finally we accurately and systematically determined the electrical conductivity from our resulting spectral functions, the thus obtained value is  $\sigma/T = (1/3 - 1) \cdot C_{em}$ . To our knowledge this is the first time a fully non-perturbative estimate of this transport coefficient is given including also systematic uncertainties.

To quantitatively analyze in what fashion our results and the enhancement in the low frequency region can account for the experimentally observed dilepton rates in this energy region [38, 117], we need to extend our analysis to incorporate the temperature and momentum dependence of our results. Then a complete analysis of dilepton rates that takes into account the hydrodynamic expansion of dense matter created in heavy ion collision will become possible [108].

First steps in this direction have been undertaken in this thesis and we quickly summarize the corresponding results in the following.

### Results on the Temperature Dependence at Vanishing Momentum

Fixing the cut-off to  $\beta = 7.457$  and thus  $a^{-1} = 12.864\text{GeV}$  we performed an analysis of the vanishing momentum vector correlation function by varying  $N_\tau = 16, 32$  and  $40$ . With these values we obtain the temperatures  $T \simeq 3.0, 1.45$  and  $1.2T_c$ , respectively. We carefully analyzed the temperature dependence of the vector correlation function, the quark number susceptibility and the thermal moments of the correlator. The latter were seen to be almost constant in  $T/T_c$ , implying only little change in the underlying spectral functions.

Additionally we fitted the data using the simple free continuum plus Breit-Wigner Ansatz motivated at  $T \simeq 1.45T_c$ . Here our systematic analysis is limited to determining the dependence on the Euclidean time window of the fit, as a continuum extrapolation that eliminates the lattice effects was not yet possible within the available computing resources.

The resulting parameters are then analyzed for the temperature dependence of the width and height of the Breit-Wigner peak. For all these quantities the parameters are seen to be almost constant in units of temperature, implying a linear dependence on the temperature. As such the width increases linearly while the height drops linearly with

increasing temperature.

A similar behavior is observed for the temperature dependence of the electrical conductivity, whereby the corresponding results are within 7% of each other over the temperature range. As a result we could establish also a linear dependence in temperature for the electrical conductivity, in accordance with perturbation theory [111].

Finally we checked of a sum rule stating the area under the Breit-Wigner peak to be constant and temperature independent [112]. Here the resulting values are seen to match within errors. However the large uncertainties encountered make it difficult to firmly establish the validity of the sum rule, even though our results lean towards this direction.

For the temperature evolution additional lattice calculations, preferably with a subsequent continuum extrapolations are highly desirable.

### **Exploratory Study of the Vector Correlation Function at Finite Momentum**

In the case of finite momentum we restricted our analysis to the lattice sized  $128^3 \times 48$  and the lattice momenta  $\vec{k} = (0, 0, p_z)$  where  $p_z = 0, 1, 2, 3$ , whereby the physical momenta are given by  $|p|/T = 2\pi \cdot |\vec{k}| \cdot N_\tau/N_\sigma$ . We could show that the longitudinal component of the vector correlation function exhibits only very little momentum dependence, both in the correlator and its thermal moments.

This is markedly different in the transverse case. Here a large momentum dependence was seen in the correlator and a somewhat weaker but nevertheless visible dependence in the second thermal moment.

All results are seen to lie on top of each other at  $\tau T \leq 0.15$ , implying the correction factor  $k(T)$  to be momentum independent.

Additionally the ratios of the data and the corresponding free correlators exhibit a decreasing trend with increasing Euclidean time, taking into account the correction factor this means the low frequency part of the interacting spectral function is in fact smaller than that of the free case.

Invoking a set of toy models we then were capable to identify, what kind of behavior is favored by both channels in the interacting case. To this extent we employed first a time-independent contribution plus the free continuum and second a time-dependent contribution modeled by the corresponding free behavior at low frequency plus the free continuum. We could show that the longitudinal vector correlation function is very well describable by a model that incorporates none or very little time dependence both in the correlator and its thermal moments. While the transverse was seen to hold a middle ground between the constant and modified free behavior. As such the corresponding model parameters deviate less from the free case in the longitudinal channel than in the transverse.

The results obtained are encouraging and suggest a determination of the spectral func-

## Summary and Concluding Remarks

tion from our data is indeed possible.

Additionally we studied the connection between the time-time and longitudinal vector correlation functions at finite momentum. We could derive two exact relations between the longitudinal and the time-time correlation functions. The first approximately connects the time-time correlator with a sum of thermal moments of the longitudinal case, while the second links the longitudinal correlator with the second derivative of the time-time case. These two relations are subsequently checked and an excellent agreement is observed in our data. As a consequence we could estimate the effect of a contribution linear in frequency in the longitudinal spectral function [114] on the time-time correlator. We found this contribution to be divergent. Such a divergence is unphysical and we therefore exclude the possibility of such a non-zero intercept in the longitudinal case.

## Remarks on the Pseudo Scalar and Renormalization Issues

Finally we turned to evaluating the pseudo scalar correlation function and the midpoints of the correlators of all channels, both at vanishing momentum.

As in the case of the vector correlator, we could combine a study of lattice, quark mass and cut-off effects for the pseudo scalar. However here the possibility to take renormalization independent ratios does not arise and a continuum extrapolation contains the additional uncertainties due to the only perturbatively known renormalization constants. Nevertheless the extrapolation was done both for the correlator and its thermal moments, revealing large non-perturbative effects at  $T \simeq 1.45T_c$ .

These effects were seen to persist also at  $T \simeq 1.2T_c$  and  $T \simeq 3.0T_c$ , even though in a somewhat reduced sense in the latter case.

At  $T \simeq 1.45T_c$  we then used a MEM analysis to obtain an estimate of the pseudo scalar spectral function. Using a number of default models which include Breit-Wigner contributions in the low frequency regime, it turned out that MEM strongly disfavors the presence of such a transport peak. Instead a dominant (non-perturbative) peak structure arises at  $\omega/T \simeq (5 - 20)$ , suggesting the survival of a resonance in the pseudo scalar channel.

To further understand the effects in the pseudo scalar channel it is important to quantify more rigorously the errors of the renormalization constants. Additionally a better theoretical understanding of the effects expected would be desirable.

Touching on the topic of the uncertainties of the renormalization constants, we compare the midpoints of the pseudo scalar and scalar as well as the vector and axial vector correlation function. Assuming to be in the symmetry restored phase at  $T \simeq 1.45T_c$ , we observe the results of the vector/axial vector ratio to be within 2% of unity while the pseudo scalar/scalar results differ by about 10%.

# Bibliography

- [1] A. Francis, F. Karsch, PoS LATTICE2010 (2010) 191
- [2] H.-T. Ding, A. Francis, O. Kaczmarek, F. Karsch, E. Laermann, W. Soeldner, Phys.Rev. D83 (2011) 034504
- [3] K. Nakamura et al. (Particle Data Group), J. Phys. G 37, (2010) 075021
- [4] M. Gell-Mann, Phys. Rev. 125, (1962) 1067-1084
- [5] N. Samios et al., Phys.Lett. 12, (1964) 134
- [6] [http://www.nobelprize.org/nobel\\_prizes/physics/laureates/1969/gell-mann.html](http://www.nobelprize.org/nobel_prizes/physics/laureates/1969/gell-mann.html)
- [7] M. Gell-Mann, Phys. Lett. 8, (1964) 214
- [8] C. N. Yang, R. Mills, Phys. Rev. 96 (1), (1954) 191
- [9] H. Fritzsch, Murray Gell-Mann, H. Leutwyler, Phys.Lett. B47 (1973) 365-368
- [10] G. 't Hooft, M. Veltman, Nucl. Phys. B44, (1972) 189
- [11] H. D. Politzer, Phys. Rev. Lett. 30, (1973) 1346;  
D. J. Gross, F. Wilczek, Phys. Rev. Lett. 30, (1973) 1343
- [12] R. Feynman, Phys. Rev. 76, (1949) 769
- [13] M. E. Peskin, D. V. Schroeder, "An introduction to quantum field theory", ISBN-10: 0201503972, Perseus Books (11.09.1995)
- [14] F. Wilczek, Nucl.Phys. A663, (2000) 3
- [15] H. Satz, "Extreme States of Matter", Lecture Notes Bielefeld University (2010)
- [16] V. N. Gribov, Sov. Phys. JETP 29 (1969) 483
- [17] <http://www.phy.duke.edu/research/NPTheory/QGP/transport/index.php>
- [18] <http://ipht.cea.fr/Pisp/francois.gelis/Physics/2011-qm.pdf>
- [19] L. McLerran, arXiv:0812.4989 [hep-ph]
- [20] J. Cleymans, K. Redlich, Phys.Rev.Lett. 81 (1998) 5284

## Bibliography

- [21] A. Bazavov et al., Phys.Rev. D80 (2009) 014504;  
M. Cheng et al. Phys.Rev. D81 (2010) 054504;  
Y. Aoki, Phys.Lett. B643 (2006) 46
- [22] H.-T. Ding, “Charmonium Correlation , Spectral Functions in Quenched Lattice QCD at Finite Temperature”, Dissertation Bielefeld University (2010)
- [23] H. Meyer, Eur.Phys.J. A47, (2011) 86
- [24] F. Jegerlehner, J.Phys.G G29 (2003) 101
- [25] F. Jegerlehner, A. Nyffeler, Phys.Rept. 477 (2009) 1;  
D. Bernecker , H. Meyer, arXiv:1107.4388
- [26] K. J. Eskola, arXiv:hep-ph/9911350.
- [27] W. Florkowski, “Phenomenology of Ultra-Relativistic Heavy-Ion Collisions”, ISBN-10: 9814280666, World Scientific Pub Co (31.05.2010)
- [28] R. Rapp, J. Wambach, Adv.Nucl.Phys. 25 (2000) 1
- [29] K. Yagi, T. Hatsuda, Y. Miake, “Quark-Gluon Plasma: From Big Bang to Little Bang”, ISBN-10: 0521089247, Cambridge University Press, Edition 1 (30.10.2008)
- [30] J. I. Kapusta, C. Gale, “Finite-Temperature Field Theory: Principles and Applications”, ISBN-10: 0521173221, Cambridge University Press, Edition 2 (25.11.2010)
- [31] M. Le Bellac, “Thermal Field Theory”, ISBN-10: 0521654777, Cambridge University Press (3.07.2000)
- [32] E. L. Feinberg, Nuovo Cim. A34 (1976) 391
- [33] L. D. McLerran, T. Toimela, Phys. Rev. D31 (1985) 545
- [34] H. A. Weldon, Phys.Rev. D42 (1990) 2384
- [35] E. Braaten, R. D. Pisarski, T.-C. Yuan, Phys. Rev. Lett.64 (1990) 2242
- [36] S.D. Drell, T.-M. Yan, Phys.Rev.Lett. 25 (1970) 316
- [37] R. H. Dalitz, Proc.Phys.Soc. A66 (1953) 710
- [38] A. Adare et al., Phys.Rev. C81 (2010) 034911
- [39] R. Feynman, Phys. Rev. 80 (1950) 440;  
C. Bernard, Phys. Rev. D9 (1974) 3312
- [40] K.G. Wilson, Phys. Rev. D 10 (1974), 2445
- [41] C. Gattringer, C. B. Lang, “Quantum Chromodynamics on the Lattice - an Introductory Presentation”, ISBN-10: 3642018491, Springer-Verlag Berlin, Heidelberg, New York, Edition 1 (16.10.2009)

- [42] T. DeGrand, C. DeTar, “Lattice Methods for Quantum Chromodynamics”, ISBN-10: 9812567275, World Scientific Pub Co, illustrated edition (30.11.2006)
- [43] I. Montvay, G. Münster, “Quantum Fields on a Lattice”, ISBN-10: 0521599172, Cambridge University Press, New Edition (6.03.1997)
- [44] H. J. Rothe, “Lattice Gauge Theories: An Introduction”, ISBN-10: 9812561684, World Scientific Pub Co, Edition 3 (06.2005)
- [45] E. Laermann, “Quantum field on a lattice”, Lecture Notes Bielefeld University (2006)
- [46] M. Lüscher, “Advanced Lattice QCD”, LXVIII Les Houches Summer School (1997)
- [47] S. Gupta, “Introduction to Lattice QCD”, LXVIII Les Houches Summer School (1997)
- [48] S.Aoki et al. [CP-PACS Collaboration], Phys. Rev. Lett. 84, (2000) 238
- [49] A. Chodos, J. B. Healy, Nucl. Phys. B127, (1977) 426;  
L. H. Karsten and J. Smit, Nucl. Phys. B183, (1981) 103;  
H. B. Nielsen and M. Ninomiya, Nucl. Phys. B185, (1981) 20;  
Nucl. Phys. B195 (1981) 541; Nucl. Phys. B193, (1981) 173
- [50] K. Symanzik, “Mathematical Problems in theoretical physics”, Lecture notes in Physics 153, Springer (1982)
- [51] B. Sheikholeslami, R. Wohlert, Nucl. Phys. B259 (1985) 572
- [52] M. Lüscher, S. Sint, R. Sommer, P. Weisz, U. Wolff, Nucl. Phys. B491, (1997) 323
- [53] M. Lüscher, S. Sint, R. Sommer, H. Wittig, Nucl. Phys. B491, (1997) 344
- [54] B. Beinlich, F. Karsch, E. Laermann, A. Peikert, Eur. Phys. J. C6 (1999) 133
- [55] C. R. Allton, hep-lat/9610016
- [56] R. G. Edwards, U. M. Heller, T. R. Klassen, Nucl. Phys. B517 (1998) 377
- [57] B. Lucini, M. Teper, U. Wenger, JHEP 0401, (2004) 061
- [58] S. Capitani, M. Luscher, R. Sommer, H. Wittig [ALPHA Collaboration], Nucl. Phys. B544, (1999) 669
- [59] M. Guagnelli, R. Petronzio, J. Rolf, S. Sint, R. Sommer, U. Wolff [ALPHA Collaboration], Nucl. Phys. B595 (2001) 44,
- [60] G. M. de Divitiis, R. Petronzio, Phys. Lett. B 419, (1998) 311
- [61] M. Bochicchio, L. Maiani, G. Martinelli, G. C. Rossi, M. Testa, Nucl. Phys. B262 (1985) 331

## *Bibliography*

- [62] T. van Ritbergen, J. A. M. Vermaseren, S. A. Larin, *Phys. Lett.* B400 (1997) 379
- [63] K. G. Chetyrkin, J. H. Kuhn, M. Steinhauser, *Comput. Phys. Commun.* 133, (2000) 43
- [64] M. Göckeler et al., *Nucl. Phys. Proc. Suppl.* 53 (1997) 896
- [65] G. P. Lepage, P. B. Mackenzie, *Phys. Rev.* D48 (1993) 2250
- [66] S. Sint, P. Weisz, *Nucl. Phys.* B502 (1997) 251
- [67] G. Parisi, Presented at 20th Int. Conf. on High Energy Physics, Madison, Wis., Jul 17-23, 1980.
- [68] T. R. Klassen, *Phys. Rev.* D51 (1995) 5130
- [69] M. Guagnelli, R. Sommer, *Nucl. Phys. B, Proc. Suppl.* 63, (1998) 886
- [70] N. Cabibbo, E. Marinari, *Phys. Lett.* B119 (1982) 387;  
A. D. Kennedy, B. J. Pendleton, *Phys. Lett.* B156 (1985) 393;  
S. L. Adler, *Phys. Rev.* D23 (1981) 2901;  
M. Creutz, *Phys. Rev.* D36 (1987) 515
- [71] M. R. Hestenes, E. Stiefel, *J. Res. Natl. Bur. Stand.* 49 (1952) 409;  
H. A. van der Vorst, *SIAM Sci, Stat. Comp.* 13 (1992) 631;  
T. A. Degrand, P. Rossi, *Comput. Phys. Commun.* 60 (1990) 211
- [72] J. Engels, “Statistische und stochastische Methoden in der Physik”, *Lecture Notes Bielefeld University* (2009)
- [73] W. Florkowski, B. L. Friman, *Z. Phys. A* 347, (1994) 271
- [74] G. Aarts, J. M. Martinez Resco, *Nucl. Phys.* B726, (2005) 93
- [75] S. Stickan, F. Karsch, E. Laermann, P. Petreczky, *Nucl.Phys.Proc.Suppl.* 129 (2004) 599
- [76] D. B. Carpenter, C. F. Baillie, *Nucl. Phys.* B260 (1985) 103
- [77] C. R. Allton et al., *Phys. Rev. D* 71, (2005) 054508
- [78] P. Petreczky, D. Teaney, *Phys. Rev.* D73 (2006) 014508
- [79] J. Hong, D. Teaney, *Phys. Rev.* C82 (2010) 044908
- [80] E. Braaten, R. D. Pisarski, *Nucl. Phys.* B337, 569 (1990)
- [81] F. Karsch, M. G. Mustafa, M. H. Thoma, *Phys. Lett. B* 497, 249 (2001)
- [82] G. 't Hooft, *gr-qc/9310026* (1993)

- [83] L. Susskind, *J.Math.Phys.* 36 (1995) 6377
- [84] L. Susskind, J. Lindesay, “The Holographic Universe: An Introduction to Black Holes, Information and the String Theory Revolution”, ISBN-10: 9812561315, World Scientific Pub Co (21.02.2005)
- [85] J.M. Maldacena, *Adv. Theor. Math. Phys.* 2 (1998) 231
- [86] R. C. Myers, A. O. Starinets, R. M. Thomson, *JHEP* 11 (2007) 091
- [87] G. Aarts, *PoS LAT2007* (2007) 001
- [88] K. Rajagopal, Presentation at Quark Matter 2011, Annecy, France; May 23, 2011
- [89] J.-P. Blaizot, E. Iancu, A. Rebhan, *Phys. Lett. B* 523, (2001) 143
- [90] R. V. Gavai, S. Gupta, P. Majumdar, *Phys. Rev. D* 65, (2002) 054506
- [91] M. Bertero, P. Boccacci, E. Pike, *Proc. Royal Soc. London* 383 (1982) 15
- [92] T. Bayes, R. Price, *Philosophical Transactions of the Royal Society of London* 53 (0), (1763) 370
- [93] S. F. Gull, G. J. Daniell, *Nature*272 (1978) 686;  
E. Laue et al., *J. Magn. Res*63 (1985) 418;  
J. Skilling, “Proceedings in Maximum Entropy and Bayesian Methods”, Cambridge 1988, pages 45, ISBN 0792302249;  
W. I. F. David, *Nature*346 (1990) 731;  
M. Jarrell, J. E. Gubernatis, *Physics Reports* 269 (1996) 133;  
M. Asakawa, T. Hatsuda, Y. Nakahara, *Prog. Part. Nucl. Phys.* 46 (2001) 459
- [94] G. Aarts, C. Allton, J. Foley, S. Hands, S. Kim, *Phys. Rev. Lett.* 99, 022002 (2007)
- [95] J. Engels, O. Vogt, *Nucl. Phys. B*832, (2010) 538
- [96] H.-T. Ding, A. Francis, O. Kaczmarek, H. Satz, F. Karsch, W. Soldner, *PoS LATTICE2010* (2010) 180;  
H.-T. Ding, O. Kaczmarek, F. Karsch, H. Satz, W. Soldner, *PoS LAT2009* (2009) 169;  
H.-T. Ding, O. Kaczmarek, F. Karsch, H. Satz, *PoS CONFINEMENT8* (2008) 108
- [97] F. Karsch, H. W. Wyld, *Phys. Rev. D*35 (1987) 2518
- [98] F. Karsch, E. Laermann, P. Petreczky, S. Stickan, I. Wetzorke, *Phys. Lett. B*530 (2002) 147
- [99] S. Gupta, *Phys. Lett. B* 597, 57 (2004)
- [100] M. Golterman, J. Smit, *Nucl. Phys. B*255, (1985) 328

## *Bibliography*

- [101] R. V. Gavai, S. Gupta, Phys. Rev. D64 (2001) 074506
- [102] R. V. Gavai, S. Gupta, P. Majumdar, Phys.Rev. D65 (2002) 054506
- [103] F. Karsch, S. Ejiri, K. Redlich, Nucl.Phys. A774 (2006) 619;  
C.R. Allton et al., Phys.Rev. D71 (2005) 054508
- [104] M. Cheng et al., Phys.Rev. D79 (2009) 074505
- [105] T. Altherr, P. Aurenche, Z.Phys. C45 (1989) 99
- [106] D. Fernandez-Fraile, A. Gomez Nicola, Eur. Phys. J. C 62, (2009) 37;  
Nucl. Phys. A 785, (2007) 166;  
Phys.Rev. D73 (2006) 045025
- [107] O. Kaczmarek, F. Karsch, F. Zantow, P. Petreczky, Phys. Rev. D 70, (2004) 074505; Phys. Rev. D 72, 059903(E) (2005)
- [108] H. van Hees, R. Rapp, Nucl. Phys. A806, (2008) 339
- [109] Y. Akamatsu, H. Hamagaki, T. Hatsuda, T. Hirano, arXiv:nucl-th/1107.3612
- [110] S. Wissel, "Mesonic Correlation Functions from Light Quarks and Their Spectral Representation in Hot Quenched Lattice QCD", Dissertation Bielefeld University (2006)
- [111] P. B. Arnold, G. D. Moore, Laurence G. Yaffe, JHEP 0011 (2000) 001;  
P. B. Arnold, G. D. Moore, Laurence G. Yaffe, JHEP 0305 (2003) 051
- [112] G. D. Moore, J.-M. Robert, hep-ph/0607172
- [113] P. F. Bedaque, Phys.Lett. B593 (2004) 82
- [114] G. Aarts, C.R. Allton, S.J. Hands, J. Foley, S. Kim, PoS LATTICE2010 (2010) 166;  
G. Aarts, C. Allton, J. Foley, S. Hands, S. Kim, AIP Conf.Proc. 1261 (2010) 203
- [115] F. Karsch, E. Laermann, In \*Hwa, R.C. (ed.) et al.: Quark gluon plasma\* 1
- [116] M. Cheng, A. Francis, S. Mukherjee et al., Eur.Phys.J. C71 (2011) 1564
- [117] D. Adamova et al., Phys. Lett. B 666, (2008) 425

# Acknowledgements

*“All the world’s a stage,  
And all the men and women merely players;  
They have their exits and their entrances;  
And one man in his time plays many parts;  
His acts being seven ages...”*

*- William Shakespeare*

For me one of these ages is the age of education in Bielefeld. And as this wonderful act of my life draws to a close, I pause to thank all those who have played their role on my stage and who will hopefully continue to do so in the future.

Even if I cannot name all of you, for that would fill many thick volumes, I hope each of you knows in his heart that they belong on this list.

Foremost I wish to thank Olaf Kaczmarek, Frithjof Karsch and Edwin Laermann for their supervision and constant support throughout this work. I deeply acknowledge the valuable lessons they tried to teach me, and I am sure I will benefit from them for all times. Thank you for giving me the privilege to learn from the best.

Indispensable for the success of this work in an entirely different arena I wish to thank Gudrun Eickmeyer and Susi von Reder. Thank you for always being there and having an open ear for our problems. You have made things possible that are nearly impossible anywhere else.

In my time here in Bielefeld many have passed through our work group and it is them that I wish to thank for their help and discussions, just to name a few these are Wolfgang Unger, Sabine Bönig, Jack Liddle, Nils Hüske, Rossella Falcone, Jens Langelage, Yannis Burnier, Jan Möller, Marina Seikel, Wolfgang Söldner and many more.

## *Acknowledgements*

At this point I want to especially thank my comrade-in-arms Heng Tong Ding. I would never want to miss the discussions and arguments we had about MEM and spectral functions. And I very cherish the memories of the times in Paris and Brookhaven.

Looking back at my time in Bielefeld, I realize I never could have done it without my friends: Stefan Fröhlich, Simon Hennig, Andre Lampe, Marc Löllmann, Maik Stuke, Borello, Pulki and recently Fabian and Idir. My heart is heavy that I will not be there for our lunch date and I wish you guys all the best.

Kisses go out to Susanne, you have helped me in more ways than you will ever know. And I love you for every one.

Finally I thank my family and my parents for providing me the environment and possibilities to follow my dreams.

14th September, 2011

Anthony S. Francis  
*In loving memory of Jason S. Francis.*

# Eigenständigkeitserklärung

Zur Dissertation mit dem Titel

**Thermal Dilepton Rates from Quenched Lattice QCD**  
**- A study of thermal spectral functions in the continuum limit of quenched lattice QCD, at vanishing and finite momentum**

Hiermit erkläre ich die vorliegende Arbeit selbständig und ohne fremde Hilfe verfasst und nur die angegebene Literatur und Hilfsmittel verwendet zu haben

Bielefeld, 14.09.2011

---

Anthony Francis